# Computational and experimental thermo-mechanics of metal additive manufacturing: stress, warpage, cracks and properties

Xufei Lu

Doctoral Degree in Structural Analysis

Thesis submitted as a compendium of publications

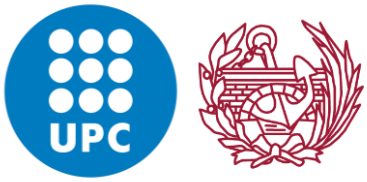


Technical University of Catalonia

Department of Civil and Environmental Engineering

Supervisors: Prof. Michele Chiumenti

Prof. Miguel Cervera

June 2022

# Acknowledgements

First and foremost, I would like to express my sincere gratitude to my supervisors, Prof. Michele Chiumenti and Prof. Miguel Cervera for the trust you put in me since the beginning and for your insightful guidance and full support. You gave me the freedom and all the support needed during my doctoral studies. Your knowledge and passion for science drove me beyond my limits and made the completion of this project possible.

I would like to acknowledge Prof. Xin Lin, Prof. Junjie Li, Prof. Weidong Huang, Prof. Hua Tan, Prof. Meng Wang, Prof. Jianrui Liu, Prof. Yufan Zhao, Dr. Liang Ma, Dr. Haiou Yang, Dr. Lilin Wang, Dr. Jun Yu at NPU in Xi'an of China for your extended help and the numerous discussions, which were a source of motivation and brought new insights to this research work. I especially thank Guohan Zhang, Aitang Xue, Hanlin Ding, Wenbo Wang and Wenyou Zhang for your strong support in the AM experiments.

The financial support provided by the China Scholarship Council is gratefully acknowledged.

I would like to sincerely thank all the members of the COMET team: Gabriel, Kim, Carlos, Mehdi, Iván, Henning, Manuel and Narges for your help in my study. I also would like to thank my colleagues from other groups at CIMNE for making my study an unforgettable experience: Raúl, Uxué, Riccardo, Saman, Christian, Ignacio, Marco, Sheraz, Sthefania, Rubén, Sebastian, Marc, Agustina, Pau and many others.

My special thanks to Yuanbing Wu, Xiangbo Bu, Yu Yin, Yang Wang, Xiao Hu, Fei Song (and many others) for your help and friendship in my life in Barcelona.

Lastly, I want to express my deepest and sincere gratitude to my family and Moon for your unwavering encouragement, support, love and patience throughout this study.

# Abstract

Metal additive manufacturing (AM) is an advanced evolutionary processing technology, which can achieve the near-net shape fabrication of arbitrary complex structures, and it has been broadly applied in different industries. However, AM is a complex multi-physics and multi-scale process characterized by the layer-by-layer building through applying a high-energy beam as the heat source. During the AM process, materials often experience repeated heating and cooling cycling, where the laser interaction with the metal powder generates thermally triggered metallurgical evolution and mechanical response. As a result, large temperature gradients and complex thermal histories easily lead to a non-uniform microstructural distribution, large residual stresses, thermal deformations and cracks. Such drawbacks pronouncedly affect the final mechanical properties of AM-builds and limit the extensive application of AM.

Therefore, the objectives of this thesis are (i) to understand the thermal, metallurgical and mechanical behavior during AM, (ii) to shed light on the generation of residual stresses and the stress-induced deformations and cracks, and (iii) to further propose several effective strategies to control such defects.

To improve the efficiency and reliability of the research investigation, an enhanced thermomechanical finite element framework for AM is developed and validated by numerous in-situ temperature and displacement measurement experiments. Furthermore, the calibrated model is employed to perform a large number of thermal and mechanical analyses in AM processes. For this purpose, Ti6Al4V titanium alloy is selected as the printing material for this investigation due to its wide application in aeronautics and astronautics.

First of all, the effect of the complex thermal histories experienced on the metallurgical evolution and the formation of layer bands in multi-layer multi-pass Ti6Al4V blocks fabricated by laser directed energy deposition (DED) are explored. Based on the analysis

of the predicted thermal histories and the experimental microstructure observation, the quantitative processing-thermal-microstructure-microhardness relationship is established.

Next, the mechanical behavior of AM-components in terms of residual stresses, part warpages and cracks are analyzed in detail. Here, the influence of the scanning strategy on the heat transfer process and the evolution of the thermally induced mechanical variables in laser-based AM are studied to reduce residual stresses and deformations of rectangular DED-parts. Next, the thermal deformation of several different thin-walled structures printed by laser powder bed fusion (LPBF) are experimentally and numerically investigated in order to control the stress-induced warpages and to increase the geometrical precision of AM lightweight components. The generation of residual stresses and the key factors for their development are elucidated. A novel strategy to optimize the design of the substrate structures is proposed to mitigate the residual stresses induced by AM process. Moreover, a systematical evaluation on the effectiveness of different strategies to control the residual stresses in AM is carried out. Lastly, the formation mechanism of cracks is explored by analyzing the mechanical behavior of two T-shape parts deposited on different substrates without and with grooves. An innovative strategy to optimize the substrate geometry lowering its mechanical stiffness is proposed to prevent cracks during LPBF.

Finally, a proposal to achieve high-quality Ti6Al4V AM-builds with lower residual stresses and homogeneous microstructures is detailed based on the better understanding on the process-structure-property interactions, and the formation and control of residual stresses in AM processes.

This thesis presents further insight into the interactive thermal-metallurgical-mechanical behavior in metal AM and provides a comprehensive framework to guide AM designers to optimize process configuration when fabricating complex metal components.

# Resumen

La Manufactura Aditiva con metal (MA) es una tecnología avanzada de procesamiento evolutivo que puede lograr la fabricación de componentes estructurales complejos en forma casi final, y que se ha aplicado en los últimos años en diferentes sectores industriales. Sin embargo, la MA es un proceso complejo que implica múltiples fenómenos físicos a diferentes escalas, caracterizado por la construcción capa por capa mediante la aplicación de un haz de alta energía como fuente de calor. Durante el proceso MA, los materiales a menudo experimentan ciclos repetidos de calentamiento y enfriamiento, donde la interacción del láser con el polvo de metal genera una evolución metalúrgica termo-activada y una respuesta mecánica. Como resultado, los fuertes gradientes de temperatura y las historias térmicas complejas pueden conducir fácilmente a una distribución micro-estructural no uniforme, grandes tensiones residuales, deformaciones térmicas y fisuras. Estos inconvenientes afectan de forma determinada a las propiedades mecánicas finales de las piezas construidas mediante MA y limitan la aplicación amplia de esta tecnología.

Esta tesis aporta una mayor comprensión del comportamiento termo-metalúrgico-mecánico interactivo en la fabricación aditiva de metal y proporciona un marco integral para ayudar a los diseñadores de fabricación aditiva para optimizar la configuración del proceso al fabricar componentes metálicos complejos.

En consecuencia, los objetivos de esta tesis son: (i) comprender el comportamiento térmico, metalúrgico y mecánico durante los procesos de MA, (ii) clarificar el proceso de generación de tensiones residuales y las deformaciones y fisuras inducidas por las tensiones generadas en el proceso de fabricación, y (iii) proponer varias estrategias efectivas para controlar dichos defectos.

La investigación se lleva a cabo en un marco termo-mecánico mejorado de elementos finitos para MA, desarrollado y validado mediante numerosos experimentos de medición

de desplazamiento y temperatura in situ. Además, el modelo calibrado se emplea para realizar una gran cantidad de análisis térmicos y mecánicos en procesos MA. Para ello, se usa la aleación de titanio Ti6Al4V como material de impresión debido a su amplia aplicación en aeronáutica y astronáutica.

En primer lugar, se explora el efecto de las historias térmicas complejas experimentadas en la evolución metalúrgica y la formación de bandas de capas en bloques de Ti6Al4V fabricados mediante deposición de energía dirigida por láser (DED). A partir del análisis de las historias térmicas pronosticadas y la observación de la microestructura experimental se establece la relación cuantitativa proceso-térmico-microestructura-microdureza.

En segundo lugar, se analiza en detalle el comportamiento mecánico de los componentes MA: tensiones residuales, deformaciones parciales y fisuras. Aquí se estudia la influencia de la estrategia de escaneo en el proceso de transferencia de calor y la evolución de las variables mecánicas inducidas térmicamente en la MA basada en láser para reducir las tensiones residuales y las deformaciones de las piezas rectangulares DED. A continuación, se investiga experimental y numéricamente la deformación térmica de varias estructuras diferentes de paredes delgadas impresas por fusión láser de lecho de polvo (LPBF) para controlar las deformaciones inducidas por las tensiones generadas y aumentar la precisión geométrica de los componentes ligeros MA. Se estudian la generación de tensiones residuales y los factores clave para su desarrollo. Se propone una estrategia novedosa para optimizar el diseño de las estructuras de sustrato para mitigar las tensiones residuales inducidas por el proceso MA. Además, se lleva a cabo una evaluación sistemática de la eficacia de diferentes estrategias para controlar las tensiones residuales en MA. Por último, se explora el mecanismo de formación de fisuras analizando el comportamiento mecánico de dos piezas en forma de T depositadas sobre diferentes sustratos con y sin ranuras. Se propone una estrategia innovadora para optimizar la geometría del sustrato reduciendo su rigidez mecánica para evitar la formación de fisuras durante LPBF.

Finalmente, se detalla una propuesta para lograr construcciones MA de Ti6Al4V de alta calidad con tensiones residuales más bajas y microestructuras más homogéneas basada en una mejor comprensión de las interacciones proceso-estructura-propiedad, y la formación y control de tensiones residuales en los procesos de MA.

# Contents

Chapter 1

# Introduction

The state of the art, objectives, scope and outline of the thesis are presented in this chapter. Firstly, the state of the art for the difficulties and challenges in metal additive manufacturing processes are discussed. Next, the objectives for solving some of the current problems existing in metal AM are proposed. Finally, a description of the research dissemination carried out in this thesis is detailed.

## 1.1 State of the art

### 1.1.1 Metal additive manufacturing

In comparison to the conventional manufacturing methods, metal additive manufacturing (AM) is based on an incremental layer-by-layer deposition technique according to a user-defined scanning strategy, eventually forming net or near-net shape components [1]. As an advanced solid free-form manufacturing technology, AM commonly utilizes powder or wire as feedstock to fabricate several complex components with high-performance.

During approximately 30 years, AM technology has been studied and developed demonstrating its superiority in unrivalled design freedom and short lead times [2].

According to the material feeding methods, metal AM technologies are mainly divided into two mainstreams: direct energy deposition (DED) and powder bed fusion (PBF) [3-6]. The DED processes mainly include laser solid forming (LSF), electron beam wire deposition (EBWD) and wire-arc additive manufacturing (WAMM). In DED the metal powder (or wire) is spread coaxially with the high-energy beam input, as shown in Figure 1.1(a). The PBF adopts a high-energy heat source to selectively melt the fine powders laid in the building chamber in advance to achieve the fabrication of 3D components. Typical PBF techniques consist of selective laser melting (SLM), electron beam melting (EBM) and selective laser sintering (SLS), as shown in Figure 1.1(b).

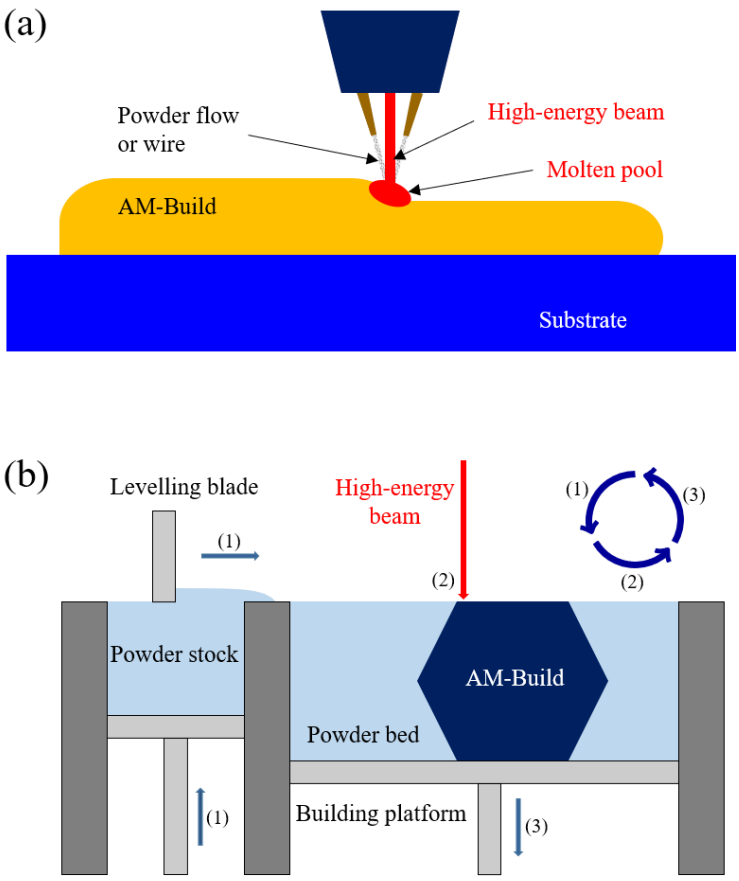


**Figure 1.1. Typical additive manufacturing (AM) technologies: (a) directed energy deposition (DED) processes; (b) powder bed fusion (PBF) processes.**

Although different machine manufacturers adopt various names as trademarks, the diverse AM processes basically share a similar approach to go from the virtual CAD model to the physical resultant component [3]. Firstly, the design concept of parts is

translated into a three-dimension CAD geometrical model. A Standard Tessellation Language (STL) file is created according to the desired geometry. Next, the STL file is sliced into several layers and, for each layer a scanning (or deposition) path is generated describing the actual material deposition sequence to build the part by the AM machine. A variety of process parameters (i.e. laser power, hatch distance, layer thickness, scanning speed, etc.) needs to be defined and optimized. Finally, the 3D-printing is carried out by the AM machine until the buildup is completed.

### 1.1.2 Residual stresses, distortions and cracks in AM

Since AM is characterized by a layer-by-layer fabrication process, the metal depositions experience a large number of intense and unsteady heating, melting, solidification and cooling cycles. This generates high temperature gradients and large thermal strains [7-9]. Typically, thick substrates with a strong stiffness are usually used for preventing part warpage, causing stress accumulations in the build. Once the magnitude of the stresses reach the yield limit or the tensile strength, part distortions and cracks occur in turn, resulting in the failure of the AM-build, as shown in Fig. 1.2 [10-12]. Thereby, these drawbacks significantly hinder the extensive application of AM technology in different industrial sectors.

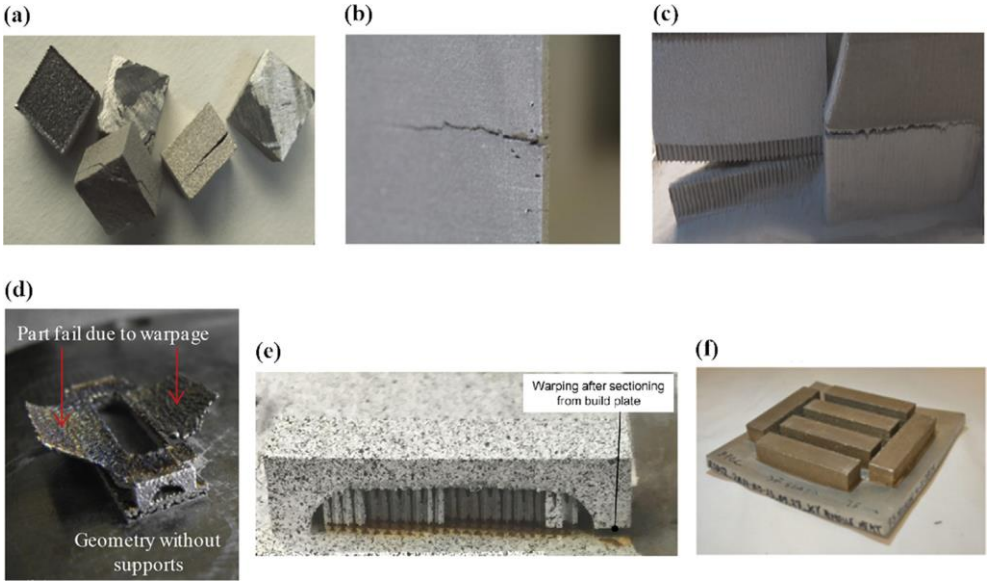


**Figure 1.2. Cracks and distortion in AM-parts [10]: (a) cracking in Inconel-718 alloy components; (b) cracking in Ti-6Al-4V alloy parts; (c) cracking in the support-part interface; (d) warpage of a cantilever structure; (e) warping of the bridge structure detached from the substrate; and (f) warping test on the printed parts.**

Residual stresses can be classified according to their length scales: types I, II and III [10]. Type I are macro-stresses over large distances or part-level sizes. High macro-stresses easily induce large deformations or even cracks in AM-parts. Type II and type III correspond to the residual stresses at mesoscopic scale (due to different phases in materials) and at atomic scale because of dislocations, respectively. Types II and III are not considered in this thesis because they have no significant effect on the as-built material performance.

In order to mitigate the residual stresses in AM, their formation must be better understood. Figure 1.3 schematically illustrates the thermally induced mechanical response in AM. Figure 1.3(a) shows the temperature and stress distributions around the Heat Affected Zone (HAZ) triggered by the moving heat source in the printing process. Note that large compressive stresses are produced in front of the molten pool because of the large thermal expansion of the heated material, often constrained by the cold substrate. The stress level in the molten pool is almost null due to the significant reduction of the yield stress when temperatures approach the melting point. After the heat source leaves, the molten pool quickly solidifies and contracts in a short time. Often, such contraction is restrained by the surrounding metal depositions. As a result, large tensile stresses are generated in the region behind the molten pool. Once the induced tensile or compressive stresses reach the yield limit, plastic deformations are developed.

To show how residual stresses generate in high-energy AM processes, two points P and Q located at the edges and the molten pool are taken as a reference, as shown in Figure 1.3. As the heat source approaches the two points, they experience increasing compressive stresses due to the thermally induced material expansion; the stress evolution firstly follows the line ab and then turns into plastic flow if the accumulated stresses exceed the yield strength, corresponding to the line bc. After the heat source crosses, the metal depositions shrink with the temperature drop and tensile stresses are developed. In the case of point P, all the tensile stresses are elastically accommodated without further plastic flow as shown by the line cd in Figure 1.3(b). Differently, point Q experiences an additional plastic flow (line de) after the elastic tensile branch (line cd) as shown in Figure 1.3(c). When the deposited materials cool down to ambient temperature, residual tensile stresses are developed and marked by the large (brown) arrows in Figure 1.3.

Two factors are responsible for the formation of residual stresses in AM-parts: (i) Maximum Temperature Gradient (MTG), induced by the applied high-energy beam heat

source; and (ii) the mechanical constraints between the adjacent materials (e.g. substrate and deposition) [13,14].

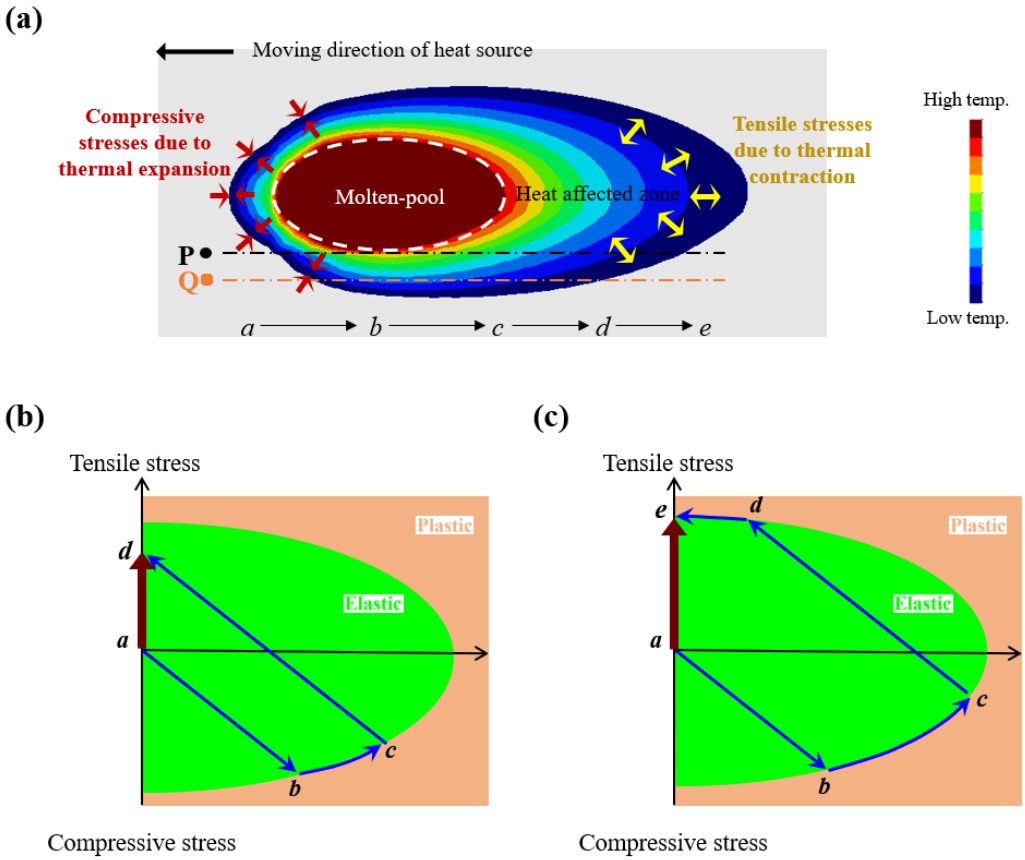


**Figure 1.3. (a) Temperature and stress distribution at the HAZ indued by a moving heat source in AM. Thermo-mechanical response at different material points: (a) point Q at the edge of the molten pool; (b) point P slightly further from the molten pool.**

### 1.1.3 Microstructures and properties of AM-parts

In AM, due to the repeated heating-cooling cycling that occurs with the deposition of each subsequent layer, the microstructure of AM-builds experiences complex changes throughout the whole fabrication process, especially for these materials with complicated metallurgical phase transformations [15-17]. On the one hand, the thermal conditions in the molten-pool region promote the epitaxial growth of columnar grains with an associated strong solidification texture [18]. On the other hand, the thermal cycling experienced in AM may engender regularly spaced layer-bands throughout the deposits along the building direction [19]. Additionally, recurring heating and quenching also may provide an intrinsic heat treatment for the previously deposited layers, causing the

occurrence of solid-state precipitation reactions and microstructural coarsening in some cases [20,21].

Although the temperature gradient and cooling rate are the critical thermodynamic factors influencing the microstructural evolution in AM, their control is quite difficult because of the varying and complicated thermal distribution in the molten pool [22]. As a consequence, AM-built products typically show non-uniform distribution of microstructures and unsatisfactory mechanical properties [23].

Understanding the relationship between the thermal history and the metallurgical evolution as well as the thermo-mechanical response during the building processes is of importance for achieving the fabrication of high-quality AM-components.

### 1.1.4 Numerical simulation for AM

To better understand the AM process, both experiments and simulations are employed to optimize the manufacturing technology taking into account a large number of variables. Experiments are time-consuming and expensive, and several parameters involved can be difficult to measure [9]. Alternatively, the Finite Element (FE) method provides a feasible and efficient way to predict these processing parameters and shed light on the underlying mechanisms of defects formation within the metal parts fabricated by AM [24-29]. In AM, several numerical models have been developed to investigate the thermal history [28,30], the mechanical response [31-34] and the microstructure evolution of the fabricated components [35-38].

The FE method is widely applied to solve the governing partial differential equations corresponding to different physical phenomena of interest. For AM modelling, the FE method solves heat transfer (balance of energy) and the mechanical (balance of momentum) equilibrium equations. The weak-form of the balance equations uses the Galerkin residual weight method [39].

Zhang et al. [40] developed a part-scale FE model which achieves the prediction of the temperature evolution of complex SLM-built geometries. Chiumenti et al. [28,41] proposed a FE framework for the numerical simulation of the heat transfer analysis of AM processes. The numerical model developed is based on the (birth-death elements) FE activation strategy technique, to follow the growth of the geometry according to the same

scanning strategy sent to the numerical control system of the AM machine. The numerical model analyses the sensitivity of the AM process to different heat dissipation mechanisms through the surrounding environment.

The mechanical behavior of AM parts depends on the thermal history. Thus, several coupled thermo-mechanical models for AM have also been developed. Denlinger [42] developed a model to simulate the thermo-mechanical responses of Ti-6Al-4V and Inconel® 625 during the AM process. They found that only in Ti-6Al-4V both residual stress and distortion are reduced due to stress relaxation. Li et al. [43] proposed a 3D FEM model considering the phase transition and volume shrinkage in the multi-track multi-layer laser PBF process. Smith et al. [44] utilized the computational phase diagram thermodynamics in the thermo-mechanical analysis via FEM, by which the microstructure, thermal distortion and the residual stress were predicted preliminarily. Lindgren et al. [30,45,46] developed a coupled thermal-mechanical FE model based on computational welding mechanics (CWM) to achieve the modelling of metal deposition. Huang et al. [47] achieved accelerating of the stress analysis of WAAM by combining the iterative substructure method, dynamic mesh refining method, and graphics processing unit based on explicit FEM analysis.

Due to the potential of AM in high-end manufacturing industry, the analysis of the microstructure evolution of built parts is of great interest [16,17]. Figure 1.4 schematically shows the microstructures forming of Ti-6Al-4V during continuous cooling [48].

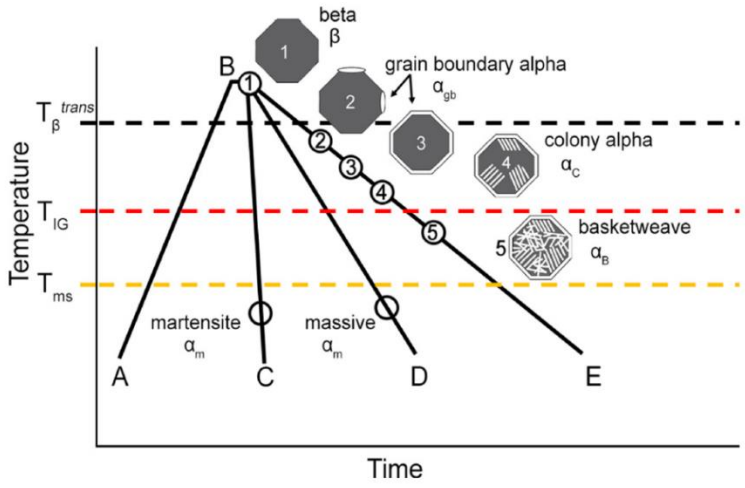


**Figure 1.4. Schematic representation of Ti6Al4V microstructures forming in continuous cooling.**

At a low cooling rate (path BE), the β→α+β diffusion-controlled transformation can be modeled by means of a Johnson-Mehl-Avrami-Kolmogorov (JMAK) equation defined by temperature-dependent parameters extracted from temperature-time-transformation (TTT) curves [49,50]. The α-lath thickness is inversely proportional to the cooling rate and it can be calculated by an empirical Arrhenius equation [51,52]. At high cooling rate (between paths BC and BD), martensite or massive α phases (αm) can form from the residual β still available once the martensite start temperature Tm (around 650–500 ℃) is reached. This transformation is considered diffusion-less and can be computed using the Koistinen-Marburger law, an empirical relationship that depends on the undercooling with respect to Tm [53].

Lindgren et al. [35,54,55] developed density type simulation methods to predict the microstructural evolution during solid-state phase-change in AM Ti-6Al-4V, especially for large-scale thermal-metallurgical-mechanical coupled problems. The phase fractions of diffusion and diffusionless phase-changes and the dependent properties can be effectively predicted by calibrated models. Baykasoğlu et al. [48] presented a coupled microstructure FE modeling framework for predicting the evolution of volumetric phase fractions and micro-hardness during DED of Ti6Al4V. The model combines the formation and dissolution kinetics of grain boundary, Widmanstätten colony/basketweave, massive/martensitic α and β phases. Tan [56] developed a thermo-metallurgical-mechanical coupling model to predict temperature, phase-change and residual stress for the multi-track multi-layer SLM of Ti6Al4V. However, their model was developed based on the unconfirmed hypothesis that the material volume decreases in the α→β phase transformation as the temperature rises.

In general, while most of the modelling works on microstructure to date are focused on small parts such as single-tracks, the metallurgical prediction in part-scale AM builds is still a challenge.

Furthermore, there is a growing research interest on developing integrated computational tools to enhance the understanding and design of AM processes. Yan et al. [57] proposed a process-structure-property modelling framework to imitate different stages in EBM. They integrated thermal-fluid flow models, a cellular automaton and self-consistent clustering analysis to predict the mechanical properties (fatigue-life) of Ti-6Al-4V. Liu et al [58] also developed a modelling framework for Ti-6Al-4V. Their tool firstly adopted FE to predict temperature fields, and then performed phase-filed simulations to predict

metallurgical evolution. Finally, the mechanical behavior was predicted by using fast Fourier transform-based elasto-viscoplastic models to analyze the obtained microstructures. Similarly, Pinomaa et al [59] achieved a prediction of the stress-strain evolution and fatigue-life of AM Ti-6Al-4V based on phase-field simulated microstructures and predicted thermal history.

### 1.1.5 Control of residual stresses and distortions in AM

In the literature, different methods have been proposed to reduce the distortions and residual stresses in AM taking advantage from the previous experience in welding processes. On the one hand, preheating the substrate prior of AM is usually regarded as an effective method to reduce the generation and accumulation of residual stresses by the MTG reduction, allowing for the inverse relationship between preheating temperature and residual stresses [25]. Klingbeil et al. [60] and Chin et al. [61] found that using a moderate preheating temperature and a better mechanical constraining on the substrate can mitigate both stresses and distortions. Nevertheless, preheating the substrate or build chamber inevitably changes the temperature field distributions and affects the microstructural evolution. On the other hand, optimizing AM process parameters (e.g. laser power, scan speed and scan path) also favors the mitigation of residual stresses and part warpages by lowering the MTG [62,63]. However, the optimization of AM variables and building strategy is relatively complex, affecting the metallurgical evolution and the resulting mechanical properties. The developed strategies based on the MTG reduction are not very efficient when high-energy beams are applied generating sharp MTG.

The application of assistant tools, like the rolling technique [26] or laser shock peening [64], during AM or the post-processing stress release (by heat or mechanical treatments) is beneficial for stress mitigation, and increases both fabricating time and cost.

Several strategies have been established to prevent stress-induced warping and cracking, but an enhanced combination between them still is necessary when manufacturing large-sized AM components with more complex geometries.

## 1.2 Objectives

The objectives of this thesis are: (i) to understand the intrinsic relationship between AM process variables, temperature field, metallurgical evolution, mechanical response and resultant properties in metal AM processes; (ii) to disclose the formation mechanisms of residual stresses and distortions as well as cracks; and (iii) to enhance the AM fabrication of high-quality metal parts by simultaneously controlling residual stresses and microstructure.

This research addresses the production of high-quality AM components cutting down of the processing costs. Although several publications have focused on the simulation of AM processes based on the FE method, the thermo-mechanical prediction and the microstructure evolution need further investigation due to the complexity of the thermal cycles in the fabrication of large-scale parts. In addition, the AM process is characterized by the highly non-linear nature of the multi-coupled physical phenomena.

Therefore, to achieve the proposed aim, an enhanced FE thermo-mechanical computational framework for AM firstly is developed. An enthalpy-based thermal model is implemented allowing for the analysis of phase changes to improve the prediction accuracy of temperature field. To achieve the microstructural prediction in part-scale builds, a quantitative thermal-metallurgical relationship is proposed by coupling microstructure with thermal history predicted by the enhanced thermal model. Also, a new constitutive model coupled with the temperature field and suitable for AM is developed to improve the material response during both the solid and the liquid phases.

This coupled thermo-mechanical model together with the thermal-metallurgical module for AM processes are calibrated and validated with Ti-6Al-4V specimens and demonstrators. In-situ experiments demonstrate the prediction capability of the model.

Through using the combination of the simulation predictions and experimental results, the temperature, the stress responses and the metallurgical evolution of Ti-6Al-4V in metal AM processes are analyzed to study several defects (e.g. thermal warpages, residual stresses and cracks) and the metallurgical features (e.g. layer band and coarsening). Specifically, the quantitative thermal-microstructure relationship and several efficient strategies to mitigate both the residual stresses, induced warpages and cracks in AM process are proposed. Finally, high-quality Ti-6Al-4V components are manufactured

based on the comprehensive understanding on the complex physical interactions involved in AM processes.

## 1.3 Thesis outline

In this thesis, the thermo-mechanics of metal additive manufacturing have been addressed: stresses, warpages, cracks, microstructure and hardness properties.

This document is conceived as a compendium of publications. Thereby, six of the Chapters (3 to 8) are a brief introduction to the corresponding articles submitted to international peer-reviewed journals.

Chapter 1 presents the state of the art, the objectives of the work, the thesis outline and the research dissemination. Chapter 2 introduces the coupled thermo-mechanical computational framework for AM analysis. Chapter 3 (first paper) presents the process-thermal-microstructure-property relationship in DED processes. Chapter 4 (second paper) introduces the effect of scan strategies on the mechanical behavior of rectangular parts fabricated by DED. Chapter 5 (third paper) presents the warpage control of thin-wall structures made by SLM. Chapter 6 (fourth and fifth papers) introduces the strategies of mitigating residual stresses in AM. Chapter 7 (sixth paper) studies the cracking mechanism and prevention in AM processes. Chapter 8 (seventh paper) presents a successful story for fabricating high-quality AM parts. Chapter 9 closes the thesis with a discussion of the conclusions and future scope of the research lines. Finally, details of all in-text references are provided.

## 1.4 Research dissemination

The doctoral Thesis is presented as a compendium of the following seven publications in international peer-reviewed journals:

- **Lu X.**, G. Zhang, J. Li, M. Cervera, M. Chiumenti, J. Chen, X. Lin & W. Huang. (2021). **Simulation-assisted investigation on the formation of layer bands and the microstructural evolution in directed energy deposition of Ti6Al4V blocks**. Virtual and Physical Prototyping, 16(4), 387-403. https://doi.org/10.1080/17452759.2021.1942077

- **Lu X.**, M. Cervera, M. Chiumenti, J. Li, X. Ji, G. Zhang & X. Lin. (2020). **Modeling of the Effect of the Building Strategy on the Thermomechanical Response of Ti-6Al-4V Rectangular Parts Manufactured by Laser Directed Energy Deposition**. Metals, 10(12), 1643. https://doi.org/10.3390/met10121643

- **Lu X.**, M. Chiumenti, M. Cervera, H. Tan, X. Lin, & S. Wang. (2021). **Warpage Analysis and Control of Thin-Walled Structures Manufactured by Laser Powder Bed Fusion**. Metals, 11(5), 686. https://doi.org/10.3390/met11050686

- **Lu X.**, M. Chiumenti, M. Cervera, J. Li, X. Lin, L. Ma, G. Zhang & E. Liang. (2021). **Substrate design to minimize residual stresses in Directed Energy Deposition AM processes**. Materials & Design, 202, 109525. https://doi.org/10.1016/j.matdes.2021.109525

- **Lu X.**, M. Cervera, M. Chiumenti & X. Lin. (2021). **Residual Stresses Control in Additive Manufacturing**. Journal of Manufacturing and Materials Processing, 5(4), 138. https://doi.org/10.3390/jmmp5040138

- **Lu X.**, M. Chiumenti and M. Cervera. (2022). **Crack-free laser powder bed fusion by substrate design optimization**. Additive Manufacturing (Submitted).

- **Lu X.**, M. Cervera, M. Chiumenti, G. Zhang & X. Lin. (2021). **Mitigation of residual stresses and microstructure homogenization in directed energy deposition processes**. Engineering with Computers. https://doi.org/10.1007/s00366-021-01563-9

Chapter 2

# Coupled thermo-mechanical framework for AM

In this chapter, the coupled thermo-mechanical computational framework developed for AM analysis is presented. This numerical framework includes: the heat transfer analysis, the mechanical (stress) analysis, the material constitutive models, the finite element strategy to deal with the AM process simulation including the definition of the scan path.

## 2.1 Thermal model

### 2.1.1 Balance of energy equation

During AM processes, heating and cooling are controlled by the energy balance equation [28]. This can be stated as:

$$\dot{H} = -\nabla \cdot \mathbf{q} + \dot{Q} + \dot{D}_{mech} \tag{2.1}$$

where $\dot{H}$ is the enthalpy rate (per unit of volume), $\mathbf{q}$ is the heat flux (per unit of surface), $\dot{Q}$ is the heat source and $\dot{D}_{mech}$ is the thermo-mechanical dissipation rate (per unit of volume).

In metal AM processes, a very intense high-energy beam (e.g. laser, electron-beam or arc) is applied as the heat source input, producing the high temperature molten-pool. Thereby, the thermo-mechanical dissipation, $D_{mech}$, can be neglected if compared to the heat source $\dot{Q}$ in AM.

During the phase transformation in heating or cooling, the material volume, $V$, can be divided into solid and liquid phases as: $V = V_S + V_L$. The solid and liquid fractions are expressed as follows: $f_S = \frac{V_S}{V}$ and $f_L = \frac{V_L}{V}$, respectively. Therefore, the evolution of the liquid fraction, $f_L$ (or $f_S = -f_L$), describes how the latent heat is released or absorbed during the phase transformation, as shown in Figure 2.1.

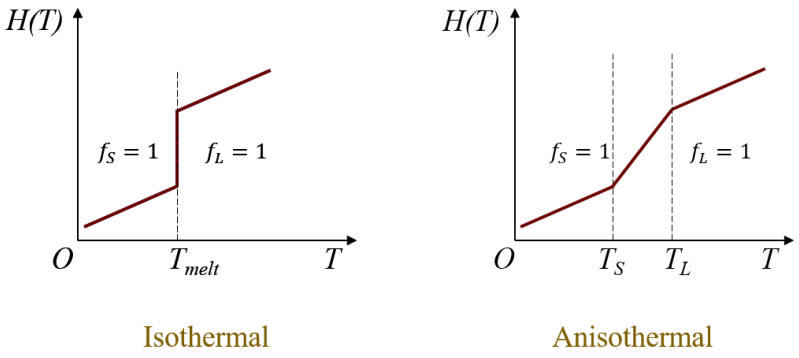


**Figure 2.1. Evolution of enthalpy $H(T)$ for isothermal and anisothermal phase transformations.**

The enthalpy, $H(T, f_L)$, is a state variable, defined as a function of the temperature, $T$, and the liquid fraction, $f_L$. Thereby, the enthalpy rate per unit of volume, $\dot{H}$, yields the following:

$$\dot{H}(T, f_L) = \frac{\partial H}{\partial T}\dot{T} + \frac{\partial H}{\partial f_L}\dot{f}_L = C(T)\dot{T} + L\dot{f}_L \tag{2.2}$$

where $L = \frac{\partial H}{\partial f_L}$ is the latent heat released/absorbed in the phase transformation process, and $C(T) = \frac{\partial H}{\partial T}$ is the temperature-dependent heat capacity coefficient, provided as the product of the density, $\rho(T)$, and the specific heat, $c(T)$, of the material used, namely, $C = c\rho$.

The heat flux per unit area, **q**, is expressed as a function of the temperature gradient, according to the Fourier's law:

$$\mathbf{q} = -k(T)\nabla T \tag{2.3}$$

where $k(T) > 0$ is the temperature-dependent thermal conductivity coefficient.

### 2.1.2 Thermal boundary conditions

Let Ω be an open, bounded domain in $\mathbb{R}^n$ where $n$ is the number of dimensions of the computational domain, closed by the smooth boundary $\Gamma = \Gamma_N \cup \Gamma_D$ in which the natural or Neumann (heat flux) and essential or Dirichlet (temperature) boundary conditions are imposed, respectively, as shown in Figure 2.2(a).

$$T = T_{\mathrm{D}} \qquad \text{on } \Gamma_D \tag{2.4}$$

$$\mathbf{q} \cdot \mathbf{n} = q_n \qquad \text{on } \Gamma_N \tag{2.5}$$

In both DED and SLM, heat conduction through the fabrication platform is the predominant heat transfer mechanism because of the high conductivity of metals. In the SLM process, heat dissipation through the loose powder also plays a key role. In addition, heat convection and radiation through all the exterior surfaces of the build and the baseplate in contact with the environment need be considered.

Figure 2.2(b) and (c) show the thermal boundary conditions in the two main types of AM processes: DED and PBF. In the PBF process, the boundary $\partial\Omega$ includes the following partitions ($\partial\Omega_{pl}$, $\partial\Omega_{pow}$, $\partial\Omega_{am}$), where $\partial\Omega_{pl}$ represents the contact surfaces with the building platform, $\partial\Omega_{pow}$ stands for the surface contacting with the powder bed, and $\partial\Omega_{am}$ represents the external surfaces in contact with the ambient. Differently, the $\partial\Omega_{pow}$ partition does not exist for DED.

These boundary conditions can be expressed as:

**(1) Heat conduction through the building platform**

Generally, the geometrical size of the printing platform (and, thus its thermal inertia) is much larger than the fabricated components and the substrates. Hereby, the temperature on the contact surface $\Omega_{pl}$ can be prescribed as:

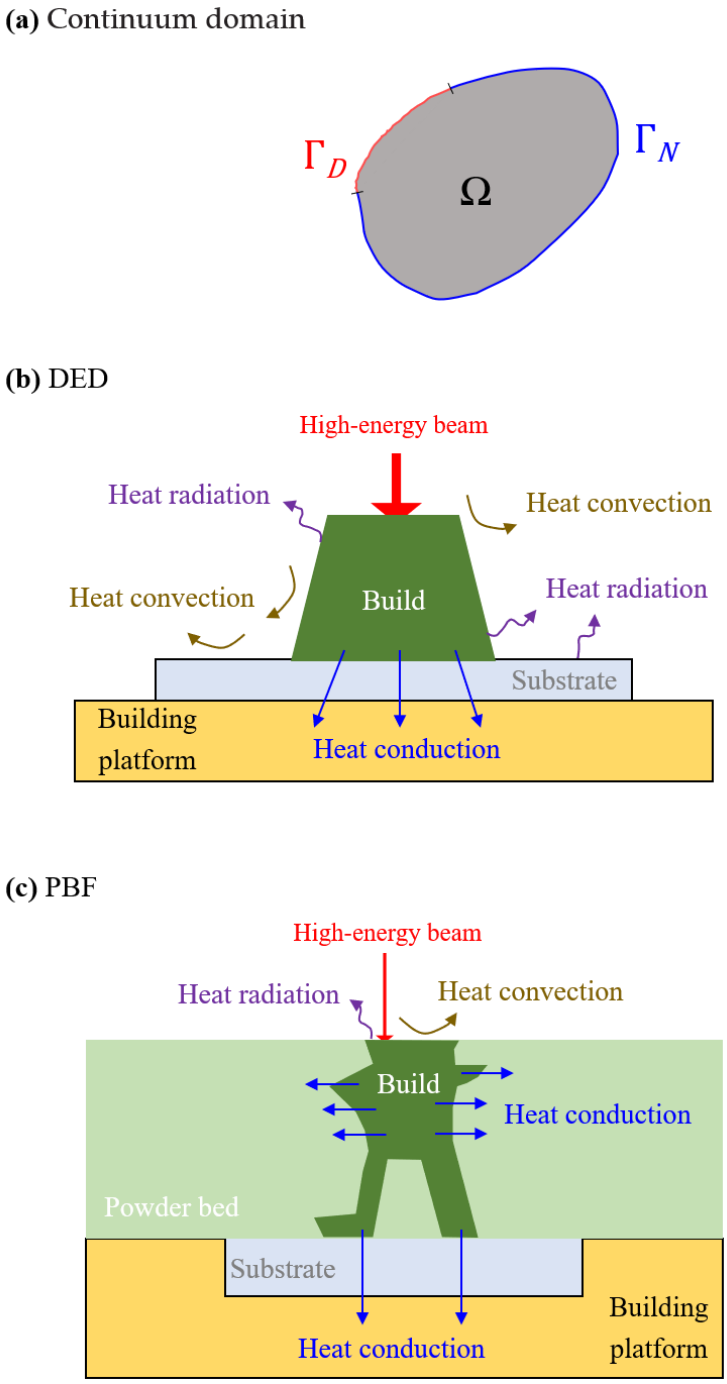


**Figure 2.2. Continuum domain and heat transfer mechanisms in AM: (i) heat convection and heat radiation through all the free surfaces of the build, (ii) heat conduction through the fabricating platform, and (iii) heat conduction through the powder bed (only for PBF).**

$$T = T_{pl}, \text{ on } \Omega_{pl}, \tag{2.6}$$

where $T_{pl}$ is the platform temperature. The heat flux due to the heat conduction process between the component and the building platform, $q_{cond}$, can be computed as follows:

$$q_{cond} = h_{cond}(T - T_{pl}), \text{ on } \Omega_{pl}, \tag{2.7}$$

where $h_{cond}$ represents the temperature-dependent Heat Transfer Coefficient (HTC) by conduction between the two materials in contact.

**(2) Heat conduction through the powder bed (only for PBF)**

If the powder bed is considered in the computational domain, the thermophysical properties of the loose power need be assessed and then used for simulating the PBF process [66]. Alternatively, the heat loss by the powder bed can be approximated using an equivalent boundary condition, based on Newton's law:

$$q_{pow} = h_{pow}(T - T_{pow}), \text{ on } \Omega_{pow}, \tag{2.8}$$

where $T_{pow}$ is the average temperature of the powder bed, and $h_{pow}$ is the HTC through conduction between the build and the powder. In this work, the powder bed is excluded in order to simplify the computational model, and $T_{pow}$ and $h_{pow}$ are assumed at 50 ℃ and 5 W/(m2 ·℃) [66], respectively.

**(3) Heat convection through the surrounding environment**

The heat dissipation through the surrounding environment, $q_{conv}$, can also be described according to Newton's law:

$$q_{conv} = h_{conv}(T - T_{room}), \text{ on } \Omega_{am}, \tag{2.9}$$

where $h_{conv}$ is the convection HTC and $T_{room}$ is the ambient temperature of the build chamber. $T_{room}$ can be assumed as constant because of the sustained shielding-gas into the chamber.

**(4) Heat radiation**

Radiation is an important mechanism for the heat loss of the molten-pool and the adjacent HAZ because of the high temperatures triggered by the heat source. The radiation heat flux, $q_{rad}$, is calculated through Stefan-Boltzmann's law:

$$q_{rad} = \varepsilon_{rad}\sigma_{rad}(T^4 - T_{room}^4), \text{ on } \Omega_{am}, \tag{2.10}$$

where $\varepsilon_{rad}$ is the emissivity of the radiating surface, and $\sigma_{rad}$ is the Stefan–Boltzmann constant. This equation can also be rewritten as:

$$q_{rad} = h_{rad}(T - T_{room}), \text{ on } \Omega_{am}, \tag{2.11}$$

where $h_{rad}(T)$ is the temperature-dependent HTC defined as:

$$h_{rad}(T) = \varepsilon_{rad}\sigma_{rad}(T^3 + T^2T_{room} - TT_{room}^2 - T_{room}^3). \quad (2.12)$$

Thus, the heat loss through the environment can be defined as a combination of radiation and convection by a computational model which assumes a combined heat transfer law:

$$q_{loss} = h_{loss}(T - T_{room}), \text{ on } \Omega_{am}. \quad (2.13)$$

In this case, $q_{loss}$ stands for the heat flux owing to the concurrent convection and radiation mechanisms, and $h_{loss}$ denotes the corresponding equivalent HTC accounting for the total heat dissipation through the surrounding environment.

### 2.1.3 Weak form of the thermal problem

Multiplying the energy balance equation in Eq. (2.1) by a test function stated in terms of the variations of the thermal field ($\delta T$) compatible with the Dirichlet boundary conditions and integrating over the computational domain ($\Omega$), the following integral expression (weak form) is obtained:

$$\int_\Omega(\dot{H}\delta T)d\Omega = -\int_\Omega[(\nabla\cdot\mathbf{q})\delta T]d\Omega + \int_\Omega\left(\dot{Q}\delta T\right)d\Omega \quad \forall\delta T \quad (2.14)$$

The chain rule for differentiation is applied to the first integral term of the right hand side to divide it in a more suitable way:

$$(\nabla\cdot\mathbf{q})\delta T = \nabla\cdot(\mathbf{q}\delta T) - \mathbf{q}\cdot\nabla(\delta T) \quad (2.15)$$

Substituting Eq. (2.15) into Eq. (2.14), applying Fourier's law in Eq. (2.3) and gathering the terms involving the unknown temperature variable in the left hand side, it yields:

$$\int_\Omega[(C\dot{T} + L\dot{f}_L)]d\Omega + \int_\Omega[k\nabla T\cdot\nabla(\delta T)]d\Omega = W_{ther}^{ext}, \quad \forall\delta T \quad (2.16)$$

where the right hand side $W_{ther}^{ext}$ stands for the external work of the thermal loads, expressed as:

$$W_{ther}^{ext} = -\int_\Omega[\nabla\cdot(\mathbf{q}\delta T)]d\Omega + \int_\Omega(\dot{Q}\delta T)d\Omega \quad (2.17)$$

Applying the divergence theorem, the first integral in $W_{ther}^{ext}$ is written in the following way:

$$\int_\Omega[\nabla\cdot(\mathbf{q}\delta T)]d\Omega = \int_\Gamma[(\mathbf{q}\cdot\mathbf{n})\delta T]d\Gamma \quad (2.18)$$

where the smooth boundary $\Gamma$ is defined as $\Gamma = \Gamma_N \cup \Gamma_D$ and the test function ($\delta T$) vanishes in the Dirichlet boundary so only the Neumann boundary remains, and $\mathbf{q} \cdot \mathbf{n}$ stands for the prescribed normal flux ($q_n$), finally getting:

$$W_{ther}^{ext} = \int_{\Omega}(\dot{Q}\delta T)d\Omega - \int_{\Gamma_N}(q_n \delta T)d\Gamma \tag{2.19}$$

Substituting Eqs. (2.19) and (2.18) into Eq. (2.16), the resulting weak form of the energy balance equation is obtained:

$$\int_{\Omega}\left[\left(C\dot{T} + L\dot{f}_L\right)\right]d\Omega + \int_{\Omega}[k\nabla T \cdot \nabla(\delta T)]d\Omega = \int_{\Omega}\left[(\dot{Q}\delta T)\right]d\Omega - \int_{\Gamma_N}[q_n \delta T]d\Gamma \tag{2.20}$$

The term $q_n$ can be split into four heat flux mechanisms: prescribed heat flux ($\bar{q}$) from the heat source, heat flux by conduction ($q_{cond}$), heat loss by convection ($q_{conv}$), heat flux ($q_{rad}$) by radiation and heat loss by heat conduction through the powder bed in PBF ($q_{pow}$). Thereby, the normal flux is written as follows:

$$q_n = \bar{q} + q_{cond} + q_{conv} + q_{rad} + q_{pow} \tag{2.21}$$

## 2.2 Mechanical model

### 2.2.1 Balance of momentum equation

The mechanical problem is governed by the balance of momentum and the continuity equations [41]. The local form of the mechanical problem, considering quasi-static conditions, can be expressed as: find the displacement field, **u**, for given prescribed force, **b**, such that:

$$\nabla \cdot \boldsymbol{\sigma}(\mathbf{u}) + \mathbf{b} = 0 \tag{2.22}$$

where $\nabla \cdot (\cdot)$ denotes the divergence operator, and $\boldsymbol{\sigma}(\mathbf{u})$ stands for the Cauchy stress tensor that can be split into its spherical (pressure), $p$, and deviatoric, $\mathbf{s}$, parts, respectively, as:

$$\boldsymbol{\sigma} = p\boldsymbol{I} + \mathbf{s}(\mathbf{u}) \tag{2.23}$$

being $\mathbf{s} = \mathrm{dev}(\boldsymbol{\sigma})$ and $p = \frac{1}{3}tr(\boldsymbol{\sigma})$. Such split is quite convenient when addressing isochoric behavior where the deformations are mainly deviatoric (liquid-phase),

especially when J2-plasticity model is adopted to describe the constitutive behavior of metallic materials.

Hence, the local form of the mechanical problem can be re-formulated as: find the pressure field, $p$ (defined as an independent variable of the problem), and the displacement field, $\mathbf{u}$, for given prescribed force, $\mathbf{b}$, such that:

$$\nabla \cdot \mathbf{s}(\mathbf{u}) + \nabla p + \mathbf{b} = 0 \tag{2.24}$$

$$(\nabla \cdot \mathbf{u} - e^T) - \frac{p}{K} = 0 \tag{2.25}$$

where $e^T$ denotes the thermal deformation, and $K(T)$ stands for the temperature-dependent bulk modulus controlling the material compressibility. Note that this mixed $\mathbf{u}/p$ formulation in Eqs. (2.24) and (2.25) is equivalent to Eq. (2.22), while it is suitable for both the incompressible and compressible cases. Especially for the liquid material, the bulk modulus $K \to \infty$, therefore, Eq. (2.25) imposes the volumetric constraint as:

$$\nabla \cdot \mathbf{u} = e^T \tag{2.26}$$

### 2.2.2 Weak form of the mechanical problem

Similarly to the previous section for the heat transfer analysis, the balance Eqs. (2.24) and (2.25) must be integrated over the volume of the domain, Ω, occupied by the solid. Let Γ be the corresponding boundary, split into $\Gamma_u$ and $\Gamma_\sigma$, being $\Gamma = \Gamma_u \cup \Gamma_\sigma$. Displacements are specified on $\Gamma_u$ while tractions are prescribed on $\Gamma_\sigma$, respectively.

The weak (integral) form of the mechanical problem defined by the mixed $\mathbf{u}/p$ formulation can be expressed as follows:

$$\begin{cases} \int_\Omega [(\nabla \cdot \mathbf{s}(\mathbf{u}))\delta\mathbf{v}]d\Omega + \int_\Omega (\nabla p \cdot \delta\mathbf{v})d\Omega + \int_\Omega (\mathbf{b} \cdot \delta\mathbf{v})d\Omega = 0 & \forall \delta\mathbf{v} \\ \int_\Omega \left[\left(\nabla \cdot \mathbf{u} - e^T - \frac{p}{K}\right)\delta p\right] d\Omega = 0 & \forall \delta p \end{cases} \tag{2.27}$$

where $\delta\mathbf{v}$ and $\delta p$ represent the variations of displacement and pressure fields, respectively.

Integrating by parts, the following expressions can be written:

$$\int_\Omega [(\nabla \cdot \mathbf{s}(\mathbf{u}))\delta\mathbf{v}]d\Omega = -\int_\Omega (\mathbf{s}(\mathbf{u}) : \nabla^s \delta\mathbf{v})d\Omega + \int_{\Gamma_\sigma} (\bar{\mathbf{t}} \cdot \delta\mathbf{v})d\Gamma \tag{2.28}$$

$$\int_\Omega (\nabla p \cdot \delta\mathbf{v})d\Omega = -\int_\Omega (p \nabla \cdot \delta\mathbf{v})d\Omega \tag{2.29}$$

where $\bar{\mathbf{t}}$ represents the prescribed tractions on $\Gamma_\sigma$.

Substituting Eqs. (2.28) and (2.29) into Eq. (2.27), the mixed $\mathbf{u}/p$ variational form of the quasi-static mechanical problem yields:

$$\begin{cases} \int_\Omega (\mathbf{s}(\mathbf{u}) : \nabla^s \delta\mathbf{v}) d\Omega + \int_\Omega (p \nabla \cdot \delta\mathbf{v}) d\Omega = W_{mech}^{ext} \\ \int_\Omega \left[ \left( \nabla \cdot \mathbf{u} - e^T - \frac{p}{K} \right) \delta p \right] d\Omega = 0 \end{cases} \tag{2.30}$$

where $W_{mech}^{ext}$ stands for the external work of the mechanical loads, stated as:

$$W_{mech}^{ext} = \int_\Omega (\mathbf{b} \cdot \delta\mathbf{v}) d\Omega + \int_{\Gamma_\sigma} (\bar{\mathbf{t}} \cdot \delta\mathbf{v}) d\Gamma \tag{2.31}$$

### 2.2.3 Material constitutive model

The material model applied to simulate the constitutive behavior takes into account the wide range of temperatures (from room temperature to very high values above the melting point) experienced during the AM process [28]. The material response reproduces both the elasto-plastic behavior and the pure viscous one observed above the melting point, simulated by an apropos thermo-elasto-visco-plastic constitutive model [67,68]. The contraction of the von Mises yield-surface with the temperature rise is addressed by the definition of temperature-dependent material properties and the thermal softening induced by the temperature-dependent yield limit. Approaching the melting point, the viscous behavior becomes predominant and the elastic limit gradually decreases till vanishing. As a consequence, the purely viscous model is recovered for the liquid-like behavior. Thereby, the solid-liquid phase transformation is driven by the temperature dependency of the material properties, forced according to the solid fraction function.

The constitutive laws for all the temperature range of AM processes are featured by a J2-thermo-elasto-visco-plastic constitutive model of the form:

$$p = \frac{K}{f_S(T)} (e^{vol} - e^T) \tag{2.32}$$

$$\mathbf{s} = \frac{2G}{f_S(T)} (\mathbf{e} - \mathbf{e}^{vp}) \tag{2.33}$$

where $K(T)$ and $G(T)$ are the temperature-dependent bulk modulus controlling the material compressibility and temperature-dependent shear modulus, respectively. The total strain tensor is calculated by the displacement fields, **u**, as:

$$\boldsymbol{\varepsilon}(\mathbf{u}) = \nabla^s \mathbf{u} \tag{2.34}$$

and its deviatoric and volumetric parts are obtained as:

$$\mathbf{e} = dev(\boldsymbol{\varepsilon}) = \boldsymbol{\varepsilon} - (\frac{e^{vol}}{3})\mathbf{I} \tag{2.35}$$

$$e^{vol} = tr(\boldsymbol{\varepsilon}) = \nabla \cdot \mathbf{u} \tag{2.36}$$

The thermal deformation $e^T$ is determined as:

$$e^T(T) = e^{cool}(T) + e^{pc}(T) \tag{2.37}$$

where $e^{cool}(T)$ denotes the thermal expansion experienced by the material from the initial temperature $T_o$ to the current temperature $T$, while $e^{pc}(T)$ is the thermal shrinkage in the liquid-to-solid phase transformation. The thermal expansion is:

$$e^{cool}(T) = 3[\alpha(T)(T - T_{room}) - \alpha(T_o)(T_o - T_{room})], \quad \begin{cases} T < T_S \\ T > T_L \end{cases} \tag{2.38}$$

where $\alpha(T)$ is the temperature-dependent secant thermal expansion coefficient.

The thermal shrinkage resulting from the density variation in the solidification interval $T_S < T < T_L$ is:

$$\frac{de^{pc}}{dt} = -\frac{1}{\rho}\frac{d\rho}{dt} \tag{2.39}$$

Integrating Eq. (2.39) produces (see [69]):

$$e^{pc}(T) = \ln\frac{\rho_o}{\rho(T)} \cong \frac{\rho_o - \rho(T)}{\rho_o}, \qquad T_S < T < T_L \tag{2.40}$$

where $\rho_o = \rho(T_o)$ represents the value of the density at the initial temperature, subjected to the restrictions:

$$\rho_o = \rho_L, \quad T_o \geq T_L \tag{2.41}$$

$$\rho_o = \rho_S, \quad T_o \leq T_S \tag{2.42}$$

where $\rho_L = \rho(T_L)$ and $\rho_S = \rho(T_S)$ are the densities at liquidus and solidus temperatures, respectively.

A temperature-dependent von-Mises yield-surface is determined as:

$$\Phi(\mathbf{s}, q_h, T) = \|\mathbf{s}\| - f_S R(q_h, T) \tag{2.43}$$

where $R(q_h, T)$ is the radius of the temperature-dependent yield-surface, defined as:

$$R(q_h, T) = \sqrt{\frac{2}{3}}\left[\sigma_y(T) - q_h\right] \tag{2.44}$$

where $\sigma_y(T)$ is the temperature-dependent yield limit, and $q_h$ is the stress-like variable controlling the isotropic strain-hardening, defined as:

$$q_h(\xi, T) = -\left[\sigma_\infty(T) - \sigma_y(T)\right]\left[1 - e^{-\delta(T)\xi}\right] - h(T)\xi \tag{2.45}$$

where $\xi$ and $\sigma_\infty$ are the isotropic strain-hardening variable and the (temperature-dependent) saturation flow stress, respectively, while $\delta$ and $h$ are the (temperature-dependent) parameters to model the exponential and linear hardening laws, respectively.

The visco-plastic strains, $\boldsymbol{\varepsilon}^{vp} = \mathbf{e}^{vp}$, are defined as purely deviatoric, and are obtained from the principle of maximum plastic dissipation together with the evolution laws of the isotropic strain-hardening variable, $\xi$, expressed as:

$$\dot{\mathbf{e}}^{vp} = \dot{\gamma}^{vp}\frac{\partial \Phi(\mathbf{s}, q_h)}{\partial \mathbf{s}} = \dot{\gamma}^{vp}\frac{\mathbf{s}}{\|\mathbf{s}\|} = \dot{\gamma}^{vp}\mathbf{n} \tag{2.46}$$

$$\dot{\xi} = \dot{\gamma}^{vp}\frac{\partial \Phi(\mathbf{s}, q_h)}{\partial q_h} = \sqrt{\frac{2}{3}}\dot{\gamma}^{vp} \tag{2.47}$$

where $\mathbf{n}$ stands for the normal to the yield surface, and $\dot{\gamma}^{vp}$ is the visco-plastic multiplier, expressed as:

$$\dot{\gamma}^{vp} = \left\langle\frac{\partial \Phi(\mathbf{s}, q_h, T)}{\eta}\right\rangle^{\frac{1}{m}} \tag{2.48}$$

where $\langle\cdot\rangle$ are the Macaulay brackets, while $m$ and $\eta$ are the temperature-dependent rate sensitivity and plastic viscosity, respectively. Thereby, when the stress level reaches the yield surface, namely $\Phi(\mathbf{s}, q_h, T) = 0$, a viscous overstress, $\eta(\dot{\gamma}^{vp})^m$, is allowed to surpass the yield surface.

The resulting equivalent stress is:

$$\boldsymbol{\sigma}_{eq} = \sqrt{\frac{3}{2}}\left[f_S R + \eta(\dot{\gamma}^{vp})^m\right] \tag{2.49}$$

**(1) Solid phase**

The particularization of the material behavior for the solid phase, $T < T_S$ and $f_S(T) = 1$, is straight-forward:

$$p = K(e^{vol} - e^{T}) \tag{2.50}$$

$$\mathbf{s} = 2G(\mathbf{e} - \mathbf{e}^{vp}) \tag{2.51}$$

where the evolution laws for the visco-plastic strains and isotropic hardening are expressed by Eqs. (2.46) and (2.47) as for the J2-thermo-elasto-visco-plastic model [70].

**(2) Liquid phase**

The liquid phase is featured by a temperature field above the liquidus temperature, $T > T_L$ and $f_S(T) = 0$. In the case of liquid-like phase, both the elastic and thermal strains vanish. Hence, an isochoric (incompressible) behavior reduces to the continuity equation for mass conservation:

$$\nabla \cdot \mathbf{u} = \mathbf{0} \tag{2.52}$$

Therefore, all the deformations are purely deviatoric (viscous), that is, Eq. (2.33) reduces to:

$$\mathbf{e} = \mathbf{e}^{vp} \tag{2.53}$$

and only shear (viscous) deformations appear. In fact, the yield-surface radius defined in Eq. (2.44) decreases with the temperature rise till vanishing ($R = 0$) when the temperature is above the liquidus temperature. Inserting this result into the evolution law of the plastic multiplier in Eq. (2.48), a purely viscous model is recovered:

$$\mathbf{s} = \eta(\dot{\gamma}^{vp})^{m-1}\dot{\mathbf{e}}^{vp} \tag{2.54}$$

as a non-Newtonian Norton-Hoff visco-plastic flow. Note that this non-Newtonian law can be written in terms of the velocity field, **v**, derived from the displacement field [71], expressed as:

$$\mathbf{s}(\mathbf{v}) = \eta(\|\dot{\mathbf{e}}\|)\dot{\mathbf{e}} \tag{2.55}$$

where $\dot{\mathbf{e}} = dev(\nabla^s \mathbf{v})$.

**(3) Mushy phase**

The material model in Eqs. (2.32) and (2.33) allows a smooth transition between the solid and liquid phases as a function of the solid fraction function, $0 < f_S(T) < 1$ in the temperature range $T_S < T < T_L$. Note that the yield stress gradually decreases in this temperature range. Compared to the visco-plastic deformations, the elastic strains become

insignificant. Thereby, the mushy phase is actually controlled by the visco-plastic flow [72,73].

## 2.3 Thermo-mechanical coupling: staggered solution

The AM simulation requires the solution of the coupled thermal and mechanical fields. This is done using a staggered procedure. Firstly, a 3D transient thermal analysis is carried out to predict the temperature field according to the heat absorption characterizing the AM process and the heat dissipation through the surrounding environment. Next, the mechanical analysis is performed to predict the strain and stress evolution of AM-parts. Observe that the energy input from the high-energy beam source is much higher than the plastic dissipation (negligible) so that the problem is weakly coupled (one way coupling). Thereby, a staggered solution arising from a fractional step approach is preferred to the monolithic method.

## 2.4 Finite element modeling of AM processes

The metal AM process is simulated by moving the heat source along a user-defined scanning path. Therefore, the computational domain is varying in time, that is, the geometry of the printed part grows in time according to the building process.

The AM simulation requires an ad-hoc procedure to move the volumetric heat source, $\dot{Q}$, in time and space to the elements affected by the moving heat input, and to include those elements forming a new deposition layer into the computational domain. This procedure is referred to as the FE activation technique.

### 2.4.1 Finite element activation procedure

In order to distinguish the element roles in each time step, the birth-death-element activation strategy is applied in this work [28]. This strategy classifies the FE meshes into three types, as shown in Figure 2.3(a):

(i) *active* (yellow) elements, representing the printing platform and the elements already activated by the AM process;

(ii) *activated* (red) elements, corresponding to the elements affected by the heat input during the current time step;

(iii) *inactive* (transparent) elements, those have not yet been activated.

Based on this, the computational domain is defined by the set of active and activated elements. To update the computational domain at the beginning of the time step, a search algorithm is adopted to recognize the elements affected by the heat source in the current time step.

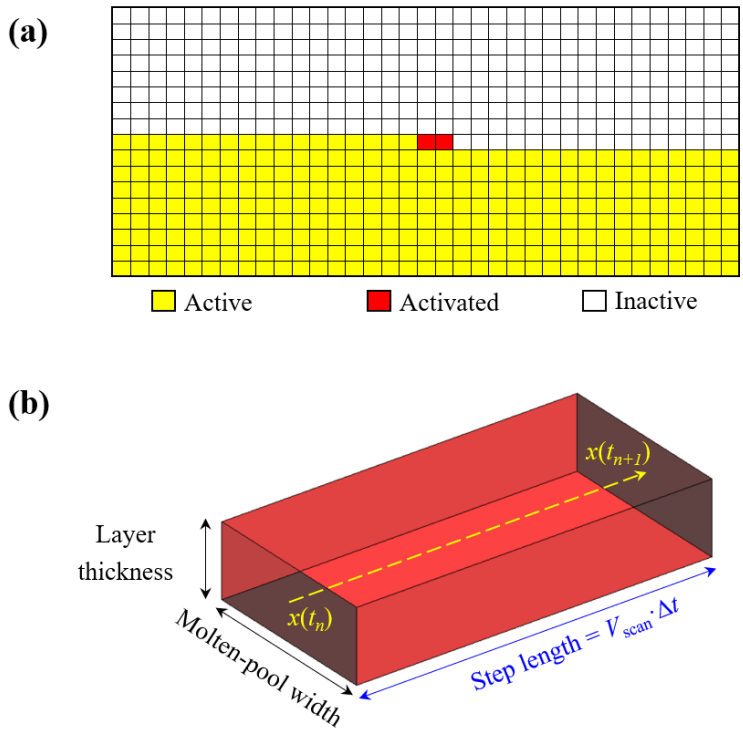


**Figure 2.3. FE activation technology for AM: (a) element classification; (b) heat load volume where for the given time step, the heat source moves from position $x(t_n)$ to $x(t_{n+1})$ according to the scan path.**

### 2.4.2 Space-time discretization

Actually, the high-energy beam follows a continuous path in AM process. Nevertheless, in the discrete problem, the molten pool moves from a given position $x_n$ to the following

position $x_{n+1}$ in the time step $\Delta t = t_{n+1} - t_n$ according to the defined build strategy. Consequently, the discrete heat input is intermittent, a drawback that can be alleviated by diminishing the time step.

The total volume influenced by the heat input in this interval, $V_{pool}^{\Delta t}$ (heat load volume (HLV)), is represented by a small cuboid with a length of $V_{scan}\Delta t$, where $V_{scan}$ is the scan speed, the width of the average beam diameter (molten-pool width), and the thickness of the deposition layer, as shown in Figure 2.3(b). The heat source term $\dot{Q}$ in Eq. (2.1) is applied to the elements inside the HLV. Although the HLV is spatially discretized using fine meshes, achieving enough spatial resolution to describe the exact volume where the heat input must be applied is still a great challenge. An octree-based search algorithm is applied to aggregate the elements corresponding to the molten pool at each time step, expressed as:

$$V_{pool}^{\Delta t} = \sum_{(e)\epsilon HLV} V^{(e)} \tag{2.56}$$

and the average heat density distribution of the heat source (per unit of volume) is calculated:

$$\dot{Q} = \frac{\eta_p \dot{P}}{V_{pool}^{\Delta t}} \tag{2.57}$$

where $P$ and $\eta_p$ are the heat source power and its absorption efficiency, respectively. Such power re-distribution preserves the total energy input, irrespective of the FE mesh used.

The balance of energy equation in Eq. (2.1) represents the equilibrium between the heat input and the heat dissipation in AM. The same concern for assessing the energy delivered by the energy beam and absorbed by the baseplate must be placed to calculate the heat lost by the boundaries of the AM-build domain. This domain is also changing with the building process and a specific searching strategy is required to update the contour surface at each time-step of the numerical computation. Following the activation process, this update is essential to compute the size of the current boundary surfaces subjected to the heat loss by radiation and convection and, consequently, perform an accurate heat transfer analysis of the AM process.

### 2.4.3 Definition of the scan strategy

As mentioned above, the heat source follows a user-defined scan path. This deposition path is defined based on a universal format, Common Layer Interface (CLI), as an input of geometry data to the model fabrication system [28]. The 3D geometry of AM-parts is sliced with parallel planes along the Z-axis (building direction) to generate several layers. Each layer is defined by its thickness and a set of contours and hatches. Contours represent the boundaries of the AM geometry within the layer and are defined by polylines. Each polyline is defined by a set of point coordinates $(x, y)$, linked in order by straight-line segments. Hatches are a set of independent straight lines, each one defined by a start and an end point. The purpose of these hatches is to define filling structures to produce the solid model, as shown in Figure 2.4.

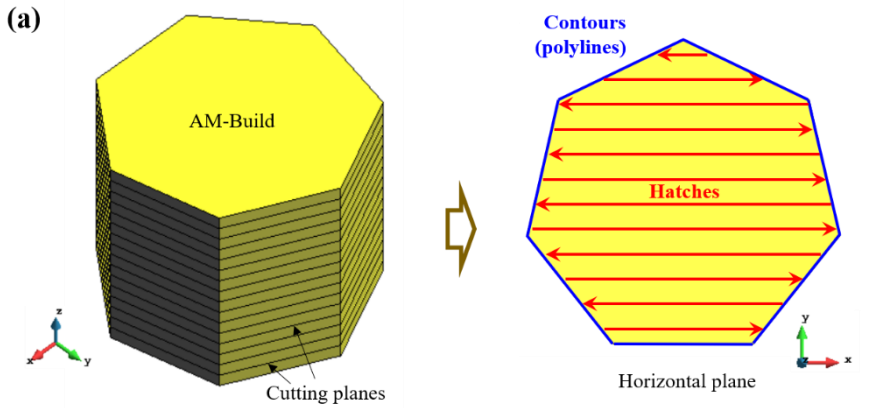


(b)

```
------------------------------------------------------------------------------------
CLI command                                          Description
------------------------------------------------------------------------------------
$$HEADERSTART                                 //An example of CLI-format//
$$ASCII                                       //File is in ASCII-format//
$$UNITS/1                                     //Coordinates are given in [mm]//
$$LAYERS/100                                  //Geometry made of 100 layers//
$$HEADEREND
$$GEOMETRYSTART                               //Start of geometry-section//
$$LAYER/1.5                                   //Layer entry level at Z=1.5mm//
$$POlYLINE/1 1 3   0 0  2 8   9 1   0 0       //3 points(x,y) defining one polyline//
$$HATCHES/1 1   0.7 1.3    0.7 58.3           //2 points(x,y) defining a hatch line//
. . .
```

**Figure 2.4. (a) Example of a 3D model slicing; (b) Example of a CLI file in ASCII-format to define the scan strategy.**

Typically, the movement of the heat source is described by two parameters: the scan speed, $V_{scan}$, and the back speed, $V_{back}$, when the high-energy beam is switched on and off, respectively. Thereby, an automatic time step, $\Delta t_{on}$, is defined by splitting each hatch (and polyline) segment according to a fix advancing step of the heat source, $\Delta x_{scan} = x(t_{n+1}) - x(t_n)$, as a function of the dimensions of the AM model (Figure 2.3(b)). When

the high-energy beam is switched off, the time increment, $\Delta t_{off}$, is computed as a function of $V_{back}$ and the distance between the coordinates of the last scan point (end of polyline or hatch) and the beginning of the following one, $\Delta x_{back}$:

$$\Delta t_{on} = \frac{\Delta x_{scan}}{V_{scan}} \tag{2.58}$$

$$\Delta t_{off} = \frac{\Delta x_{back}}{V_{back}} \tag{2.59}$$

Chapter 3

# Processing-thermal-microstructure-property relationship in AM

## 3.1 Data of the first article

This chapter presents the first paper of the compendium and the details are:

Title: Simulation-assisted investigation on the formation of layer bands and the microstructural evolution in directed energy deposition of Ti6Al4V blocks

Authors: Xufei Lu, Guohao Zhang, Junjie Li, Miguel Cervera, Michele Chiumenti, Jing Chen, Xin Lin and Weidong Huang

Journal: Virtual and Physical Prototyping

Received: 4 May 2021; Accepted: 9 June 2021

DOI: 10.1080/17452759.2021.1942077

## 3.2 Abstract of the first article

Directed energy deposition of titanium alloy entails severe microstructural heterogeneity and layer bands due to diverse thermal histories. While the thermal-microstructure relationship in additive manufacturing has been reported, the details on how complex thermal histories influence the microstructural features and evolution have not been so addressed, and the mechanism of the band formation in multi-layer multi-pass builds is still unclear. To undertake such investigation, a thermal model is firstly calibrated using two part-scale Ti6Al4V blocks fabricated on differently sized substrates, and then used to study the relationship between key microstructural characteristics and the thermal cycling involved. Results show that the different evolutions of the temperature ranges just underneath the β-transus temperature (Tβ) controlled by the printing path are responsible for the different band distributions at the center and corner of the blocks. Also, the α sizes in the normal region are closely linked to the integral area obtained from the thermal curve as temperature fluctuates between Tβ and α dissolution temperature, which helps linking the processing variables to metallurgy. This further demonstrates that the α coarsening during thermal cycles is primarily driven by multi dissolution and precipation transformations instead of Ostwald ripening. Finally, the quantitative thermal-microstructure-microhardness relationship is established, this being helpful for the microstructural design.

## 3.3 Scientific contribution of the first article

The microstructure and mechanical properties of AM-parts are closely related to the thermal histories experienced during the building process, including the direct or indirect influences from the heating, cooling and subsequent thermal cycling. Hence, understanding the thermal history of a metal part during AM is essential for process design and microstructural control.

On the one hand, this paper demonstrates that a well-calibrated computational thermal model can help to understand how choices on the processing parameters can influence the microstructure and hardness properties. On the other hand, the quantitative processing-thermal-microstructure-property relationship is established by combining the experimental microstructural observations with thermal simulations. This work provides

a new solution to predict and further design the microstructures in order to improve the mechanical properties (i.e. hardness) of large-scale AM components.

Chapter 4

# Effect of scan strategies on the mechanical behavior of AM-parts

## 4.1 Data of the second article

This chapter presents the second article of the compendium and the details are:

Title: Modeling of the Effect of the Building Strategy on the Thermomechanical Response of Ti-6Al-4V Rectangular Parts Manufactured by Laser Directed Energy Deposition

Authors: Xufei Lu, Miguel Cervera, Michele Chiumenti, Junjie Li, Xianglin Ji, Guohao Zhang and Xin Lin

Journal: Metals

Received: 19 October 2020; Accepted: 4 December 2020; Published: 6 December 2020

DOI: 10.3390/met10121643

## 4.2 Abstract of the second article

Part warpage and residual stress are two of the main challenges for metal additive manufacturing (AM) as they result in lower geometric precision and poor mechanical properties of the products. This work investigates the effect of the building strategy on the heat transfer process and the evolution of the thermally induced mechanical variables in laser directed energy deposition (L-DED) in order to minimize residual stresses and deformations. A 3D finite element (FE) thermo-mechanical model is firstly calibrated through in-situ experiments of rectangular workpieces fabricated by L-DED technology, and, secondly, the coupled thermo-mechanical responses for different process parameters and scanning patterns are discussed in detail. On the calibration stage, a remarkable agreement is achieved between predicted results and experimental data. Regarding the modeling stage, the numerical results indicate that minimization of the part warpage can be achieved by increasing the back speed and shortening the scanning lines during the building process. Both residual stresses and deformations can be further reduced if preheating the baseplate is added before L-DED.

## 4.3 Scientific contribution of the second article

High temperature gradients during AM generate large residual stresses because of uneven volumetric expansions and contractions, leading to weak or cracked components. Because the movement of the heat source follows the scanning path and changes the temperature field distribution, it directly affects the magnitude and distribution of the thermal gradients and, by association, the residual stresses.

This paper evaluates the effect of six different scanning paths on the thermo-mechanical response of a complex Ti6Al4V rectangular component fabricated by DED, based on the well-calibrated thermomechanical model. The findings obtained provide a scientific guide for AM designers to optimize the processing parameters involved to control both residual stresses and deformations in the printing process.

Chapter 5

# Warpage control of thin-wall AM structures

## 5.1 Data of the third article

This chapter presents the third article of the compendium and the details are:

Title: Warpage Analysis and Control of Thin-Walled Structures Manufactured by Laser Powder Bed Fusion

Authors: Xufei Lu, Michele Chiumenti, Miguel Cervera, Hua Tan, Xin Lin and Song Wang

Journal: Metals

Received: 23 March 2021; Accepted: 20 April 2021; Published: 22 April 2021

DOI: 10.3390/met11050686

## 5.2 Abstract of the third article

Thin-walled structures are of great interest because of their use as lightweight components in aeronautical and aerospace engineering. The fabrication of these components by Additive Manufacturing (AM) often produces undesired warpage because of the thermal stresses induced by the manufacturing process and their reduced structural stiffness. The objective of this study is to analyse the distortion of several thin-walled components fabricated by Laser Powder Bed Fusion (LPBF). Experiments are performed to investigate the sensitivity to warpage of thin-walled structures fabricated by LPBF to different design parameters such as the wall thickness and the component height in several open and closed shapes. A 3D-scanner is used to measure the residual distortions in terms of the out-of-plane displacement. Moreover, an in-house finite element software is firstly calibrated and then used to enhance the original design in order to minimize the warpage induced by the LPBF printing process. The outcome of this shows that open geometries are more prone to warping than closed ones, as well as how vertical stiffeners can mitigate the component warpage by increasing its stiffness.

## 5.3 Scientific contribution of the third article

Thin-wall components are a key part to functional products, like antennas and heat exchangers, and play an important role in different industrial fields. Nevertheless, thin-wall structures typically suffer from significant deformations during AM processes due to their poor stiffness. Thereby, controlling their warpage in the building process is of critical significance.

This paper analyzes experimentally and numerically the thermal distortions of several different thin-walled structures fabricated by SLM and summarizes their warpage features; it also proposes a useful strategy of optimization of the local structural stiffness to reduce part warpage. This work provides a guide to the structural design of AM-parts when fabricating thin-walled geometries with increased complexity.

Chapter 6

# Mitigation of residual stresses in AM

## 6.1 Data of the fourth and fifth article

This chapter presents the fourth and fifth articles of the compendium, and the details for them are as follows:

Title 1: Residual Stresses Control in Additive Manufacturing

Authors: Xufei Lu, Miguel Cervera, Michele Chiumenti and Xin Lin

Journal: Journal of Manufacturing and Materials Processing

Received: 25 November 2021; Accepted: 14 December 2021; Published: 16 December 2021

DOI: 10.3390/jmmp5040138

Title 2: Substrate design to minimize residual stresses in Directed Energy Deposition AM processes

Authors: Xufei Lu, Michele Chiumenti, Miguel Cervera, Junjie Li, Xin Lin, Liang Ma, Guohao Zhang, Enquan Liang

Journal: Materials and Design

Received: 30 September 2020; Accepted: 24 January 2021; Available online: 28 January 2021

DOI: 10.1016/j.matdes.2021.109525

## 6.2 Abstracts of the fourth and fifth article

Residual stresses are one of the primary causes for the failure of parts or systems in metal additive manufacturing (AM), since they easily induce crack propagation and structural distortion. Although the formation of residual stresses has been extensively studied, the core factors steering their development in AM have not been completely uncovered. To date, several strategies based on reducing the thermal gradients have been developed to mitigate the manifestation of residual stresses in AM; however, how to choose the optimal processing plan is still unclear for AM designers. In this regard, the concept of the yield temperature, related to the thermal deformation and the mechanical constraint, plays a crucial role for controlling the residual stresses, but it has not been duly investigated, and the corresponding approach to control stresses is also yet lacking. To undertake such study, a three-bar model is firstly used to illustrate the formation mechanism of the residual stresses and their key causes. Next, an experimentally calibrated thermomechanical finite element model is used to analyze the sensitivity of the residual stresses to the scan pattern, preheating, energy density, and the part geometry and size, as well as the substrate constraints. Based on the numerical results obtained from this analysis, recommendations on how to minimize the residual stresses during the AM process are provided.

This paper proposes a strategy to optimize the design of the substrate structures used in Additive Manufacturing (AM) by Directed Energy Deposition (DED) to minimise the residual stresses induced by this fabrication process. To this end, several numerical

analyses were performed to analyse different substrate designs in order: (i) to reduce the sensitivity to the initial non-steady stage when the first layers of material are deposited, (ii) to optimize the heat flux through the substrate to reduce the Maximum Temperature Gradients (MTG) and, (iii) to modify the substrate stiffness and its mechanical constraining to the thermal deformations during the building process and the cooling phase. To ensure the reliability of the numerical simulations, an in-house software is calibrated to allow for an accurate analysis of DED. Thus, an experimental setting is undergone to feed the numerical model with suitable values of both material and process parameters through temperature and displacement measurements and numerical fitting. Once calibrated, the software is used to evaluate the performance of several substrate designs to mitigate the residual stresses induced by the DED process. A thin-walled rectangular part selected as industrial demonstrator showed a significant reduction (up to 62%) of the maximum tensile stresses.

## 6.3 Scientific contribution of the fourth and fifth articles

In this work, the formation of residual stresses and the two key factors driving their development in the AM processes are uncovered. While the stress control strategies previously developed by reducing MTG have been widely reported, this is not the case for the yield temperature factor. Thus, this work illustrates the importance of yield temperature on the development of residual stresses, and proposes the corresponding strategy for preventing stress accumulation in AM processes. Moreover, the systematical assessment on the effectiveness of different strategies on residual stresses control is useful for AM fabricators to mitigate both residual stresses and warpages during AM processes.

Chapter 7

# Cracking mechanism and prevention in AM

## 7.1 Data of the sixth article

This chapter presents the sixth article of the compendium, and the detail is:

Title: Crack-free laser powder bed fusion by substrate design optimization

Authors: Xufei Lu, Michele Chiumenti and Miguel Cervera

Journal: Additive Manufacturing (submitted)

## 7.2 Abstract of the sixth article

Additively manufactured components by Laser Powder Bed Fusion (LPBF) easily suffer from stress-induced cracking. Lots of LPBF experiments have showed that cracks (e.g. delamination) often appear at the part-substrate interface due to the simultaneous presence of large thermal gradients and strong mechanical constraining by the substrate.

This work proposes an innovative strategy to prevent cracks during LPBF by optimizing the geometry of the substrate in order to reduce its mechanical stiffness. To assess its feasibility, the thermo-mechanical behavior of two T-shape parts deposited on the typical and patterned substrates, respectively, is computationally simulated to investigate the formation mechanism of cracks in LPBF of Ti-6Al-4V. It is found that by adding grooves cut through the thickness of the substrate, a crack-free component can be manufactured without compromising its microstructure and resultant microhardness. This approach is an alternative to the common practice consisting in reducing the thermal gradients during additive manufacturing.

## 7.3 Scientific contribution of the sixth article

This work reveals the formation mechanism of cracks and proposes a novel substrate design strategy to produce crack-free AM-parts without compromising their microstructure and microhardness. On the one hand, this favors the improvement of printability of the materials with high crack sensitivity. On the other hand, it widens the AM processing window because the process parameters used in AM are usually limited within a small range allowing for both the microstructure optimization and the defect prevention.

Chapter 8

# On the fabrication of high-quality AM parts

## 8.1 Data of the seventh article

This chapter presents the last article of the compendium, and the detail is:

Title: Mitigation of residual stresses and microstructure homogenization in directed energy deposition processes

Authors: Xufei Lu, Michele Chiumenti, Miguel Cervera, Guohao Zhang and Xin Lin

Journal: Engineering with Computers

Received: 18 October 2021; Accepted: 28 November 2021

DOI: 10.1007/s00366-021-01563-9

## 8.2 Abstract of the seventh article

In additive manufacturing (AM), residual stresses and microstructural inhomogeneity are detrimental to the mechanical properties of as-built AM components. In previous studies the mitigation of the residual stresses and the optimization of the microstructure have been treated separately. Nevertheless, the ability to control both them at the same time is mandatory for improving the final quality of AM parts. This is the main goal of this paper. Thus, a thermo-mechanical finite element model is firstly calibrated by simulating a multi-track 40-layer Ti-6Al-4V block fabricated by Directed Energy Deposition (DED). Next, the numerical tool is used to study the effect of the baseplate dimensions and the energy density on both residual stresses and microstructure evolution. On the one hand, the results indicate that the large baseplate causes higher residual stresses but produces more uniform microstructures, and contrariwise for the smaller baseplate. On the other hand, increasing the energy density favors stress relief, but its effect fails to prevent the stress concentration at the built basement. Based on these results, two approaches are proposed to control both the stress accumulation and the metallurgical evolution during the DED processes: (i) the use of a forced cooling suitable for small baseplates and, (ii) the adoption of grooves when large baseplates are used. The numerical predictions demonstrated the effectiveness of the proposed manufacturing strategies.

## 8.3 Scientific contribution of the seventh article

Based on the in-depth understanding of the thermal-metallurgical-mechanical interactions in AM, this paper demonstrates how to mitigate the residual stresses and control the microstructural evolution at the same time by simultaneously optimizing the thermal boundaries and the mechanical constraint from the substrate. This work provides a comprehensive guideline to additively manufacture high-quality Ti6Al4V parts with lower residual stresses and homogeneous microstructures and properties.

Chapter 9

# Conclusion and outlook

The outline of this concluding Chapter is as follows. Section 9.1 summarizes this doctoral thesis. Section 9.2 lists the conclusions of the research. Section 9.3 presents the main contributions of this work. Section 9.4 suggests the lines for future study.

## 9.1 Summary

This thesis is focused on understanding the intrinsic relationship between process parameters, thermal history, microstructural evolution, mechanical response and resulting properties in metal AM processes through combining in-situ experiments with FE thermo-mechanical simulations. Figure 9.1 shows the entire framework of this thesis. The core objective is to provide more insight into the complex interactions between different physical fields involved in AM and to achieve the AM fabrication of high-quality metal components.

The summary of this doctoral thesis is as follows:

**Chapter 2** introduces the coupled thermo-mechanical computational framework for the AM analysis. In detail, the heat transfer analysis including the phase-change, the mechanical analysis, the constitutive models considering the thermo-elasto-visco-plastic

behavior of materials, the thermo-mechanical coupling and the FE modeling of AM process are introduced in order.

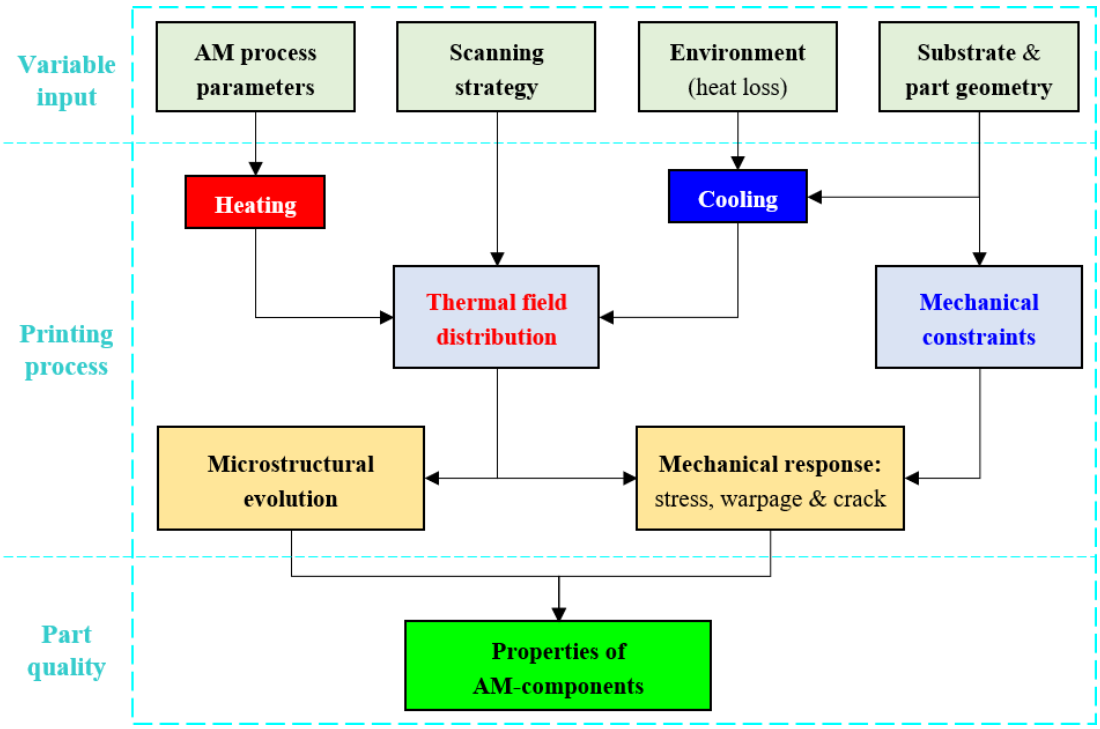


**Figure 9.1. The study framework of the thesis.**

In **Chapter 3**, the FE thermal model is applied to predict the evolution of the temperature field in the DED process of multi-track and multi-layer Ti6Al4V blocks. The objective of revealing the layer-band formation and determining the thermal-metallurgical-property relationship in AM Ti6Al4V is achieved by analyzing the thermal histories and the microstructure observations.

**Chapters 4-7** focus on the thermally induced residual stresses, part warpages and cracks including their formation mechanisms, the related influence factors and the corresponding control approaches. In **Chapter 4**, the effect of different printing patterns on the thermo-mechanical behavior of rectangular components fabricated by laser-based DED is numerically assessed based on the experimentally calibrated thermo-mechanical model. The optimal building strategy to reduce both residual stresses and deformations is selected. In **Chapter 5**, the warpage of several thin-walled structures manufactured by LPBF are experimentally and computationally analyzed, and the general strategy for the distortion control is provided. **Chapter 6** is the core of this thesis: understanding the formation mechanism of residual stresses induced by AM. A systematical evaluation on the effectiveness of different stress-control strategies is performed. In **Chapter 7**, the

formation of the stress-induced cracks during the LPBF process of the T-shape structure are investigated, and a crack-free LPBF part is obtained by substrate design optimization.

In **Chapter 8**, the ultimate aim of additively manufacturing high-quality Ti6Al4V parts with lower residual stresses and uniform microstructure and hardness is accomplished by assembling the acquired insight on the parameter-thermal-metallurgical-property relationship and the control of residual stresses.

## 9.2 Conclusions

The following conclusions can be drawn from the work presented in this thesis:

**(1) Contribution of the FE computational framework for AM**

- The coupled thermo-mechanical FE model is a powerful tool to predict the thermal histories, the evolution of full-field stresses and strains during AM processes. Once validated and calibrated with in-situ experiment measurements, it can be used to study the complex process-thermal-metallurgical-mechanical interactions.

**(2) Understanding the thermal-microstructure-property relationship**

- The layer bands are evenly spaced through the deposits, 2 and 4 layer-thick apart in the center and corner of two part-scale blocks, respectively, due to the different evolution of the relevant temperature range just underneath the β-transus temperature controlled by the scan pattern used.
- An integral area index is proposed to assess the coarsening of α-lath and to link AM variables with metallurgy of AM Ti6Al4V.
- The quantitative thermal-microstructure-microhardness relationship is established.

**(3) Formation and control of residual stresses, warpages and cracks**

- AM variables (e.g. scanning path, process parameters, protective atmosphere, the size and geometry of the substrate and part) significantly affect the distributions

of temperature field and the evolution of the thermally induced mechanical variables in AM processes.

- The numerical results of the residual stresses and distortions of the rectangular parts fabricated by directed energy deposition (DED) under six different deposition paths show that the part warpage can be minimized by reducing the length of scanning lines and increasing the back speed during the printing process.

- The mechanical analysis of different thin-walled components with weak structural stiffness helps to understand their distortion behavior during laser powder bed fusion process (LPBF). Thicker walled structures can restrict the deformation development, and open structures (like semi-cylinder) are more prone to warpage than closed ones (like square geometry). However, adding vertical stiffeners can enhance the structural stiffness of thin-walled structures, mitigating the warpage.

- The formation of residual stresses in AM is mainly driven by two key factors: (i) maximum temperature gradients (MTG) and (ii) yield temperature, related to the mechanical constraining during thermal deformation. By increasing yield temperature through optimizing the substrate structures, it is possible to minimize the residual stresses and cracks.

- The systematical evaluation of different strategies on residual stresses reduction illustrates that the strategies previously developed based on the MTG reduction favor the mitigation of the inner residual stresses but fail to avoid the stress concentrations at the deposited basement, this often being the source of cracking and failure of AM-parts. Contrariwise, the proposed substrate design approach remarkably curbs the stress development and concentration in AM-components.

- The stress concentrations are directly responsible for the initiation of cracks at the part-substrate interface where both larger thermal gradients and stronger mechanical constraining exist. However, optimizing the substrate geometry by adding the groove-pattern can reduce the residual stresses and avoid cracking without compromising the metallurgy and microhardness of the builds.

**(4) How to fabricate high-quality AM-parts**

- The concurrent control of the stress accumulation and the microstructural evolution during AM can be achieved by optimizing the thermal histories and reducing the mechanical constraining of the substrate at the same time.
- In AM Ti6Al4V, thicker substrates can faster dissipate the heat input allowing for a finer and more uniform microstructure, while the higher stiffness produces larger residual stresses; contrariwise for thinner substrates. Two strategies can address this problem: (i) the residual stresses can be reduced through adding a groove pattern into the thick substrate; (ii) the formation of more uniform microstructures can be achieved by using forced cooling under the bottom surface of thin substrates to increase the heat loss from the builds.

## 9.3 Main contributions

The research in this doctoral thesis presents the following original contributions:

- An in-depth study on the complex multi-physics and multi-scale interactions between the process parameters, the thermal histories, the metallurgical evolution and the mechanical response is carried out, favoring the optimization of AM process parameters and the final material properties.
- A quantitative relationship between the thermal histories and key microstructural features of Ti6Al4V fabricated by DED is established. This helps the design of the microstructure of AM titanium alloys.
- The formation mechanisms of the residual stresses and distortion as well as macro-cracks are elucidated. The two core factors of MTG and yield temperature also were extracted from the complex mechanics in AM.
- Several innovative strategies (e.g. designing substrate structure, optimizing scan path and using stiffeners for thin-walled parts) are proposed to control residual stresses and part warpages in AM processes.
- A comprehensive technical framework for fabricating high-quality AM components is presented (see Figure 9.1).

## 9.4 Outlook

This thesis provides additional insight into the thermal-metallurgical-property relationship of AM Ti6Al4V and the understanding of the thermally induced mechanical behavior affected by various input variables, especially for the formation of residual stresses and their control. The following lines of future work need to be pursued:

- **Assistance to the development of new materials.** To date, the materials suitable for AM are quite limited if compared to conventional processing. One of the main reasons for this is the poor printability of many metallic materials with high crack sensitivity. To address this challenge, future works will focus on the combination of the structure design with the MTG reduction and the specific material characteristics to improve the printability of new materials.

- **Advancement to lower-cost and high-quality AM fabrication.** The proposed technical framework for building high-quality AM-parts will be further enhanced by considering other defect preventions (like porosity) and the whole processing optimization. It will be expanded to different alloy systems to reduce the manufacturing cost while improving the quality of AM products.

- **Development of powerful metallurgical and crystal-plastic models.** In order to further deepen the understanding of the microstructural evolution in AM, a more powerful metallurgical model considering the liquid flow inside the molten pool, the crystal growth during solidification, and its coupling with thermo-mechanical modules is needed. Moreover, it is necessary to develop a crystal-plastic model to achieve more accurate predictions of both the residual stresses at grain scale and the tensile and fatigue properties of AM-parts. Taking into account the limited computational efficiency of physical-based models, machine learning may be introduced into the microstructure and mechanical investigations in metal AM.

- **Enhancement of the structural optimization for AM.** The concept of residual stress control proposed in this thesis will be applied in the AM structural design, especially in the design of support structures in LPBF and the topological optimization for AM

# References


[1] Herzog, Dirk, Vanessa Seyda, Eric Wycisk, and Claus Emmelmann. "Additive manufacturing of metals." Acta Materialia 117 (2016): 371-392.

[2] Kranz, Jannis, Dirk Herzog, and Claus Emmelmann. "Design guidelines for laser additive manufacturing of lightweight structures in TiAl6V4." Journal of Laser Applications 27, no. S1 (2015): S14001.

[3] Gibson, Ian, David W. Rosen, Brent Stucker, Mahyar Khorasani, David Rosen, Brent Stucker, and Mahyar Khorasani. Additive manufacturing technologies. Vol. 17. Cham, Switzerland: Springer, 2021.

[4] Emmelmann, Claus, Jannis Kranz, Dirk Herzog, and Eric Wycisk. "Laser additive manufacturing of metals." In Laser technology in biomimetics, pp. 143-162. Springer, Berlin, Heidelberg, 2013.

[5] Gatsos, Theofilos, Karim A. Elsayed, Yuwei Zhai, and Diana A. Lados. "Review on computational modeling of process–microstructure–property relationships in metal additive manufacturing." JOM 72, no. 1 (2020): 403-419.

[6] Satish Kumar, P., L. Suvarna Raju, and L. Siva Rama Krishna. "A Review on Wire Arc Additive Manufacturing (WAAM) Fabricated Components of Ti6AL4V and Steels." In International Conference on Emerging Trends in Engineering (ICETE), pp. 587-600. Springer, Cham, 2020.

[7] Lu, Xufei, Xin Lin, Michele Chiumenti, Miguel Cervera, Yunlong Hu, Xianglin Ji, Liang Ma, and Weidong Huang. "In situ measurements and thermo-mechanical simulation of Ti–6Al–4V laser solid forming processes." International Journal of Mechanical Sciences 153 (2019): 119-130.

[8] Wu, Qianru, Tuhin Mukherjee, Changmeng Liu, Jiping Lu, and Tarasankar DebRoy. "Residual stresses and distortion in the patterned printing of titanium and nickel alloys." Additive Manufacturing 29 (2019): 100808.

[9] Gouge, Michael, and Pan Michaleris, eds. Thermo-mechanical modeling of additive manufacturing. Butterworth-Heinemann, 2017.

[10] Fang, Ze-Chen, Zhi-Lin Wu, Chen-Guang Huang, and Chen-Wu Wu. "Review on residual stress in selective laser melting additive manufacturing of alloy parts." Optics & Laser Technology 129 (2020): 106283.

[11] Lu, Xufei, Xin Lin, Michele Chiumenti, Miguel Cervera, Yunlong Hu, Xianglin Ji, Liang Ma, Haiou Yang, and Weidong Huang. "Residual stress and distortion of rectangular and S-shaped Ti-6Al-4V parts by Directed Energy Deposition: Modelling and experimental calibration." Additive Manufacturing 26 (2019): 166-179.

[12] Tran, Hai T., Qian Chen, Jonathan Mohan, and Albert C. To. "A new method for predicting cracking at the interface between solid and lattice support during laser powder bed fusion additive manufacturing." Additive Manufacturing 32 (2020): 101050.

[13] Mercelis, Peter, and Jean-Pierre Kruth. "Residual stresses in selective laser sintering and selective laser melting." Rapid prototyping journal (2006).

[14] Ding, Jialuo. "Thermo-mechanical analysis of wire and arc additive manufacturing process." (2012).

[15] Promoppatum, Patcharapit, Shi-Chune Yao, P. Chris Pistorius, and Anthony D. Rollett. "A comprehensive comparison of the analytical and numerical prediction of the thermal history and solidification microstructure of Inconel 718 products made by laser powder-bed fusion." Engineering 3, no. 5 (2017): 685-694.

[16] Li, Jinghao, Xianglin Zhou, Mathieu Brochu, Nikolas Provatas, and Yaoyao Fiona Zhao. "Solidification microstructure simulation of Ti-6Al-4V in metal additive manufacturing: A review." Additive Manufacturing 31 (2020): 100989.

[17] Tan, Joel Heang Kuan, Swee Leong Sing, and Wai Yee Yeong. "Microstructure modelling for metallic additive manufacturing: A review." Virtual and Physical Prototyping 15, no. 1 (2020): 87-105.

[18] Xiao, Hui, Manping Cheng, and Lijun Song. "Direct fabrication of single-crystal-like structure using quasi-continuous-wave laser additive manufacturing." Journal of Materials Science & Technology 60 (2021): 216-221.

[19] Ho, Alistair, Hao Zhao, Jon W. Fellowes, Filomeno Martina, Alec E. Davis, and Philip B. Prangnell. "On the origin of microstructural banding in Ti-6Al4V wire-arc based high deposition rate additive manufacturing." Acta Materialia 166 (2019): 306-323.

[20] Damon, James, Robin Koch, Daniel Kaiser, Gregor Graf, Stefan Dietrich, and Volker Schulze. "Process development and impact of intrinsic heat treatment on

the mechanical performance of selective laser melted AISI 4140." Additive Manufacturing 28 (2019): 275-284.

[21] Yang, Min, Lu Wang, and Wentao Yan. "Phase-field modeling of grain evolutions in additive manufacturing from nucleation, growth, to coarsening." Npj Computational Materials 7, no. 1 (2021): 1-12.

[22] Vecchiato, F. L., H. De Winton, P. A. Hooper, and M. R. Wenman. "Melt pool microstructure and morphology from single exposures in laser powder bed fusion of 316L stainless steel." Additive Manufacturing 36 (2020): 101401.

[23] Liu, Zhiyuan, Dandan Zhao, Pei Wang, Ming Yan, Can Yang, Zhangwei Chen, Jian Lu, and Zhaoping Lu. "Additive manufacturing of metals: Microstructure evolution and multistage control." Journal of Materials Science & Technology 100 (2022): 224-236.

[24] Cao, Jun, Michael A. Gharghouri, and Philip Nash. "Finite-element analysis and experimental validation of thermal residual stress and distortion in electron beam additive manufactured Ti-6Al-4V build plates." Journal of Materials Processing Technology 237 (2016): 409-419.

[25] Lu, Xufei, Xin Lin, Michele Chiumenti, Miguel Cervera, JunJie Li, Liang Ma, Lei Wei, Yunlong Hu, and Weidong Huang. "Finite element analysis and experimental validation of the thermomechanical behavior in laser solid forming of Ti-6Al-4V." Additive Manufacturing 21 (2018): 30-40.

[26] Hönnige, J. R., Paul A. Colegrove, B. Ahmad, M. E. Fitzpatrick, Supriyo Ganguly, T. L. Lee, and Stewart W. Williams. "Residual stress and texture control in Ti-6Al-4V wire+ arc additively manufactured intersections by stress relief and rolling." Materials & Design 150 (2018): 193-205.

[27] Baykasoglu, Cengiz, Oncu Akyildiz, Duygu Candemir, Qingcheng Yang, and Albert C. To. "Predicting microstructure evolution during directed energy deposition additive manufacturing of Ti-6Al-4V." Journal of Manufacturing Science and Engineering 140, no. 5 (2018).

[28] Chiumenti, Michele, Xin Lin, Miguel Cervera, Wei Lei, Yuxiang Zheng, and Weidong Huang. "Numerical simulation and experimental calibration of additive manufacturing by blown powder technology. Part I: thermal analysis." Rapid Prototyping Journal (2017).

[29] Fallah, Vahid, Masoud Alimardani, Stephen F. Corbin, and Amir Khajepour. "Temporal development of melt-pool morphology and clad geometry in laser powder deposition." Computational materials science 50, no. 7 (2011): 2124-2134.

[30] Lundbäck, Andreas, and Lars-Erik Lindgren. "Modelling of metal deposition." Finite Elements in Analysis and Design 47, no. 10 (2011): 1169-1177.

[31] Chiumenti, Michele, Miguel Cervera, Alessandro Salmi, Carlos Agelet De Saracibar, Narges Dialami, and Kazumi Matsui. "Finite element modeling of multi-pass welding and shaped metal deposition processes." Computer methods in applied mechanics and engineering 199, no. 37-40 (2010): 2343-2359.

[32] Gouge, Michael F. Advancements in thermo-material modeling of direct energy deposition processes. The Pennsylvania State University, 2016.

[33] Woo, Wanchuck, Dong-Kyu Kim, Ed J. Kingston, Vladmir Luzin, Floriana Salvemini, and Michael R. Hill. "Effect of interlayers and scanning strategies on through-thickness residual stress distributions in additive manufactured ferritic-austenitic steel structure." Materials Science and Engineering: A 744 (2019): 618-629.

[34] Wang, Zhuqing, Erik Denlinger, Panagiotis Michaleris, Alexandru D. Stoica, Dong Ma, and Allison M. Beese. "Residual stress mapping in Inconel 625 fabricated through additive manufacturing: Method for neutron diffraction measurements to validate thermomechanical model predictions." Materials & Design 113 (2017): 169-177.

[35] Lindgren, Lars-Erik, Andreas Lundb äck, Martin Fisk, Robert Pederson, and Joel Andersson. "Simulation of additive manufacturing using coupled constitutive and microstructure models." Additive Manufacturing 12 (2016): 144-158.

[36] Weisz-Patrault, Daniel. "Fast simulation of temperature and phase transitions in directed energy deposition additive manufacturing." Additive Manufacturing 31 (2020): 100990.

[37] Kelly, Shawn Michael. "Thermal and microstructure modeling of metal deposition processes with application to Ti-6Al-4V." PhD diss., Virginia Tech, 2004.

[38] Charles, Corinne. "Microstructure model for Ti-6Al-4V used in simulation of additive manufacturing." PhD diss., Lule åtekniska universitet, 2016.

[39] Reddy, Junuthula Narasimha, and David K. Gartling. The finite element method in heat transfer and fluid dynamics. CRC press, 2010.

[40] Zhang, Yancheng, Gildas Guillemot, Marc Bernacki, and Michel Bellet. "Macroscopic thermal finite element modeling of additive metal manufacturing by selective laser melting process." Computer Methods in Applied Mechanics and Engineering 331 (2018): 514-535.

[41] Chiumenti, Michele, Miguel Cervera, Narges Dialami, Bin Wu, L. Jinwei, and C. Agelet de Saracibar. "Numerical modeling of the electron beam welding and its experimental validation." Finite Elements in Analysis and Design 121 (2016): 118-133.

[42] Denlinger, Erik R., and Pan Michaleris. "Effect of stress relaxation on distortion in additive manufacturing process modeling." Additive Manufacturing 12 (2016): 51-59.

[43] Li, Yingli, Kun Zhou, Pengfei Tan, Shu Beng Tor, Chee Kai Chua, and Kah Fai Leong. "Modeling temperature and residual stress fields in selective laser melting." International Journal of Mechanical Sciences 136 (2018): 24-35.

[44] Smith, Jacob, Wei Xiong, Jian Cao, and Wing Kam Liu. "Thermodynamically consistent microstructure prediction of additively manufactured materials." Computational mechanics 57, no. 3 (2016): 359-370.

[45] Lindgren, Lars-Erik, Andreas Lundbäck, and Andreas Malmelöv. "Thermal stresses and computational welding mechanics." Journal of Thermal Stresses 42, no. 1 (2019): 107-121.

[46] Malmelöv, Andreas, Andreas Lundbäck, and Lars-Erik Lindgren. "History reduction by lumping for time-efficient simulation of additive manufacturing." Metals 10, no. 1 (2019): 58.

[47] Huang, Hui, Ninshu Ma, Jian Chen, Zhili Feng, and Hidekazu Murakawa. "Toward large-scale simulation of residual stress and distortion in wire and arc additive manufacturing." Additive Manufacturing 34 (2020): 101248.

[48] Baykasoğlu, Cengiz, Oncu Akyildiz, Merve Tunay, and Albert C. To. "A process-microstructure finite element simulation framework for predicting phase transformations and microhardness for directed energy deposition of Ti6Al4V." Additive Manufacturing 35 (2020): 101252.

[49] Salsi, Emilio, Michele Chiumenti, and Miguel Cervera. "Modeling of microstructure evolution of Ti6Al4V for additive manufacturing." Metals 8, no. 8 (2018): 633.

[50] Avrami, Melvin. "Granulation, phase change, and microstructure kinetics of phase change. III." The Journal of chemical physics 9, no. 2 (1941): 177-184.

[51] Porter, David A., and Kenneth E. Easterling. Phase transformations in metals and alloys (revised reprint). CRC press, 2009.

[52] Gil, F. J., M. P. Ginebra, J. M. Manero, and J. A. Planell. "Formation of α-Widmanstätten structure: effects of grain size and cooling rate on the Widmanstätten morphologies and on the mechanical properties in Ti6Al4V alloy." Journal of Alloys and Compounds 329, no. 1-2 (2001): 142-152.

[53] Koistinen, Donald P. "A general equation prescribing the extent of the austenite-martensite transformation in pure iron-carbon alloys and plain carbon steels." acta metallurgica 7 (1959): 59-60.

[54] Murgau, C. Charles, Robert Pederson, and Lars-Erik Lindgren. "A model for Ti–6Al–4V microstructure evolution for arbitrary temperature changes." Modelling and Simulation in Materials Science and Engineering 20, no. 5 (2012): 055006.

[55] Babu, Bijish, Andreas Lundbäck, and Lars-Erik Lindgren. "Simulation of Ti-6Al-4V additive manufacturing using coupled physically based flow stress and metallurgical model." Materials 12, no. 23 (2019): 3844.

[56] Tan, Pengfei, Fei Shen, Wei Shian Tey, and Kun Zhou. "A numerical study on the packing quality of fibre/polymer composite powder for powder bed fusion additive manufacturing." Virtual and Physical Prototyping 16, no. sup1 (2021): S1-S18.

[57] Yan, Wentao, Yanping Lian, Cheng Yu, Orion L. Kafka, Zeliang Liu, Wing Kam Liu, and Gregory J. Wagner. "An integrated process–structure–property modeling framework for additive manufacturing." Computer Methods in Applied Mechanics and Engineering 339 (2018): 184-204.

[58] Liu, P. W., Z. Wang, Y. H. Xiao, Ricardo A. Lebensohn, Y. C. Liu, Mark F. Horstemeyer, X. Y. Cui, and L. Chen. "Integration of phase-field model and crystal plasticity for the prediction of process-structure-property relation of additively manufactured metallic materials." International Journal of Plasticity 128 (2020): 102670.

[59] Pinomaa, Tatu, Ivan Yashchuk, Matti Lindroos, Tom Andersson, Nikolas Provatas, and Anssi Laukkanen. "Process-structure-properties-performance modeling for selective laser melting." Metals 9, no. 11 (2019): 1138.

[60] Klingbeil, Nathan W., Jack L. Beuth, R. K. Chin, and C. H. Amon. "Residual stress-induced warping in direct metal solid freeform fabrication." International Journal of Mechanical Sciences 44, no. 1 (2002): 57-77.

[61] Chin, R. K., J. L. Beuth, and C. H. Amon. "Control of residual thermal stresses in shape deposition manufacturing." In 1995 International Solid Freeform Fabrication Symposium. 1995.

[62] Levkulich, N. C., S. L. Semiatin, J. E. Gockel, J. R. Middendorf, A. T. DeWald, and N. W. Klingbeil. "The effect of process parameters on residual stress evolution and distortion in the laser powder bed fusion of Ti-6Al-4V." Additive Manufacturing 28 (2019): 475-484.

[63] Mugwagwa, L., D. Dimitrov, S. Matope, and I. Yadroitsev. "Influence of process parameters on residual stress related distortions in selective laser melting." Procedia Manufacturing 21 (2018): 92-99.

[64] Kalentics, Nikola, Eric Boillat, Patrice Peyre, Snežana Ćirić-Kostić, Nebojša Bogojević, and Roland E. Logé. "Tailoring residual stress profile of selective laser melted parts by laser shock peening." Additive Manufacturing 16 (2017): 90-97.

[65] Feulvarch, E., and J-M. Bergheau. "An implicit fixed-grid method for the finite-element analysis of heat transfer involving phase changes." Numerical Heat Transfer, Part B: Fundamentals 51, no. 6 (2007): 585-610.

[66] Chiumenti, Michele, Eric Neiva, Emilio Salsi, Miguel Cervera, Santiago Badia, Joan Moya, Zhuoer Chen, Caroline Lee, and Christopher Davies. "Numerical modelling and experimental validation in Selective Laser Melting." Additive Manufacturing 18 (2017): 171-185.

[67] Simo, Juan C., and Thomas JR Hughes. Computational inelasticity. Vol. 7. Springer Science & Business Media, 2006.

[68] De Saracibar, C. Agelet, Miguel Cervera, and M. Chiumenti. "On the formulation of coupled thermoplastic problems with phase-change." International journal of plasticity 15, no. 1 (1999): 1-34.

[69] Bellet, Michel, and Brian G. Thomas. "Solidification macroprocesses-Thermal-mechanical Modeling of Stress, Distortion and Hot Tearing." (2007): Chapter-27.

[70] Cervera, Miguel, Carlos Agelet De Saracibar, and Michele Chiumenti. "Thermo-mechanical analysis of industrial solidification processes." International Journal for Numerical Methods in Engineering 46, no. 9 (1999): 1575-1591.

[71] Bellet, Michel, Victor D. Fachinotti, Olivier Jaouen, Sophie De La Chapelle, Isabelle Poitrault, and Benoît Lusson. "Application of the arbitrary Eulerian Lagrangian finite element formulation to the thermomechanical simulation of casting processes, with focus on pipe shrinkage prediction." In 10th International Conference on Modeling of Casting, Welding and Advanced Solidification Processes, pp. pages-361. The Minerals, Metals & Materials Society, Warrendale, Pennsylvania, USA, 2003.

[72] Chiumenti, M., Miguel Cervera, C. Agelet de Saracibar, and Narges Dialami. "Numerical modeling of friction stir welding processes." Computer methods in applied mechanics and engineering 254 (2013): 353-369.

[73] Dialami, Narges, Michele Chiumenti, Miguel Cervera, and Carlos Agelet de Saracibar. "An apropos kinematic framework for the numerical modeling of friction stir welding." Computers & Structures 117 (2013): 48-57.

# Publications included in the compendium

# Simulation-assisted investigation on the formation of layer bands and the microstructural evolution in directed energy deposition of Ti6Al4V blocks

X. Lu, G. Zhang, J. Li, M. Cervera, M. Chiumenti, J. Chen, X. Lin & W. Huang.

*Virtual and Physical Prototyping*

*Vol. 16, issue 4, pp. 387-403, (2021)*

https://doi.org/10.1080/17452759.2021.1942077

# Modeling of the Effect of the Building Strategy on the Thermomechanical Response of Ti-6Al-4V Rectangular Parts Manufactured by Laser Directed Energy Deposition

X. Lu, M. Cervera, M. Chiumenti, J. Li, X. Ji, G. Zhang & X. Lin

*Metals*

Vol. 10, issue 12, pp. 1643, (2020)

https://doi.org/10.3390/met10121643

metals

MDPI

*Article*

# Modeling of the Effect of the Building Strategy on the Thermomechanical Response of Ti-6Al-4V Rectangular Parts Manufactured by Laser Directed Energy Deposition

**Xufei Lu [1,2], Miguel Cervera [1,*], Michele Chiumenti [1], Junjie Li [2,3], Xianglin Ji [4], Guohao Zhang [2,3] and Xin Lin [2,3,*]**

1 International Center for Numerical Methods in Engineering (CIMNE), Universidad Politécnica de Cataluña (UPC), Edificio C1, Campus Norte, Gran Capitán s/n, 08034 Barcelona, Spain; xlu@cimne.upc.edu (X.L.); michele@cimne.upc.edu (M.C.)

2 Key Laboratory of Metal High Performance Additive Manufacturing and Innovative Design, MIIT China, Northwestern Polytechnical University, Youyixilu, Xi'an 710072, China; lijunjie@nwpu.edu.cn (J.L.); zghao@mail.nwpu.edu.cn (G.Z.)

3 State Key Laboratory of Solidification Processing, Northwestern Polytechnical University, Youyixilu, Xi'an 710072, China

4 Department of Biomedical Engineering, City University of Hong Kong, Kowloon, Hong Kong SAR 999077, China; xiangliji3-c@my.cityu.edu.hk

* Correspondence: miguel.cervera@upc.edu (M.C.); xlin@nwpu.edu.cn (X.L.); Tel.: +34-934-016-492 (M.C.); +86-029-8849-4001 (X.L.)

Received: 19 October 2020; Accepted: 4 December 2020; Published: 6 December 2020


**Abstract:** Part warpage and residual stress are two of the main challenges for metal additive manufacturing (AM) as they result in lower geometric precision and poor mechanical properties of the products. This work investigates the effect of the building strategy on the heat transfer process and the evolution of the thermally induced mechanical variables in laser directed energy deposition (L-DED) in order to minimize residual stresses and deformations. A 3D finite element (FE) thermo-mechanical model is firstly calibrated through in-situ experiments of rectangular workpieces fabricated by L-DED technology, and, secondly, the coupled thermo-mechanical responses for different process parameters and scanning patterns are discussed in detail. On the calibration stage, the remarkable agreement is achieved between predicted results and experimental data. Regarding the modeling stage, the numerical results indicate that minimization of the part warpage is achieved by reducing the back speed and shortening the scanning lines during the building process. Both residual stress and deformation can be further reduced if preheating the baseplate is added before L-DED.

**Keywords:** laser directed energy deposition (L-DED); thermo-mechanical simulation; process parameters; scanning pattern; part warpage; residual stress

## 1. Introduction

Laser directed energy deposition (L-DED), one of the advanced additive manufacturing (AM) technologies, has been extensively applied in different industrial fields due to its high deposition efficiency and near-net-shape fabrication [1,2]. The metal powder is concentrically blown into the melting pool generated by a laser beam. During the L-DED process, the materials experience rapid heating and cooling cycles according to the particular building strategy, resulting in high-temperature gradients and plastic strains. After the depositing process is completed, undesired residual stress and

distortion, detrimental to the geometric precision and mechanical properties of the fabricated part, remain in the built [3–5].

AM is a complex multi-physics and multi-scale process involving the interaction of the laser with the powder, heat transfer, and thermo-mechanical deformation. In order to obtain a deeper understanding of AM processes, both experiments and simulations are used. The ultimate good is to optimize the fabricating process, taking into account an extended amount of variables. Experimental procedures are expensive and time-consuming. Some parameters are also difficult to measure [6,7]. Instead, the finite element method (FEM) provides an efficient and feasible approach to simulate the AM process and to reveal the underlying mechanisms of defect formation within the fabricated workpieces by AM, such as part deformation and residual stresses [8–12]. Lindgren et al. [8] developed a thermo-mechanical finite element (FE) model based on computational welding mechanics (CWM) able to predict thermal stresses and distortions during AM. Denlinger et al. [9] simulated the thermo-mechanical responses of Ti-6Al-4V and Inconel® 625 during the L-DED process and found that compared with Inconel® 625, an allotropic phase transformation (PT) in Ti-6Al-4V triggers both significant stress relaxation and distortion mitigation. They achieved the best match between the calculated result and in-situ measurement with a PT temperature of 690 °C. However, Chen et al. [10] investigated the PT temperature of Ti-6Al-4V using variable temperature XRD measurements; they finally determined the temperature of 850 °C by comparing the numerical prediction via a developed model in ANSYS with the experimental work in Denlinger [9]. Moreover, Wang et al. [11] used compression experiments at 600 °C and 700 °C with in-situ neutron diffraction to study the stress relaxation of Ti-6Al-4V fabricated through conventional processing and AM. They found that stress is released sooner as the temperature increases, owing to the dislocation glide and climb. Hence, the level of stress relaxation of Ti-6Al-4V strongly depends on the building strategy in terms of the process parameters and scanning pattern because they significantly affect the thermal history in the L-DED process.

Several studies have demonstrated that process parameters (laser power, scan speed, build height, and substrate condition) greatly affect the development of distortions and residual stresses in AM processes [12–19]. LevkulichL et al. [14] investigated the effect of process parameters on stress evolution and deformations in selective laser melting (SLM) of Ti-6Al-4V; they found that the residual stress on the deposit surface is mitigated by increasing the laser power and reducing the scan speed. However, the numerical results presented in reference [15] showed that higher laser power or lower scan speed causes a higher level of residual stress at the single-track end of Ti-6Al-4V by SLM. Lu et al. [5] showed that preheating the substrate before AM greatly eliminates the residual stress and warpage in the built parts.

Wu et al. [16] compared the effect of three deposition patterns on the mechanical responses of Ti-6Al-4V and Inconel 718 rectangular components by wire-arc additive manufacturing (WAAM) experimentally and numerically. They found that printing with a short track length could reduce residual stresses and distortion for both alloys. Ramos et al. [17] proposed a geometric-based scanning strategy aimed at mitigating residual stresses and deformation, taking into consideration the reduction of heat concentration during SLM processes. Cheng et al. [18] numerically evaluated the effect of six different deposition strategies on deformation and residual stress of Inconel 718 parts by SLM. The result showed that residual stress fluctuations from all building patterns are less than 5% compared to the average value. In addition, Robinson et al. [19] found that using a chequerboard scanning path only achieves a little minimization on residual stresses.

Obviously, the influence of the building strategy on the mechanical behavior of AM built is not yet fully understood, especially for complex structures. This given, the goal of this paper is to explore the influence of the building strategy (process parameters and scanning path) on the stress relief and warpage development entailed by the L-DED process as complex rectangular Ti-6Al-4V workpieces are deposited. Firstly, in-situ experiments under three process parameters are carried out by an L-DED machine in order to calibrate a 3D coupled thermo-mechanical finite element (FE) model framework

for AM. Next, the validated high-fidelity model is employed to study the thermo-mechanical behaviors for different building strategies.

## 2. Experimental and Modeling Methodology

### *2.1. Experimental Procedure*

Three rectangular-shaped workpieces are fabricated on an annealed Ti-6Al-4V baseplate ($140 \times 50 \times 6$ mm$^3$) clamped as a cantilever. The spherical filler metal particle is Ti-6Al-4 powder with a size between 53 and 150 µm. Figure 1 shows the adopted L-DED system, which includes a YLS-3000 IPG Photonics fiber laser with a wavelength range from 960 to 1200 nm, a DPSF-2 high-precision adjustable automatic powder feeder, and a robot numerical control system. In-situ measurement equipment is also used to record the temperature and the vertical displacement of the baseplate.

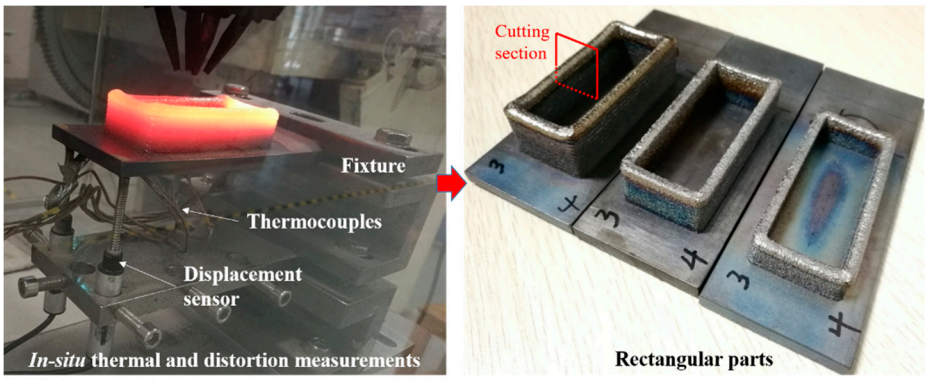


**Figure 1.** In-situ measurement setup during the laser directed energy deposition (L-DED) process.

Figure 2 shows the deposition strategy and the workpiece dimensions of the rectangular part, as well as the locations of the thermocouples and displacement sensors. Note that the rectangular structures are built with 4 different sequences looped every 4-layers. The components consist of 44 L-DED layers.

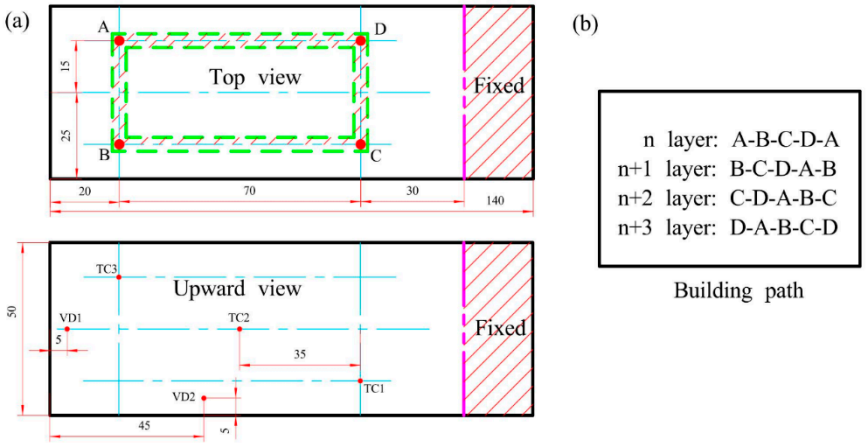


**Figure 2.** Rectangular part: (**a**) part dimensions (mm) and locations of the thermocouples and displacement sensors; (**b**) building path.

Two WXXY PM11-R1-20L displacement sensors with measurement inaccuracy of 0.02% and a maximum range of 20 mm are employed to record the vertical displacement of points DS1 and DS2 at the bottom surface of the baseplate, as shown in Figure 2. Omega GG-K-30 thermocouples (OMEGA Engineering, Norwalk, CT, USA) with measurement inaccuracy of 7.5% or 2.2 °C are used to

capture the temperature histories of the plate bottom. All thermal and displacement signals are collected by a Graphtec GL-900 8-channel high-speed data-logger (Graphtec Corporation, Yokohama, Japan). Table 1 shows three different sets of process parameters adopted to fabricate the rectangular parts.

**Table 1.** Processing parameters of laser directed energy deposition (L-DED).

| Case | 1 | 2 | 3 |
|---|---|---|---|
| Laser power P (W) | 1500 | 1000 | 1000 |
| Beam radius d (mm) | 4 | 4 | 4 |
| Scanning speed V (mm/s) | 10 | 10 | 10 |
| Back speed Vb (mm/s) | 10 | 10 | 10 |
| Up-lift height ΔZ (mm) | 0.45 | 0.40 | 0.25 |
| Feeding rate f (g/min) | 12.0 | 12.0 | 8.0 |

### 2.2. Modeling Methodology for L-DED Processes

COMET, a coupled thermo-mechanical FE software developed at CIMNE [20], is used to predict the L-DED processes for the different building strategies. The simulation procedure is achieved by moving the heat source along the user-defined printing strategy. Deposited elements are gradually activated by a born-dead-element technique to identify whether the elements belong to the molten pool area [3]. At each time step, a staggered solution is sequentially implemented for the thermal and mechanical analyses. Hence, a weak coupled thermo-mechanical analysis is done via the user-defined temperature-dependent material database. A detailed description of the employed thermo-viscoelasto-viscoplastic constitutive model suitable for AM used in this paper can be found in references [3,21].

Figure 3 shows the FE model of the rectangular structure of 70 mm length and 30 mm width, which is utilized to calibrate the L-DED model. It consists of 57,880 Q1P0 hexahedral elements and 71,391 nodes. The sizes of the deposited elements are $1 \times 1$ mm$^2$ in the horizontal plane and one element per layer, based on mesh sensitivity analyses [4,7]. Note that the substrate mesh is proportionally coarsened far from the metal deposition zone, guaranteeing the numerical accuracy of the solution and the computational efficiency.

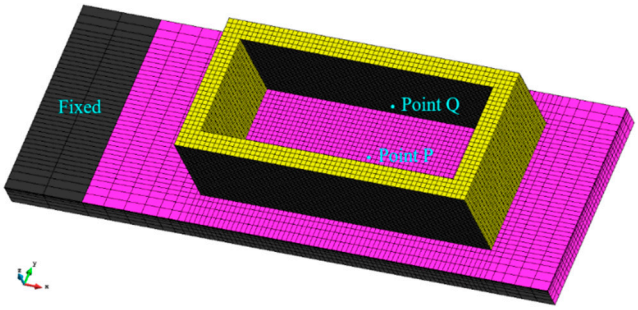


**Figure 3.** The finite element (FE) mesh model of the rectangular part used to calibrate the FE model.

Both the baseplate and metal powder are considered to be isotropic and to have the same physical and mechanical properties. Table 2 lists the material properties of the Ti-6Al-4V alloy dependent on temperature, adopted in all the analyses [22]. The effect of temperature above the molten point in the molten pool results in an artificially assumed high heat conductivity, as reported in reference [23].

**Table 2.** Temperature-dependent material properties of Ti-6Al-4V alloy, data from [22,23].

| Temperature (°C) | 20 | 205 | 500 | 995 | 1100 | 1200 | 1600 | 1650 | 2000 |
|---|---|---|---|---|---|---|---|---|---|
| Density (kg/m$^3$) | 4420 | 4395 | 4350 | 4282 | 4267 | 4252 | 4198 | 3886 | 3818 |
| Thermal conductivity (W/(m·°C)) | 7 | 8.75 | 12.6 | 22.7 | 19.3 | 21 | 25.8 | 83.5 | 83.5 |
| Heat capacity (J/(kg·°C)) | 546 | 584 | 651 | 753 | 641 | 660 | 732 | 831 | 831 |
| Poisson's ratio | 0.345 | 0.35 | 0.37 | 0.43 | 0.43 | 0.43 | 0.43 | 0.43 | 0.43 |
| Thermal expansion coefficient (μm/m/°C) | 8.78 | 10 | 11.2 | 12.3 | 12.4 | 12.42 | 12.5 | 12.5 | 12.5 |
| Young's modulus (GPa) | 110 | 100 | 76 | 15 | 5 | 4 | 1 | 0.1 | 0.01 |
| Elastic limit (MPa) | 850 | 630 | 470 | 13 | 5 | 1 | 0.5 | 0.1 | 0.01 |

During the thermal analysis for the L-DED process, radiation and convection effects between the part and its surroundings are considered in all the external surfaces of both the baseplate and the depositions. In the L-DED process, a heat convective coefficient of $h = 1$ W/(m$^2$·°C) is used, and the heat transfer coefficient (HTC) by emissivity is fixed to $\varepsilon = 0.285$. A higher HTC of $h = 50$ W/(m$^2$·°C) is applied to simulate the heat transfer condition at the contact interface between the fixture and the baseplate. Room temperature is kept at $T_{env} = 25$ °C, and the laser absorptivity for the L-DED process is set at $\eta = 0.3$. All processing and material parameters applied in the numerical prediction are determined from experimental evidence.

## 3. Model Calibration

Before the thermo-mechanical software is used to investigate the effect of the alternative building strategies on the response of the parts, the computational model needs to be calibrated and its accuracy assessed. This procedure, regarding the rectangular parts examined in this work, has been performed and reported in reference [5]. Figure 4 summarizes the results obtained in the calibration stage. It is remarkable that numerical predictions agree with experimental measurements for all cases. In addition, it can be observed that increasing the laser power remarkably increases the part temperature and the final vertical displacement of the free end of the baseplate, while varying the power feeding rate hardly affects the thermo-mechanical responses.

There is a slight difference between the experimental and the numerical results. The major reason for this is the simplification of the boundary conditions used in the numerical simulation and the measuring errors during the L-DED process. Notably, in the initial fabrication phase, the geometric dimension of the molten pool is notoriously limited by the cold baseplate, contributing to a small width and thickness of the cladding track, as shown in Figure 5a. As the deposited layers increase, the built layer sizes gradually increase until it stabilizes [24,25]. However, the geometric mesh model uses an average layer-thickness (and width) calculated by the final built height divided as fact the total number of layers [26–28]. This is responsible for the initial mismatch in the displacement prediction. In order to improve the resulting accuracy of the mechanical model, a modified geometry mesh model referring to the actual deposition sizes is used, as shown in Figure 5b. Figure 6 compares the predicted displacement histories between the improved model and the experimental reference. A remarkable improvement in the warpage prediction is achieved by the upgraded model. The developed numerical technique can be implemented in other applications of AM research. In this work, the slight variation of the layer dimensions in the initial deposition process for different building strategies is not implemented as the qualitative comparison of the thermal and mechanical responses due to the building strategy is investigated. Therefore, all the numerical investigations for different building strategies use uniform layer thickness.

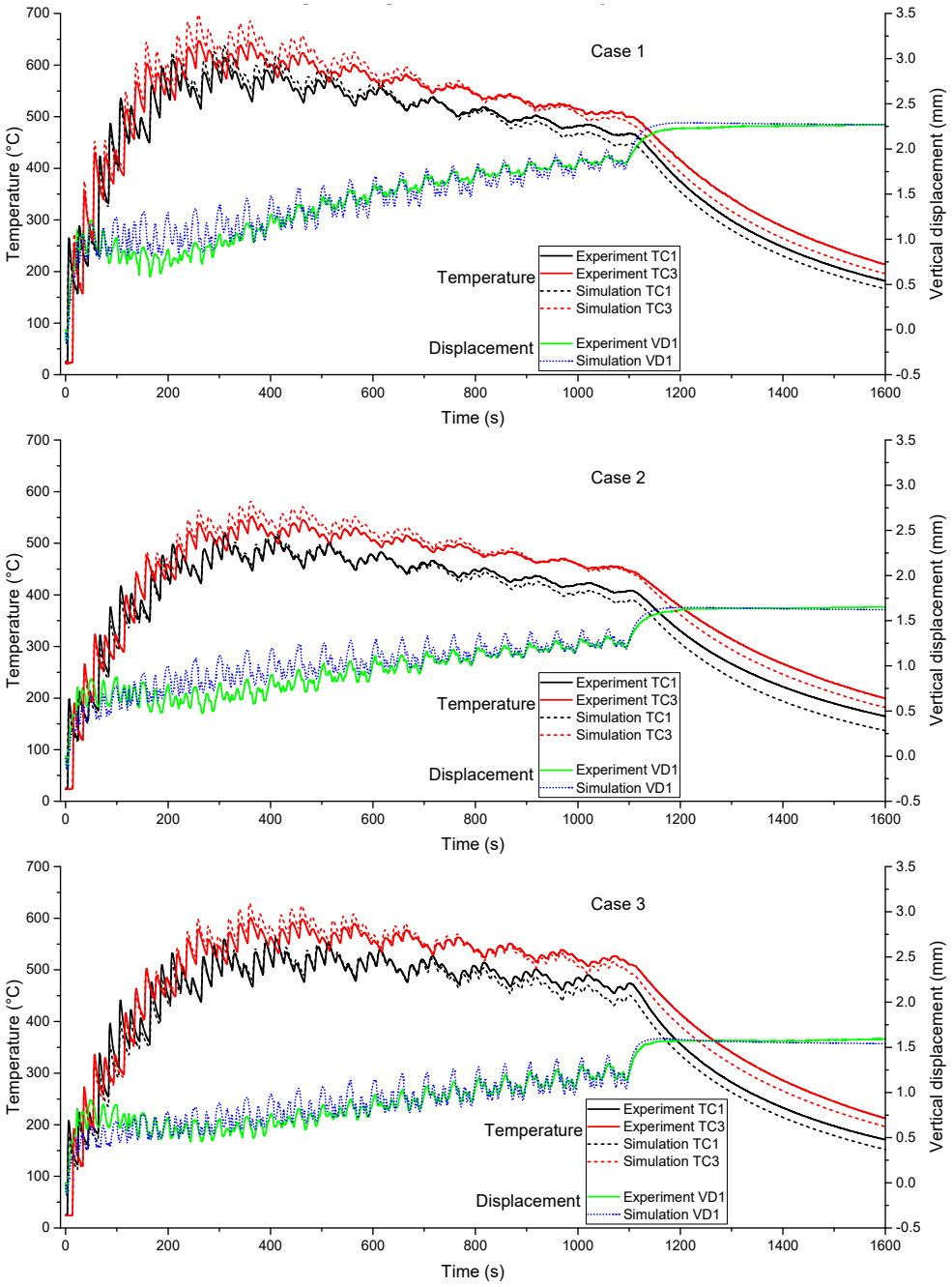


**Figure 4.** Comparison between calculated and experimental thermo-mechanical results of the rectangular parts under three different process parameters.

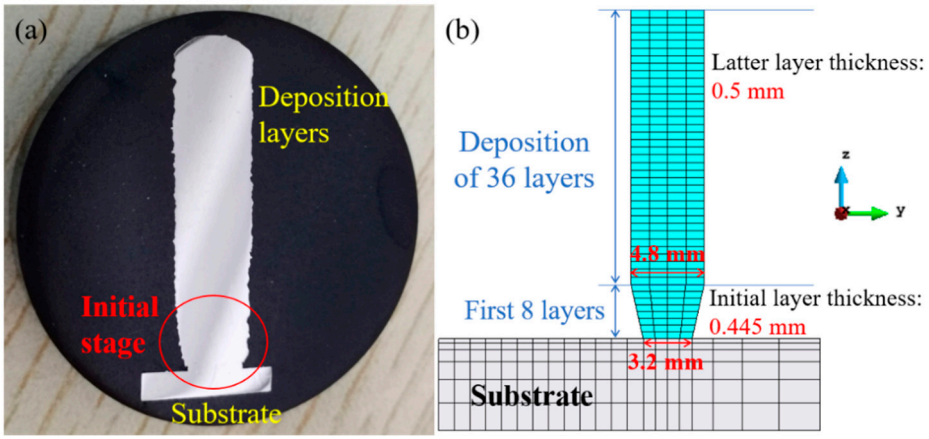


**Figure 5.** (**a**) Varying layer sizes in the initial building stage (see Figure 1); (**b**) modified geometric mesh model referring to the actual workpiece.

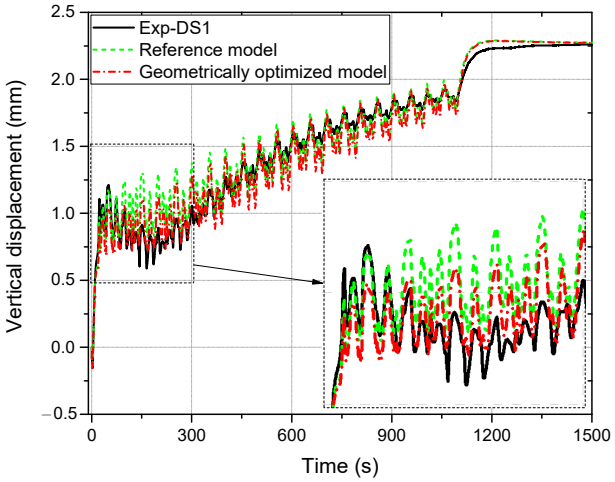


**Figure 6.** Rectangle under Case 1: comparison of the distortion histories of the substrate between the reference simulation and the upgraded model.

## 4. Effect of the Building Strategy

To study the residual stresses and warpage of rectangular Ti-6Al-4V parts, six types of scanning patterns are designed, as shown in Figure 7. Path A uses a cycling printing strategy for the entire buildup. In paths B and C, each layer is split into two parts to be cladded, but the laser start point is different for both. Path D adopts alternative start points in the middle of the long-walls to deposit each layer. In the case of path E, the short-walls and long-walls are scanned counterclockwise and clockwise, respectively. Finally, path E uses several short scan vectors and changes the deposition sequence between the odd and even layers.

It is to be mentioned that the back speed has an influence on the dwell-time as discontinuous scanning lines within the same layer or between adjacent layers occur. Hence, the effect of different back speeds on thermo-mechanical responses of rectangular parts first is investigated to decrease the interference of the dwell-time. Next, a higher back speed of 50 mm/s is used in all numerical samples to study six different scanning paths (Figure 7). For each case, the settings of the substrate and deposition sizes, the boundary conditions, and the process parameters (Table 1) in simulations are in line with the numerical model of the actual rectangular workpieces.

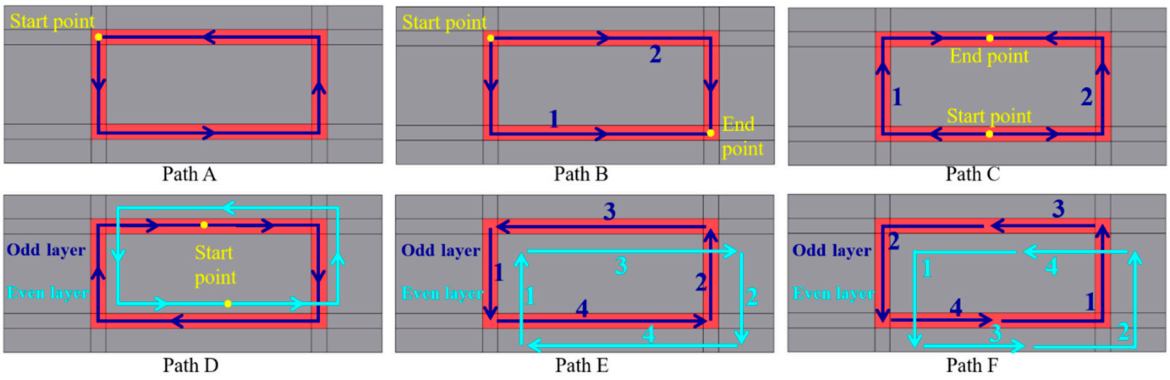


**Figure 7.** Schematic of six different building strategies for rectangular parts in L-DED.

## *4.1. Effect of the Back Speed*

### 4.1.1. Thermal Response

Based on the validated FE model, the thermal responses of the rectangular specimens using different back speeds are predicted. Figure 8 compares the temperature histories of point P at the middle/top of the baseplate (see Figure 3) for the three cases in Table 1 and two different back speeds. Point P is selected to represent the temperature field evolution of the baseplate. Note that increasing the back speed enlarges the heat accumulation in the part while reducing the buildup time by about 200 s. Compared with the original reference representing the actual part, both the peak and final values of temperature after completing the last layer increase by approximately 30 °C using a higher back speed of 50 mm/s. The reason for this is that the higher the back speed, the shorter the dwell-time (cooling time) becomes during the building process. As a result, the increasing heat accumulation favors stress relaxation in the built [1,9].

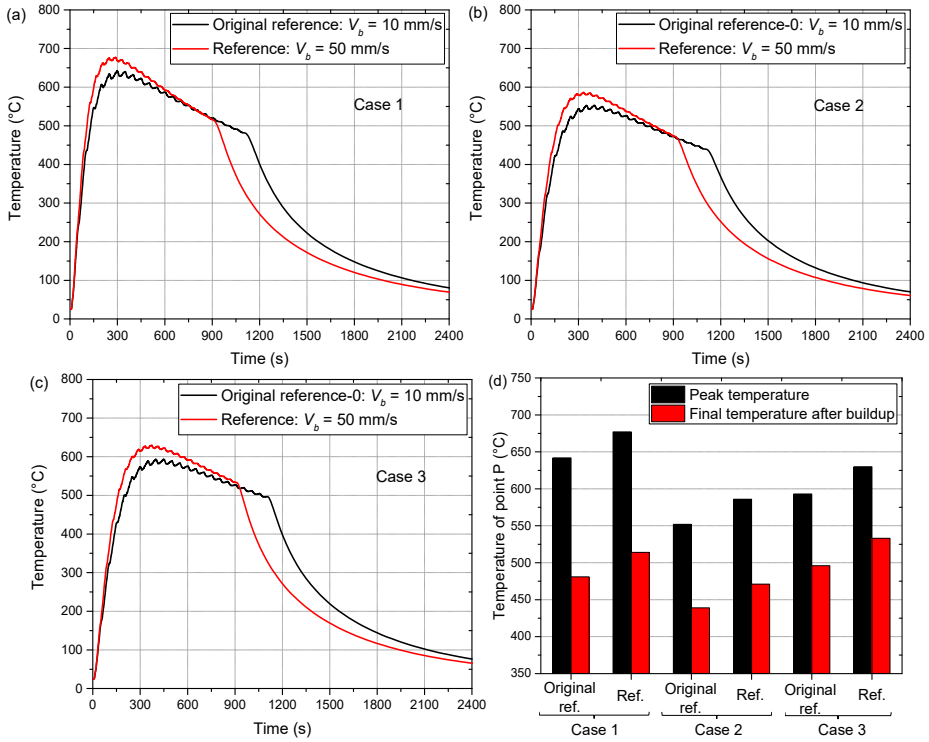


**Figure 8.** Temperature histories of point P (see Figure 3): (**a**) Case 1; (**b**) Case 2; (**c**) Case 3; (**d**) comparison of peak and final temperatures after the last layer for the three cases.

### 4.1.2. Mechanical Response

Figure 9 compares the evolution of the vertical displacement of point DS1 (Figure 2) when varying the back speed. It can be seen that using a higher back speed achieves a notable warpage reduction due to stress relief. For the three cases studied, the decreased amount of the final vertical displacement is 0.5 mm, 0.26 mm, and 0.29 mm, respectively. Obviously, Case 1, with higher laser power, achieves the larger stress relief and warpage mitigation.

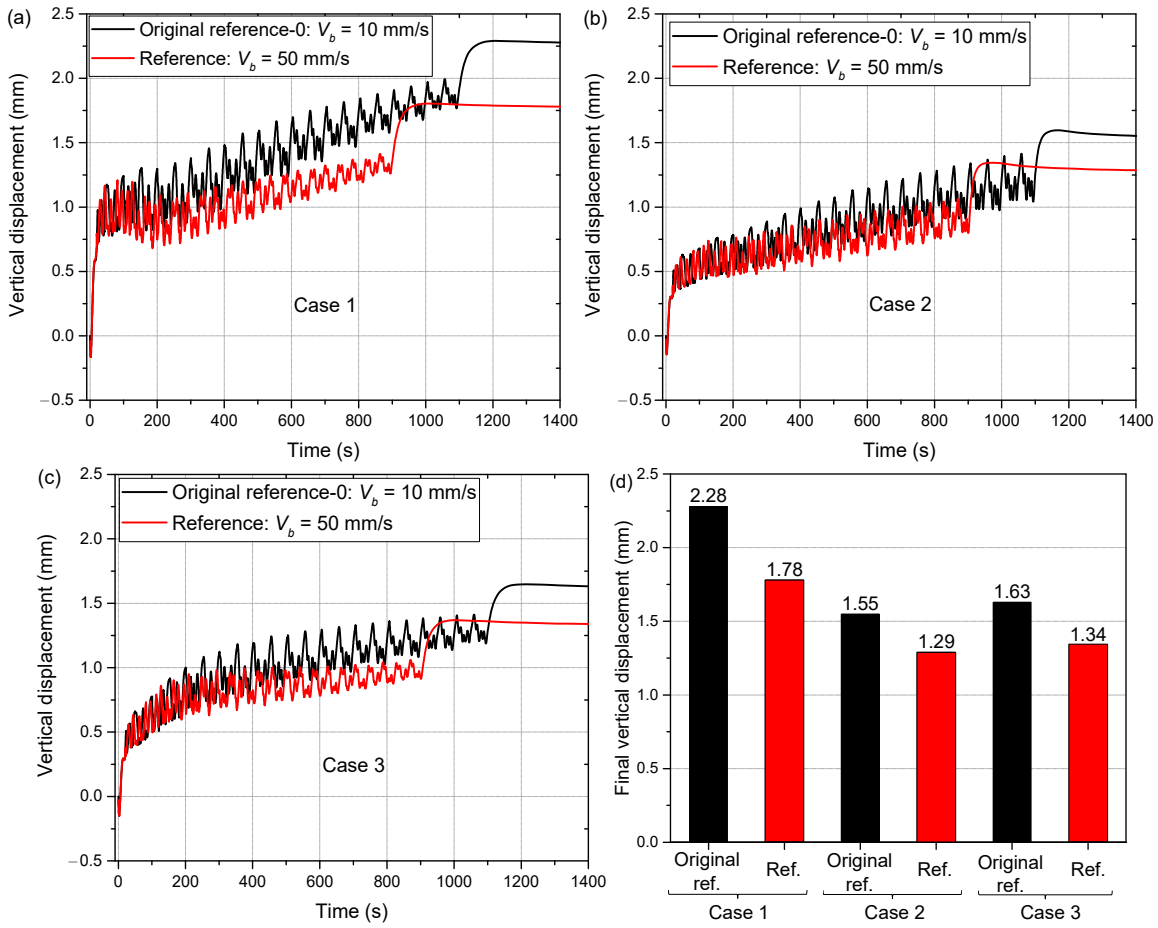


**Figure 9.** Evolutions of the vertical displacement of point DS1 (see Figure 2): (**a**) Case 1; (**b**) Case 2; (**c**) Case 3; (**d**) final displacement under three cases.

Figure 10 compares the residual von Mises stress field distributions for two different back speeds. It can be seen that the biggest stresses are located at the interfaces between the deposition and baseplate for all samples. Although increasing the back speed fails to reduce the largest stress at the corners of the rectangular parts, it mitigates the compressive stress level on the substrate top. This demonstrates that smaller tensile stresses are generated in the rectangular sample during the building process.

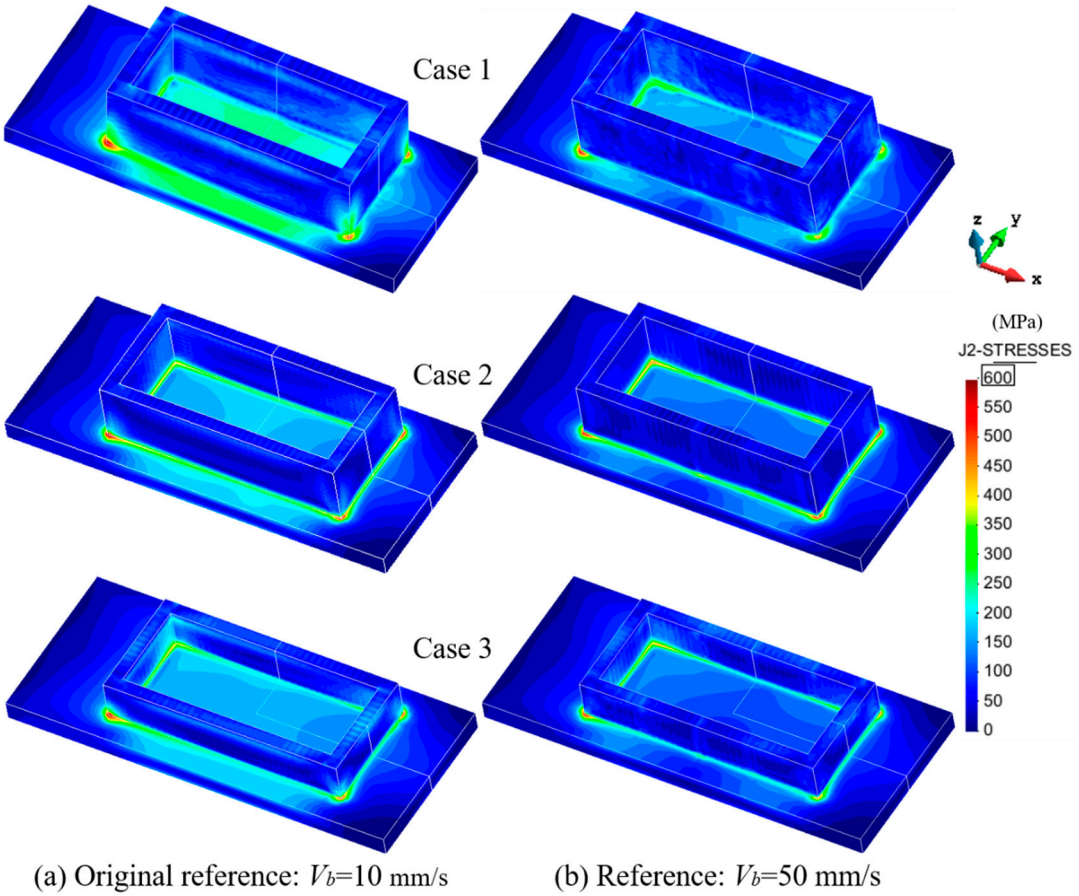


**Figure 10.** Residual von Mises stress fields for the three cases in Table 1 and two different back speeds.

### *4.2. Effect of the Scanning Pattern*

To reduce the dwell-time effect, the high back speed of 50 mm/s is now used in all numerical samples to analyze the influence of the scanning pattern on the thermo-mechanical response in the L-DED process.

#### 4.2.1. Temperature Evolution

On the basis of the validated FE model, the temperature evolution for six different scanning strategies are predicted. Figure 11 shows the thermal histories of point P (see Figure 3) under Case 1 during the building process. It can be seen from Figure 11a that varying the scanning strategy hardly changes the temperature profile. The shorter the building process, the higher the peak temperature. It can be seen in Figure 11b that compared with the reference, only the specimen using path A attains a slightly increased temperature, while the other cases produce lower or unchanged temperature levels.

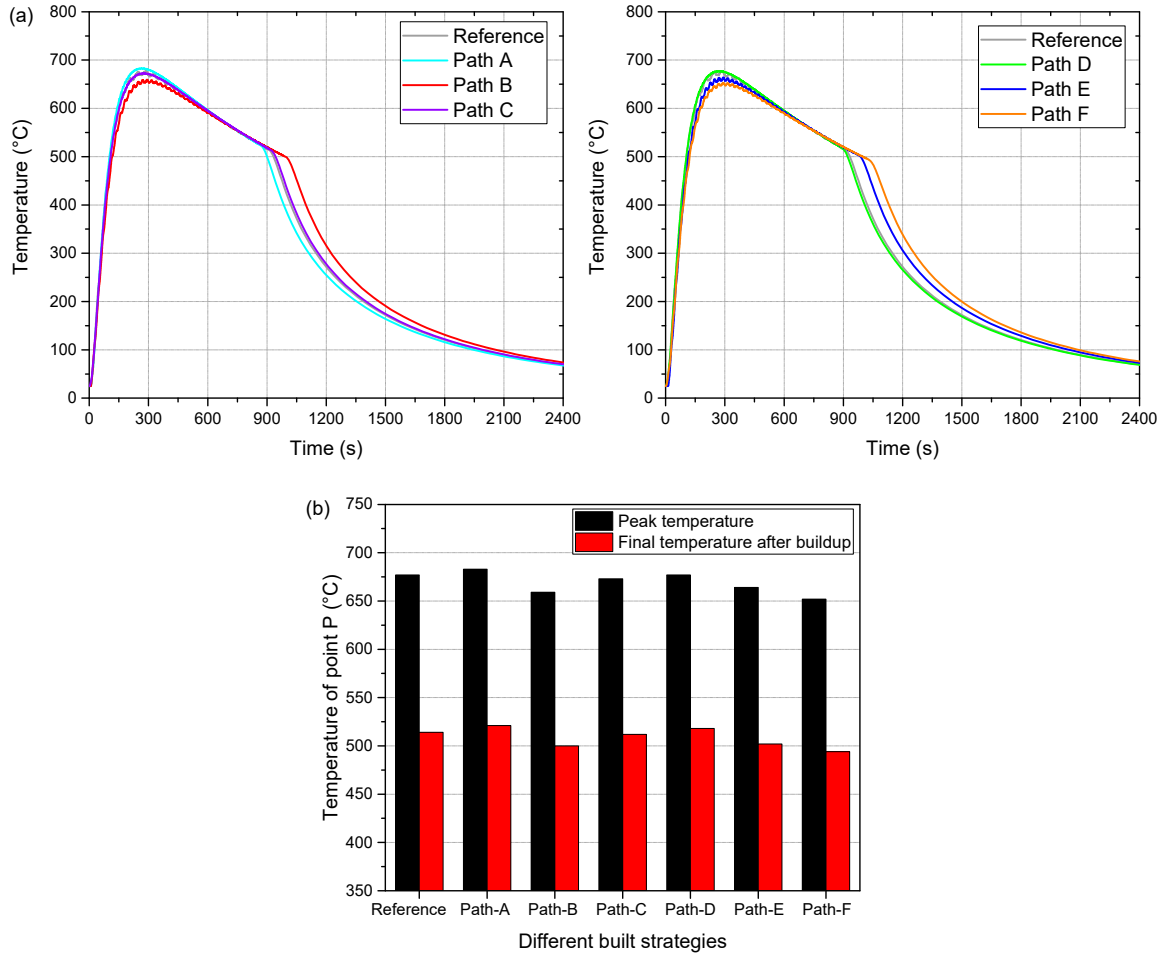


**Figure 11.** Predicted thermal responses of point P (see Figure 3) for Case 1: (**a**) thermal histories; (**b**) peak and final temperatures after the last layer under different scanning strategies.

### 4.2.2. Displacement history

Figure 12a shows the vertical displacement histories of point DS1 (Figure 2) for Case 1 for different scanning strategies. Figure 12b compares the final displacements of the baseplate. Note that, compared with the reference, using paths A and C achieves a noteworthy warpage reduction, but larger residual displacements are produced for paths E and F. The displacement for path B is almost the same as for the reference, and only slight deformation mitigation is obtained by adopting path D. These results can be explained by the following.

In path A, there is no dwell-time during the building process, contributing to heat accumulation in part and consequent stress relief. In path C, the length of the longitudinal scanning vectors is cut down, which decreases the tensile stress along the long-wall direction [29]. Therefore, small part warpage is generated in these two cases. Compared with path C, path D entails a larger displacement because it has a long scanning vector for each deposited layer. Furthermore, the longitudinal long scanning vectors in paths B and E are responsible for the deformation of the baseplate. Finally, although path F eliminates the long scanning vector, the discontinuous depositions lead to an increasing dwell-time during the building process and, consequently, the triggering of a pronounced warpage accumulation.

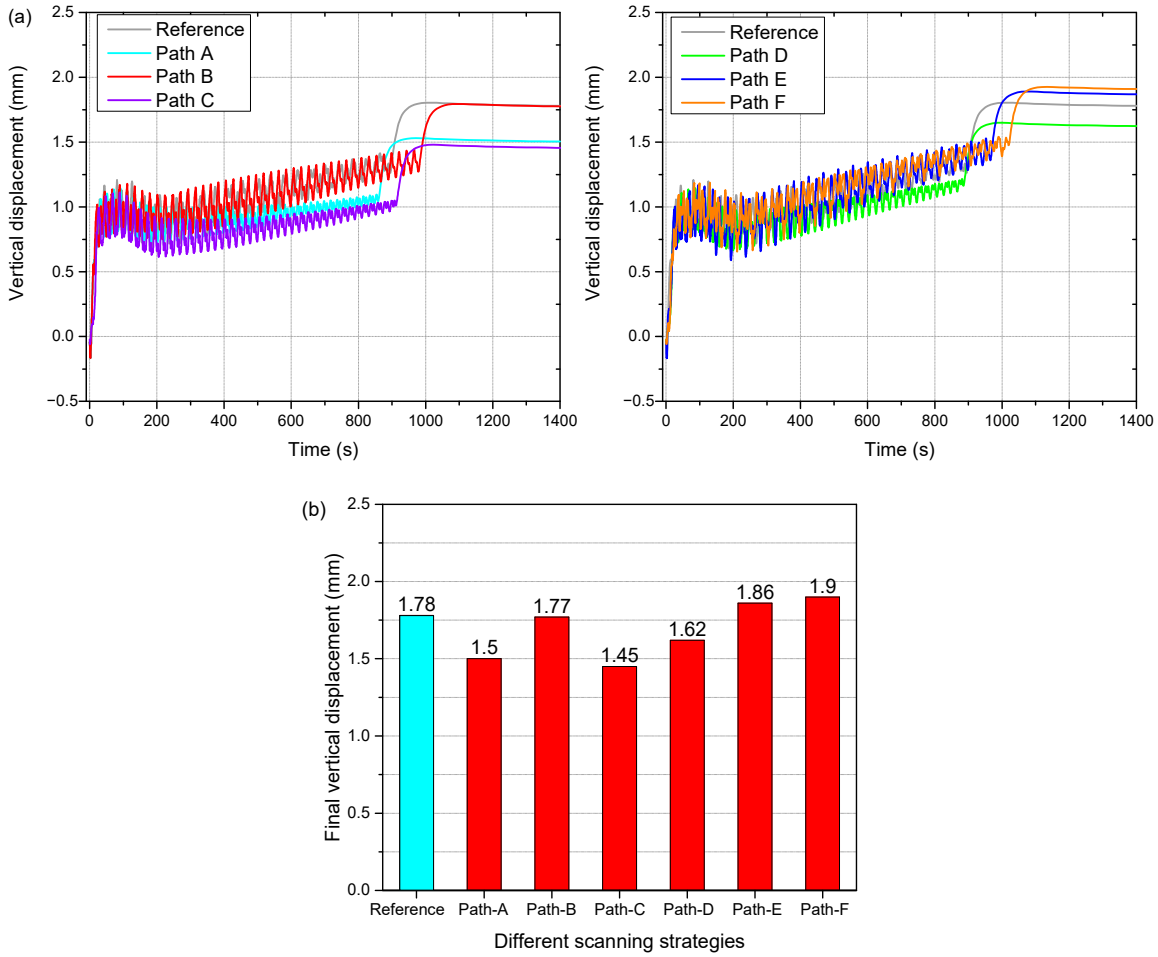


**Figure 12.** Predicted substrate warpage for Case 1 for different scanning strategies: (**a**) vertical displacement history of point DS1; (**b**) final vertical displacements of point DS1.

Figure 13 compares the displacement histories of point DS1 between the reference path and path C under Cases 2 and 3. Employing path B strategy achieves a notable deformation reduction for both cases. Table 3 summarizes the warpage reduction of point DS1 for different building strategies in terms of the scanning path and process parameters. When path B is used, the final displacements under the three cases are mitigated by 36.4%, 25.8%, and 32.5%, respectively.

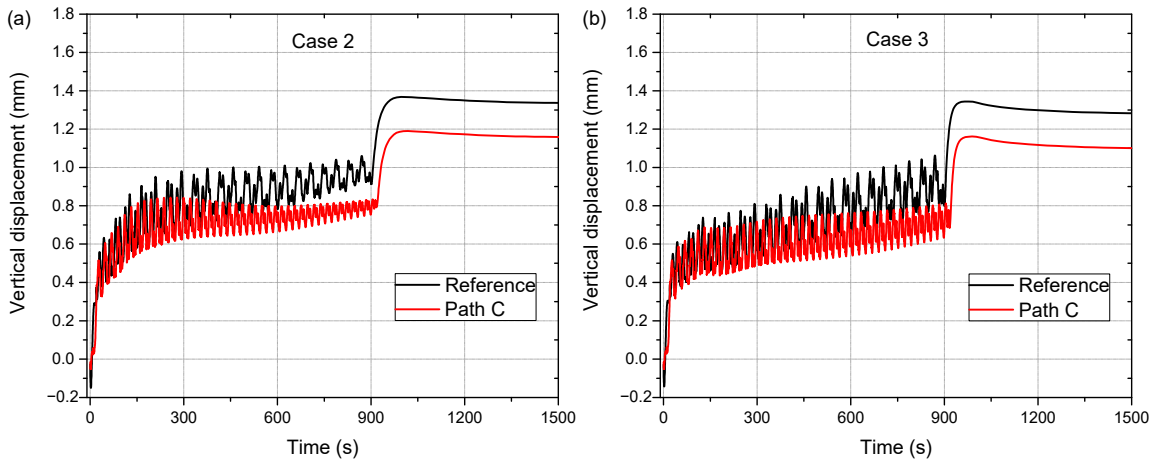


**Figure 13.** Comparison of the displacement evolutions of point DS1 between the reference and path C: (**a**) Case 1; (**b**) Case 2.

**Table 3.** Warpage reduction (%) of point DS1 for different building strategies compared to the original reference (100%).

| | Case 1 | | | | | | | Case 2 | | Case 3 | |
|---|---|---|---|---|---|---|---|---|---|---|---|
| | **Ref.** | **Path A** | **Path B** | **Path C** | **Path D** | **Path E** | **Path F** | **Ref.** | **Path C** | **Ref.** | **Path C** |
| Warpage reduction | 21.9 | 34.2 | 22.4 | 36.4 | 28.9 | 18.4 | 16.7 | 16.8 | 25.8 | 17.8 | 32.5 |

#### 4.2.3. Residual Stresses

In order to understand why a shorter scanning vector can generate smaller part warpage (see Figures 12 and 13), the evolution of the longitudinal stress field between the original reference (Figure 2) and path C under Case 1 is compared and shown in Figure 14. Correspondingly, Figure 15 gives the comparison of the variation of the temperature and longitudinal stress of point Q at the bottom/middle of the deposited long-wall (see Figure 3).

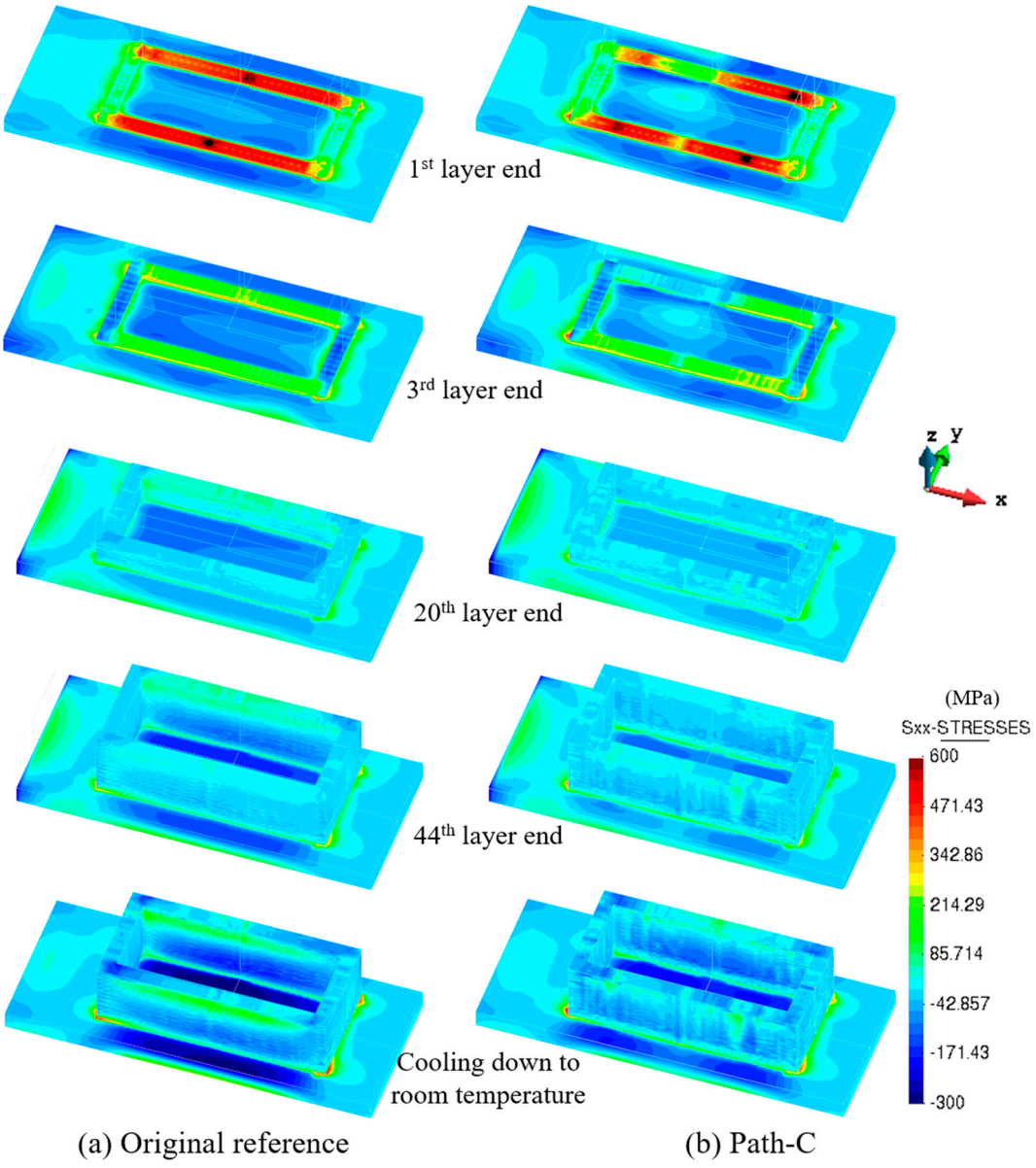


**Figure 14.** Rectangular part: the evolution of the longitudinal stress ($\sigma_{xx}$) field under Case 1 for different building times.

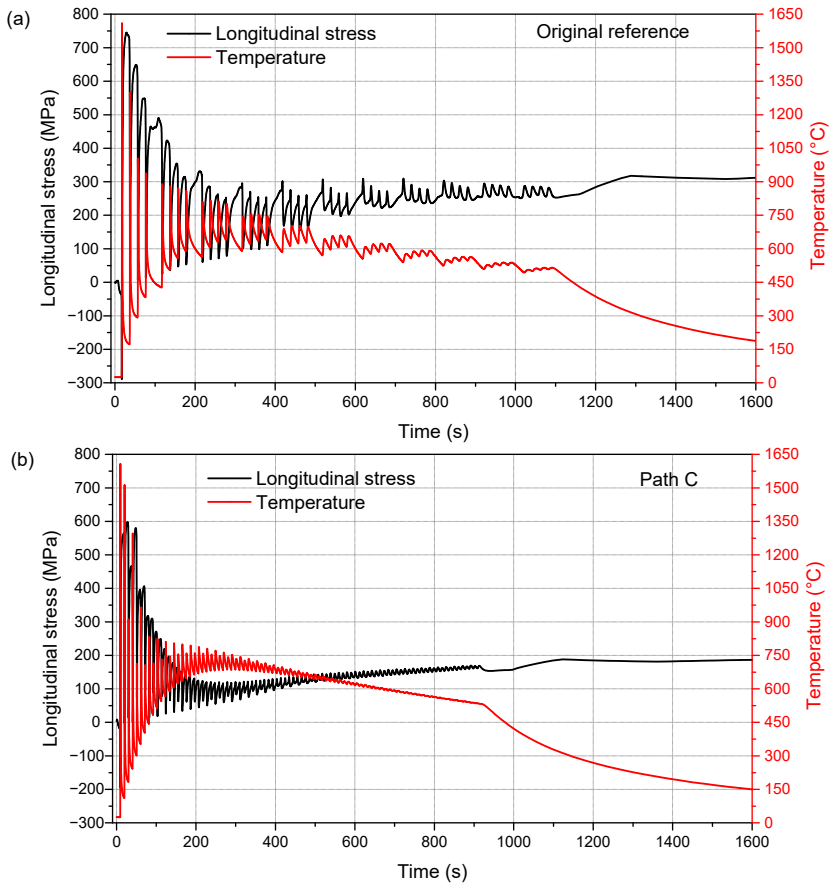


**Figure 15.** Comparison between the temperature and longitudinal stress ($\sigma_{xx}$) of point Q (see Figure 3): (**a**) original reference; (**b**) path C.

It can be observed from Figure 14 that after the building of the first layer, both cases produce higher stress along the long-wall due to the rapid cooling and shrinkage of the cladding layer. Notably, the distributions of the longitudinal stresses are, respectively, continuous and discontinuous for the original reference and path C when the first layer is deposited. Such a situation is maintained for upper deposited layers even if the stress level decreases dramatically on account of the increasing substrate temperature. After the buildup, the reference sample generates larger compressive stresses on the substrate top than the case under path C, owing to the continuous longitudinal stress along the long-wall. In addition, it can be seen in Figure 15 that the higher the temperature becomes, the lower the corresponding stress is, and vice versa. Compared with the original reference, the sample under path C experiences lower longitudinal stress during the fabricating process, contributing to the small displacement along the building direction (see Figure 12).

Figure 16 compares the residual von Mises stress fields for Case 1 for different scanning paths. It can be found that the highest residual stress zone still occurs on the interface between the deposition and substrate for all cases. Compared with the reference, path C produces a slightly smaller residual stress on the top surface of the substrate. However, there are no obvious differences in the stress profiles for different cases. Figure 17 shows the comparison of the residual von Mises stress field between the reference path and path C under Cases 2 and 3. Again, the difference in the residual stress fields is small. Hence, varying the scanning strategy fails to mitigate the residual stresses of the rectangular workpieces.

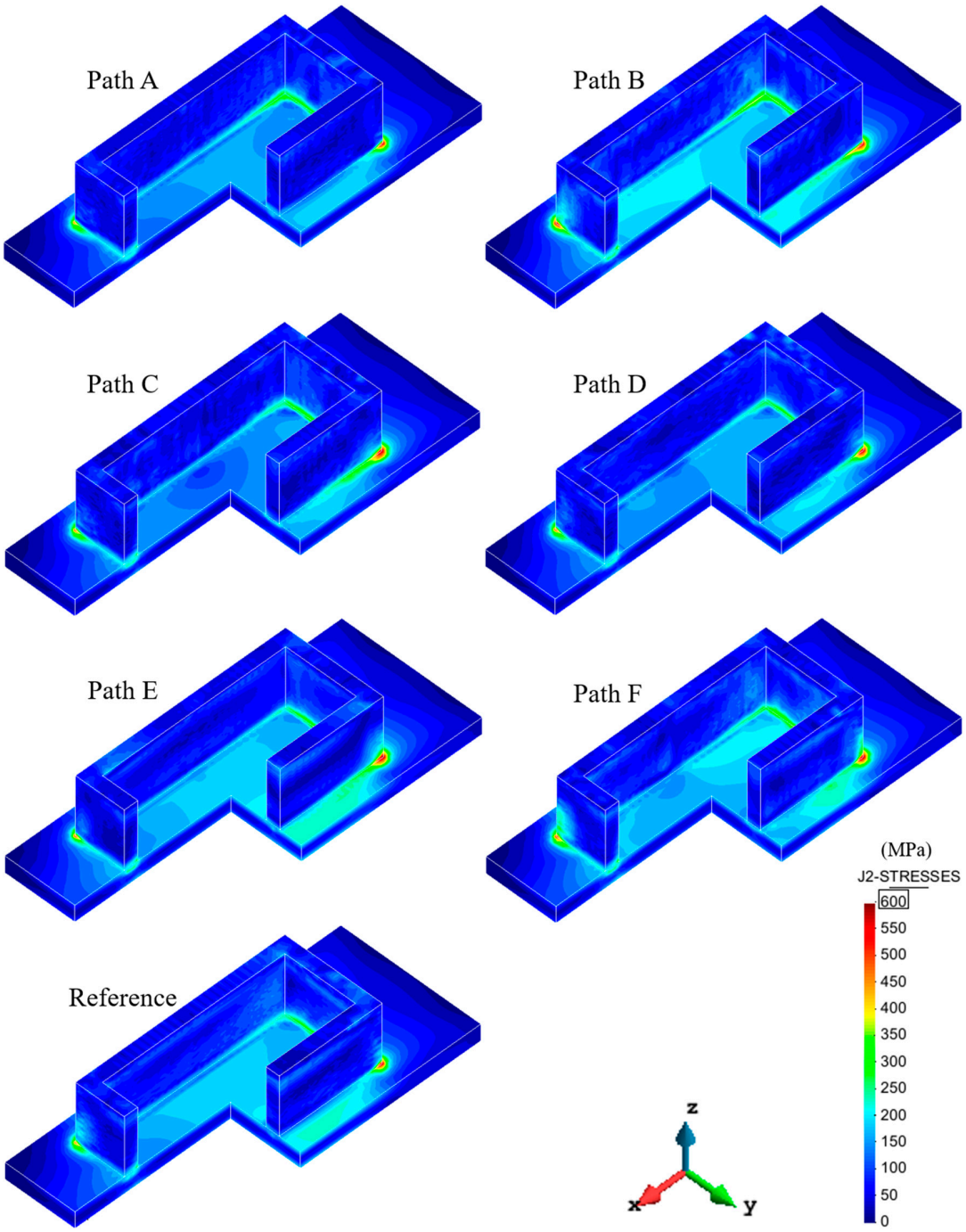


**Figure 16.** Comparison of residual von Mises stress field under Case 1 for different building strategies.

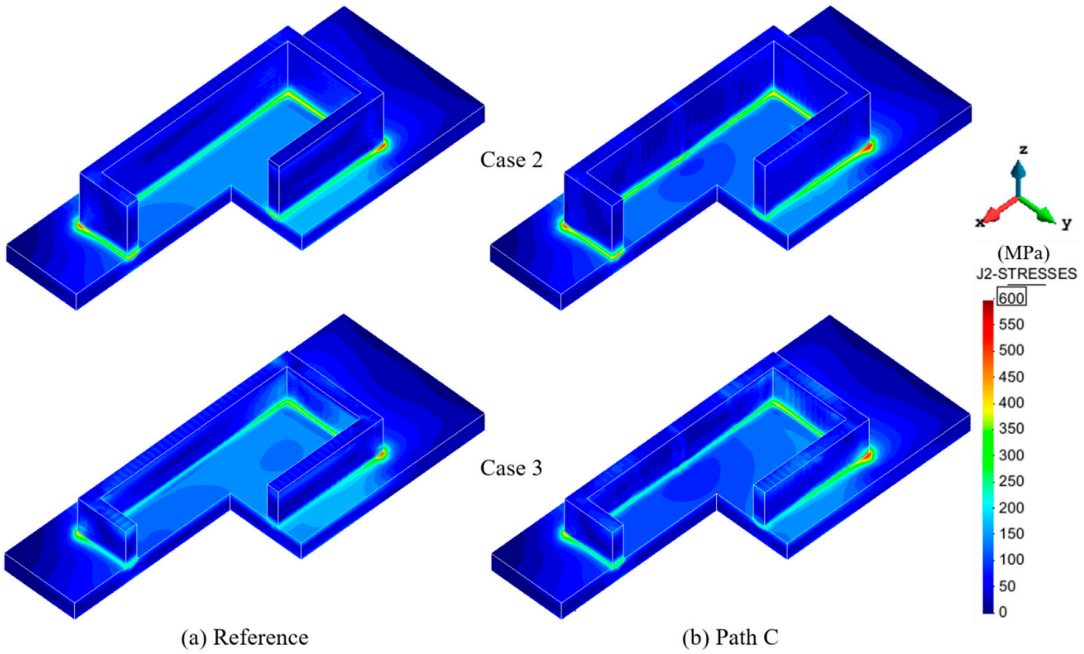


**Figure 17.** Comparison of residual von Mises stress field between the reference path and path C under Cases 2 and 3.

## 5. Conclusions

In this paper, an experimentally calibrated 3D FE model for AM is used to study the effect of different building strategies on the warpage and stress development of Ti-6Al-4V rectangular workpieces manufactured by the L-DED technology. Distinctive conclusions are:

1. Remarkable agreement between the predicted and experimental thermal and mechanical results provides confidence for adopting the high-fidelity model to explore diverse thermo-mechanical problems in the AM. Considering the actual layer sizes in numerical modeling improves the accuracy of the mechanical predictions.
2. Controlling the back speed is beneficial to reduce the dwell-time during the manufacturing process. The shorter the dwell-time is, the higher the heat accumulation becomes, which triggers heat softening and stress relief, leading to the mitigation of both residual stress and distortion.
3. Shortening the longitudinal scanning vectors significantly alleviates the effect of the longitudinal tensile stress along the long-wall direction, contributing to the reduction of the part warpage.
4. Using an optimized scanning strategy can achieve a pronounced minimization in vertical displacement (36.4%) but fails to control the development of the thermal stresses in the manufacturing process.
5. In order to control both residual stress and deformation of the rectangular workpieces, the combination of shortening the scanning vector and preheating the baseplate before L-DED is needed [5].

**Author Contributions:** Conceptualization, X.L. (Xufei Lu) and M.C. (Michele Chiumenti); methodology and software, M.C. (Michele Chiumenti) and M.C. (Miguel Cervera); data curation, X.J. and X.L. (Xufei Lu); writing—original draft preparation, X.L. (Xufei Lu) and J.L.; writing—review and editing, G.Z., M.C. (Miguel Cervera), and X.L. (Xin Lin); supervision, J.L. and X.L. (Xin Lin). All authors have read and agreed to the published version of the manuscript.

**Funding:** This research was funded by the National Key Technologies R & D Program (No. 2016YFB1100104) and the China Scholarship Council (No. 201906290011). Funding from the Spanish Ministry of Economy and Competitivity (MINECO) under the ADaMANT project: *Computational Framework for Additive Manufacturing of Titanium Alloy Components* (ref: DPI2017-85998-P), within the Excellency Programme for Knowledge Generation, is gratefully acknowledged. CIMNE is the recipient of the Severo Ochoa Award of Excellence

from MINECO. This work was also funded by the European KYKLOS 4.0 project: *An Advanced Circular and Agile Manufacturing Ecosystem based on rapid reconfigurable manufacturing process and individualized consumer preferences* (No. H2020-DT-2019-1).

**Conflicts of Interest:** The authors declare no conflict of interest.

## References

1. Lu, X.; Lin, X.; Chiumenti, M.; Cervera, M.; Li, J.; Ma, L.; Wei, L.; Hu, Y.; Huang, W. Finite element analysis and experimental validation of the thermomechanical behavior in Laser Laser Directed energy deposition of Ti-6Al-4V. *Addit. Manuf.* **2018**, *21*, 30–40.
2. Guo, P.; Lin, X.; Liu, J.; Xu, J.; Li, J.; Zhang, Y.; Lu, X.; Qu, N.; Lan, H.; Huang, W. Passive behavior of nickel-based superalloys prepared by high-deposition-rate laser solid forming additive manufacturing. *Corros. Sci.* **2020**, *177*, 109036. [CrossRef]
3. Chiumenti, M.; Cervera, M.; Salmi, A.; De Saracibar, C.A.; Dialami, N.; Matsui, K. Finite element modeling of multi-pass welding and shaped metal deposition processes. *Comput. Methods Appl. Mech. Eng.* **2010**, *199*, 2343–2359. [CrossRef]
4. Cao, J.; Gharghouri, M.A.; Nash, P. Finite-element analysis and experimental validation of thermal residual stress and distortion in electron beam additive manufactured Ti-6Al-4V build plates. *J. Mater. Process. Technol.* **2016**, *237*, 409–419. [CrossRef]
5. Lu, X.; Lin, X.; Chiumenti, M.; Cervera, M.; Hu, Y.; Ji, X.; Ma, L.; Yang, H.; Huang, W. Residual stress and distortion of rectangular and S-shaped Ti-6Al-4V parts by Directed Energy Deposition: Modelling and experimental calibration. *Addit. Manuf.* **2019**, *26*, 166–179. [CrossRef]
6. Michael, G.; Michaleris, P. (Eds.) *Thermo-Mechanical Modeling of Additive Manufacturing*; Butterworth-Heinemann: Oxford, UK, 2017.
7. Chiumenti, M.; Lin, X.; Cervera, M.; Lei, W.; Zheng, Y.; Huang, W. Numerical simulation and experimental calibration of additive manufacturing by blown powder technology. Part I: Thermal analysis. *Rapid Prototyp. J.* **2017**, *23*, 448–463. [CrossRef]
8. Lindgren, L.-E.; Lundbäck, A.; Malmelöv, A. Thermal stresses and computational welding mechanics. *J. Therm. Stress.* **2019**, *42*, 107–121. [CrossRef]
9. Denlinger, E.R.; Michaleris, P. Effect of stress relaxation on distortion in additive manufacturing process modeling. *Addit. Manuf.* **2016**, *12*, 51–59. [CrossRef]
10. Chen, Z.; Ye, H.; Xu, H. Distortion control in a wire-fed electron-beam thin-walled Ti-6Al-4V freeform. *J. Mater. Process. Technol.* **2018**, *258*, 286–295. [CrossRef]
11. Wang, Z.; Stoica, A.D.; Ma, D.; Beese, A.M. Stress relaxation behavior and mechanisms in Ti-6Al-4V determined via in situ neutron diffraction: Application to additive manufacturing. *Mater. Sci. Eng. A* **2017**, *707*, 585–592. [CrossRef]
12. Setien, I.; Chiumenti, M.; Van Der Veen, S.; Sebastian, M.S.; Garciandía, F.; Echeverría, A. Empirical methodology to determine inherent strains in additive manufacturing. *Comput. Math. Appl.* **2019**, *78*, 2282–2295. [CrossRef]
13. Lu, X.; Lin, X.; Chiumenti, M.; Cervera, M.; Hu, Y.; Ji, X.; Ma, L.; Huang, W. In situ Measurements and Thermo-mechanical Simulation of Ti-6Al-4V Laser Laser Directed energy deposition Processes. *Int. J. Mech. Sci.* **2019**, *153*, 119–130. [CrossRef]
14. Levkulich, N.; Semiatin, S.; Gockel, J.; Middendorf, J.; Dewald, A.; Klingbeil, N. The effect of process parameters on residual stress evolution and distortion in the laser powder bed fusion of Ti-6Al-4V. *Addit. Manuf.* **2019**, *28*, 475–484. [CrossRef]
15. Li, H.; Ramezani, M.; Chen, Z.; Singamneni, S. Effects of Process Parameters on Temperature and Stress Distributions During Selective Laser Melting of Ti-6Al-4V. *Trans. Indian Inst. Met.* **2019**, *72*, 3201–3214. [CrossRef]
16. Wu, Q.; Mukherjee, T.; Liu, C.; Lu, J.; Debroy, T. Residual stresses and distortion in the patterned printing of titanium and nickel alloys. *Addit. Manuf.* **2019**, *29*, 100808. [CrossRef]
17. Ramos, D.; Belblidia, F.; Sienz, J. New scanning strategy to reduce warpage in additive manufacturing. *Addit. Manuf.* **2019**, *28*, 554–564. [CrossRef]

18. Cheng, B.; Shrestha, S.; Chou, K. Stress and deformation evaluations of scanning strategy effect in selective laser melting. *Addit. Manuf.* **2016**, *12*, 240–251. [CrossRef]
19. Robinson, J.; Ashton, I.; Fox, P.; Jones, E.; Sutcliffe, C. Determination of the effect of scan strategy on residual stress in laser powder bed fusion additive manufacturing. *Addit. Manuf.* **2018**, *23*, 13–24. [CrossRef]
20. Cervera, M.; de Saracibar, C.A.; Chiumenti, M. COMET: Coupled Mechanical and Thermal Analysis. Data Input Manual, Version 5.0, Technical Report IT-308. 2002.
21. Chiumenti, M.; Cervera, M.; Dialami, N.; Wu, B.; Jinwei, L.; De Saracibar, C.A. Numerical modeling of the electron beam welding and its experimental validation. *Finite Elem. Anal. Des.* **2016**, *121*, 118–133. [CrossRef]
22. Parry, L.; Ashcroft, I.A.; Wildman, R.D. Understanding the effect of laser scan strategy on residual stress in selective laser melting through thermo-mechanical simulation. *Addit. Manuf.* **2016**, *12*, 1–15. [CrossRef]
23. Fallah, V.; Alimardani, M.; Corbin, S.F.; Khajepour, A. Temporal development of melt-pool morphology and clad geometry in laser powder deposition. *Comput. Mater. Sci.* **2011**, *50*, 2124–2134. [CrossRef]
24. Wang, J.; Lin, X.; Li, J.; Hu, Y.; Zhou, Y.; Wang, C.; Li, Q.; Huang, W. Effects of deposition strategies on macro/microstructure and mechanical properties of wire and arc additive manufactured Ti 6Al 4V. *Mater. Sci. Eng. A* **2019**, *754*, 735–749. [CrossRef]
25. Baykasoğlu, C.; Akyildiz, O.; Tunay, M.; To, A.C. A process-microstructure finite element simulation framework for predicting phase transformations and microhardness for directed energy deposition of Ti6Al4V. *Addit. Manuf.* **2020**, *35*, 101252. [CrossRef]
26. Hönnige, J.; Colegrove, P.; Ahmad, B.; Fitzpatrick, M.; Ganguly, S.; Lee, T.; Williams, S. Residual stress and texture control in Ti-6Al-4V wire + arc additively manufactured intersections by stress relief and rolling. *Mater. Des.* **2018**, *150*, 193–205. [CrossRef]
27. Xiong, J.; Li, R.; Lei, Y.; Chen, H. Heat propagation of circular thin-walled parts fabricated in additive manufacturing using gas metal arc welding. *J. Mater. Process. Technol.* **2018**, *251*, 12–19. [CrossRef]
28. Denlinger, E.R.; Heigel, J.C.; Michaleris, P. Residual stress and distortion modeling of electron beam direct manufacturing Ti-6Al-4V. *Proc. Inst. Mech. Eng. Part B J. Eng. Manuf.* **2015**, *229*, 1803–1813. [CrossRef]
29. Promoppatum, P.; Yao, S.-C. Influence of scanning length and energy input on residual stress reduction in metal additive manufacturing: Numerical and experimental studies. *J. Manuf. Process.* **2020**, *49*, 247–259. [CrossRef]

# Warpage Analysis and Control of Thin-Walled Structures Manufactured by Laser Powder Bed Fusion

X. Lu, M. Chiumenti, M. Cervera, H. Tan, X. Lin, & S. Wang

*Metals*

Vol. 11, issue 5, pp. 686, (2021)

https://doi.org/10.3390/met11050686

*metals*

MDPI

*Article*

# Warpage Analysis and Control of Thin-Walled Structures Manufactured by Laser Powder Bed Fusion

**Xufei Lu [1], Michele Chiumenti [1], Miguel Cervera [1,*], Hua Tan [2,*], Xin Lin [2] and Song Wang [2]**

[1] International Center for Numerical Methods in Engineering, Technical University of Catalonia, 08034 Barcelona, Spain; xufei.lu@upc.edu (X.L.); michele.chiumenti@upc.edu (M.C.)
[2] State Key Laboratory of Solidification Processing, Northwestern Polytechnical University, Xi'an 710072, China; xlin@nwpu.edu.cn (X.L.); m15702930675@163.com (S.W.)
* Correspondence: miguel.cervera@upc.edu (M.C.); tanhua@nwpu.edu.cn (H.T.); Tel.: +34-934-016-492 (M.C.); +86-029-8849-4001 (H.T.)

**Abstract:** Thin-walled structures are of great interest because of their use as lightweight components in aeronautical and aerospace engineering. The fabrication of these components by additive manufacturing (AM) often produces undesired warpage because of the thermal stresses induced by the manufacturing process and the components' reduced structural stiffness. The objective of this study is to analyze the distortion of several thin-walled components fabricated by Laser Powder Bed Fusion (LPBF). Experiments are performed to investigate the sensitivity of the warpage of thin-walled structures fabricated by LPBF to different design parameters such as the wall thickness and the component height in several open and closed shapes. A 3D-scanner is used to measure the residual distortions in terms of the out-of-plane displacement. Moreover, an in-house finite element software is firstly calibrated and then used to enhance the original design in order to minimize the warpage induced by the LPBF printing process. The outcome of this shows that open geometries are more prone to warping than closed ones, as well as how vertical stiffeners can mitigate component warpage by increasing stiffness.

**Keywords:** additive manufacturing; laser powder bed fusion; thin-walled structures; warpage; finite element analysis



**Citation:** Lu, X.; Chiumenti, M.; Cervera, M.; Tan, H.; Lin, X.; Wang, S. Warpage Analysis and Control of Thin-Walled Structures Manufactured by Laser Powder Bed Fusion. *Metals* **2021**, *11*, 686. https://doi.org/10.3390/met11050686

Academic Editor: Mohammad Jahazi

Received: 23 March 2021
Accepted: 20 April 2021
Published: 22 April 2021



## 1. Introduction

Additive manufacturing (AM) is an industrial process increasingly integrated in the production chain. Nowadays, the aerospace and aeronautical industries are "printing" several high-performance metallic components [1,2]. Laser Powder Bed Fusion (LPBF), also known as Selective Laser Melting (SLM), is the most widely adopted AM technology to fabricate complex structures through a layer-by-layer metal deposition sequence, as it provides remarkable geometrical accuracy and satisfactory mechanical properties from a wide range of metallic powders [3,4]. The LPBF process is carried out in a closed chamber with controlled atmosphere (e.g., argon) to prevent oxidation. The 3D-printing process consists of the following steps: (i) a new powder layer (30~60 μm) is spread, (ii) the high-energy laser beam selectively melts the power bed according to a user defined scanning sequence, and, (iii) the base-plate is lowered to allow for the deposition of a new powder layer. This sequence is repeated until the building process is completed. At the end of the AM process, the loose powder is removed, allowing for the final cooling stage at ambient temperature.

In AM, the material undergoes repeated heating and cooling cycles, high temperature gradients are generated and, consequently, large thermal deformations are induced. The temperature gradient between layers produces residual stresses and plastic deformations because the material cannot freely expand and contract. As a result, the accumulated

stresses generate warpage and, eventually, cracking in thin-walled structures, compromising both the geometrical accuracy and the structural integrity of the AM component [5–8].

Part warpage and the accumulation of residual stresses are closely related to the actual parameters of the printing process, the scanning strategy and the geometrical features of the built. Compared to the blown powder or wire feeding AM techniques, in LPBF processes the size of the melting pool is smaller, the scanning speed is higher and, consequently, the thermal gradients are also higher (up to $10^7$ °C/m), particularly when printing thin-walled structures [9–13].

Several experimental and numerical analyses have been performed to mitigate both residual stress and distortion in AM [14–21]. Yakout et al. [15] studied the effect of the thermal expansion coefficient and the thermal diffusivity in the Thermo-Mechanically Affected Zone (TMAZ) of SLM samples by experimental measurements and finite element (FE) analysis. Lu et al. [22] proposed a substrate design strategy to mitigate the residual stresses in AM processes. Ramos et al. [23] optimized the building strategy to reduce both deformations and residual stresses by controlling heat concentration during the LPBF process. LevkulichL et al. [24] performed sensitivity analysis of the process parameters in SLM to study their effects on the stress evolution of Ti-6Al-4V built. Their results showed that, by increasing the laser power and reducing the scanning speed, it is possible to mitigate the residual stresses of metal deposition. Contrarily, Li et al. [25] found that similar process parameters induce higher residual stresses at the single-track end of SLM Ti-6Al-4V. Cao et al. [6] investigated the effect of substrate preheating. They found that by increasing the preheating temperature it is possible to minimize part distortion and residual stresses. Recently, some researches introduced geometric compensation as an effective strategy to counterbalance the part distortions induced by the thermal field in AM [26–28].

Several works [29–31] have studied the warpage of single-walled parts by LPBF. Among them, Li et al. [29] showed the influence of the scanning sequence and, particularly, the scanning length on the warpage of components. Chen et al. [30] analyzed the maximum warpage of Ti6Al4V adopting different wall thicknesses. Ahmed et al. [31] investigated the dimensional accuracy of AlSi10Mg parts. Contrariwise, the warpage mechanism of thin-walled components of greater geometrical complexity has scarcely been investigated. Furthermore, no strategy for warpage control has been developed for them. This is the main objective of the present investigation.

In this work, a variety of thin-walled components are printed by LPBF, varying their wall-thickness and building-height. Different open and closed shapes are compared and a 3D-scanner is used to measure their actual warpage. These results are used to calibrate a thermo-mechanical FE model implemented in an in-house 3D-printing FE software used for the numerical simulation of the AM process. Thereby, this numerical tool is used to define a structural optimization strategy to mitigate the warpage of thin-walled parts printed by LPBF.

## 2. Experimental Campaign

The experimental campaign is carried out using a Concept Laser M2 powder bed machine (Concept Laser, Lichtenfels, Germany). This equipment uses a Yb-fibre laser with a maximum input power of 400 W (D4 Sigma Gaussian beam). The building process takes place in a closed chamber (250 × 250 × 280 $mm^3$) with an annealed Ti-6Al-4V base-plate (250 × 250 × 25 $mm^3$) and a controlled atmosphere of pure argon (the oxygen content is restricted to 100 ppm).

In this research, the gas atomized Ti-6Al-4V powder used for building has a spherical shape, with a size of 15~53 μm. The chemical composition of this powder is given in Table 1. Before the printing process, the powder is dried in a vacuum oven (Fengxun, Shanghai, China) (vacuum degree less than 80 kPa) at 125 °C during 2.5 h.

**Table 1.** Composition of Ti-6Al-4V alloy powder (wt.%).

| Al | V | O | H | N | C | Fe | Si | Ti |
|---|---|---|---|---|---|---|---|---|
| 6.28 | 3.90 | 0.098 | 0.002 | 0.020 | 0.008 | 0.022 | 0.026 | Balance |

The 3D-printing is characterized by a 90° rotating scan pattern. Table 2 reports the processing parameters adopted for the manufacturing process. In addition, no preheating is used in this work.

**Table 2.** Processing parameters used in the PLBF process.

| Laser Power (W) | Layer Thickness (μm) | Scan Speed (mm/s) | Hatch Spacing (μm) | Laser BeamDiameter (μm) |
|---|---|---|---|---|
| 200 | 30 | 1000 | 100 | 100 |

Figure 1 shows the thin-walled structures printed on the LPBF base-plate after removing the loose powder. These include:

- Single-wall structures of different thicknesses and heights;
- Cylindrical structures of different diameters and heights;
- Square-section structures of several thicknesses;
- Open-section structures (e.g., semi-cylinder, L-shape, etc.).

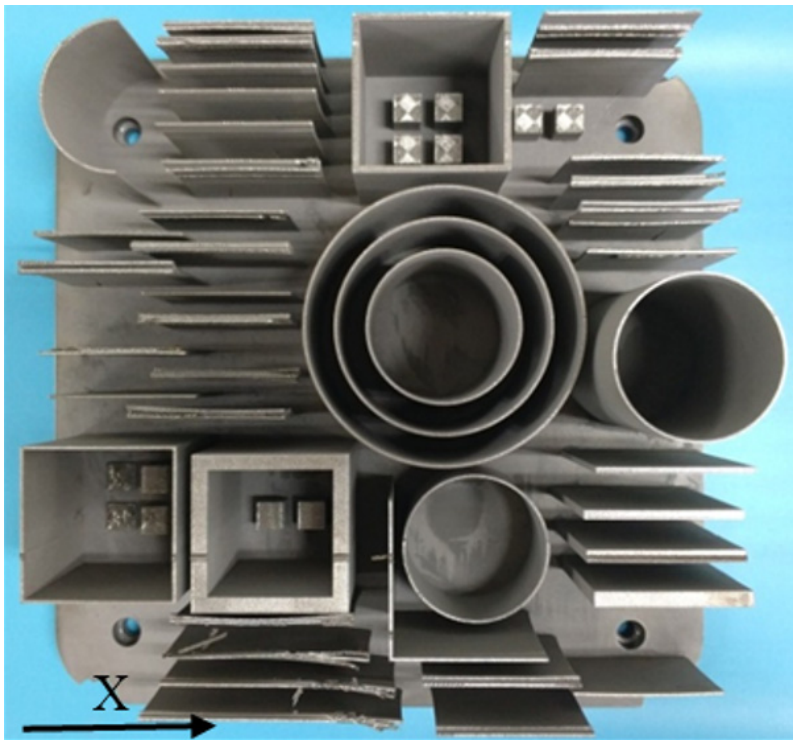


**Figure 1.** Typical thin-walled structures printed by LPBF.

Figure 2 shows the *Breuckmann SmartSCAN3D* scanner (Aniwaa, Central Singapore, Singapore) with the measurement accuracy of 0.015 mm, used to measure the actual distortion of all the components after the 3D-printing process. The relative component warpage is calculated by the Geomagic Qualify software (3D Systems, Rock Hill, Washington, DC, USA) by comparing the experimental 3D-scan images with the nominal CAD geometries. It should be mentioned that all the measurements are done before the removal of the substrate (cutting phase).

**Figure 2.** *Breuckmann SmartSCAN3D* scanner for the warpage measurements.

*Scale Effect on the Part Warpage*

In this section, the sensitivity to the dimensions (e.g., wall-thickness, building height and component size) of the thin-walled components is examined. Therefore, the warpage is measured by 3D-scanning to obtain its relation with the actual dimensions of the 3D-printed structures.

The first assessment study considers a single-wall geometry with a base length of 50 mm and a total height of 50 mm. Three thicknesses of 1 mm, 2 mm and 5 mm, respectively, are investigated.

Figure 3 compares the final warpage distributions as measured for the three wall thicknesses used. It can be seen that the thinnest wall presents the more pronounced warpage, up to 0.41 mm in the middle of the final cambered surface. As the wall-thickness increases, the warpage rapidly decreases; the maximum out-of-plane displacement for the 5 mm thickness wall is only of about 0.03 mm. Hence, as the thickness is increased, the wall warpage is restrained by the enhanced structural stiffness of the component. Simultaneously, higher residual stresses are induced by the printing process.

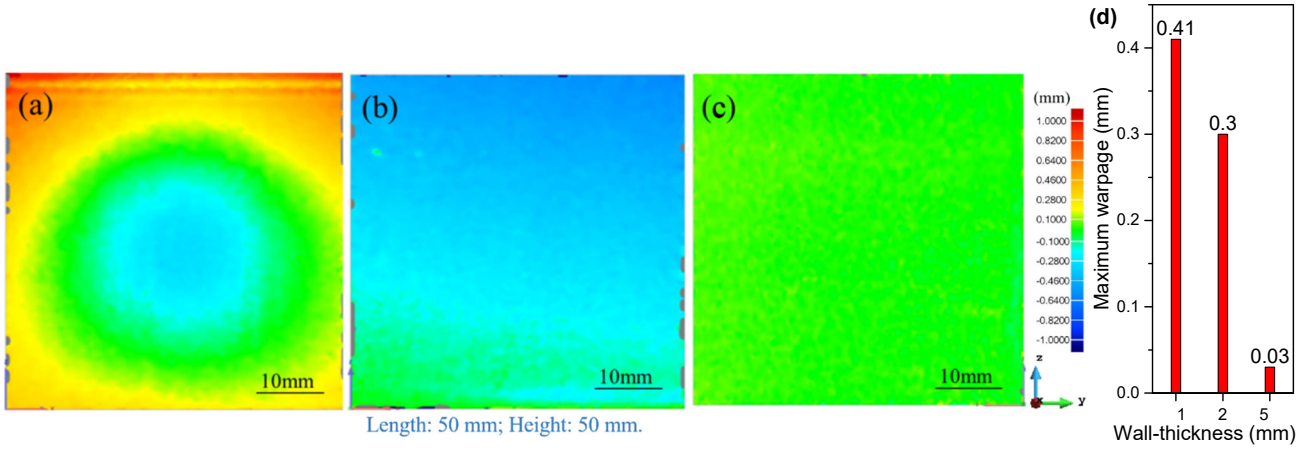


**Figure 3.** Residual warpage (out-of-plane displacement) for the single-wall structures for different wall-thicknesses: (**a**) 1 mm; (**b**) 2 mm; (**c**) 5 mm, respectively. (**d**) Maximum warpage recorded in the middle section.

A second study analyses three different wall heights (37 mm, 43 mm and 50 mm, respectively) for the same single-walled geometry and a fixed thickness of 1 mm. Figure 4 compares the residual warpages of the three thin-walled structures. It is possible to observe that increasing the component height results in larger part warpage. This is not only because of the reduced wall thickness, but also because the higher the component, the less sensitive it is to the clamping conditions at the base and, thus, the more free it is to deform.

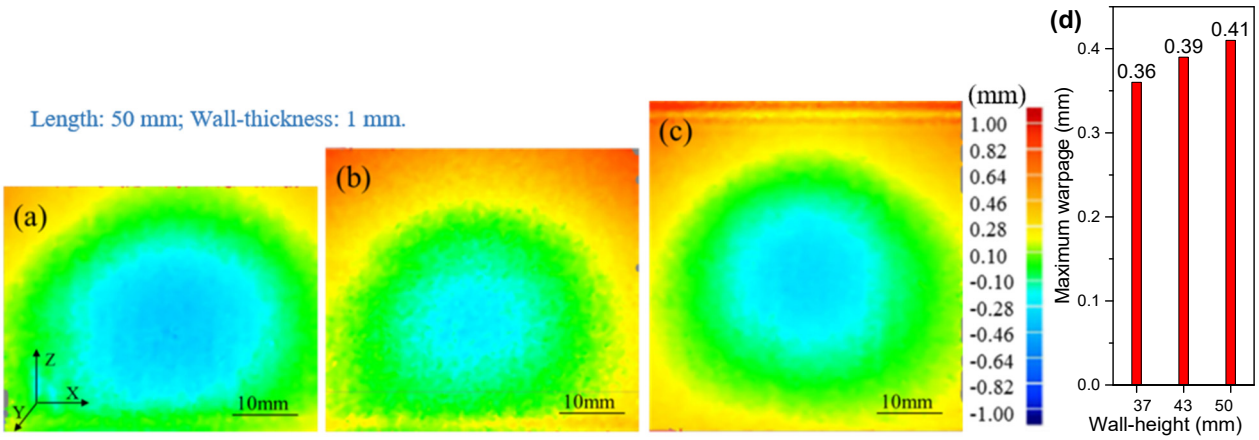


**Figure 4.** Residual warpage contour-fills of the thin-walled structures with different heights: (**a**) 37 mm; (**b**) 43 mm; (**c**) 50 mm, respectively. (**d**) Maximum warpages recorded in the middle section.

Next, a closed thin-wall cylindrical structure is studied. The diameter is 50 mm and the wall thickness is to 1 mm. The cylinder heights are of 30 mm, 50 mm and 70 mm, respectively.

Figure 5 shows the contour-fills of the warpage for the three cylindrical structures with different heights. It can be found that increasing the height leads to larger warpages as observed for the single-wall. However, the maximum warpage is remarkably lower than in both the single-wall and the square thin-wall structures. In this case, the (cylindrical) shape noticeably improves the structural stiffness of the printed structure for the same reduced wall thickness and component height.

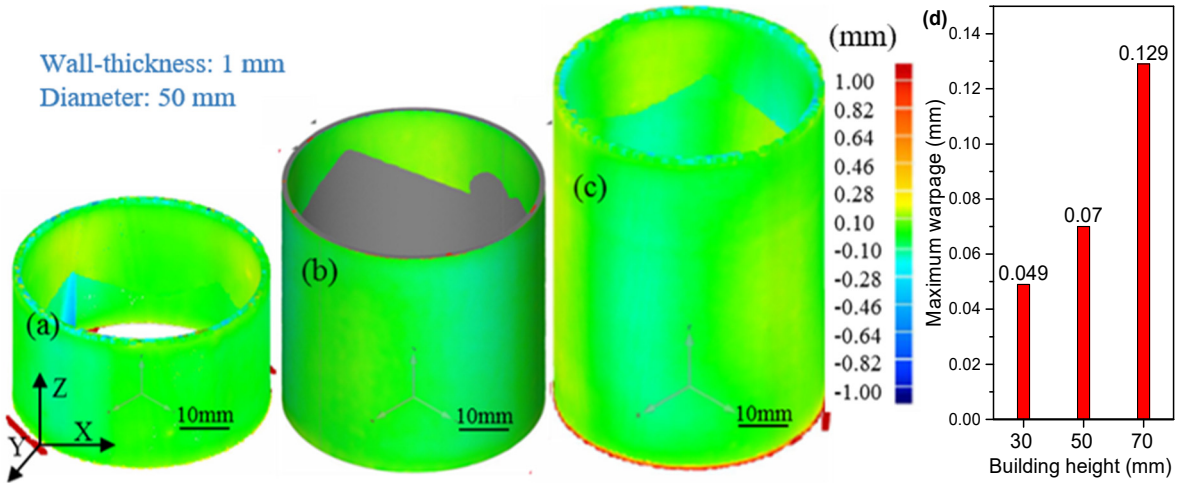


**Figure 5.** Contour-fills of the final warpage of the cylindrical thin-wall structures with different building heights: (**a**) 30 mm; (**b**) 50 mm; (**c**) 70mm, respectively. (**d**) Maximum warpages recorded in the middle section.

A further assessment study is performed assuming a thin-wall cylindrical geometry with a thickness of 1 mm and a height of 50 mm. Different cylinder diameters of 50 mm, 70 mm and 90 mm are studied. Figure 6 depicts the contour-fills of the final warpage of the three cylinders. As expected, by increasing the diameter, the warpage is also more

pronounced. Eventually, if very large diameters are considered, the results of the open single-wall should be replicated.

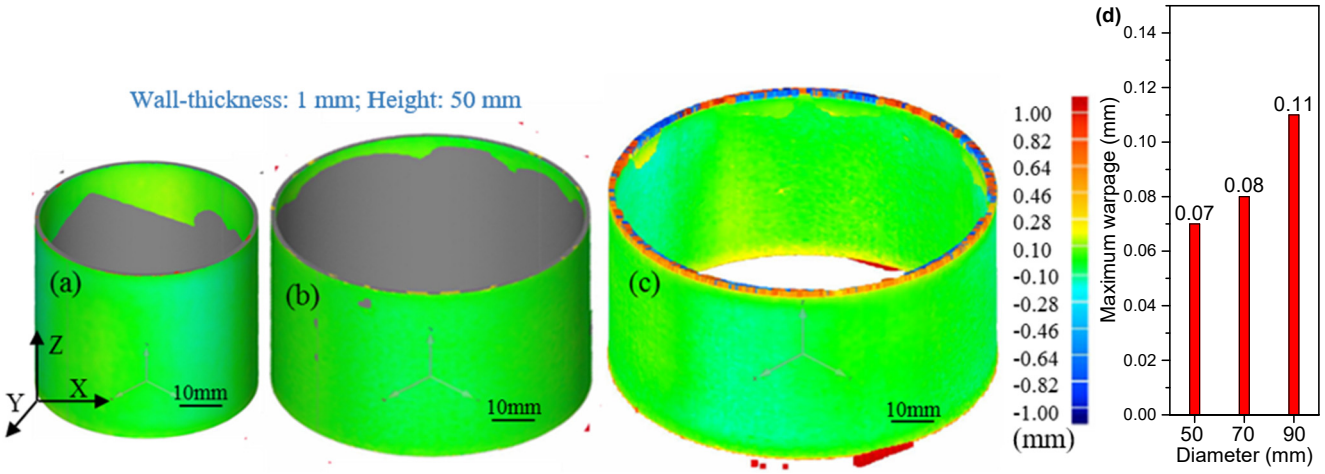


**Figure 6.** Contour-fills of the final warpage of the cylindrical thin-wall structures with different diameters of: (**a**) 50 mm; (**b**) 70 mm; (**c**) 90 mm; (**d**) Maximum warpages recorded in the middle section.

Finally, the last assessment studies a closed square thin-wall section. The same base length and height of 50 mm are used, while wall thicknesses of 1 mm, 2 mm and 5 mm are investigated. Figure 7 shows the contour-fills of the residual warpage for the three AM structures. Once again, it can be observed that the thicker the wall-thickness, the smaller the observed warpage. Therefore, a pronounced bulging is shown by the component with the thinnest wall. Nevertheless, the overall structural stiffness of the closed section allows for a reduction of the maximum out-of-plane displacements: 0.37 mm compared to 0.41 mm as measured for the open single-wall. This is because the deformation of each one of the walls conforming the square thin-wall section is constrained by the substrate and also laterally. Notably, the cylinder of similar dimensions shows a much better performance than the square thin-wall section of similar dimensions, Figures 5b and 7a, respectively. This is explained as follows. In LPBF, high tensile stresses in the hoop/wall direction exist at the top for two components. Large tensile stresses also happen along the corners of the square part due to the high cooling rates at such locations; this builds up compressive stresses in the central region of each square wall so that any small disturbance can favour the bulging perpendicular to the wall. This is not the case for the cylinder.

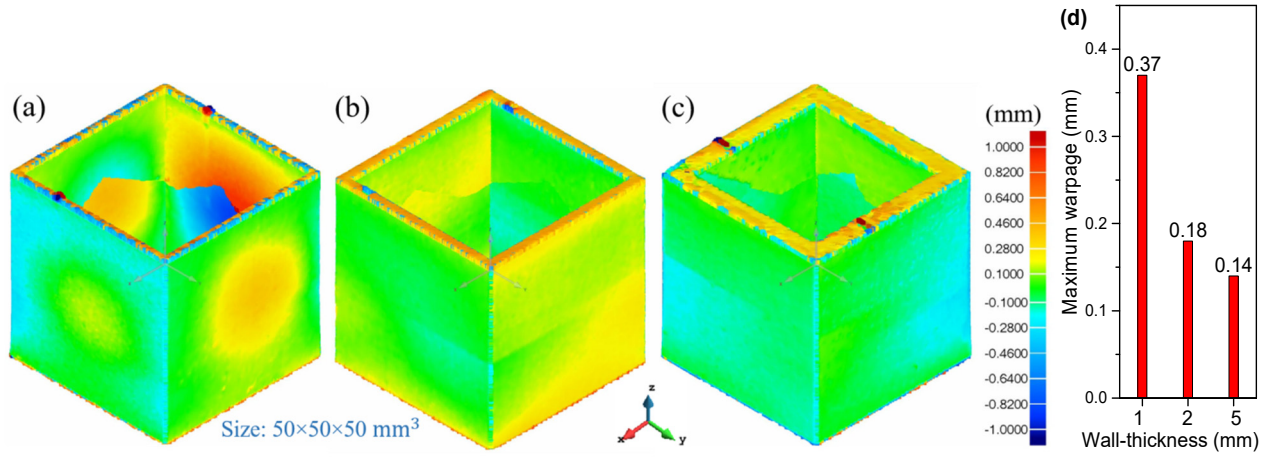


**Figure 7.** Contour-fills of the final warpage of the square thin-wall section with different wall-thicknesses: (**a**) 1 mm; (**b**) 2 mm; (**c**) 5 mm, respectively. (**d**) Maximum warpages recorded in the middle section.

## 3. Numerical Modeling

In LPBF the following two operations are repeated for each layer (see Figure 8):

1. *Recoating*: the baseplate is lowered to accommodate a new powder layer;
2. *Laser-scanning*: the laser heat source generates a molten pool which follows a user-defined trajectory to selectively melt the powder bed consolidating the new layer comprising the AM build.

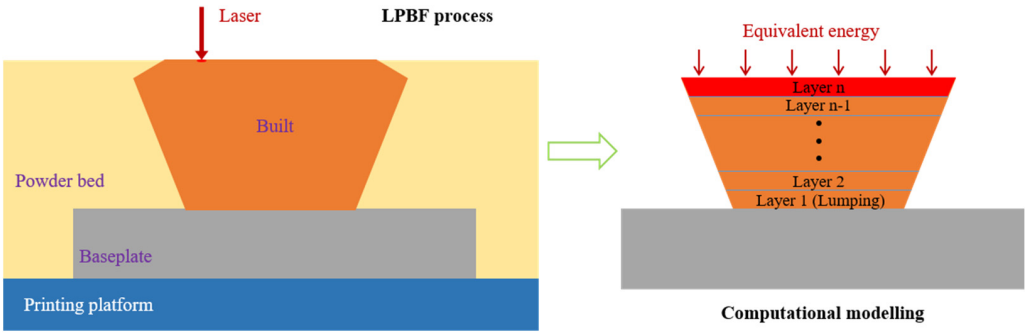


**Figure 8.** The schematic of the used layer-by-layer model for LPBF.

The most suitable numerical strategy to approach the simulation of the LPBF process is by the inherent strain method [32]. This method allows for a fast prediction of the distortions and residual stresses of the fabricated component. Therefore, the detailed simulation of the laser movement along the scanning trajectory is replaced by a layer-by-layer (or even multi-layer) analysis. This assumption is generally accepted when simulating LPBF processes because the scanning speed is very high (up to 1 m/s) compared to other AM technologies and the TMAZ is very localized, and it affects only the last few (2–3) layers. As a consequence, thermo-plastic (inherent) strains are only generated within the TMAZ.

This given, the original CAD geometry is firstly sliced according to the thickness of the powder-bed and then the FE discretization is generated accordingly. The birth-death FE activation technique is adopted [19,33] to progressively add the elements belonging to each new layer to the computational domain, Ω. In the initial FE discretization of the nominal CAD geometry, all elements are inactive. Inactive elements are not computed or assembled into the global system of equations. The numerical simulation of the building process consists of a sequence of layer activations. Hence, at each time-step, the elements belonging to the next layer are switched on (activated), becoming part of the current computational domain. For each time-step, the thermo-mechanical analysis is performed for all the active elements, until the whole layer-by-layer deposition sequence is completed.

### *3.1. Mechanical Problem*

The stress analysis enforces the conservation of the balance of momentum and the continuity equations within the current active domain:

$$\bigtriangledown \mathbf{s} + \bigtriangledown p + \mathbf{b} = 0 \tag{1}$$

$$(\bigtriangledown \mathbf{u} - e^T) - p/K = 0 \tag{2}$$

where $\mathbf{b}$ are the body forces per unit of volume and $K(T)$ is the temperature-dependent bulk modulus and $p$ and $\mathbf{s}$, are the hydrostatic (pressure) and the deviatoric components of the Cauchy stress tensor, $\sigma$. Thus:

$$\sigma = p\mathbf{I} + \mathbf{s} \tag{3}$$

The strain tensor, $\varepsilon(\mathbf{u}) = \bigtriangledown^s \mathbf{u}$, can also be split in its volumetric and deviatoric parts, $e_{vol} = \bigtriangledown \cdot \mathbf{u}$ and $\mathbf{e}$, respectively, so that:

$$\varepsilon = e_{vol}\mathbf{I}/3 + \mathbf{e} \tag{4}$$

The deviatoric stress tensor is computed as:

$$\mathbf{s}(\mathbf{u}) = 2G(\mathbf{e}(\mathbf{u}) - \mathbf{e}^{inh}) \tag{5}$$

where $G(T)$ is the temperature-dependent shear modulus and $\mathbf{e}^{inh}$ is the inherent strain tensor, as:

$$\mathbf{e}^{inh} = e^{T}\boldsymbol{I} + \mathbf{e}^{vp} \tag{6}$$

which typically includes both the thermal deformation, $e^{T}(T)$, and the visco-plastic strains, $\mathbf{e}^{vp}$.

Commonly, the inherent strain method does not contemplate the solution of the thermal problem. Therefore, the inherent strain tensor is assumed as a (constant) user-defined material parameter depending on the material and process characterization. Its value can be obtained either experimentally or numerically, through the detailed simulation of the molten pool solidification.

In this work, a staggered thermo-mechanical solution is adopted to solve the AM problem [34,35]. Therefore, both the thermal and the mechanical analyses are carried out in a layer-by-layer manner. On the one hand, the thermal deformations can be computed from the actual (non-uniform) temperature field (inherent shrinkage method). On the other hand, the (inherent) visco-plastic deformations are defined as:

$$\mathbf{e}^{vp} = \mathrm{diag}(e_l, e_t, e_z) = \boldsymbol{I}(e_l, e_t, e_z)^{\mathrm{T}} \tag{7}$$

where $e_l$, $e_t$ and $e_z$ are the longitudinal (aligned with the scanning direction), transversal and vertical (building direction) visco-plastic components, respectively [33–35]. In LPBF, the thickness of the deposited layer is very small, so $e_z$ can be neglected. Additionally, thin-walled parts can be assumed to be in a quasi-plane-stress condition, so that the only inherent strain component to be considered is the one along the mid-line of the cross-section, regardless of the scanning pattern.

### *3.2. Thermal Problem*

$H$ being the hatch spacing, the total travelled scanning length for each layer is:

$$l_{scan} = A/H \tag{8}$$

where $A$ is the area of the current layer. The volume of the Heat Affected Zone (HAZ) is given by:

$$V_{HAZ} = l_{scan} \times d \times s = (d/H) \times (s/t) \times V \tag{9}$$

where $d$ is the laser beam diameter and $s$ is the penetration (depth) of the melt-pool, while $V = A{\cdot}t$ is the volume of the layer, being $t$ its thickness. In this work, $d = H$ (no overlapping) and $s = t$ (the melt-pool depth is the layer thickness). Thus, the volume of the HAZ corresponds to the volume of the layer being activated.

Hence, the heat source density accounting for the total energy input during the scanning sequence of the whole layer is computed as:

$$q = \eta P/V \tag{10}$$

where $\eta$ is the laser absorptivity and $P$ is the laser power. This heat source is delivered during the whole scanning phase, which is characterized by a time interval, $\Delta t_{scan}$ computed as:

$$\Delta t_{scan} = l_{scan}/V_{scan} = A/(H \times V_{scan}) \tag{11}$$

where $V_{scan}$ is the scanning velocity. Observe that the LPBF process also includes the recoating operation, that is a cooling phase of duration $\Delta t_{cool}$.

Often, the thermo-mechanical analysis is accelerated by lumping several layers into a single time-step. Therefore, the equivalent time-step of the analysis results in:

$$\Delta t_{eq} = \mathrm{n}\cdot(\Delta t_{scan} + \Delta t_{cool}) \tag{12}$$

where n is the number of lumped layers (in this work n = 10) and the power input is uniformly spread in the lumped volume, $V_{lump}$, so that:

$$q_{eq} = \eta P / V_{lump} \tag{13}$$

### *3.3. Geometrical Models and FE Meshes*

The coupled thermo-mechanical analysis is performed using the in-house FE software, *COMET*, developed at the International Centre for Numerical Methods in Engineering (CIMNE) [36,37]. The definition of the CAD geometries, and the corresponding the FE mesh generation as well as the pre/post-processing operations are carried out using the in-house pre/post-processor GiD [38]. The hardware used to run the simulation incorporates an Intel(R) Core (TM) i7-9700, 3.0 GHz processor and 16.0 GB of RAM.

Figure 9 shows the FE meshes of three different thin-walled geometries including both open and closed structures with a fixed thickness of 1 mm. The dimensions of these structures and the corresponding numbers of the hexahedral elements and nodes are listed in Table 3.

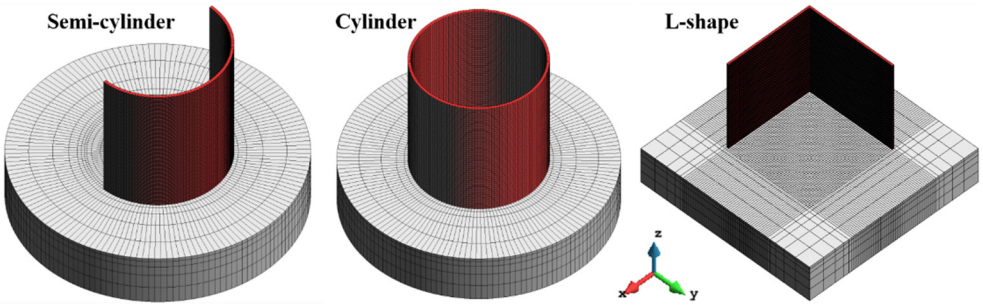


**Figure 9.** 3D FE mesh models of thin-walled structures.

**Table 3.** Dimensions of the proposed thin-walled structures and the numbers of FE elements and nodes.

| Thin-Walled Parts | Dimensions | Number of FE Elements | Number of Nodes |
|---|---|---|---|
| Semi-cylindrical part | Φ50 mm × H50 mm | 21,606 | 37,618 |
| Cylindrical part | Φ50 mm × H50 mm | 34,632 | 63,336 |
| L-shaped part | L50 mm × W50 mm × H50 mm | 34,366 | 55,392 |

The average mesh size in all cases is of about 1 × 1 $mm^2$ within the horizontal XY plane, and 0.3 mm in the building direction (a lumping layer-height). All these thin-walled work-pieces have the same height of 50 mm. The LPBF process is simulated with a sequence of 167 time-steps through a layer-by-layer activation strategy. Each layer used for the simulation has a thickness of 0.3 mm, thus including 10 physical layers (30 µm of loose powder is spread at each recoating step).

The temperature-dependent thermal and mechanical properties used to feed the constitutive model of Ti-6Al-4V alloy have been calibrated in a previous work [5], as shown in Table 4.

The thermal boundary conditions adopted in all the proposed analyses are defined through a heat convection coefficient of 12.7 W/(°C·$m^2$) and an emissivity of 0.35 [39]. The ambient temperature is set to 26°C during the whole LPBF process. The efficiency of the LPBF process, when Ti-6Al-4V loose powder is used, is defined in terms of the heat power absorption coefficient fixed to $\eta$ = 0.4 [39].

**Table 4.** Temperature-dependent material properties of Ti-6Al-4V alloy [5].

| Temperature (°C) | Density (kg/m$^3$) | Specific Heat (J/(kg·°C)) | Thermal Conductivity (W/(m·°C)) | Poisson's Ratio | Young's Modulus (GPa) | Thermal Dilatancy (μm/m/ °C) | Yield Stress (MPa) |
|---|---|---|---|---|---|---|---|
| 20 | 4420 | 546 | 7 | 0.345 | 110 | 8.78 | 850 |
| 205 | 4395 | 584 | 8.75 | 0.35 | 100 | 10 | 630 |
| 500 | 4350 | 651 | 12.6 | 0.37 | 76 | 11.2 | 470 |
| 995 | 4282 | 753 | 22.7 | 0.43 | 15 | 12.3 | 13 |
| 1100 | 4267 | 641 | 19.3 | 0.43 | 5 | 12.4 | 5 |
| 1200 | 4252 | 660 | 21 | 0.43 | 4 | 12.42 | 1 |
| 1600 | 4198 | 732 | 25.8 | 0.43 | 1 | 12.5 | 0.5 |
| 1650 | 3886 | 831 | 35 | 0.43 | 0.1 | 12.5 | 0.1 |
| 2000 | 3818 | 831 | 35 | 0.43 | 0.01 | 12.5 | 0.01 |

All the thin-walled structures are printed at the same time (see Figure 1). Nevertheless, the simulation strategy assumes that each component is printed separately. This is because the heat conductivity of the loose powder is extremely low, so that most of the heat is evacuated by radiation through the upper surface of the layer being printed as well as by heat conduction through the baseplate. Therefore, the in-plane (XY) heat flux through the loose powder is negligible compared to the heat flow in the vertical (building) direction.

## 4. Calibration and Results

### *4.1. Calibration of the Numerical Model*

In order to calibrate the numerical model used for LPBF, the warpage profiles of the thin-wall semi-cylindrical, cylindrical and L-shaped structures are computationally predicted and compared with the experimental 3D-scan results.

Figure 10a,b shows the out-of-plane displacements of the semi-cylindrical and cylindrical parts, respectively. The displacements at several control points are specifically used as a reference to assess the accuracy of the simulation. Similarly, Figure 11 compares the experimental and computed displacements of the L-shaped part. Once calibrated, the numerical model is able to faithfully reproduce the experimental results obtained by 3D scanning.

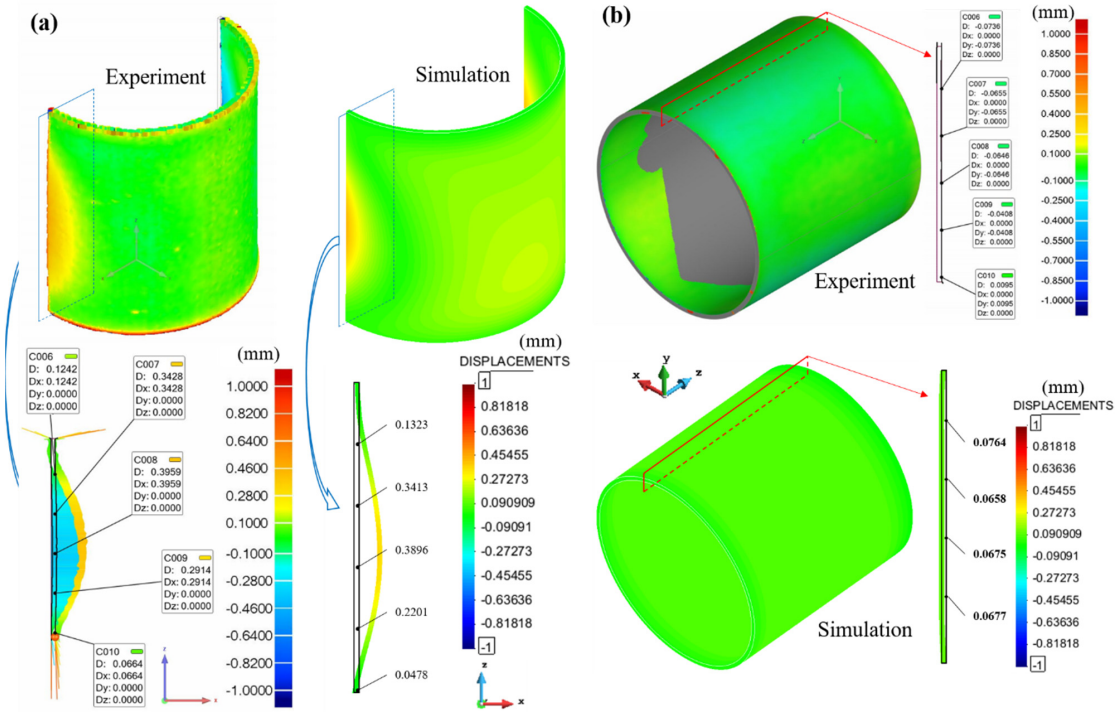


**Figure 10.** Comparison of the out-of-plane displacement fields obtained through 3D scanning and numerical simulation: (**a**) semi-cylinder; (**b**) cylinder.

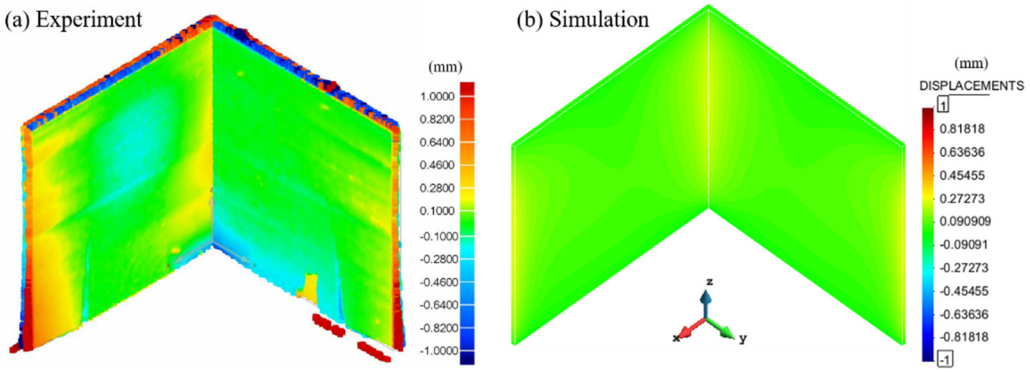


**Figure 11.** Comparison of the out-of-plane displacement fields obtained through (**a**) 3D scanning and (**b**) numerical simulation for the L-shaped structure.

It can be seen in Figure 10a that a visible bulge (of approximately 0.4 mm) occurs at opposite sides of the semi-cylindrical part, while the cylindrical geometry just shows very small radial displacements (less than 0.08 mm), these being more pronounced in the mid-section. The open L-shaped thin-wall structure also shows large deformations at the edges of each wall, as shown in Figure 11 and successfully predicted by the numerical model.

The slight discrepancies between the experimental and computed results are attributed to the mutual thermal influence among all the components as they are printed together (see Figure 1); this influence is disregarded in the FE simulation.

### *4.2. Results and Discussion on the Warpage Mechanism of the Thin-Walled Structures*

Understanding the mechanical response of the 3D-printed geometries is necessary to establish a procedure to alleviate the warpage phenomenon in LPBF manufacture. As an example, the above results clearly illustrate that open thin-wall structures are more prone to deformation than closed ones.

Focusing on the open thin-walled semi-cylindrical geometry (Figure 10a), it is observed that the formation of the bulging progresses as the LPBF printing process moves away from the substrate as shown in Figure 12a. The bulging gets more pronounced when printing the upper half of the component because the mechanical constraining from the substrate restrains the development of the distortion in the bottom half. Figure 12b,c shows the evolution of the longitudinal and vertical stresses, $\sigma_{xx}$ and $\sigma_{zz}$, respectively, at two stages of the manufacturing. It can be noted in Figure 12b that the internal surface sustains compressive stresses while tensile stresses are induced in the external surface. As a consequence, the wall deforms outwards. The vertical tensile stresses induced by the high cooling rate and the small bending stiffness of these structures also promote the bulging as shown in Figure 12c.

Contrarily, the closed thin-walled cylindrical part presents a much higher structural stiffness, and thus the AM process only produces a small deformation in the radial direction.

Dunbar et al. [40] studied the warpage of two thin-walled cylinders built by SLM. They also found that the warpage is relatively small. Throughout the printing process, the maximum warpage occurs several layers below the most recently deposited layer. This confers a final concave shape to the component.

Next, the warpage mechanism of the thin-wall L-shape structure is analyzed. Figure 13 shows the evolution of the longitudinal stresses ($\sigma_{xx}$) and the vertical stresses ($\sigma_{zz}$). During the building process, large tensile stresses develop at the top and two side edges while compressive stresses are produced in the central area of the built. As a result, warpage is visible along the lateral edges (see Figure 11). Note that a similar stress distribution and bulging phenomenon also take place when fabricating the single-wall and the square thin-walled section (see Figures 4 and 5).

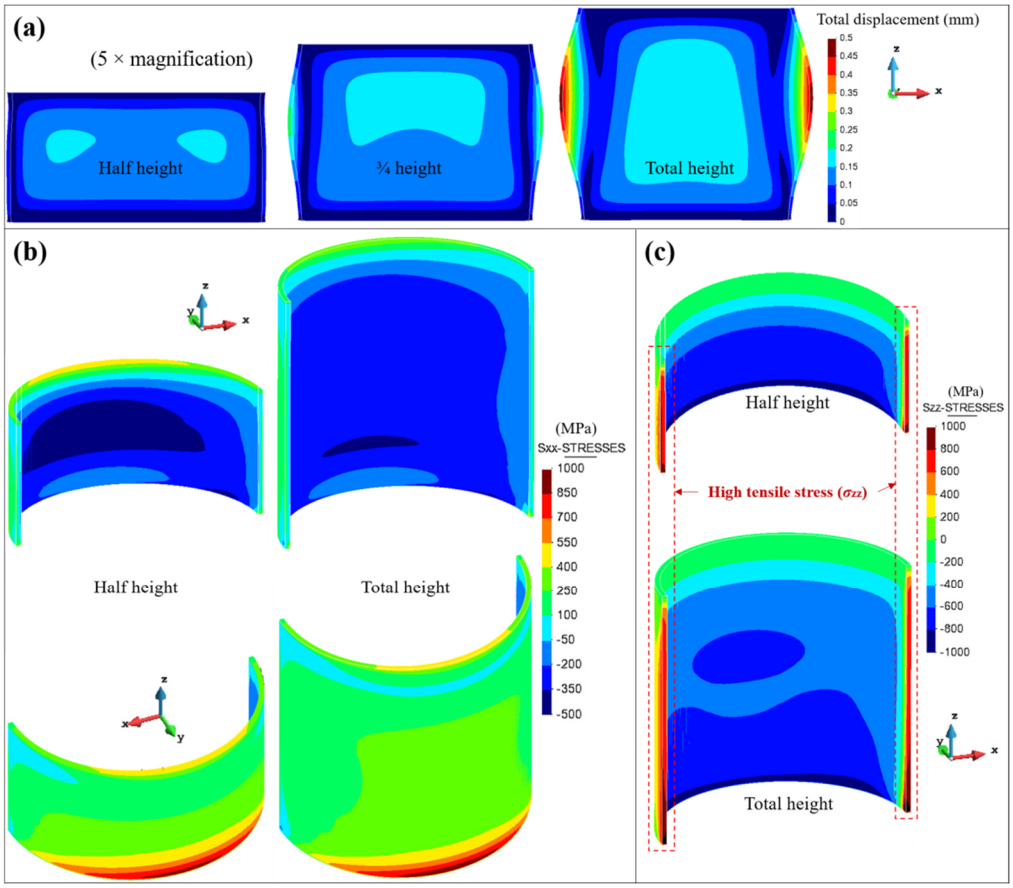


**Figure 12.** Semi-cylindrical part: the evolutions of (**a**) total displacements and (**b**) longitudinal stresses ($\sigma_{xx}$) as well as (**c**) vertical stresses ($\sigma_{zz}$).

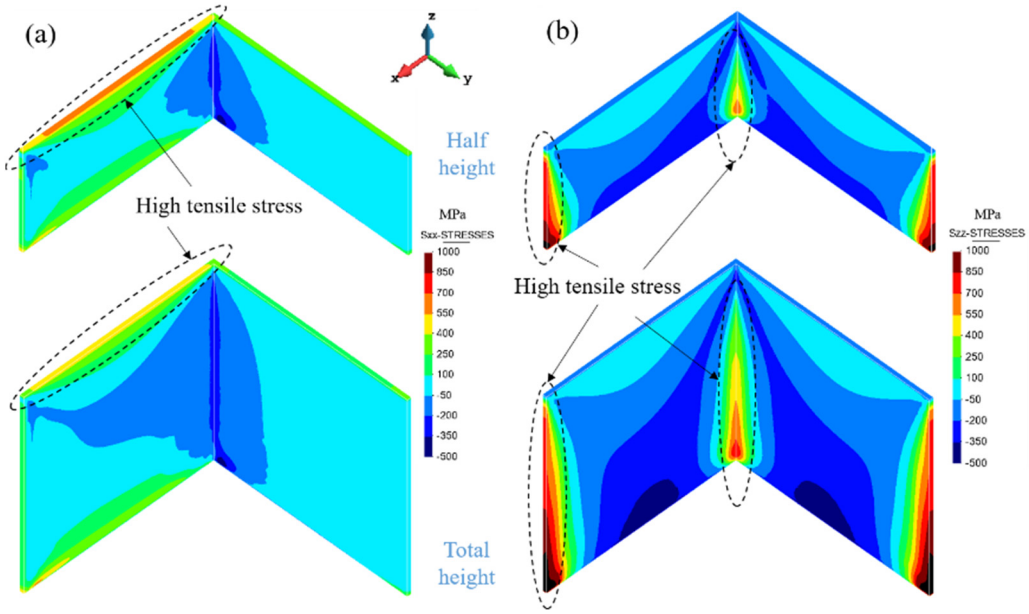


**Figure 13.** L-shape component: evolutions of (**a**) longitudinal stresses and (**b**) vertical stresses.

Yang et al. [41] also carried out a distortion analysis of thin-walled L-shaped and cross structures; their results showed that the side with longitudinal scan suffers larger distortion, whereas the side with transverse scan is distortion-free. Obviously, the mechanical response of thin-walled structures is closely related with the scan strategy.

## 5. Structural Optimization for Warpage Control

As above mentioned, the main difficulty for fabricating thin-walled AM components is their low structural stiffness and the high thermal stresses, especially at the sharp corners. In order to minimize the part warpage, a structural optimization strategy is proposed to enhance the overall stiffness of the component and particularly when open sections must be fabricated. The idea consists in adding vertical stiffeners able to resist the thermal stresses by locally increasing the structural stiffness and, at the same time, reducing the cooling rate at the edges of AM components as shown in Figure 14.

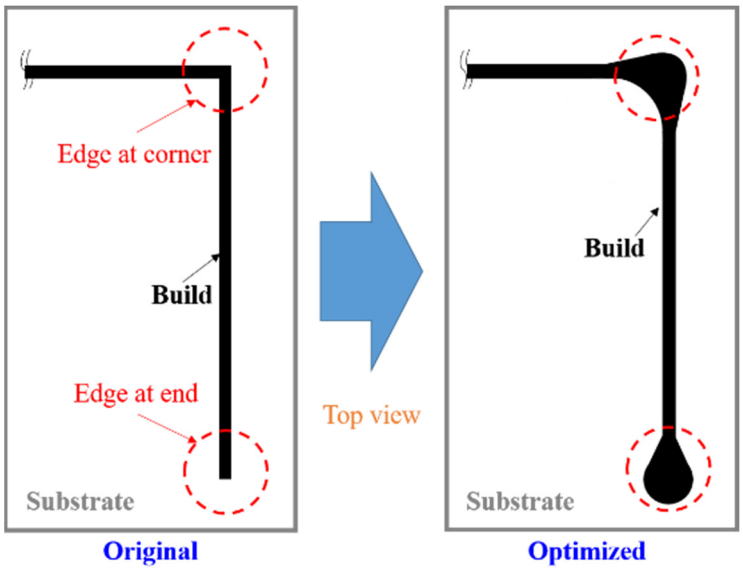


**Figure 14.** Proposed modification of the local stiffness of thin-walled structures.

Figure 15 shows the final warpage of both the open semi-cylindrical and L-shaped thin-walled parts with and without the vertical stiffeners. The warpage minimization is noticeably achieved.

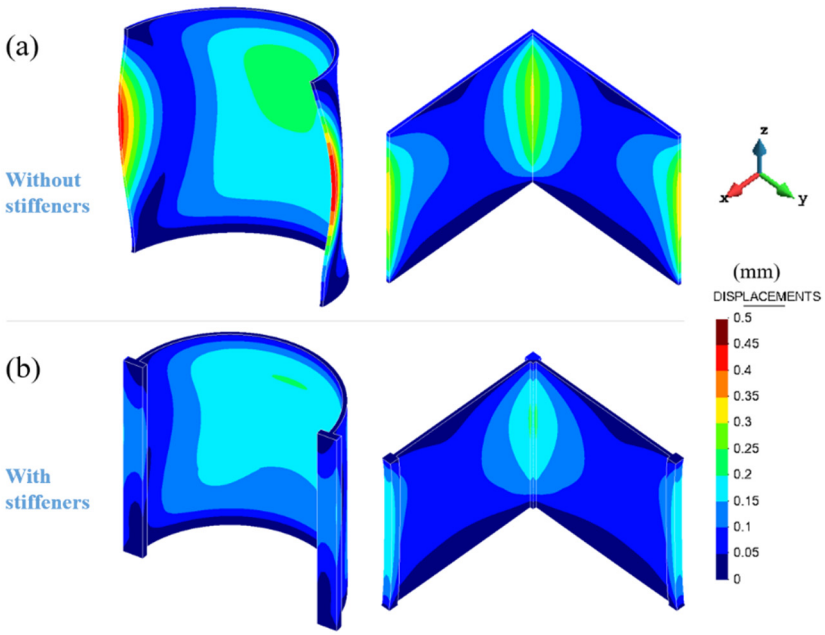


**Figure 15.** Warpage of the open (**a**) semi-cylindrical and (**b**) L-shaped thin-walled parts with and without vertical stiffeners.

Figure 16 shows the residual von Mises stresses of the open semi-cylindrical and L-shaped thin-walled structures. These residual stresses are mitigated by lowering the cooling rates at the edges of the two structures, thus increasing the local heat accumulation. Note that there still exist large residual stresses in the bottom area of both components. However, substrate preheating just before LPBF can successfully mitigate the residual stresses in this area to achieve high-quality fabrication of thin-walled components [5,7].

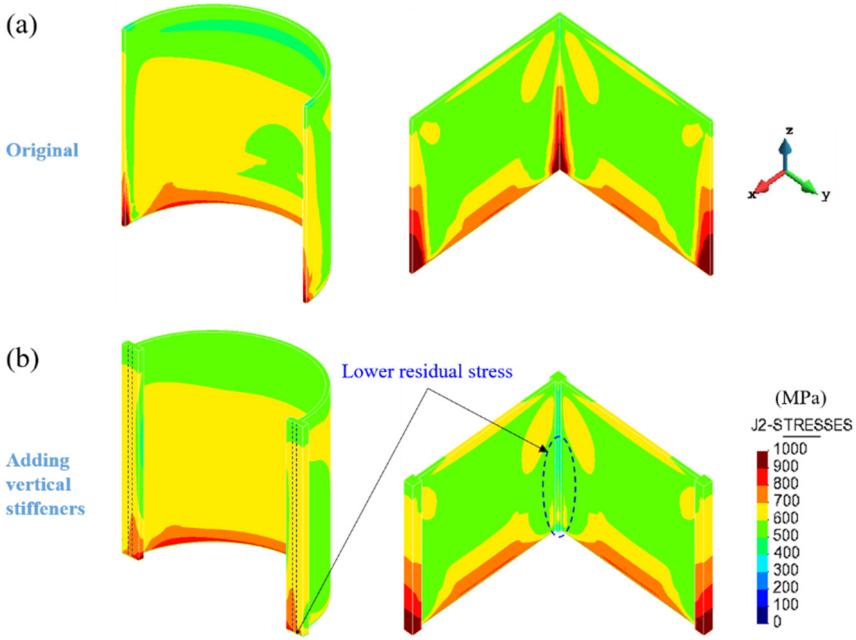


**Figure 16.** Residual von Mises stresses of the open (**a**) semi-cylindrical and (**b**) L-shaped parts with and without vertical stiffeners.

## 6. Conclusions

In this work, the warpage of several thin-walled structures fabricated by LPBF is investigated. The major conclusions of this study are:

1. The wall thickness plays a significant role on the warpage of the final part. Thicker walled structures present reduced warpage.
2. Increasing the build height as well as reducing the wall curvature causes larger warpage, as shown for the cylindrical structures.
3. Open sections (e.g., semi-cylinder, L-shape, etc.) are more prone to warpage than closed ones (e.g., cylinder and square section) because of their reduced structural stiffness.
4. The use of vertical stiffeners enables locally enhancing the structural stiffness of thin-walled structures, minimizing the residual warpage induced by the LPBF process.
5. FE analysis of LPBF processes is a useful tool to analyse different thin-walled structures in order to predict the actual warpage. The developed FE model has been calibrated with experimental 3D-scanning images.

**Author Contributions:** Conceptualization, X.L. (Xufei Lu) and M.C. (Michele Chiumenti); methodology and software, M.C. (Miguel Cervera) and H.T.; data curation, S.W. and X.L. (Xufei Lu); writing—original draft preparation, X.L. (Xufei Lu) and M.C. (Michele Chiumenti); writing—review and editing, M.C. (Miguel Cervera), and X.L. (Xin Lin); supervision, H.T. and X.L. (Xin Lin). All authors have read and agreed to the published version of the manuscript.

**Funding:** This work was funded by the National Key Technologies R & D Program (No. 2016YFB1100104), the European KYKLOS 4.0 project (An Advanced Circular and Agile Manufacturing Ecosystem based on rapid reconfigurable manufacturing process and individualized consumer preferences—Grant

Agreement No. 872570), the Severo Ochoa Programme for Centres of Excellence in R&D (CEX2018-000797-S) and the China Scholarship Council (No. 201906290011).

**Data Availability Statement:** Data are contained within the article.

**Conflicts of Interest:** The authors declare no conflict of interest.

## References

1. Herzog, D.; Seyda, V.; Wycisk, E.; Emmelmann, C. Additive manufacturing of metals. *Acta Mater.* **2016**, *117*, 371–392. [CrossRef]
2. DebRoy, T.; Wei, H.L.; Zuback, J.S.; Mukherjee, T.; Elmer, J.W.; Milewski, J.O.; Beese, A.M.; Wilson-Heid, A.; De, A.; Zhang, W. Additive manufacturing of metallic components—Process, structure and properties. *Prog. Mater. Sci.* **2018**, *92*, 112–224. [CrossRef]
3. Lu, X.; Zhao, T.; Ji, X.; Hu, J.; Li, T.; Lin, X.; Huang, W. 3D printing well organized porous iron-nickel/ polyaniline nanocages multiscale supercapacitor. *J. Alloys Compd.* **2018**, *760*, 78–83. [CrossRef]
4. Zheng, M.; Wei, L.; Chen, J.; Zhang, Q.; Zhong, C.; Lin, X.; Huang, W. A novel method for the molten pool and porosity formation modelling in selective laser melting. *Int. J. Heat Mass Transf.* **2019**, *140*, 1091–1105. [CrossRef]
5. Lu, X.; Lin, X.; Chiumenti, M.; Cervera, M.; Li, J.; Ma, L.; Wei, L.; Hu, Y.; Huang, W. Finite element analysis and experimental validation of the thermomechanical behavior in Laser Laser Directed energy deposition of Ti-6Al-4V. *Addit. Manuf.* **2018**, *21*, 30–40.
6. Cao, J.; Gharghouri, M.A.; Nash, P. Finite-element analysis and experimental validation of thermal residual stress and distortion in electron beam additive manufactured Ti-6Al-4V build plates. *J. Mater. Process. Technol.* **2016**, *237*, 409–419. [CrossRef]
7. Lu, X.; Lin, X.; Chiumenti, M.; Cervera, M.; Hu, Y.; Ji, X.; Ma, L.; Yang, H.; Huang, W. Residual stress and distortion of rectangular and S-shaped Ti-6Al-4V parts by Directed Energy Deposition: Modelling and experimental calibration. *Addit. Manuf.* **2019**, *26*, 166–179. [CrossRef]
8. Lu, X.; Lin, X.; Chiumenti, M.; Cervera, M.; Hu, Y.; Ji, X.; Ma, L.; Huang, W. In situ Measurements and Thermo-mechanical Simulation of Ti-6Al-4V Laser Laser Directed energy deposition Processes. *Int. J. Mech. Sci.* **2019**, *153*, 119–130. [CrossRef]
9. Liu, Y.J.; Liu, Z.; Jiang, Y.; Wang, G.W.; Yang, Y.; Zhang, L.C. Gradient in microstructure and mechanical property of selective laser melted AlSi10Mg. *J. Alloys Compd.* **2018**, *735*, 1414–1421. [CrossRef]
10. Fang, Z.C.; Wu, Z.L.; Huang, C.G.; Wu, C.W. Review on residual stress in selective laser melting additive manufacturing of alloy parts. *Opt. Laser Technol.* **2020**, *129*, 106283. [CrossRef]
11. Lu, Y.; Wu, S.; Gan, Y.; Huang, T.; Yang, C.; Li, J.; Lin, J. Study on the microstructure, mechanical property and residual stress of SLM inconel-718 alloy manufactured by differing island scanning strategy. *Opt. Laser Technol.* **2015**, *75*, 197–206. [CrossRef]
12. Zaeh, M.F.; Branner, G. Investigations on residual stresses and deformations in selective laser melting. *Prod. Eng.* **2009**, *4*, 35–45. [CrossRef]
13. Vora, P.; Mumtaz, K.; Todd, I.; Hopkinson, N. AlSi12 in-situ alloy formation and residual stress reduction using anchorless selective laser melting. *Addit. Manuf.* **2015**, *7*, 12–19. [CrossRef]
14. Lu, X.; Cervera, M.; Chiumenti, M.; Li, J.; Ji, X.; Zhang, G.; Lin, X. Modeling of the Effect of the Building Strategy on the Thermomechancial Response of Ti-6Al-4V Rectangular Parts Manufactured by Laser Directed Energy Deposition. *Metals* **2020**, *10*, 1643. [CrossRef]
15. Yakout, M.; Elbestawi, M.; Veldhuis, S.; Nangle-Smith, S. Influence of thermal properties on residual stresses in SLM of aerospace alloys. *Rapid Prototyp. J.* **2020**, *26*, 213–222. [CrossRef]
16. Chiumenti, M.; Neiva, E.; Salsi, E.; Cervera, M.; Badia, S.; Moya, J.; Chen, Z.; Lee, C.; Davies, C. Numerical modelling and experimental validation in Selective Laser Melting. *Addit. Manuf.* **2017**, *18*, 171–185. [CrossRef]
17. Neiva, E.; Chiumenti, M.; Cervera, M.; Salsi, E.; Piscopo, G.; Badia, S.; Martín, A.F.; Chen, Z.; Lee, C.; Davies, C. Numerical modelling of heat transfer and experimental validation in powder-bed fusion with the virtual domain approximation. *Finite Elem. Anal. Des.* **2020**, *168*, 103343. [CrossRef]
18. Lindgren, L.-E.; Lundbäck, A.; Malmelöv, A. Thermal stresses and computational welding mechanics. *J. Therm. Stresses* **2019**, *42*, 107–121. [CrossRef]
19. Lundbäck, A.; Lindgren, L.-E. Modelling of metal deposition. *Finite Elem. Anal. Des.* **2011**, *47*, 1169–1177. [CrossRef]
20. Williams, R.; Catrin, J.; Davies, M.; Hooper, P.A. A pragmatic part scale model for residual stress and distortion prediction in powder bed fusion. *Addit. Manuf.* **2018**, *22*, 416–425. [CrossRef]
21. Baiges, J.; Chiumenti, M.; Moreira, C.A.; Cervera, M.; Codina, R. An Adaptive Finite Element strategy for the numerical simulation of Additive Manufacturing processes. *Addit. Manuf.* **2021**, *37*, 101650.
22. Lu, X.; Chiumenti, M.; Cervera, M.; Li, J.; Lin, X.; Ma, L.; Zhang, G.; Liang, E. Substrate design to minimize residual stresses in Directed Energy Deposition AM processes. *Mater. Des.* **2021**, *202*, 109525. [CrossRef]
23. Ramos, D.; Belblidia, F.; Sienz, J. New scanning strategy to reduce warpage in additive manufacturing. *Addit. Manuf.* **2019**, *28*, 554–564. [CrossRef]
24. Levkulich, N.; Semiatin, S.; Gockel, J.; Middendorf, J.; Dewald, A.; Klingbeil, N. The effect of process parameters on residual stress evolution and distortion in the laser powder bed fusion of Ti-6Al-4V. *Addit. Manuf.* **2019**, *28*, 475–484. [CrossRef]
25. Li, H.; Ramezani, M.; Chen, Z.; Singamneni, S. Effects of Process Parameters on Temperature and Stress Distributions During Selective Laser Melting of Ti-6Al-4V. *Trans. Indian Inst. Met.* **2019**, *72*, 3201–3214. [CrossRef]

26. Afazov, S.; Denmark, W.A.; Toralles, B.L.; Holloway, A.; Yaghi, A. Distortion prediction and compensation in selective laser melting. *Addit. Manuf.* **2017**, *17*, 15–22. [CrossRef]
27. Yaghi, A.; Ayvar-Soberanis, S.; Moturu, S.; Bilkhu, R.; Afazov, S. Design against distortion for additive manufacturing. *Addit. Manuf.* **2019**, *27*, 224–235. [CrossRef]
28. Biegler, M.; Elsner, B.A.; Graf, B.; Rethmeier, M. Geometric distortion-compensation via transient numerical simulation for directed energy deposition additive manufacturing. *Sci. Technol. Weld. Join.* **2020**, *25*, 468–475. [CrossRef]
29. Li, Z.; Xu, R.; Zhang, Z.; Kucukkoc, I. The influence of scan length on fabricating thin-walled components in selective laser melting. *Int. J. Mach. Tools Manuf.* **2018**, *126*, 1–12. [CrossRef]
30. Chen, C.; Xiao, Z.; Zhu, H.; Zeng, X. Deformation and control method of thin-walled part during laser powder bed fusion of Ti–6Al–4V alloy. *Int. J. Adv. Manuf. Technol.* **2020**, *110*, 3467–3478. [CrossRef]
31. Ahmed, A.; Majeed, A.; Atta, Z.; Jia, G. Dimensional Quality and Distortion Analysis of Thin-Walled Alloy Parts of AlSi10Mg Manufactured by Selective Laser Melting. *J. Manuf. Mater. Process.* **2019**, *3*, 51. [CrossRef]
32. Setien, I.; Chiumenti, M.; Van Der Veen, S.; Sebastian, M.S.; Garciandía, F.; Echeverría, A. Empirical methodology to determine inherent strains in additive manufacturing. *Comput. Math. Appl.* **2019**, *78*, 2282–2295. [CrossRef]
33. Chiumenti, M.; Lin, X.; Cervera, M.; Lei, W.; Zheng, Y.; Huang, W. Numerical simulation and experimental calibration of additive manufacturing by blown powder technology. Part I: Thermal analysis. *Rapid Prototyp. J.* **2017**, *23*, 448–463. [CrossRef]
34. Chiumenti, M.; Cervera, M.; Salmi, A.; De Saracibar, C.A.; Dialami, N.; Matsui, K. Finite element modeling of multi-pass welding and shaped metal deposition processes. *Comput. Methods Appl. Mech. Eng.* **2010**, *199*, 2343–2359. [CrossRef]
35. Chiumenti, M.; Cervera, M.; Dialami, N.; Wu, B.; Jinwei, L.; De Saracibar, C.A. Numerical modeling of the electron beam welding and its experimental validation. *Finite Elem. Anal. Des.* **2016**, *121*, 118–133. [CrossRef]
36. Cervera, M.; de Saracibar, C.A.; Chiumenti, M. *COMET: Coupled Mechanical and Thermal Analysis*; Data Input Manual, Version 5.0, Technical Report IT-308; CIMNE: Barcelona, Spain, 2002.
37. Dialami, N.; Cervera, M.; Chiumenti, M.; De Saracibar, C.A. A fast and accurate two-stage strategy to evaluate the effect of the pin tool profile on metal flow, torque and forces in friction stir welding. *Int. J. Mech. Sci.* **2017**, *122*, 215–227. [CrossRef]
38. Ribó, R.; Pasenau, M.; Escolano, E.; Pérez, J.; Coll, A.; Melendo, A. *GiD The Personal Pre and Postprocessor*; Reference Manual; CIMNE: Barcelona, Spain, 2006.
39. Zhang, W.; Tong, M.; Harrison, N.M. Resolution, energy and time dependency on layer scaling in finite element modelling of laser beam powder bed fusion additive manufacturing. *Addit. Manuf.* **2019**, *28*, 610–620. [CrossRef]
40. Dunbar, A.J.; Denlinger, E.R.; Gouge, M.F.; Michaleris, P. Experimental validation of finite element modeling for laser powder bed fusion deformation. *Addit. Manuf.* **2016**, *12*, 108–120. [CrossRef]
41. Yang, T.; Xie, D.; Yue, W.; Wang, S.; Rong, P.; Shen, L.; Zhao, J.; Wang, C. Distortion of Thin-Walled Structure Fabricated by Selective Laser Melting Based on Assumption of Constraining Force-Induced Distortion. *Metals* **2019**, *9*, 1281. [CrossRef]

# Substrate design to minimize residual stresses in Directed Energy Deposition AM processes

X. Lu, M. Chiumenti, M. Cervera, J. Li, X. Lin, L. Ma, G. Zhang & E. Liang.

*Materials & Design*

*Vol. 202, pp.* 109525, (2021)

https://doi.org/10.1016/j.matdes.2021.109525

Materials and Design 202 (2021) 109525

Contents lists available at ScienceDirect

Materials and Design

journal homepage: www.elsevier.com/locate/matdes

# Substrate design to minimize residual stresses in Directed Energy Deposition AM processes

Xufei Lu [a,b,c], Michele Chiumenti [a,*], Miguel Cervera [a], Junjie Li [b,c], Xin Lin [b,c,**], Liang Ma [b,c], Guohao Zhang [b,c], Enquan Liang [d]

[a] International Center for Numerical Methods in Engineering, Universidad Politécnica de Cataluña, 08034 Barcelona, Spain
[b] State Key Laboratory of Solidification Processing, Northwestern Polytechnical University, Xi'an, Shaanxi 710072, China
[c] Key Laboratory of Metal High Performance Additive Manufacturing and Innovative Design, MIIT China, Northwestern Polytechnical University, Xi'an, Shaanxi 710072, China
[d] Shanghai Aircraft Design and Research Institute, Commercial Aircraft Corporation of China, Shanghai 200232, China

## HIGHLIGHTS

- Substrate design optimization to reduce the residual stresses in DED.
- Coupled thermomechanical analysis for AM by an in-house calibrated software.
- Sensitivity of conformal and non-conformal substrates to the lower built surface.
- Sensitivity of substrate stiffness and thermal resistance on residual stresses.

## GRAPHICAL ABSTRACT

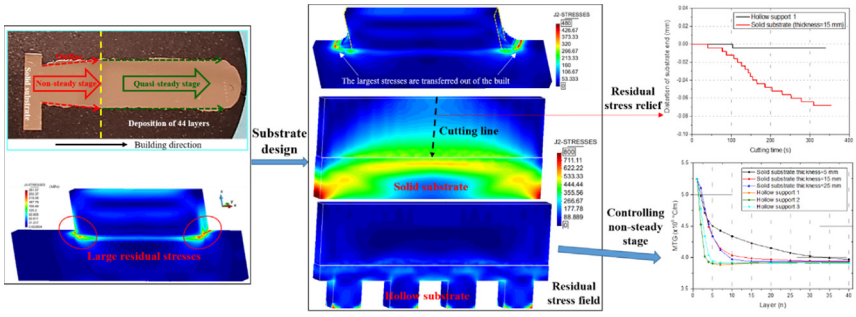


## ARTICLE INFO

*Article history:*
Received 30 September 2020
Received in revised form 12 January 2021
Accepted 24 January 2021
Available online 28 January 2021

*Keywords:*
Directed energy deposition (DED)
Substrate design
Residual stresses
Thermo-mechanical analysis

## ABSTRACT

This paper proposes a strategy to optimize the design of the substrate structures used in Additive Manufacturing (AM) by Directed Energy Deposition (DED) to minimize the residual stresses induced by this fabrication process. To this end, several numerical analyses were performed to analyse different substrate designs in order: (i) to reduce the sensitivity to the initial non-steady stage when the first layers of material are deposited, (ii) to optimize the heat flux through the substrate to reduce the Maximum Temperature Gradients (MTG) and, (iii) to modify the substrate stiffness and its mechanical constraining to the thermal deformations during the building process and the cooling phase. To ensure the reliability of the numerical simulations, an in-house software is calibrated to allow for an accurate analysis of DED. Thus, an experimental setting is undergone to feed the numerical model with suitable values of both material and process parameters through temperature and displacement measurements and numerical fitting. Once calibrated, the software is used to evaluate the performance of several substrate designs to mitigate the residual stresses induced by the DED process. A thin-walled rectangular part selected as industrial demonstrator showed a significant reduction (up to 62%) of the maximum tensile stresses.



## 1. Introduction

Additive manufacturing (AM) is an advanced industrial technology for manufacturing high-performance metallic parts through a layer-by-layer material deposition [1,2]. In Directed Energy Deposition (DED) the metal powder is blown into the melting pool generated by a coaxial high energy source (e.g. laser or electron beam). Despite

* Corresponding author.
** Corresponding author at: State Key Laboratory of Solidification Processing, Northwestern Polytechnical University, Xi'an, Shaanxi 710072, China.
*E-mail addresses:* michele.chiumenti@upc.edu (M. Chiumenti), xlin@nwpu.edu.cn (X. Lin).

https://doi.org/10.1016/j.matdes.2021.109525

being one of the most versatile AM processes used either to fabricate new components or to repair damaged parts [3], the DED technology is characterized by high-energy sources which generate high temperature fields as well as high temperature gradients. As a consequence, both residual (tensile) stresses and plastic deformations generally affect the final metallurgy as well as the structural performance of in service AM parts [3–5,38,39].

To mitigate the residual stresses and distortions of AM components, several researchers have investigated the sensitivity of the DED process to the scanning strategy, the process parameters and the geometry of the built structures. It has been observed that the residual stresses can be mitigated by reducing the local heat accumulation during the metal deposition. This can be achieved by reducing the scanning length and/or by increasing the scanning speed [6–8]. The substrate distortion can be alleviated by optimizing the process parameters (e.g. source power, scanning speed, feeding rate, etc.) [9–11]. Some other research works [12–15] revealed that the geometry of the component and, in particular, its local stiffness, also plays an important role in the development of residual stresses in the build. Mukherjee et al. [16,17] demonstrated how the thermal distortion of AM parts depends on the material properties, the deposition strategy, the process parameters, the geometry of the component, as well as the preheating and the cooling conditions. Mitigation of residual stresses can be achieved by preheating the substrate before the AM process, thus reducing of the large thermal gradients during the metal deposition of the first few layers [18–20]. Li et al. [21] reported a remarkable reduction of both longitudinal bending and angular distortion by replacing continuous clamping condition with a more flexible multi-point support strategy. Denlinger et al. [22] optimized the metal deposition on the base plate to mitigate the longitudinal bending effects induced by the thermal field. Afazov et al. [23,24] proposed the geometry compensation strategy to modify the nominal geometry of AM components according to the thermal deformation predicted by the numerical analysis. Finally, Hönnige et al. [25,26] showed the advantages of the rolling techniques in WAAM processes to reduce distortions and residual stresses.

Fig. 1 shows the transition from the "*non-steady stage*" to the "*quasi-steady stage*" during the DED process of a Ti-6Al-4V rectangular frame [12]. During the entire non-steady stage, both the thickness and the width of the deposited layers are affected by the heat absorption through the (initially) cold substrate. As a general conclusion, in DED process net-shape (nominal) geometries can obtained by reducing the Maximum Thermal Gradients (MTG). Such MTG generally appear when the first layers of metal are deposited on the cold substrate. Therefore, to enhance the DED process it is mandatory to reduce the MTG by either pre-heating the substrate [18–20] or reducing the heat flux from the Heat Affected Zone (HAZ) to the workbench through the substrate [6–9,25–28]. Thereby, the first objective of this work consists of optimizing the non-steady stage to obtain high quality DED parts.

In Selected Laser Melting (SLM) the workbench is very thick and rigid. Therefore, the focus is placed on the stiffness and the heat flux transfer of the support structures [29–31]; these are necessary when printing overhangs in SLM and they affect the development of thermal stresses and deformations of the build [29–33]. Contrariwise, in DED processes the material is directly deposited on the substrate and the use of supporting structure is generally avoided. Therefore, the overall stiffness of the building structure depends on the design of the substrate and its optimization is marginally studied in the literature. A thick substrate fixed on the work-bench is generally used to prevent the development of undesired thermal deformations. However, a very rigid substrate generates large residual stresses which can transform into plastic deformations during the cooling process. Moreover, during the cutting process when the substrate is removed, the residual stresses relaxation induces a further distortion of the component [17]. Thus, the optimization of the substrate stiffness in order to mitigate the residual stresses and the component distortion is the second objective of this work.

## 2. Numerical model

The numerical framework used for the high-fidelity modelling of AM processes is based on a coupled 3D thermo-mechanical FE module for transient analysis as part of the in-house software platform COMET [34] developed at the *International Centre for Numerical Methods in Engineering* (CIMNE). The thermo-mechanical coupling is handled by a staggered solution: at each time-step, the transient heat transfer problem is solved first. Next, the mechanical analysis is solved accounting for the temperature-dependent material parameter data-base.

### 2.1. Thermal analysis for AM

The balance of energy is the governing equation used to solve the heat transfer analysis. The local (strong) form of this equation is:

$$\dot{H} = -\nabla\cdot\mathbf{q} + + \dot{Q} \tag{1}$$

where $\dot{H}$ is the enthalpy rate. The heat flux $\mathbf{q}$ is defined through Fourier's law:

$$\mathbf{q} = -k\nabla T \tag{2}$$

where $k$ is the temperature-dependent thermal conductivity.

The heat source (per unit of volume), $\dot{Q}$, is defined in terms of the total energy input (e.g. laser source), $\dot{P}$, the heat absorption efficiency, $\eta_p$ and the volume of the melt pool, $V_{pool}^{\Delta t}$, as:

$$\dot{Q} = \frac{\eta_p \dot{P}}{V_{pool}^{\Delta t}} \tag{3}$$

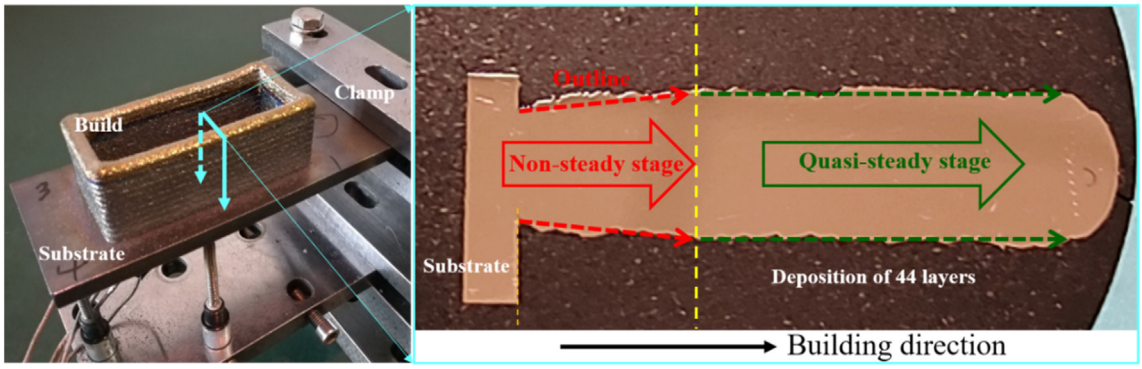


**Fig. 1.** The transition from the non-steady stage to quasi-steady stage of a Ti-6Al-4V part deposited by DED.

Hence, the heat source is uniformly spread inside the melt-pool because of the lack of resolution of the FE meshes generally used for the AM analysis at global (component) level [35–37].

The heat loss by convection is computed by using Newton's law:

$$q_{conv} = h_{conv}(T - T_{env}) \tag{4}$$

where $h_{conv}$ is the temperature-dependent Heat Transfer Coefficient (HTC) by convection, $T$ is the temperature at the component surface and $T_{env}$ is the environment temperature.

The heat dissipation by the radiation is defined by Stefan-Boltzmann's law:

$$q_{rad} = \varepsilon_{rad}\sigma_{rad}\left(T^4 - T_{env}^4\right) \tag{5}$$

where $\varepsilon_{rad}$ is the surface emissivity and $\sigma_{rad}$ is the Stefan-Boltzmann constant.

Note that the heat dissipation by convection and radiation mechanism depends on the actual boundary condition (i.e. the current external surfaces of the built). Thus, the heat flow is proportional to the evolution of the building process [35–37].

### 2.2. Mechanical analysis

The mechanical problem is determined by the balance of momentum and the continuity equations:

$$\nabla\cdot\mathbf{s} + \nabla p + \mathbf{b} = 0 \tag{6}$$

$$(\nabla\cdot\mathbf{u} - e^T) - \frac{p}{K} = 0 \tag{7}$$

where the Cauchy stress tensor, $\boldsymbol{\sigma}$ is split into its hydrostatic (pressure), $p$ and deviatoric parts $\mathbf{s}$, respectively, as:

$$\boldsymbol{\sigma} = p\boldsymbol{I} + \mathbf{s}(\mathbf{u}) \tag{8}$$

$\mathbf{b}$ are the body forces per unit of volume and $K(T)$ is the temperature-dependent bulk modulus, controlling the material compressibility. The thermal deformation, $e^T$ is expressed as:

$$e^T(T, f_S) = e^{cool}(T) + e^{pc}(f_S) \tag{9}$$

$e^{cool}(T)$ and $e^{pc}(f_S)$ are the thermal expansion/contraction and thermal shrinkage during the liquid-to-solid phase-change, as a function of the initial temperature $T_0$ and the solid fraction $f_S$, respectively, and defined as:

$$e^{cool}(T) = \alpha(T)(T - T_0) \tag{10}$$

$$e^{pc}(f_S) = \beta f_S \tag{11}$$

where $\alpha = \alpha(T)$ and $\beta = \frac{\Delta V^{pc}}{V_0}$ are the thermal expansion and the shrinkage coefficients, respectively.

Note that the mechanical problem defined by Eqs. (6)–(7) depends on both the displacements, $\mathbf{u}$, and the pressure field, $p$ and is suitable for both compressible and the fully incompressible (isochoric) material behaviors.

In AM, the temperature field varies from the room temperature to (and above) the melting point. Thereby, the material must be characterized in its solid, mushy and liquid phases.

A *J2*-thermo-elasto-visco-plastic model is assumed in the solid phase, from the room to the annealing temperature. All the material properties are assumed as temperature-dependent. The von-Mises yield-surface is defined as:

$$\Phi(\mathbf{s}, q_h, T) = \|\mathbf{s}\| - \sqrt{\frac{2}{3}}\left[\sigma_y(T) - q_h\right] \tag{12}$$

where $\sigma_y(T)$ is the temperature-dependent elastic limit controlling the thermal softening and $q_h$ is the stress-like variable controlling the isotropic strain-hardening, expressed as:

$$q_h(\xi, T) = -\left[\sigma_\infty(T) - \sigma_y(T)\right]\left[1 - e^{-\delta(T)\xi}\right] - h(T)\xi \tag{13}$$

where $\xi$ is the isotropic strain-hardening variable, $\sigma_\infty(T)$ is the temperature-dependent saturation flow stress, while $\delta(T)$ and $h(T)$ are the temperature-dependent parameters to control the exponential and linear hardening laws, respectively.

The deviatoric counterpart of Cauchy's stress tensor is computed as:

$$\mathbf{s} = 2G(\mathbf{e} - \mathbf{e}^{vp}) \tag{14}$$

where $G = G(T)$ is the temperature-dependent shear modulus, while $\mathbf{e}$ and $\mathbf{e}^{vp}$ are the total (deviatoric) and the visco-plastic strain, respectively. The former is extracted from the total strain tensor $\boldsymbol{\varepsilon}(\mathbf{u}) = \nabla^{sym}(\mathbf{u})$, while the evolution laws of both the visco-plastic strain tensor and the isotropic strain-hardening variable are obtained through the principle of maximum plastic dissipation as:

$$\dot{\mathbf{e}}\, vp = \dot{\gamma}\, vp \frac{\partial\Phi(\mathbf{s}, q_h)}{\partial\mathbf{s}} = \dot{\gamma}\, vp \frac{\mathbf{s}}{\|\mathbf{s}\|} = \dot{\gamma}\, vp\mathbf{n} \tag{15}$$

$$\dot{\xi} = \dot{\gamma}\, vp \frac{\partial\Phi(\mathbf{s}, q_h)}{\partial q_h} = \sqrt{\frac{2}{3}}\dot{\gamma}\, vp \tag{16}$$

where $\mathbf{n}$ is the normal of the yield surface, and $\dot{\gamma}\, vp$ is the visco-plastic multiplier, defined as:

$$\dot{\gamma}\, vp = \left\langle \frac{\partial\Phi(\mathbf{s}, q_h)}{\eta} \right\rangle^{\frac{1}{m}} \tag{17}$$

where $\langle\cdot\rangle$ is the Macaulay bracket, while $\eta = \eta(T)$ and $m = m(T)$ are the temperature-dependent plastic viscosity and rate sensitivity, respectively.

Note that, when the temperature is approaching the annealing value, $\sigma_y(T) \to 0$. Thus, the deviatoric Cauchy stress reduces to:

$$\mathbf{s} = \eta(\dot{\gamma}\, vp)^m\mathbf{n} = \eta_{eff}\dot{\mathbf{e}}\, vp \tag{18}$$

where $\eta_{eff} = \eta(\dot{\gamma}\, vp)^{m-1}$ is the effective viscosity. Thereby, above the annealing temperature the material is characterized by a purely viscous law [36,37]. A non-Newtonian behavior $m > 1$ is used for the mushy phase (from the annealing to the liquid temperature), while a Newtonian law, $m = 1$, characterizes the liquid phase (temperature values above the melting point).

### 2.3. FE modelling of the DED process

To simulate the DED process, a time discretization is required. A time step, $\Delta t = t^{n+1} - t^n$, characterizes the time-marching scheme. Thereby, the melt-pool is allowed to move step-by-step along the scanning pattern from the actual position defined at time $t^n$ to that at time $t^{n+1}$. Within this interval, the heat is distributed to the elements belonging to the melt pool volume and, at the same time, the blown powder conforms the metal deposition which characterizes this AM process.

The numerical simulation of the DED process needs an ad-hoc procedure to classify the elements into: *active*, *inactive* and *activated* elements. At each time-step, an octree-based searching algorithm is used to find the elements belonging to the melt-pool (*active*) and to the new metal deposition (*activated*). Thus, the software reads the same input file (Common Layer Interface – CLI format) following the actual

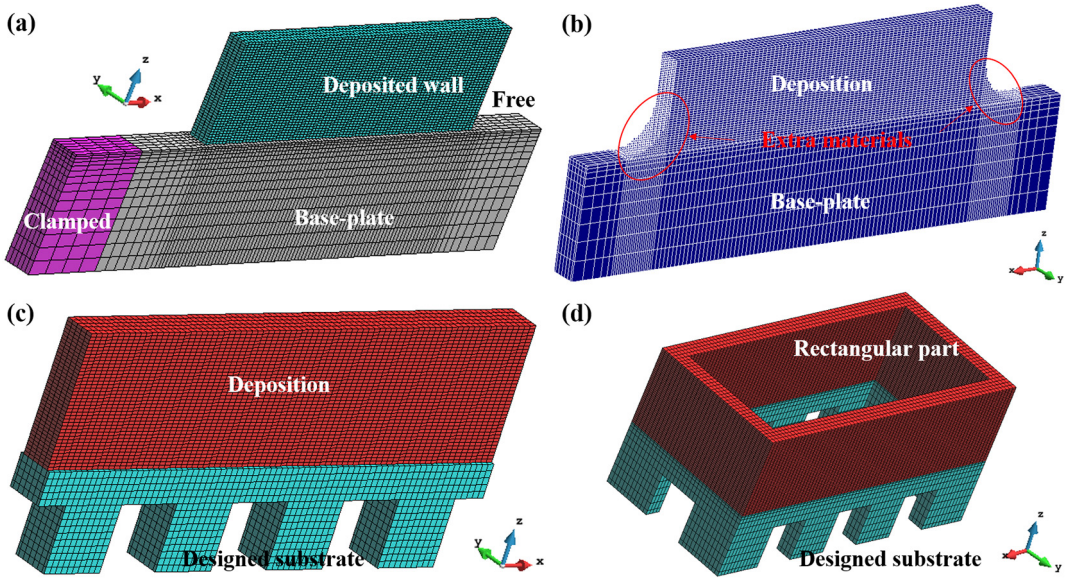


**Fig. 2.** 3D FE meshes used for analysing the DED process: (a) single-wall used to calibrate the AM model; (b) single-wall with rounded corners; (c) hollow structure design for the substrate; (d) demonstrator with hollowed structure substrate.

**Table 1**
Temperature-dependent material properties of Ti-6Al-4V [12].

| Temperature (°C) | Density (kg/m$^3$) | Thermal Conductivity (W/(m·°C)) | Heat Capacity (J/(kg·°C)) | Poisson's Ratio | Thermal Expansion Coefficient (μm/(m·°C)) | Young's Modulus (GPa) | Elastic Limit (MPa) |
|---|---|---|---|---|---|---|---|
| 20 | 4420 | 7 | 546 | 0.345 | 8.78 | 110 | 850 |
| 205 | 4395 | 8.75 | 584 | 0.35 | 10 | 100 | 630 |
| 500 | 4350 | 12.6 | 651 | 0.37 | 11.2 | 76 | 470 |
| 995 | 4282 | 22.7 | 753 | 0.43 | 12.3 | 15 | 13 |
| 1100 | 4267 | 19.3 | 641 | 0.43 | 12.4 | 5 | 5 |
| 1200 | 4252 | 21 | 660 | 0.43 | 12.42 | 4 | 1 |
| 1600 | 4198 | 25.8 | 732 | 0.43 | 12.5 | 1 | 0.5 |
| 1650 | 3886 | 83.5 | 831 | 0.43 | 12.5 | 0.1 | 0.1 |
| 2000 | 3818 | 83.5 | 831 | 0.43 | 12.5 | 0.01 | 0.01 |

scanning sequence as used to inform the DED machine. The birth-and-death-element technique is used to activate the elements belonging to the new deposited layer. Both *active* and *activated* elements belong to the current computational domain, while the *inactive* elements are neither computed nor assembled into the global matrix of the problem [35].

### 2.4. Geometry model and FE meshes

The generation of the CAD geometry, the meshing operation as well as the post-processing of the results are carried out using the in-house pre-post-processor GiD [40]. Fig. 2 shows the 3D geometries and the corresponding FE meshes of different builds. Fig. 2(a) shows the single-wall model used to calibrate the AM software: it consists of 19,040 hexahedral elements and 24,285 nodes. The base plate is clamped on the left-hand side as a cantilever beam, while the other end is free. Fig. 2(b) shows the same geometry but including some extra material to alleviate the stress concentrations at the corners where the wall is attached to the substrate. Fig. 2(c) depicts a new substrate design characterized by a hollow structure, proposed to reduce the residual stresses and the sensitivity to the initial non-steady stage. Finally, a more complex part is presented in Fig. 2(d) and it is used as the industrial demonstrator to validate the optimization strategy for the substrate design. The corresponding mesh consists of 44,000 hexahedral elements and 56,400 nodes.

### 2.5. Material properties and boundary conditions

The temperature-dependent thermal and mechanical properties of Ti-6Al-4V adopted for the material characterization are listed in Table 1 [12]. Note that the thermal conductivity is increased up to 83.5 W/(m·°C) to take into account the convective flow inside the melting pool when the temperature is above the melt point [41].

The thermal boundary conditions adopted for all the numerical simulations account for the heat loss by convection and radiation through the external surfaces of both the build and the substrate. The HTC by convection and the emissivity are $h_{conv} = 8$ W/(m$^2$·°C) and $\varepsilon_{rad} = 0.7$, respectively. The HTC by conduction controlling the heat flux at the contact interface between the base-plate and the clamping system (or the workbench) is set to $h_{conv} = 100$ W/(m$^2$·°C). During the AM process, the ambient temperature was $T_{env} = 25$ °C. The power absorption in DED process when using Ti-6Al-4V is set to $\eta_p = 0.3$.

These parameters have been calibrated using the experimental data obtained through the in situ measurements as described in the next section.

## 3. Experimental setting

Fig. 3 shows the experimental setting used for the calibration of the software platform. The single-wall shown in Fig. 2(a) is used for this

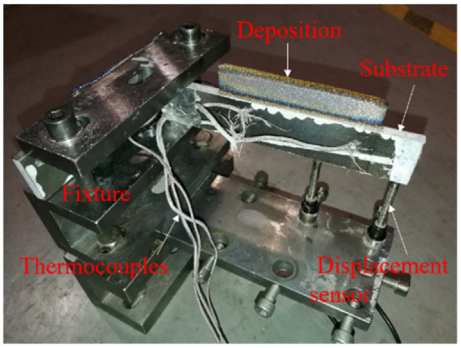


**Fig. 3.** In-situ measurement set-up for the calibration of the numerical simulation of the DED process: single-wall on a substrate fixed as a cantilever.

purpose. An annealed Ti-6Al-4V substrate 140 mm long, 6 mm wide and 25 mm high is used for the DED process.

Fig. 4 shows the locations of the thermocouples and the displacement sensor. The displacement sensor (WXXY PM11-R1-20L) has an accuracy of 0.02%, a maximum range of 20 mm and was employed for the in-situ measurement of the vertical displacement at point DS placed on the bottom surface of the substrate during the entire DED process. Omega GG-K-30 type thermocouples with a recording uncertainty of ±0.75% (or 2.2 °C) were used to measure the temperature history at points CH1, CH2, and CH3 of the substrate. Additionally, a Graphtec GL-900 high-speed eight-channel data-logger was used to record the signals from the thermocouples and displacement sensors.

Spherical Ti-6Al-4V powder (45–325 μm) produced via a plasma rotating electrode process is dried in a vacuum oven at 120 °C during 2.5 h before the blown-powder process. The DED machine is equipped with a YLS-3000 IPG Photonics fibre laser system having a wave-length ranging between 960 and 1200 nm and a maximum output power of 3 kW. During the fabrication, the laser power used was 1.5 kW with 3 mm of spot size and a Gaussian distribution profile. The laser scanning speed is 10 mm/s. The up-lift height is set to 0.5 mm with a feeding rate of 12.0 g/min. The average penetration depth is 0.5 mm.

The metal deposition is made of 40 layers, approximately 20 mm high, 80 mm long and 4 mm wide (one single hatching). The whole building process is carried out in a closed chamber with protective gas (pure argon).

## 4. Calibration of DED model

The thermo-mechanical FE model as well as the material data used in this work have been validated in previous works [3,12,19,35–37]. Here, only the heat dissipation by convection and conduction are calibrated. The numerical fitting of the experimental measurements is

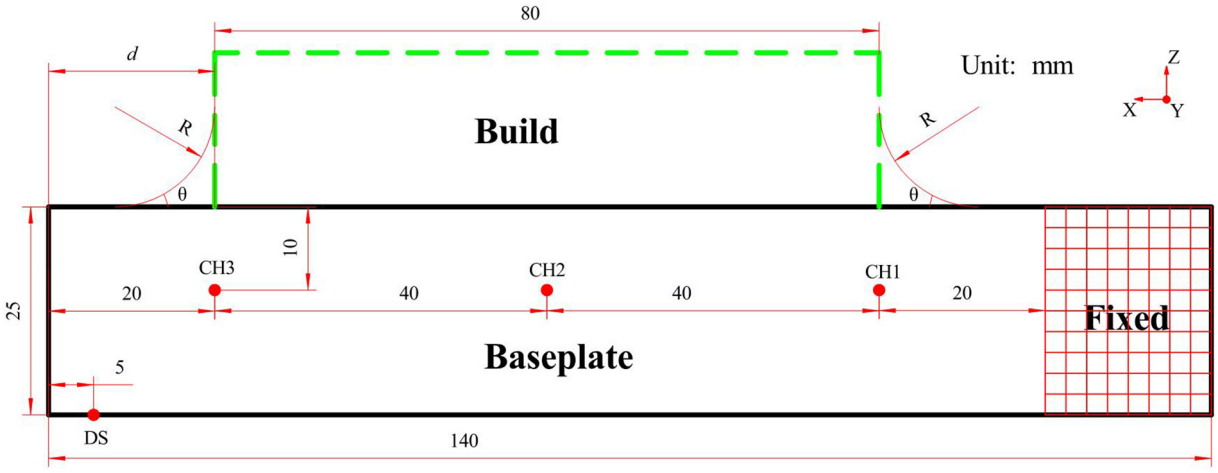


**Fig. 4.** Single-wall: dimensions and location of the thermocouples (CH1, CH2 and CH3) and the displacement sensor (DS).

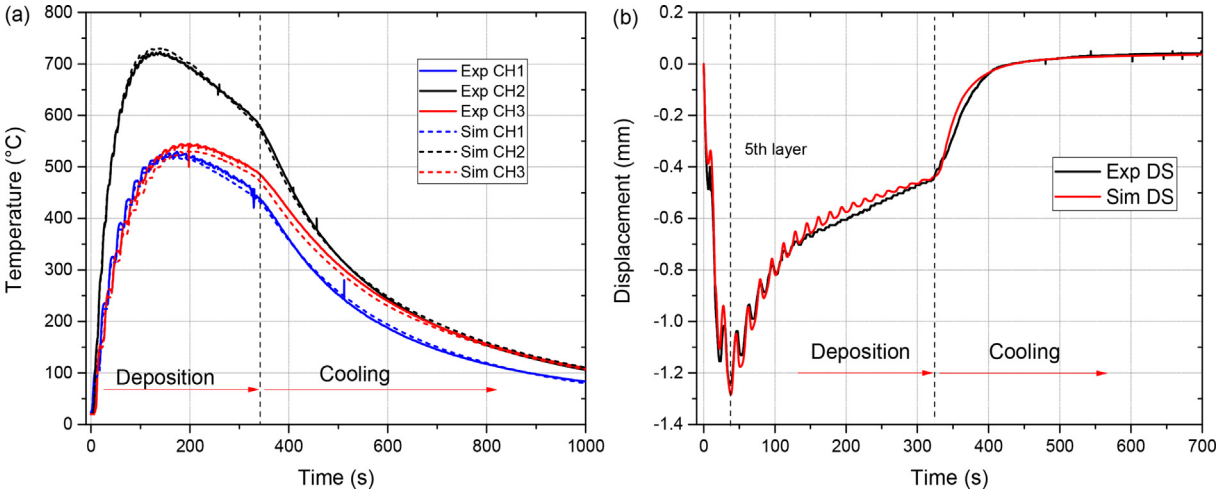


**Fig. 5.** Experimental measurements and numerical results: (a) temperature evolution at CH1, CH2 and CH3; (b) vertical displacement history at DS point.

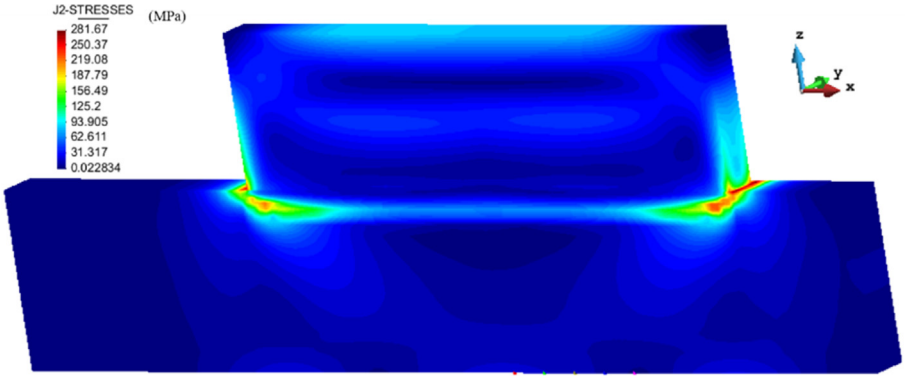


**Fig. 6.** Residual von Mises stress field of the single-wall.

shown in Fig. 5. In this figure, the temperature curves shown corresponds to the measurements at the thermocouple locations CH1, CH2 and CH3, while the vertical displacement is obtained at point DS (see Fig. 4). The agreement between experiments and numerical results is remarkable.

## 5. Substrate optimization strategy

Fig. 6 shows the von Mises stress indicator corresponding to the residual stress field at the end of the DED process. The highest values are located at the basement of the single-wall deposition, as previously observed in [3,12,17]. This is mainly due to the large temperature gradients generated during the deposition of the first layers of the building over the cold substrate during the initial non-steady stage. The contraction of these layers is restrained by the substrate, thus generating large residual stresses.

The optimization of the substrate geometry aims both to enhance the heat dissipation through the substrate and to reduce its global stiffness. On the one hand, if the heat flux is reduced, the thermal gradients during the initial non-steady stage of the metal deposition can be reduced also. On the other hand, by reducing the global stiffness of the substrate, it is possible to achieve a weaker mechanical constraining between the AM-build and the substrate, reducing the formation of plastic deformations. The drawback of the latter is the possibility of inducing a larger distortion of the component.

### 5.1. Minimization of the stress concentrations

In order to minimize the stress concentrations at the interface between the building structure and the substrate, two possibilities are investigated: (i) rounding off the sharp angles where the part is attached to the substrate; and (ii) conforming the substrate to the bottom surface of the build.

The first idea is very well known and is actually applied in many fabrication processes to avoid crack initiation at the stress concentration points. Therefore, all the corners are rounded off to avoid sharp angles.

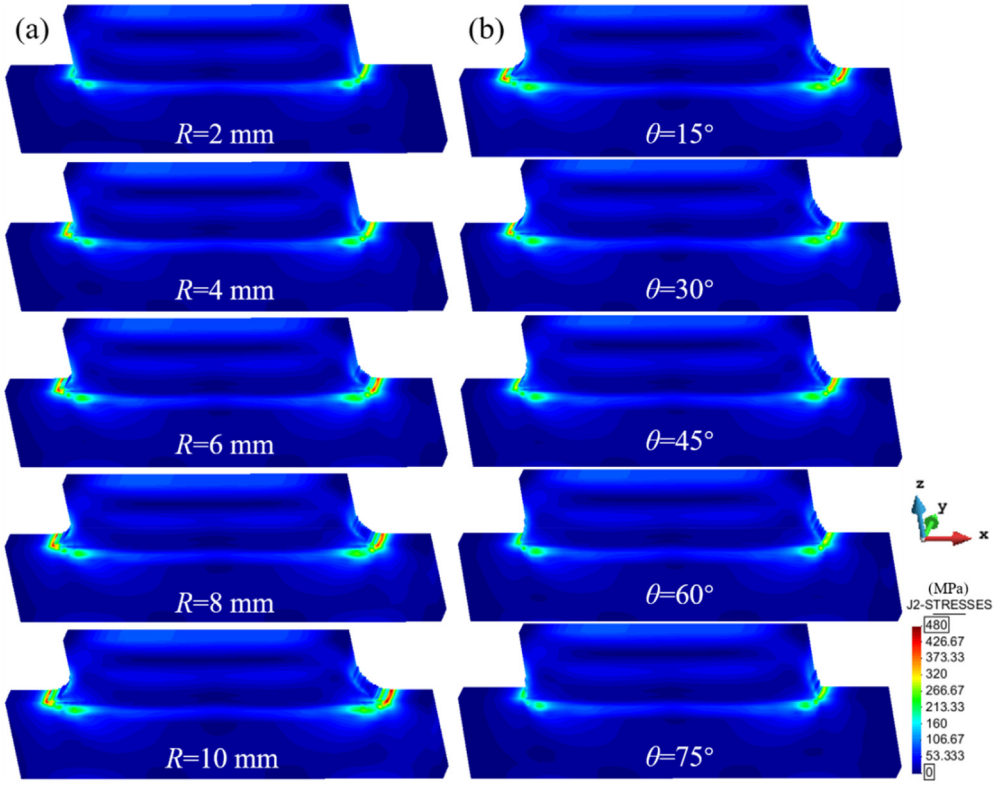


**Fig. 7.** Predicted residual von Mises stress field: (a) by rounding off the corners using different arc radii (R). (b) by using different tangent angles ($\theta$) with respect to the substrate.

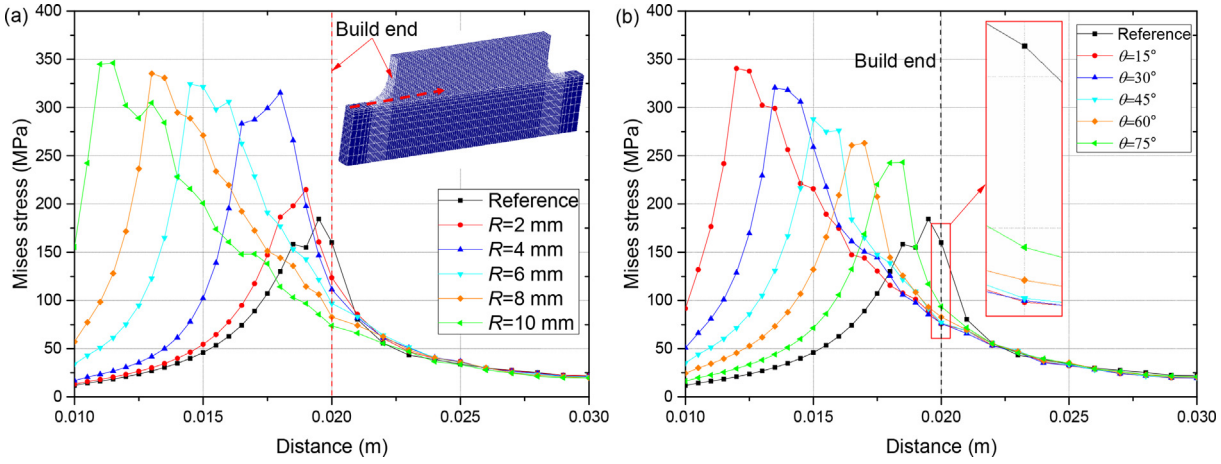


**Fig. 8.** Comparison of the residual von Mises stress distributions along the top surface of the substrate: (a) by rounding off the corners using different arc radii (R); (b) by using different tangent angles ($\theta$) with respect to the substrate.

The effectiveness of this method in AM is tested in this work by taking the rounding angle $\theta$ between top surface of the substrate and the single-wall as the design parameter. The sample with sharp angles is used as the reference.

Figs. 7(a) and 8(a) show the contour fills and the distributions of the residual von Mises stress using different rounding radii varying from 2 to 10 mm. In both figures, it can be observed that the maximum residual stresses increase by expanding the arc radius. This is due to the fast cooling of the extra material used to print this small zone. However, the highest stress values are located outside the nominal geometry of the single-wall, and more precisely, at the external sides of the material used for the rounding off. Thus, the residual stresses are effectively minimized in the actual build.

As an alternative, the material supply for the rounding off can be reduced assuming non-tangent configurations where the angle $\theta$ with respect to the substrate is varied from 15° to 75°. Also in this case, the values of the residual von Mises stress depicted in Fig. 7(b) and Fig. 8(b) are increasing when reducing $\theta$ but, again, the corresponding highest values are moved far away from the nominal geometry of the wall. Taking into account the material waste and practical experience, it is found that $\theta = 45°$ is the optimal choice for minimizing the stress concentration and preventing crack initiation.

### 5.2. Size optimization of the substrate

In this section, the optimization of the substrate size is investigated. The distance, $d$, between the left-hand side of the substrate and the single-wall is used as design parameter (see Fig. 4). This dimension is progressively reduced from 20 mm to 15 mm, 10 mm, 5 mm and 0 mm, respectively.

The evolution of the vertical displacement recorded during the entire DED process simulation is shown in Fig. 9(a) for all the test-cases. As the wall of the AM deposition gets closer to the free-end of the substrate, the vertical displacement of the substrate at point DS gradually decreases. It is also relevant to observe that most of the substrate distortion occurs during the non-steady stage, when the first 5 layers are deposited on the cold substrate. If compared with the reference configuration ($d =$ 20 mm), when $d = 0$ mm (i.e. the substrate conforms to the lower surface of the build), this vertical displacement is reduced by 30%. The longitudinal residual stress ($\sigma_{xx}$) distributions at the basement of the build are plotted in Fig. 9(b) and in the contour-fills shown in Fig. 10. It can be seen that the stress concentration on the right-hand side of the single-wall gradually decreases according to the size of the substrate, to vanish when $d = 0$. This is because the mechanical constraining induced by the substrate is gradually reduced, allowing for the free thermal

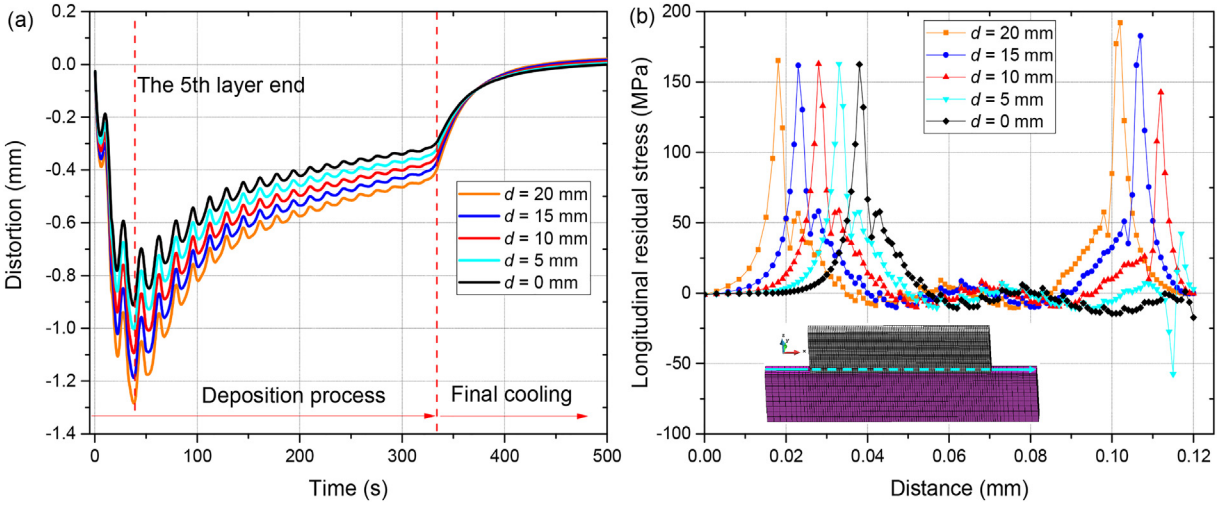


**Fig. 9.** Optimization of the substrate size for the single-wall: (a) vertical displacement histories at point DS; (b) distribution of longitudinal residual stresses ($\sigma_{xx}$) on the top surface of the substrate.

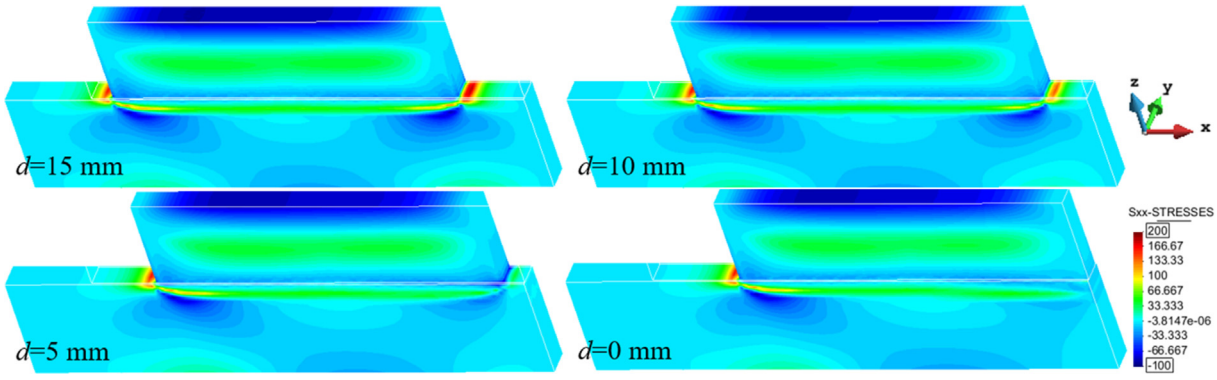


**Fig. 10.** Contour-fill of the longitudinal residual stress ($\sigma_{xx}$).

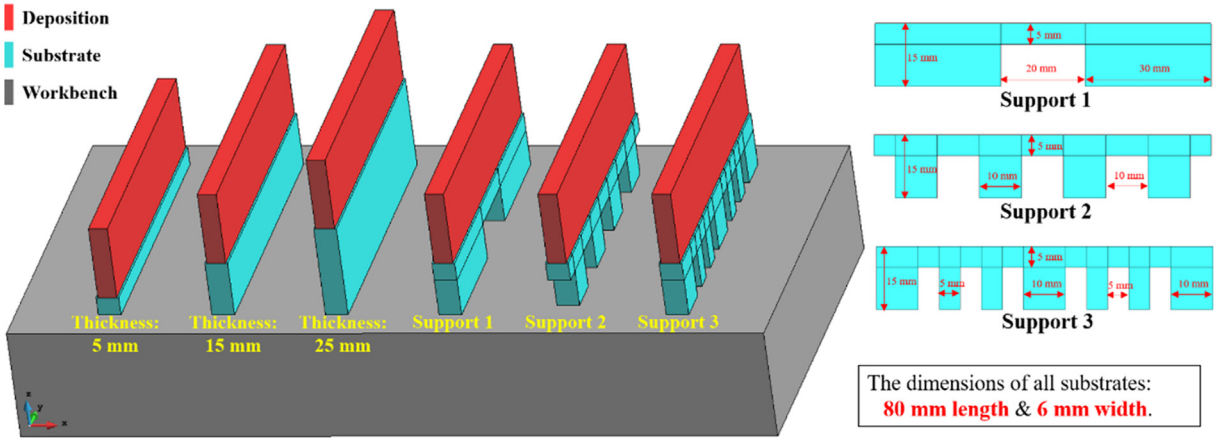


**Fig. 11.** Different substrates for the metal deposition part during DED process.

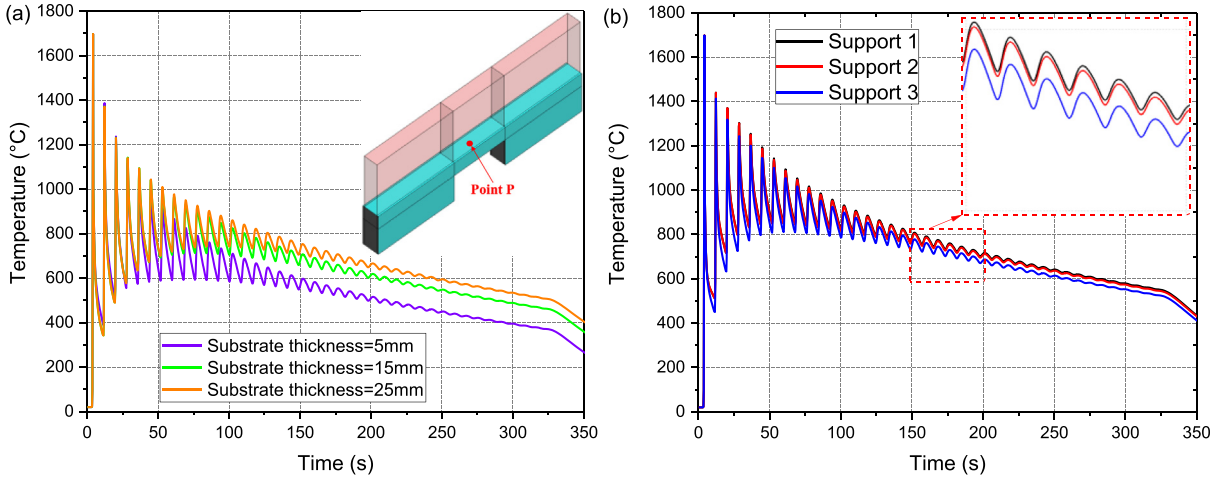


**Fig. 12.** Temperature evolution of point P: (a) solid substrates with increasing height; (b) hollow substrates.

expansion/contraction of the deposited materials. Thus, residual stresses during the AM process can be satisfactorily mitigated.

### 5.3. Optimization of the substrate design

In this section, the design optimization of the substrate structure is investigated. Two types of substrates are analyzed: (i) solid substrates with increasing height of 5 mm, 15 mm, and 25 mm, respectively; and (ii) hollow substrates with a fixed height of 15 mm but with different hollow shapes, as shown in Fig. 11. These structures are suitable for industrial DED fabrications and respond to two objectives: (1) reducing the heat flux through the substrate, and (2) reducing the substrate stiffness. As a consequence, the initial non-steady phase can be minimized because of a faster substrate heating. Moreover, the mechanical constraining due to the substrate stiffness is also reduced and thus, the residual stresses induced by the metal deposition process are mitigated.

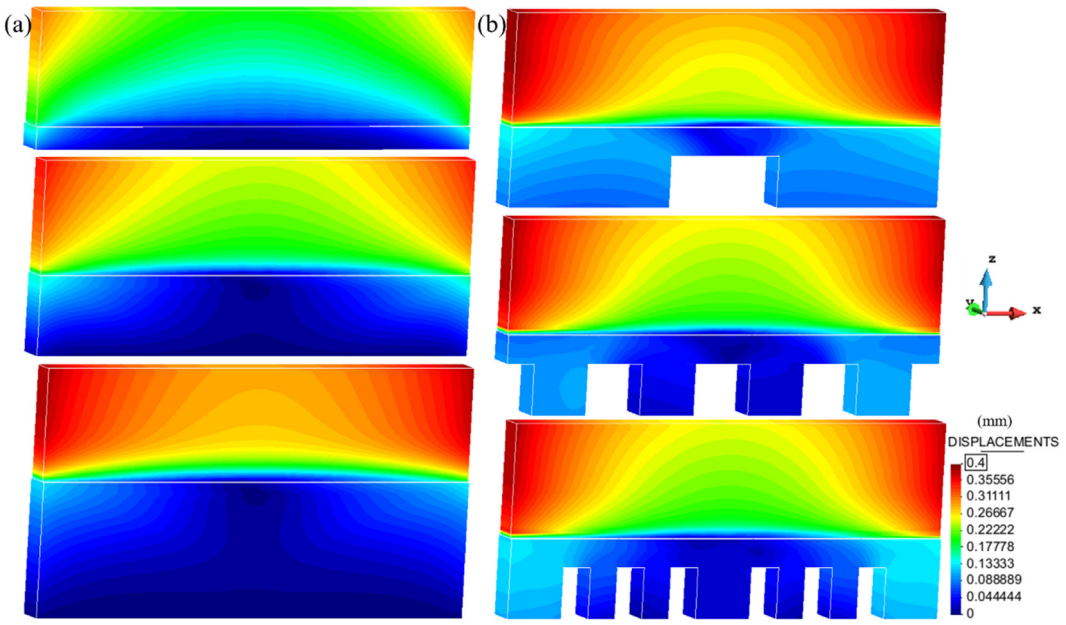


**Fig. 13.** Norm of the displacements of the single-wall according to the different substrates analyzed: (a) solid substrates; (b) hollow substrates.

The workbench is assumed as rigid, so the displacements at the bottom surface of the substrate are fixed as in the actual DED process. Moreover, the size of the substrate is reduced to 80 mm, the same as the single-wall. Therefore, the stress concentrations at both side of the single wall are avoided.

Fig. 12 shows the temperature evolution in the middle point of the top surface of the substrate for the three substrate thicknesses and for the three different hollow substrates. On the one hand, the higher is the substrate, the slower is the heat dissipation from the HAZ to the workbench through the substrate. Hence, the steady state conditions can be reached faster. On the other hand, the average temperature when using the hollow substrates is higher than in the cases of solid substrates. Therefore, the proposed design is helpful to increase the substrate temperature and to reduce the non-steady phase at the beginning of the DED process.

Fig. 13 shows the norm of the displacement field at the end of the DED process, for all the tested substrate structures. As shown in Fig. 13(a), by increasing the height of the solid substrate, the angular distortion of the build is also incremented. Thus, the hot material deposited during the fabrication of the single-wall is no longer able to contract because of the higher constraining of the substrate. However, the increased stiffness reduces the formation of residual stresses, as shown in Fig. 14(a).

A different behavior is appreciated when using the proposed hollow structures. In this case, the distortion is reduced by increasing the number of hollows without compromising the residual stress distribution as shown in Figs. 13(b) and 14(b), respectively.

Fig. 15 shows the predicted residual stresses at the interface between the single-wall and the substrate, for all the analyzed substrates.

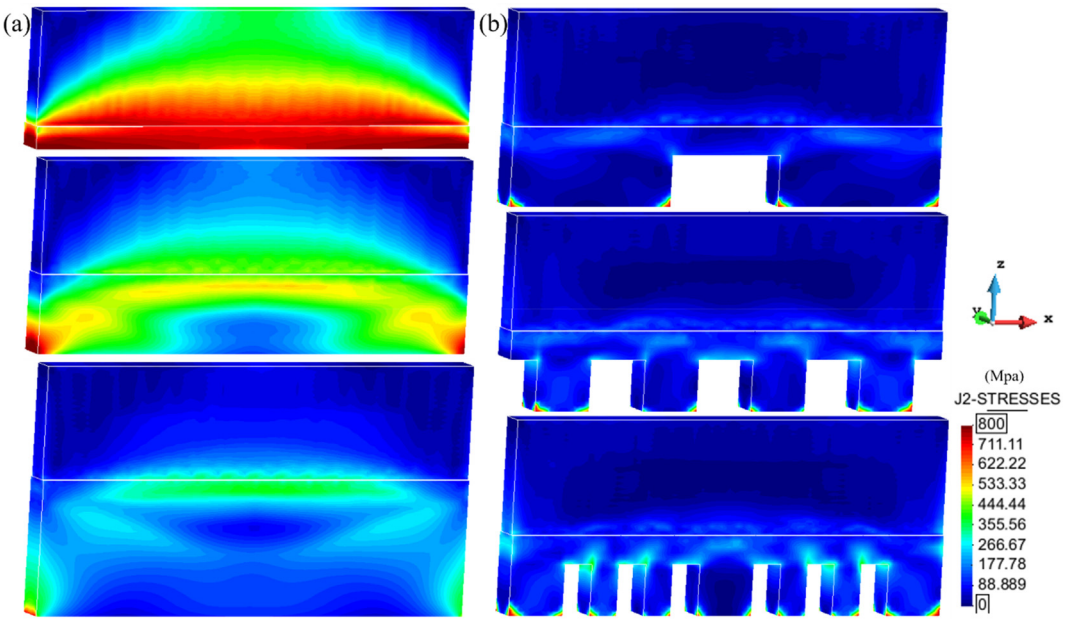


**Fig. 14.** Von Mises residual stress field at the end of the DED process: (a) solid substrates; (b) hollow substrates.

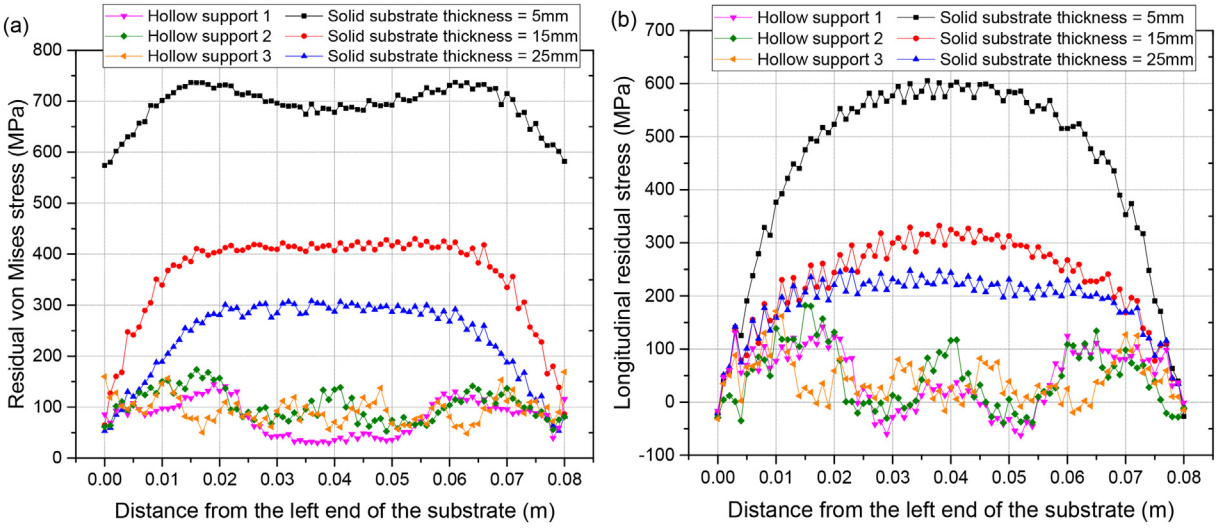


**Fig. 15.** Residual stress distributions on the wall-substrate interface for the different substrate structures: (a) von Mises stresses; (b) longitudinal stresses.

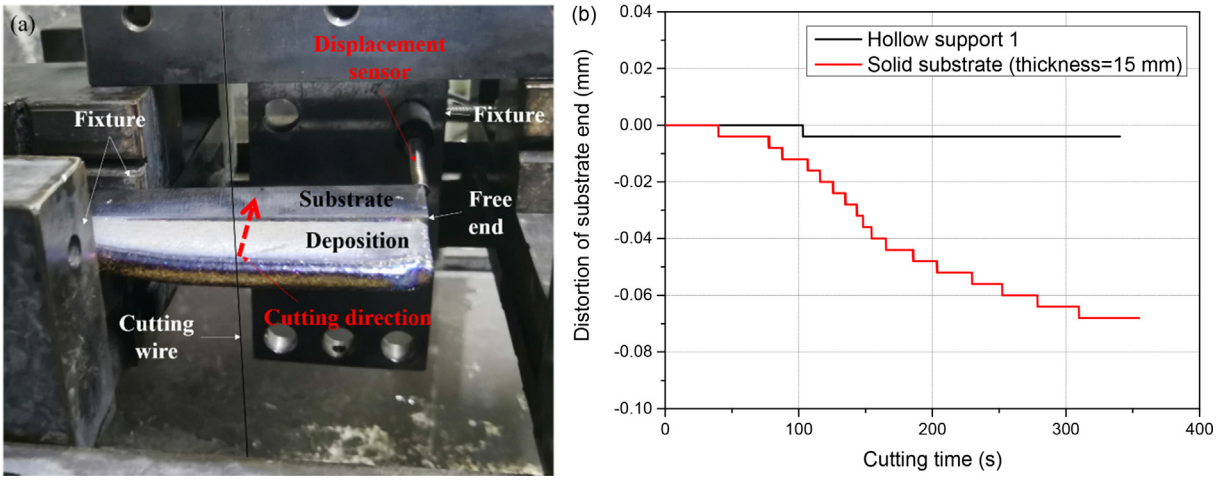


**Fig. 16.** Wire-cutting process: (a) cutting process; (b) evolution of the vertical displacement at the free end of the substrates as a function of the cutting time.

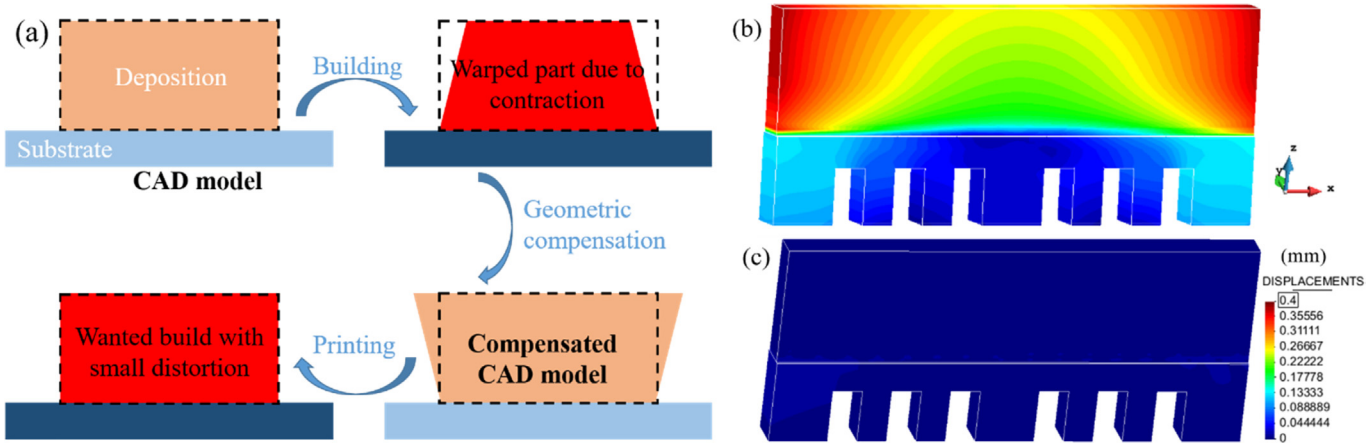


**Fig. 17.** Geometry compensation strategy: (a) required steps for the geometric compensation; (b) single-wall AM analysis without geometric compensation; (c) with geometric compensation.

Both longitudinal and von Mises stresses are mitigated when adopting hollow substrates.

To prove the effective mitigation of the residual stresses, both solid and hollow substrates are removed by wire-cutting, as shown in Fig. 16(a). The evolution of the vertical displacement at the free end of the part is presented in Fig. 16(b) as a function of the cutting time. It can be observed that the stress release induced by the cutting process of the solid substrate generates a pronounced residual distortion of the AM part. Contrarily, removing the hollow substrate only affects marginally the distortion of the single-wall. Therefore, the amount of residual stresses accumulated in the AM part when using the solid substrate is larger than for the hollow substrate.

As shown in Fig. 13, the drawback when reducing the substrate stiffness is the increase of thermal warpage. A possible solution to recover the nominal geometry is using the geometry compensation technique [23,24,42]. Fig. 17(a) summarizes the necessary steps: (1) starting from the nominal geometry, the DED process is simulated to compute the warpage due to the thermal deformation and material shrinkage; (2) this information is used to modify the nominal geometry generating the compensated model; (3) the process simulation is repeated to check if the resulting distortions do not exceed the fabrication tolerances. If this is not the case, steps (2) and (3) are repeated until the desired geometrical accuracy is reached. Fig. 17(b) illustrates the residual part distortion without geometry compensation, at the end of step (1), and at the end of the compensation loop (see Fig. 17(c)). Hence, this strategy can be efficiently used to obtain high precision AM components [42].

## 6. Validation of the substrate design strategy

The validation of the proposed methodology to improve the AM fabrication by DED is carried out using the rectangular-shape geometry shown in Fig. 18(a), used as demonstrator. The AM thermo-mechanical analysis of this component was reported in a previous work [12]. Here, the objective is to investigate three new substrate designs referred to as: solid, rectangular and hollow substrates, respectively. Also in this case, the workbench is not simulated and the bottom surface of all substrates is fixed.

The temperature evolution at point T for all substrates is depicted in Fig. 18(b), while the corresponding MTG ($G_{xx}$) along the scanning direction are shown in Fig. 18(c). As for the single-wall, reducing the mass of the substrate or/and defining a hollow structure induces higher peak and average temperatures of the substrate. Hence, the substrate is forced to heat faster reducing the transient stage. Also in this case, the hollow substrate shows the fastest fall of the MTG (Fig. 18 (c)), indicating the rapid establishment of the quasi-steady stage and a better performance being the preferred design for its industrialization.

Fig. 19 compares the evolution of the longitudinal stress ($\sigma_{xx}$) at the mid-point of the YZ cross-section for all the proposed substrate structures. This figure shows that, also in this case, the maximum longitudinal tensile stresses are produced at the interface between the part and the substrate just after the deposition of the first layer. By increasing the number of layers, the tensile stresses gradually reduce according to the reduction of the MTG (see Fig. 18(c)). Nevertheless, more flexible substrates produce lower tensile stresses in the build. The hollow substrate showed a 62% reduction of the maximum longitudinal tensile stress. Fig. 20 shows both the final distortion of the part (displacements norm) and the residual von Mises stress indicator for the different substrates analyzed. Also for the selected demonstrator, more flexible substrates generate lower residual stresses even if the final distortion can be slightly higher.

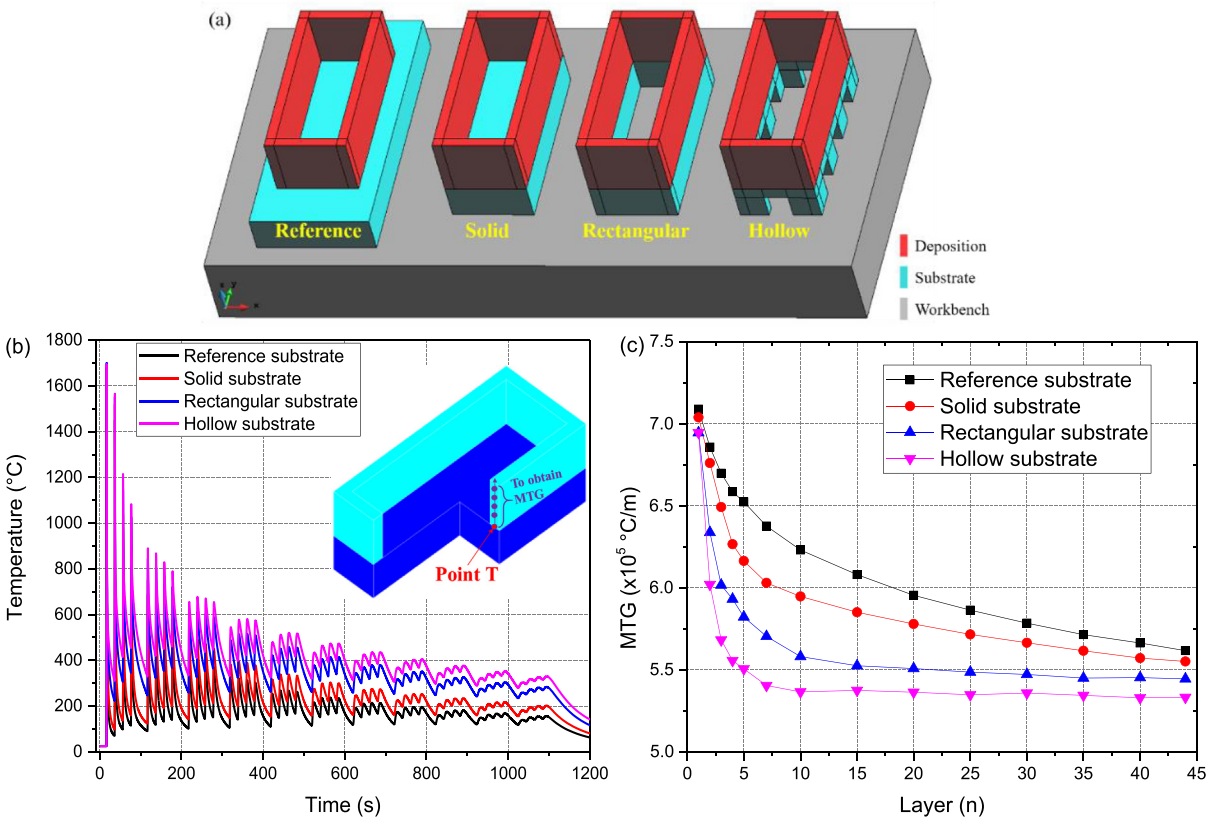


**Fig. 18.** Substrate structure optimization: (a) CAD geometries of the different substrates analyzed; (b) thermal histories at point T; (c) MTG ($G_{xx}$) evolution as a function of the number of deposited layers.

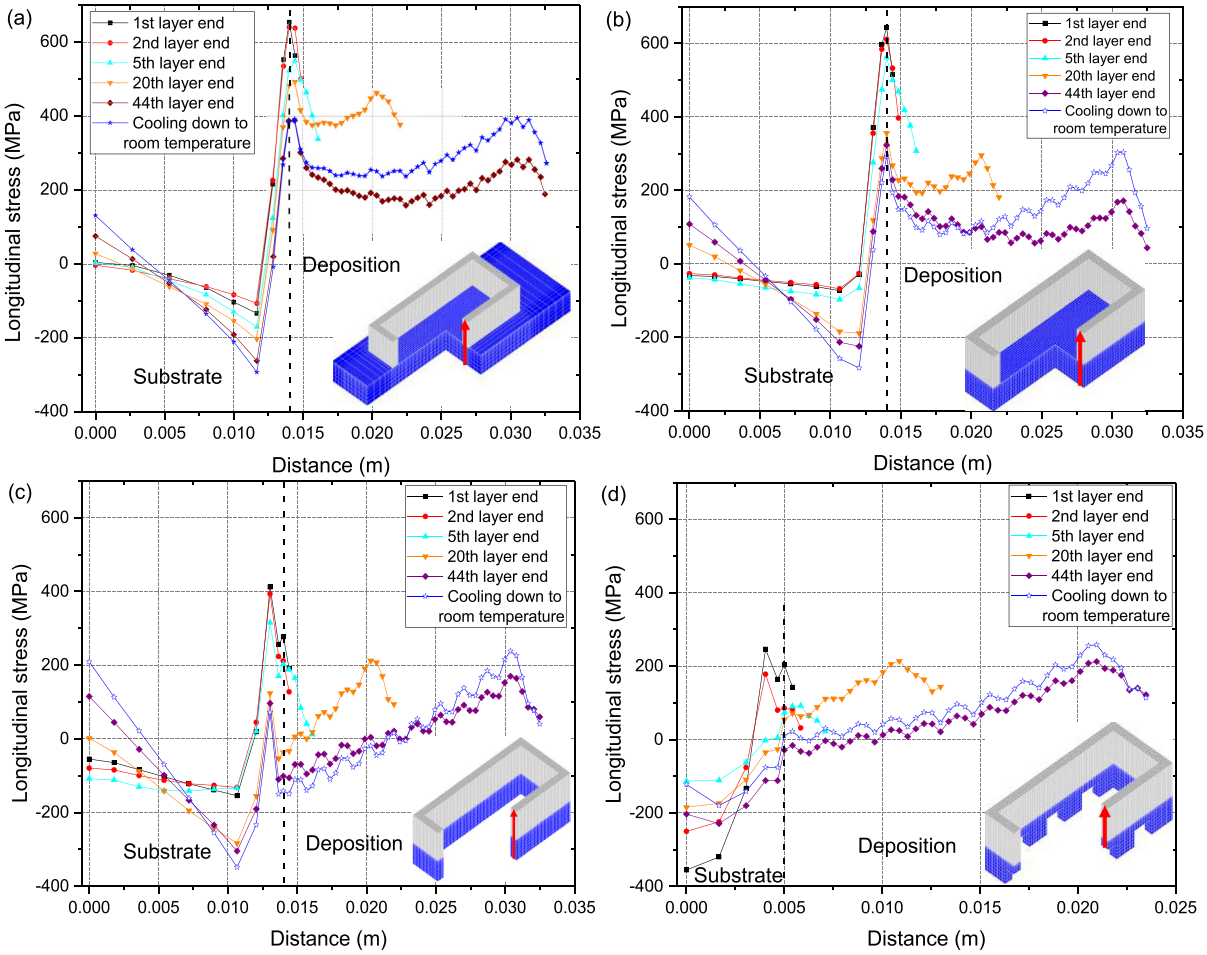


**Fig. 19.** Evolution of the longitudinal stresses ($\sigma_{xx}$) at the mid YZ cross section during the AM process: (a) reference substrate; (b) solid substrate; (c) rectangular substrate; (d) hollow substrate.

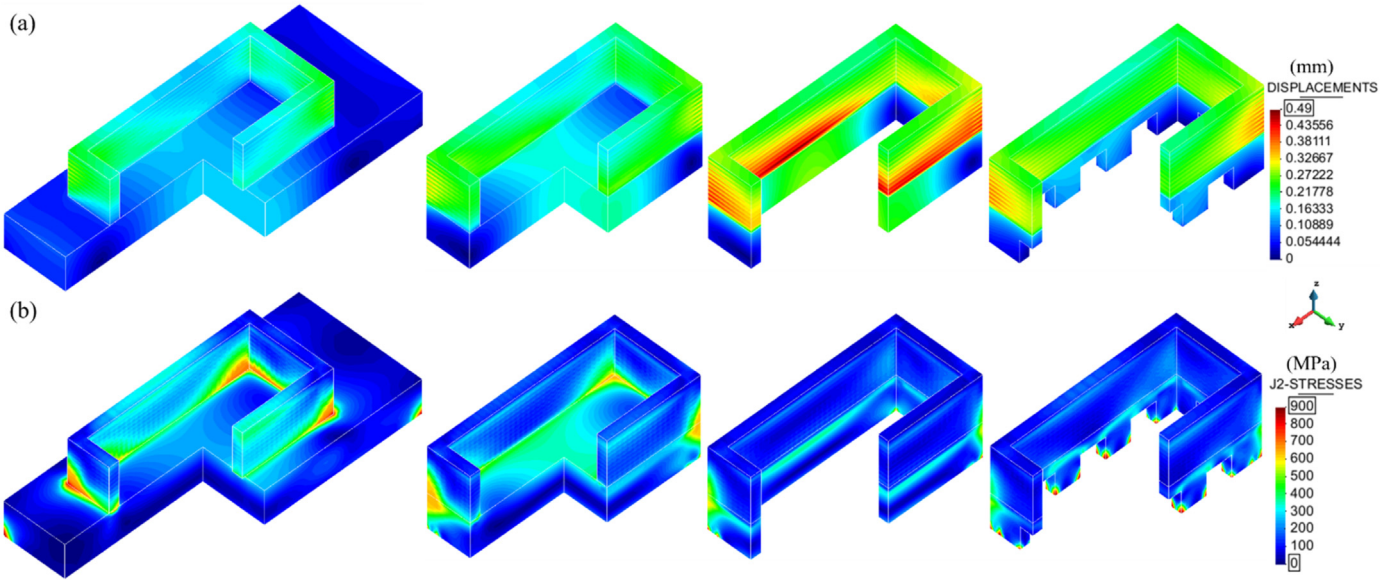


**Fig. 20.** Mechanical responses of the demonstrator: (a) final distortions (displacements norm); (b) residual von Mises stresses.

## 7. Concluding remarks

A 3D thermo-mechanical FE model is calibrated by in-situ experimental measurements using the single-wall structure fabricated by DED processes. This done, the software platform is used to analyse different substrate structures and some fabrication recommendations are drawn:

(1) Most of the residual stresses in DED processes are generated during the deposition of the first layers, when the substrate is still cold and very high temperature gradients develop. When the quasi-steady conditions are reached, much lower residual stresses are generated during the metal deposition.
(2) Rounding off sharp angles is a good practice to reduce the stress concentrations in AM as observed in many other fabrication processes. Moreover, focussing on the size of the substrate, the best option is to consider a substrate conformal to the bottom surface of the AM component, so that possible sharp angles are avoided and the flexibility of the substrate is enhanced.
(3) Reducing the size of the substrate is beneficial to mitigate residual stresses because both the heat flux and the stiffness are reduced, allowing for a faster non-steady stage and a lower mechanical constraining.
(4) Reducing the stiffness of the substrate can increase the final distortion and warpage of the AM-build. The geometric compensation strategy can be employed to recover the nominal geometry at the end of the fabrication.
(5) Hollow substrate structures reduce the transient stage of the DED fabrication. The heat flow through the substrate to the workbench is slowed. Hence, the substrate heats up much faster than in the case of a solid structures.

## Declaration of Competing Interest

The authors declare no conflict of interest.

## Acknowledgements

This research was funded by the National Key Technologies R & D Program (No. 2016YFB1100104) and the Natural Science Foundation of Shaanxi Province of China (Grant No. 2018JM5115). Funding from the Spanish Ministry of Economy and Competitivity (MINECO) under the ADaMANT project: Computational Framework for Additive Manufacturing of Titanium Alloy Components (ref: DPI2017-85998-P), within the Excellency Programme for Knowledge Generation is gratefully acknowledged. CIMNE is recipient of the Severo Ochoa Award of Excellence from MINECO. This work was also funded by the European KYKLOS 4.0 project: An Advanced *Circular and Agile Manufacturing Ecosystem based on rapid reconfigurable manufacturing process and individualized consumer preferences* (No. H2020-DT-2019-1).

## References

[1] D. Herzog, V. Seyda, E. Wycisk, et al., Additive manufacturing of metals[J], Acta Mater. 117 (2016) 371–392.
[2] H. Huang, N. Ma, J. Chen, et al., Toward large-scale simulation of residual stress and distortion in wire and arc additive manufacturing[J], Add. Manufact. 34 (2020) 101248.
[3] X. Lu, X. Lin, M. Chiumenti, et al., In situ measurements and Thermo-mechanical simulation of Ti-6Al-4V laser solid forming processes[J], Int. J. Mech. Sci. 153 (2019) 119–130.
[4] Q. Wang, J. Shi, L. Zhang, et al., Impacts of laser cladding residual stress and material properties of functionally graded layers on titanium alloy sheet[J], Add. Manufact. 35 (2020) 101303.
[5] J.M. Shi, N. Ma, L.X. Zhang, et al., Residual stress and fracture strength of brazed joint of ceramic and titanium alloy with the aid of laser deposited functionally graded material layers[J], J. Manuf. Process. 34 (2018) 495–502.
[6] W. Woo, D.K. Kim, E.J. Kingston, et al., Effect of interlayers and scanning strategies on through-thickness residual stress distributions in additive manufactured ferritic-austenitic steel structure[J], Mater. Sci. Eng. A 744 (2019) 618–629.
[7] K. Ren, Y. Chew, J.Y.H. Fuh, et al., Thermo-mechanical analyses for optimized path planning in laser aided additive manufacturing processes[J], Mater. Des. 162 (2018) 80–93.
[8] Q. Wu, T. Mukherjee, C. Liu, et al., Residual stresses and distortion in the patterned printing of titanium and nickel alloys[J], Add. Manufact. 29 (2019) 100808.
[9] Y. Lee, Y. Bandari, P. Nandwana, et al., Effect of interlayer cooling time, constraint and tool path strategy on deformation of large components made by laser metal deposition with wire[J], Appl. Sci. 9 (23) (2019) 5115.
[10] F. Soffel, D. Eisenbarth, K. Wegener, Minimizing Substrate Distortion in Direct Metal Deposition (DMD) with Optimized Process Parameters and Buildup Strategies[C]// 3rd International Symposium on Additive Manufacturing (ISAM 2019), 2019.
[11] Z. Wang, E. Denlinger, P. Michaleris, et al., Residual stress mapping in Inconel 625 fabricated through additive manufacturing: method for neutron diffraction measurements to validate thermomechanical model predictions[J], Mater. Des. 113 (2017) 169–177.
[12] X. Lu, X. Lin, M. Chiumenti, et al., Residual stress and distortion of rectangular and S-shaped Ti-6Al-4V parts by directed energy deposition: modelling and experimental calibration[J], Add. Manufact. 26 (2019) 166–179.
[13] Q. Yang, P. Zhang, L. Cheng, et al., Finite element modeling and validation of thermomechanical behavior of Ti-6Al-4V in directed energy deposition additive manufacturing[J], Add. Manufact. 12 (2016) 169–177.
[14] A. Grégoire, L. Jakabčin, Taking into account thermal residual stresses in topology optimization of structures built by additive manufacturing[J], Math. Models Methods Appl. Sci. 28 (12) (2018) 2313–2366.
[15] R. Ranjan, Y. Yang, C. Ayas, et al., Controlling local overheating in topology optimization for additive manufacturing[C], Dimensional Accuracy and Surface Finish in Additive Manufacturing, 2017.
[16] T. Mukherjee, V. Manvatkar, A. De, et al., Mitigation of thermal distortion during additive manufacturing[J], Scr. Mater. 127 (2017) 79–83.
[17] H.L. Wei, T. Mukherjee, W. Zhang, et al., Mechanistic models for additive manufacturing of metallic components[J], Prog. Mater. Sci. 100703 (2020).
[18] J. Cao, M.A. Gharghouri, P. Nash, Finite-element analysis and experimental validation of thermal residual stress and distortion in electron beam additive manufactured Ti-6Al-4V build plates[J], J. Mater. Process. Technol. 237 (2016) 409–419.
[19] D.J. Corbin, A.R. Nassar, E.W. Reutzel, et al., Effect of substrate thickness and preheating on the distortion of laser deposited Ti–6Al–4V[J], J. Manuf. Sci. Eng. 140 (6) (2018), 061009.
[20] X. Lu, X. Lin, M. Chiumenti, et al., Finite element analysis and experimental validation of the thermomechanical behavior in laser solid forming of Ti-6Al-4V[J], Add. Manufact. 21 (2018) 30–40.
[21] F. Li, S. Chen, J. Shi, et al., In-process control of distortion in wire and arc additive manufacturing based on a flexible multi-point support fixture[J], Sci. Technol. Weld. Join. 24 (1) (2019) 36–42.
[22] E.R. Denlinger, P. Michaleris, Mitigation of distortion in large additive manufacturing parts[J], Proc. Inst. Mech. Eng. B J. Eng. Manuf. 231 (6) (2017) 983–993.
[23] S. Afazov, A. Okioga, A. Holloway, et al., A methodology for precision additive manufacturing through compensation[J], Precis. Eng. 50 (2017) 269–274.
[24] A. Yaghi, S. Ayvar-Soberanis, S. Moturu, et al., Design against distortion for additive manufacturing[J], Add. Manufact. 27 (2019) 224–235.
[25] J.R. Hönnige, P.A. Colegrove, B. Ahmad, et al., Residual stress and texture control in Ti-6Al-4V wire + arc additively manufactured intersections by stress relief and rolling[J], Mater. Des. 150 (2018) 193–205.
[26] J.R. Hönnige, P.A. Colegrove, S. Ganguly, et al., Control of residual stress and distortion in aluminium wire + arc additive manufacture with rolling[J], Add. Manufact. 22 (2018) 775–783.
[27] C. Baykasoğlu, O. Akyildiz, M. Tunay, et al., A process-microstructure finite element simulation framework for predicting phase transformations and microhardness for directed energy deposition of Ti6Al4V[J], Add. Manufact. 35 (2020) 101252.
[28] C. Baykasoglu, O. Akyildiz, D. Candemir, et al., Predicting microstructure evolution during directed energy deposition additive manufacturing of Ti-6Al-4V[J], J. Manuf. Sci. Eng. 140 (5) (2018), 051003.
[29] F. Calignano, Design optimization of supports for overhanging structures in aluminum and titanium alloys by selective laser melting[J], Mater. Des. 64 (2014) 203–213.
[30] M. Langelaar, Combined optimization of part topology, support structure layout and build orientation for additive manufacturing[J], Struct. Multidiscip. Optim. 57 (5) (2018) 1985–2004.
[31] G. Allaire, B. Bogosel, Optimizing supports for additive manufacturing[J], Struct. Multidiscip. Optim. 58 (6) (2018) 2493–2515.
[32] L. Cheng, X. Liang, J. Bai, et al., On utilizing topology optimization to design support structure to prevent residual stress induced build failure in laser powder bed metal additive manufacturing[J], Add. Manufact. 27 (2019) 290–304.
[33] N. Gardan, A. Schneider, Topological optimization of internal patterns and support in additive manufacturing[J], J. Manuf. Syst. 37 (2015) 417–425.
[34] M. Cervera, C. Agelet de Saracibar, M. Chiumenti, COMET: Coupled mechanical and thermal analysis, Data Input Manual, Version 5.0, Technical Report IT-308, 2002 http://www.cimne.com.
[35] M. Chiumenti, X. Lin, M. Cervera, et al., Numerical simulation and experimental calibration of additive manufacturing by blown powder technology. Part I: thermal analysis[J], Rapid Prototyp. J. 23 (2) (2017) 448–463.

[36] M. Chiumenti, M. Cervera, A. Salmi, et al., Finite element modeling of multi-pass welding and shaped metal deposition processes[J], Comput. Methods Appl. Mech. Eng. 199 (37–40) (2010) 2343–2359.
[37] M. Chiumenti, M. Cervera, N. Dialami, et al., Numerical modeling of the electron beam welding and its experimental validation[J], Finite Elements Analysis Design 121 (2016) 118–133.
[38] Y. Ueda, H. Murakawa, N. Ma, Welding Deformation and Residual Stress Prevention, Elsevier, 2012.
[39] Erik R. Denlinger, P. Michaleris, Effect of stress relaxation on distortion in additive manufacturing process modeling[J], Add. Manufact. 12 (2016) 51–59.
[40] T. Kawaoka, Introduction of the personal pre-post processor GiD[J], Proceed. Design Systems Conf. 12 (2002) 151–153.
[41] V. Fallah, M. Alimardani, S.F. Corbin, et al., Temporal development of melt-pool morphology and clad geometry in laser powder deposition[J], Comput. Mater. Sci. 50 (7) (2011) 2124–2134.
[42] S. Afazov, W.A.D. Denmark, B.L. Toralles, et al., Distortion prediction and compensation in selective laser melting[J], Add. Manufact. 17 (2017) 15–22.

# Residual Stresses Control in Additive Manufacturing

X. Lu, M. Cervera, M. Chiumenti & X. Lin

*Journal of Manufacturing and Materials Processing*

Vol. 5, issue 4, pp. 138, (2021)

https://doi.org/10.3390/jmmp5040138

Journal of
*Manufacturing and Materials Processing*

MDPI

*Article*

# Residual Stresses Control in Additive Manufacturing

**Xufei Lu [1,*], Miguel Cervera [1], Michele Chiumenti [1] and Xin Lin [2]**

[1] International Centre for Numerical Methods in Engineering, Universidad Politécnica de Cataluña, 08034 Barcelona, Spain; miguel.cervera@upc.edu (M.C.); michele.chiumenti@upc.edu (M.C.)
[2] State Key Laboratory of Solidification Processing, Northwestern Polytechnical University, Xi'an 710072, China; xlin@nwpu.edu.cn
* Correspondence: xlu@cimne.upc.edu

**Abstract:** Residual stresses are one of the primary causes for the failure of parts or systems in metal additive manufacturing (AM), since they easily induce crack propagation and structural distortion. Although the formation of residual stresses has been extensively studied, the core factors steering their development in AM have not been completely uncovered. To date, several strategies based on reducing the thermal gradients have been developed to mitigate the manifestation of residual stresses in AM; however, how to choose the optimal processing plan is still unclear for AM designers. In this regard, the concept of the yield temperature, related to the thermal deformation and the mechanical constraint, plays a crucial role for controlling the residual stresses, but it has not been duly investigated, and the corresponding approach to control stresses is also yet lacking. To undertake such study, a three-bar model is firstly used to illustrate the formation mechanism of the residual stress and its key causes. Next, an experimentally calibrated thermomechanical finite element model is used to analyze the sensitivity of the residual stresses to the scan pattern, preheating, energy density, and the part geometry and size, as well as the substrate constraints. Based on the numerical results obtained from this analysis, recommendations on how to minimize the residual stresses during the AM process are provided.

**Keywords:** additive manufacturing; residual stress control; thermomechanical simulation; strategical assessment



**Citation:** Lu, X.; Cervera, M.; Chiumenti, M.; Lin, X. Residual Stresses Control in Additive Manufacturing. *J. Manuf. Mater. Process.* **2021**, *5*, 138. https://doi.org/10.3390/jmmp5040138

Academic Editor: Steven Y. Liang

Received: 25 November 2021
Accepted: 14 December 2021
Published: 16 December 2021



## 1. Introduction

Metal additive manufacturing (AM) is an advanced processing technology of increasing industrial significance due to its unique advantages and its feasibility to fabricate complex structures with high-performance [1,2]. During the AM process, the material experiences repeated spatially variable heating and cooling cycles. Locally, non-uniform thermal expansion and contraction happen at the vicinity of the melt pool, where high temperature gradients arise during the printing process and lead to thermal deformations and residual stresses, these being detrimental for the geometrical accuracy and the final mechanical properties of the AM components [3,4].

Due to the large number of variables involved in the AM process, the combination of experiments and numerical simulations is quite useful to study the thermo-mechanical behavior, duly accounting for the limitations of experimental measurements and the mandatory validation of the computational models [5–9]. In this line, Lu et al. [6,7] studied the residual stresses and distortion of Ti-6Al-4V single-wall and rectangular parts using a finite element (FE) model calibrated by establishing an in situ system with integrated infrared imaging sensor, thermocouples, digital image correlation, and displacement sensor, which can measure the detailed temperature and distortion of Ti-6Al-4V parts manufactured by directed energy deposition (DED). Cao et al. [8] developed an efficient FE model by combining the dynamic mesh method and the equivalent boundary condition to accelerate the thermo-mechanical simulations of laser powder bed fusion (LPBF).

Several studies have been performed on the optimization of the process to reduce the residual stresses and distortion. It is found that optimizing the deposition sequence or the process parameters [5,10–12] and preheating the substrate before the AM [3,9] can minimize the residual stresses and warpage. Nevertheless, such strategies based on managing the thermal gradients in metal AM are limited, due to the use of a high-energy beam as the heat source. For example, preheating the substrate or build chamber may increase the risk of microstructure coarsening; the optimization of path and process parameters is relatively complex, and it needs to give consideration to the microstructural evolution. Additionally, the use of assistant tools, such as in the rolling technique [13] and laser shock peening [14], during AM or the post-processing stress relieving (by heat or mechanical treatments) [15,16] favor stress reduction, but increase both manufacturing time and cost. Although these strategies have been proposed, their combined necessary comparison and evaluation for optimizing the AM process when printing complex components must be further investigated.

To date, the formation of residual stresses is mainly attributed in the existing literature to the "temperature gradient mechanism" [17–19]; little attention has been paid to the "yield temperature", another crucial factor related to the mechanical constraint. As known, free temperature deformation causes no stress, even if the thermal gradient is important. Based on this concept, the optimization of the substrate restraints should be addressed to reduce the stress development during the metal AM processes, as a new control route, parallel to the conventional thermal gradient management.

Thereby, the objective of this work is to uncover the key mechanisms that drive the residual stresses in AM and to make a comprehensive assessment on their control strategies. To this end, a simple three-bar model used in welding is firstly employed to illustrate the two core factors, namely, the thermal gradient and the yield temperature, as responsible for the emergence of the residual stresses in AM. Based on this new appreciation, the sensitivity of the stress development to the scan pattern, preheating, the part geometry and size, and the mechanical constraint of the substrate is studied using a 3D coupled thermo-mechanical FE model for AM. Finally, some recommendations for fabricating high-quality AM parts are given.

## 2. Experimental Setup

A 40-layer Ti-6Al-4V block ($125 \times 35 \times 20$ mm$^3$) was deposited by DED on an annealed Ti-6Al-4V substrate ($200 \times 100 \times 25$ mm$^3$) clamped as a cantilever, as shown in Figure 1a. The laser-based DED machine employed includes a semiconductor laser diode with a maximum output power of 6 kW, a DPSF-2 high-accuracy powder feeder, a five-axis numerical control robot and a hermetic processing chamber filled with argon. Before DED, the Ti-6Al-4V powders with a diameter of between 53–325 µm were dried in a vacuum oven at 130 °C for 2 h.

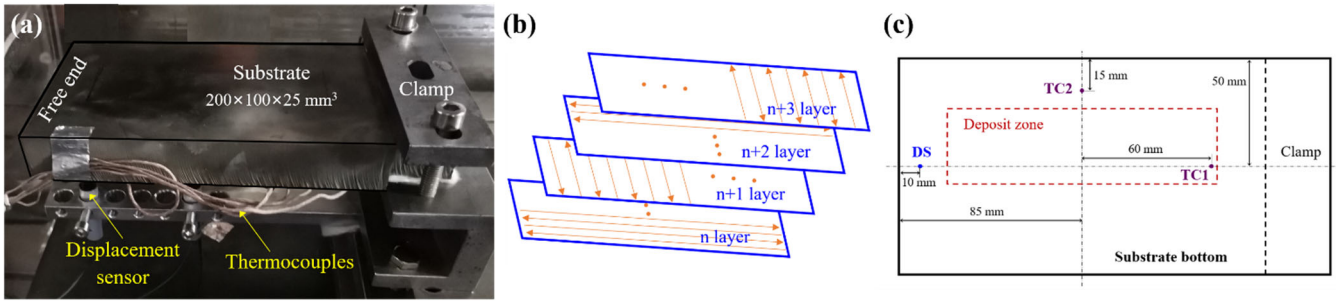


**Figure 1.** DED process: (**a**) in situ experimental set-up; (**b**) scanning path used; (**c**) locations of two thermocouples (TC1-TC2) and one displacement sensor (DS) at the bottom surface of the substrate.

The process parameters are: a laser power of 2 kW, a scan speed of 15.0 mm/s, a laser beam diameter of 5.0 mm, and an up-lift height of 0.5 mm; an alternating longitudinal-

transverse printing pattern is used, as shown in Figure 1b. During the DED process, two *Omega GG-K-30* thermocouples and one *WXXY PM11-R1-20L* displacement sensor are used to measure the temperature and the vertical displacement of the bottom of the substrate without preheating, as shown in Figure 1c.

## 3. Numerical Simulation

### *3.1. Thermomechanical Analysis for AM*

In this work, an in-house coupled thermo-mechanical FE software, *COMET* [20,21], is utilized to perform the mechanical analyses. For each time step, the thermal analysis is performed firstly, and then the computed temperature field is used to solve the stress problem.

The energy balance equation for the transient thermal analysis is:

$$\dot{H} = -\nabla \cdot \mathbf{q} + \dot{Q}, \tag{1}$$

where $\dot{H}$ is the enthalpy rate, $\dot{Q}$ is the heat source, and $\mathbf{q}$ is the heat flux, defined by Fourier's law:

$$\mathbf{q} = -k\nabla T, \tag{2}$$

where $k$ is the thermal conductivity, and $\nabla T$ is the temperature gradient.

The convective heat dissipation is computed by Newton's law:

$$q_{conv} = h_{conv}(T - T_{am}), \tag{3}$$

where $h_{conv}$ is the heat convective coefficient, $T$ is the component temperature, and $T_{am}$ is the ambient temperature.

The heat loss by radiation, $q_{rad}$, is defined by Stefan–Boltzmann's law:

$$q_{rad} = \varepsilon_{rad}\sigma_{rad}\left(T^4 - T_{am}^4\right), \tag{4}$$

where $\varepsilon_{rad}$ is the surface emissivity, and $\sigma_{rad}$ is the Stefan–Boltzmann constant.

The balance of momentum equation for the stress analysis is:

$$\nabla \cdot \mathbf{s} + \nabla p + \mathbf{b} = 0 \tag{5}$$

$$\left(\nabla \cdot \mathbf{u} - e^T\right) - \frac{p}{K} = 0, \tag{6}$$

where the Cauchy stress tensor $\boldsymbol{\sigma}$ is split into its deviatoric and spherical parts, $\mathbf{s}$ and $p$, respectively, as

$$\boldsymbol{\sigma} = p\boldsymbol{I} + \mathbf{s}(\mathbf{u}), \tag{7}$$

$\mathbf{b}$ is the body force, $\mathbf{u}$ is the displacement, $K$ is the bulk modulus, and $e^T$ is the thermal deformation, defined as:

$$e^T(T, f_S) = \alpha(T - T_0) + \beta f_S, \tag{8}$$

where $f_S$ is the solid fraction, $T_0$ is the initial temperature, and $\alpha$ and $\beta$ are the thermal expansion and shrinkage coefficients, respectively.

In this work, a *J2*-thermo-elasto-visco-plastic model is utilized in the solid phase, corresponding to the temperatures from $T_{am}$ to the annealing temperature, $T_{anneal}$. All the material properties are supposed to be temperature dependent. The von Mises yield surface is expressed as:

$$\Phi(\mathbf{s}, q_h, T) = \|\mathbf{s}\| - \sqrt{\frac{2}{3}}\left[\sigma_y(T) - q_h\right], \tag{9}$$

where $\sigma_y$ is the yield stress, and $q_h$ is the stress-like variable controlling the hardening, defined as:

$$q_h(\xi, T) = -\left[\sigma_\infty(T) - \sigma_y(T)\right]\left[1 - e^{-\delta(T)\xi}\right] - h(T)\xi, \tag{10}$$

where $\xi$ is the isotropic strain-hardening variable, $\sigma_\infty$ is the saturation flow stress, and the parameters $h$ and $\delta$ are used to model the linear and exponential hardening laws, respectively. The deviatoric counterpart of Cauchy's stress tensor is defined as:

$$\mathbf{s} = 2G(\mathbf{e} - \mathbf{e}^{vp}), \tag{11}$$

where $G$ is the shear modulus, $\mathbf{e}$ is the total (deviatoric) strain obtained from the total strain tensor $\boldsymbol{\varepsilon}(\mathbf{u}) = \nabla^{sym}(\mathbf{u})$, and $\mathbf{e}^{vp}$ is the visco-plastic strain. Based on the principle of maximum plastic dissipation, the evolutions of both the visco-plastic strain tensor and the isotropic strain-hardening variable are expressed as:

$$\dot{\mathbf{e}}^{vp} = \dot{\gamma}^{vp}\frac{\partial\Phi(\mathbf{s}, q_h)}{\partial\mathbf{s}} = \dot{\gamma}^{vp}\frac{\mathbf{s}}{\|\mathbf{s}\|} = \dot{\gamma}^{vp}\mathbf{n} \tag{12}$$

$$\dot{\xi} = \dot{\gamma}^{vp}\frac{\partial\Phi(\mathbf{s}, q_h)}{\partial q_h} = \sqrt{\frac{2}{3}}\dot{\gamma}^{vp}, \tag{13}$$

where $\mathbf{n}$ stands for the normal vector to the yield surface, and $\dot{\gamma}^{vp}$ is the visco-plastic multiplier, defined as:

$$\dot{\gamma}^{vp} = \left\langle\frac{\partial\Phi(\mathbf{s}, q_h)}{\eta}\right\rangle^{\frac{1}{m}}, \tag{14}$$

where $m$ is the rate sensitivity and $\eta$ is plastic viscosity.

Note that as $T \to T_{anneal}$, the yield stress tends to null. Hence, the deviatoric Cauchy stress is reduced to:

$$\mathbf{s} = \eta\left(\dot{\gamma}^{vp}\right)^m\mathbf{n} = \eta_{eff}\dot{\mathbf{e}}^{vp}, \tag{15}$$

where $\eta_{eff} = \eta\left(\dot{\gamma}^{vp}\right)^{m-1}$ stands for the effective viscosity. Hereby, the materials are characterized by a purely viscous law when $T > T_{anneal}$. A non-Newtonian behavior with $m > 1$ is used for the mushy phase ($T_{anneal} < T < T_{melt}$), while a Newtonian law, $m = 1$, features the liquid phase ($T > T_{melt}$). The details of this model for AM simulation are given in previous works [22–24].

### 3.2. FE Modelling of AM

To model the printing process, a time-marching scheme, featured by a time step, $\Delta t = t^{n+1} - t^n$, is used, allowing for the time discretization. Hence, the melting pool can move according to the deposition path from the current position at time $t^n$ to that at time $t^{n+1}$. In this interval, the elements corresponding to the melting pool are heated and, at the same time, the feeding powders conform the metal deposition.

Thereby, the simulation software parses the same file (CLI format) following the real printing path as used to inform the 3D printer. The *birth-and-death-element* technique is utilized to activate the elements belonging to the new deposit layer. Thus, the simulated strategy for the building process requires an ad hoc procedure to classify the elements into: activated, active, and inactive element. At each time step, the elements corresponding to the melting pool (active) and to the deposit layers (activated) are sought by an octree-based searching algorithm. Both the active and activated elements are included in the current computational domain, but the inactive ones are neither assembled nor computed.

Figure 2 shows the different AM geometries and the corresponding FE meshes. The geometry in Figure 2a corresponds to the in situ experimental work-piece, while Figure 2b,c depict the two four-layer blocks with the different geometries: rectangular and square shapes, respectively. The mesh size is $1\times1\times0.5$ mm$^3$ for the deposit, while it is larger for the substrate, increasing with the distance from the printing region. The temperature-

dependent mechanical and thermal properties of Ti-6Al-4V, used for both the build and the substrate, are from references [25,26].

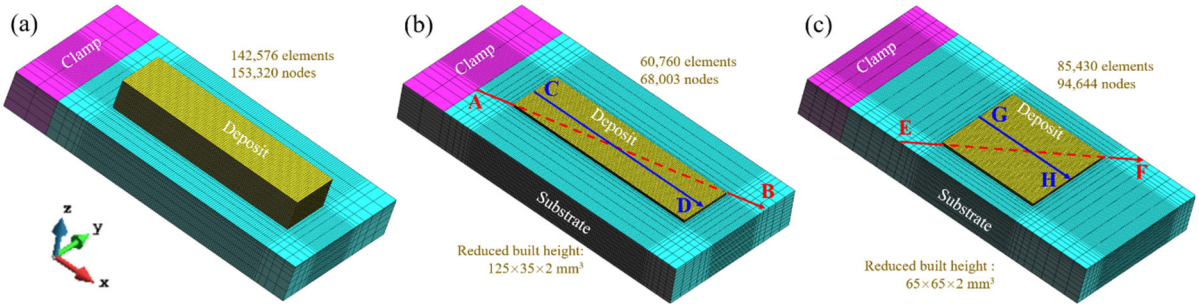


**Figure 2.** FE mesh models: (**a**) 40-layer rectangular block; (**b**) 4-layer rectangular block; (**c**) 4-layer square block. The lines AB and EF at the build-substrate interface are used to analyze the residual stresses while the lines CD and GH at the deposit top are used to analyze the displacement of DED parts.

### *3.3. Model Calibration*

Prior to studying the sensitivity of the residual stresses to the AM variables, the thermo-mechanical model needs to be calibrated to ensure its prediction accuracy. Figure 3 compares the measured and calculated thermo-mechanical results of the 40-layer block. Note that the agreement between the simulation and the experiment is remarkable, as reported in reference [20]. The fluctuations in the plots are due to the use of the alternating longitudinal-transverse scan path (Figure 1b) in the DED process. The differences between the numerical and experimental results are attributed to the simplifications of the thermal boundary conditions in the building process. For instance, the non-uniform gas flow inside the processing chamber adopted to avoid oxidation during DED process is not modeled.

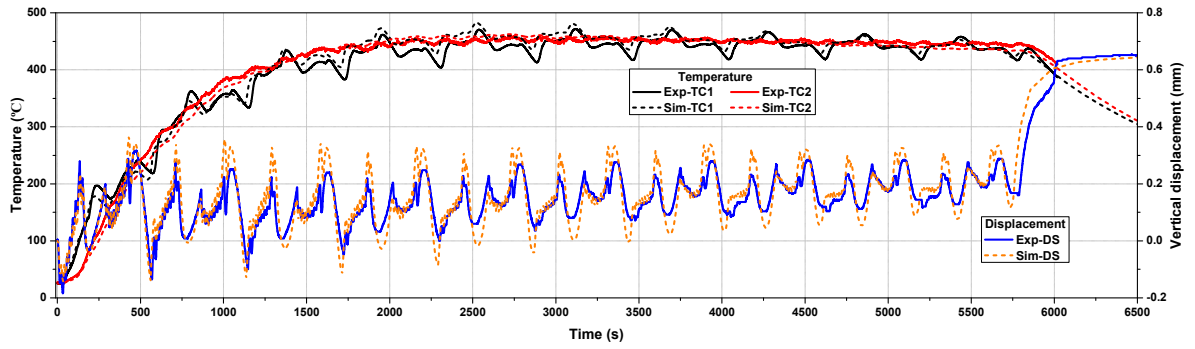


**Figure 3.** Comparison between simulated and measured thermo-mechanical results of the block.

The thermal boundary conditions used for the simulation are: a laser efficiency of 0.37, a heat convection coefficient of 5 W/(m$^2$·°C), a heat emissivity of 0.45, and an ambient temperature of 25·°C.

This successful model calibration illustrates that the FE software is a powerful pool to predict the AM process. Thereby, the software can be employed to study the effect of different AM variables in order to optimize the fabrication process.

## 4. Residual Stresses and Distortions

First, the generation of residual stresses and their key factors are analyzed based on a simple three-bar model. Next, the effect of the scan pattern, the preheating, the energy density, the part geometry, and the mechanical constraint of the substrate on the mechanical responses during the AM process are studied to identify the optimal strategy to mitigate residual stress and distortion.

### 4.1. Key Factors for the Formation of Residual Stresses in AM

From the viewpoint of the mechanical response, the AM process is similar to welding due to the use of a high energy beam as the input heat in both cases, as shown in Figure 4a,b. In welding, a three-bar model [27] is employed to demonstrate the formation of residual stresses, as shown in Figure 4c. The three bars are one central AM-bar and two lateral base-bars of equal lengths, and their cross-sectional areas are $S_{AM}$ and $S_{base}/2$, respectively. The left end of all three bars is fixed, while the right end is bound with a movable rigid link. For simplicity, the material of the three-bars is assumed to be elastic-perfectly plastic under loading, with a temperature-independent Young's modulus $E$, a thermal expansion coefficient $\alpha$, and a yield stress $\sigma_Y$. As thermal straining depends on incremental temperature, the base-bar temperature is set at 0 °C for simplicity. When heating the AM-bar, its thermomechanical response is subjected to the maximum heating temperature $T_{max}$ (points $A$, $B$, or $D$), as shown in Figure 4d. Figure 4e lists the residual stresses in the AM-bar for different heating processes; the detailed deduction can be found in reference [27]. Here, $T_Y$ is the yield temperature, which is defined as the temperature that causes the material yielding in the AM-bar fixed at both ends either by heating or cooling, and expressed as:

$$T_Y = \left(\frac{S_{AM}}{S_{base}} + 1\right)\frac{\sigma_Y}{\alpha E} = m\frac{\sigma_Y}{\alpha E}, \tag{16}$$

where $m$ represents the degree of mechanical restraint from the base-bars. Usually, $m$ is unchanged in welding, allowing for the fixed geometry and size of the given weldments (see Figure 4a), but this is not the case for AM, because the substrate size can be chosen before printing a component (see Figure 4b).

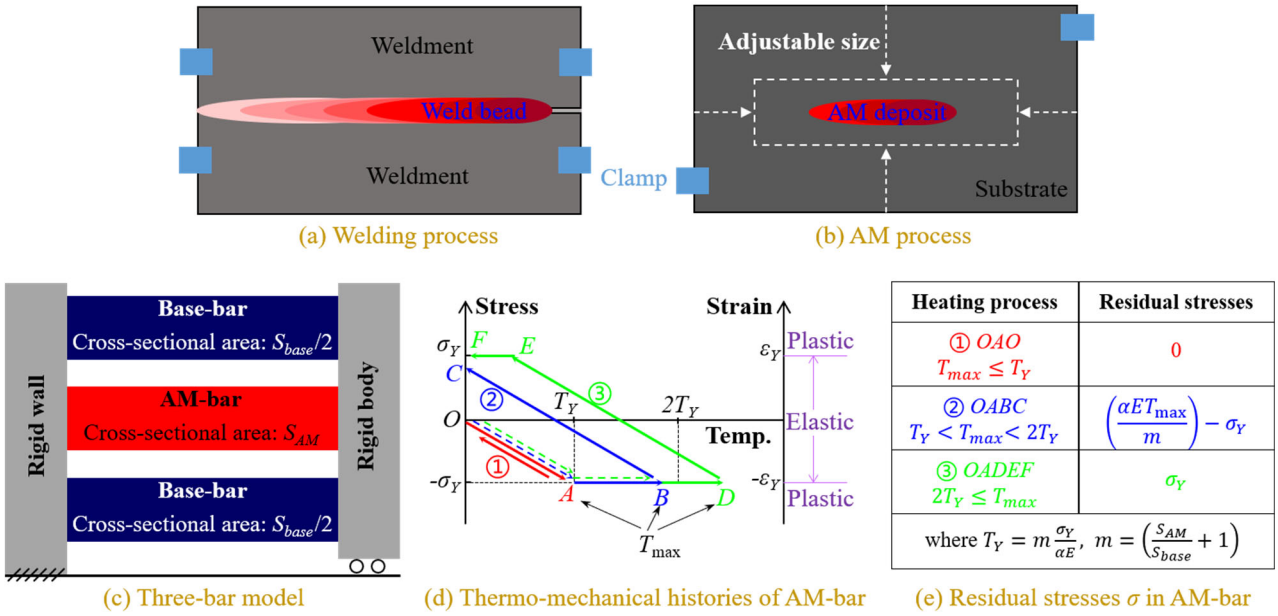


**Figure 4.** The formation of residual stresses in welding and AM processes.

Based on this three-bar model, two key factors are identified as responsible for the development of residual stresses in AM.

The first one is the maximum temperature difference (MTD) between the AM-bar and the base-bar during the thermal cycling. As the base-bar temperature is 0 °C, MTD is equal to the maximum heating temperature $T_{max}$ reached in the AM-bar. As known, MTD corresponds to the maximum temperature gradient (MTG) around the melt pool during the printing process. It can be seen from Figure 4d that the smaller the $T_{max}$, the smaller the developed residual stresses.

The second factor is the yield temperature, $T_Y$, which is very important but not commonly considered in the past. By reducing $S_{base}$, $T_Y$ is increased, and this favors the reduction in the residual stresses by reducing the formation of plastic strain (see stages $\rightarrow\rightarrow$ in Figure 4d). In addition, the slope of the line $OA$ in elasticity, $|k_{OA}| = \frac{\alpha E}{m}$, which determines the range of the elastic behavior, is also a function of $m$.

### 4.2. Effect of the Scan Pattern

In this section, four different scan patterns are chosen to investigate their effect on the residual stress and distortion: 90° alternating scan, outer-inner scan, island scan, and S scan proposed in [28]; they are shown in Figure 5a.

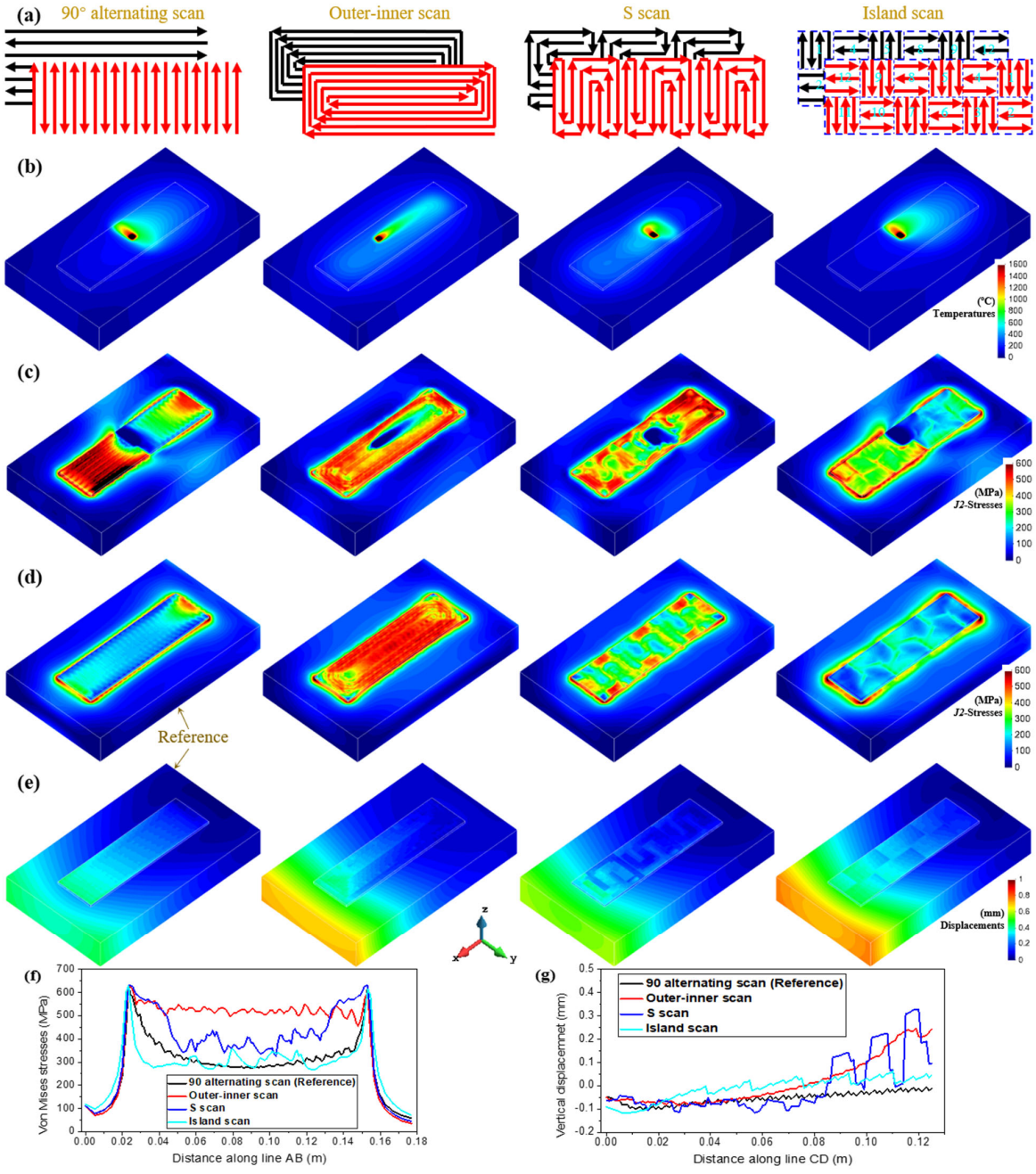


**Figure 5.** Rectangular block: (**a**) scan patterns; (**b**) temperature and (**c**) von Mises stress during the deposition of the 2nd layer; (**d**) residual stresses; (**e**) final distortions (displacements norm); (**f**) residual von Mises stresses along the AB line at the baseplate top; (**g**) final vertical displacements along the CD line at the deposit top.

Figure 5b,c show the computed temperature and the corresponding stress fields when depositing the second layer, respectively. Note that, for the 90° alternating scan, the large residual stress produced after the 1st layer is significantly alleviated during the printing of the second layer, because using the shorter scan path increases the heat concentration, favoring the MTG reduction and stress relaxation. Likewise, the island pattern with the shorter scan line yields the lowest stress level in the four cases. Contrariwise, high stresses appear in the deposit manufactured by the outer–inner scan (covering many long scan lines), which increases the nonuniformity of the temperature distribution (see Figure 5b). The S-pattern presents a slight reduction in the stresses due to its shorter scan line.

Figure 5d,f show the contour-fills of von Mises residual stresses and the stress distributions at the build–substrate interface for the different building strategies. It can be seen that the 90° alternating and island patterns yield the smallest residual stresses, whereas the outer-inner scan displays a conspicuous stress accumulation. Although the S-pattern favors stress mitigation, its effect is limited.

Figure 5e,g show the final distortion contour-fills and the vertical displacement distributions on the built top for the different scan patterns. The 90° alternating and island scans produce the smallest vertical displacement due to their shorter scan line. The outer–inner and S scans lead to a noticeable longitudinal bending of the deposit and an undulant displacement distribution, respectively, thus reducing the geometrical precision of the parts.

Although optimizing the printing path can minimize MTG and the residual stresses in the inner of the deposit by uniformizing the temperature distribution during AM process, it fails to alleviate the stress concentrations (see Figure 5d) at the built basement where the highest MTG occurs with the strongest mechanical constraint.

### *4.3. Influence of Preheating, Deposit Height and Energy Density*

Usually, preheating the substrate before AM is a very efficient method to reduce the MTG induced by the printing process. Here, two different preheating conditions are considered: (i) a 500 °C preheating temperature for the whole substrate and (ii) using the transverse scan to preheat the deposit surface of the substrate, respectively. Figure 6a,b show the corresponding mechanical responses of the four-layer rectangular block. Note that, compared with the reference with no preheating (see Figure 5), the laser preheating fails to refrain the development of the stresses, while preheating the whole baseplate achieves a pronounced reduction in the residual stresses (see Figure 6g). Regrettably, a high preheating temperature easily causes microstructural coarsening and yields poor mechanical properties [29]. Additionally, no obvious difference is found in the part displacements for the different preheating conditions (see Figures 5g and 6h).

The deposited height of the AM part also affects the residual stresses, allowing for the potential intrinsic heat treatment (IHT) effect on the stress relaxation as the printing process extends [13]. Figure 6c,d present the contour-fills of the residual stresses and deformations of the rectangular blocks with an increased built height: 4 mm (8-layer) and 6 mm (12-layer), respectively. Apparently, the inner residual stresses are gradually mitigated as the printing height increases, due to IHT and reduced MTG. However, stress concentrations still hold at the corner of the builds. The part distortions are barely changed with the built height.

As is known, the laser energy density can significantly influence the magnitude of the MTG during the AM process. Thereby, its effect on the mechanical behavior of AM components is examined next. Figure 6e,f show the predicted mechanical results for the low and high energy densities, $ED$, respectively. Observe that increasing the $ED$ favors stress minimization but leads to a larger part warpage. The reason for this is that a higher $ED$ tends to yield larger MTG and plastic deformation; it can also promote stress relief by ITH if the localized heat is sufficiently accumulated (see Figure 5c), especially for AM Ti-6Al-4V [30] or low-temperature transformation alloys [31], in which their solid-state phase-transformations can help stress relaxation.

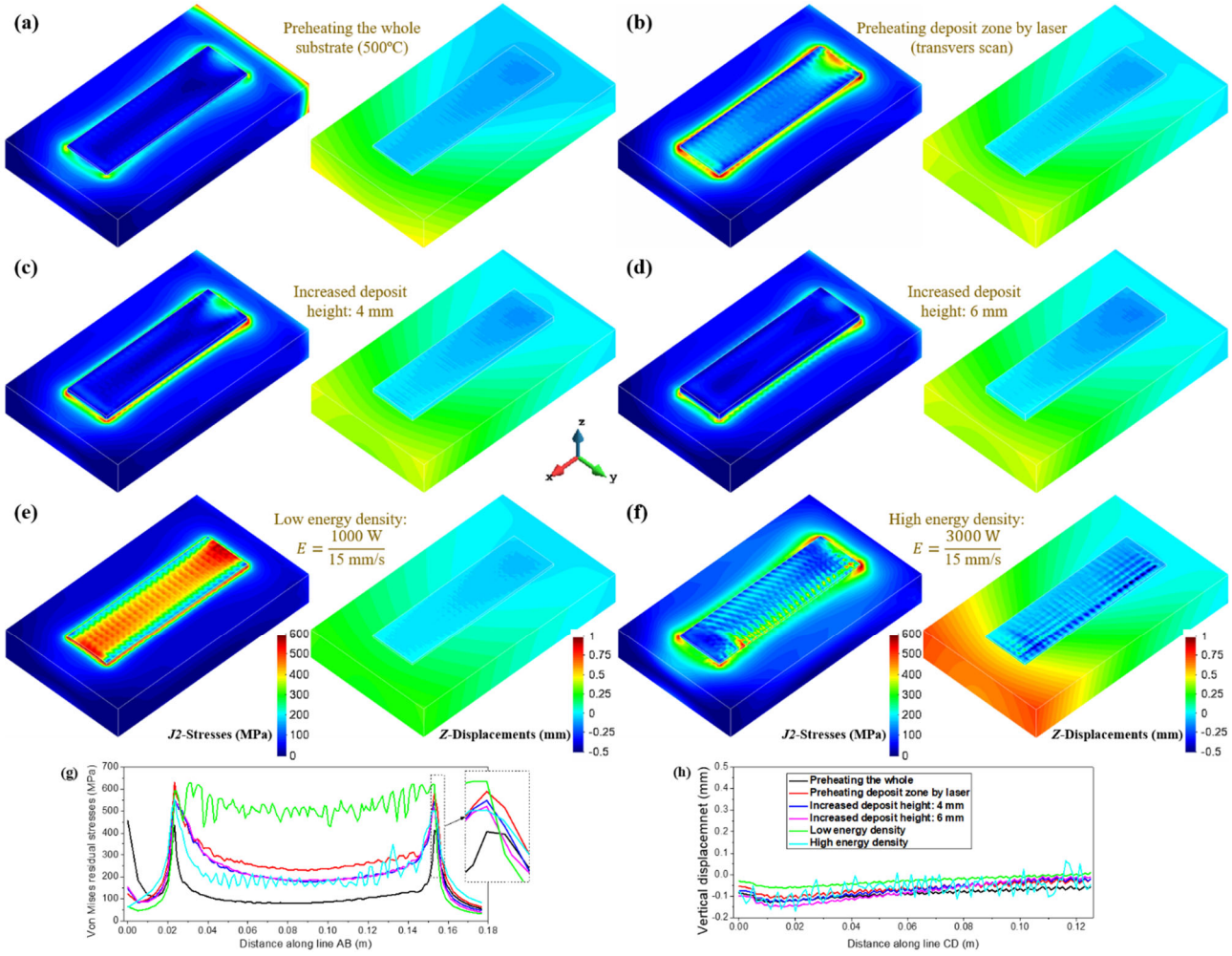


**Figure 6.** Contour-fills of residual von Mises stresses and the vertical displacements for different AM processes: preheating (**a**) the whole substrate to 500 °C and (**b**) the deposit region on the substrate surface by laser (transverse scan); increasing the deposit height to (**c**) 4 mm and (**d**) 6 mm, respectively; using the (**e**) lower and (**f**) higher energy to fabricate AM block, respectively; (**g**) residual von Mises stresses along the AB line at the substrate top; (**h**) vertical displacements along the CD line at the deposit top.

### *4.4. Effect of the Substrate Stiffness and the Part Geometry*

While the residual stresses in AM can be reduced using the above approaches focusing on reducing the MTG, they have no effect on preventing stress concentrations (see Figures 5d and 6). To address this problem, it is possible to prevent the residual stress initiation by increasing $T_Y$ (reducing the substrate restraint) from the purely mechanical point of view (see Figure 4). Thereby, the sensitivity of the mechanical constraints of the substrate on residual stresses is evaluated by simulating the four-layer square blocks fabricated on the same sized substrates but with different cut settings, as shown in Figure 7a.

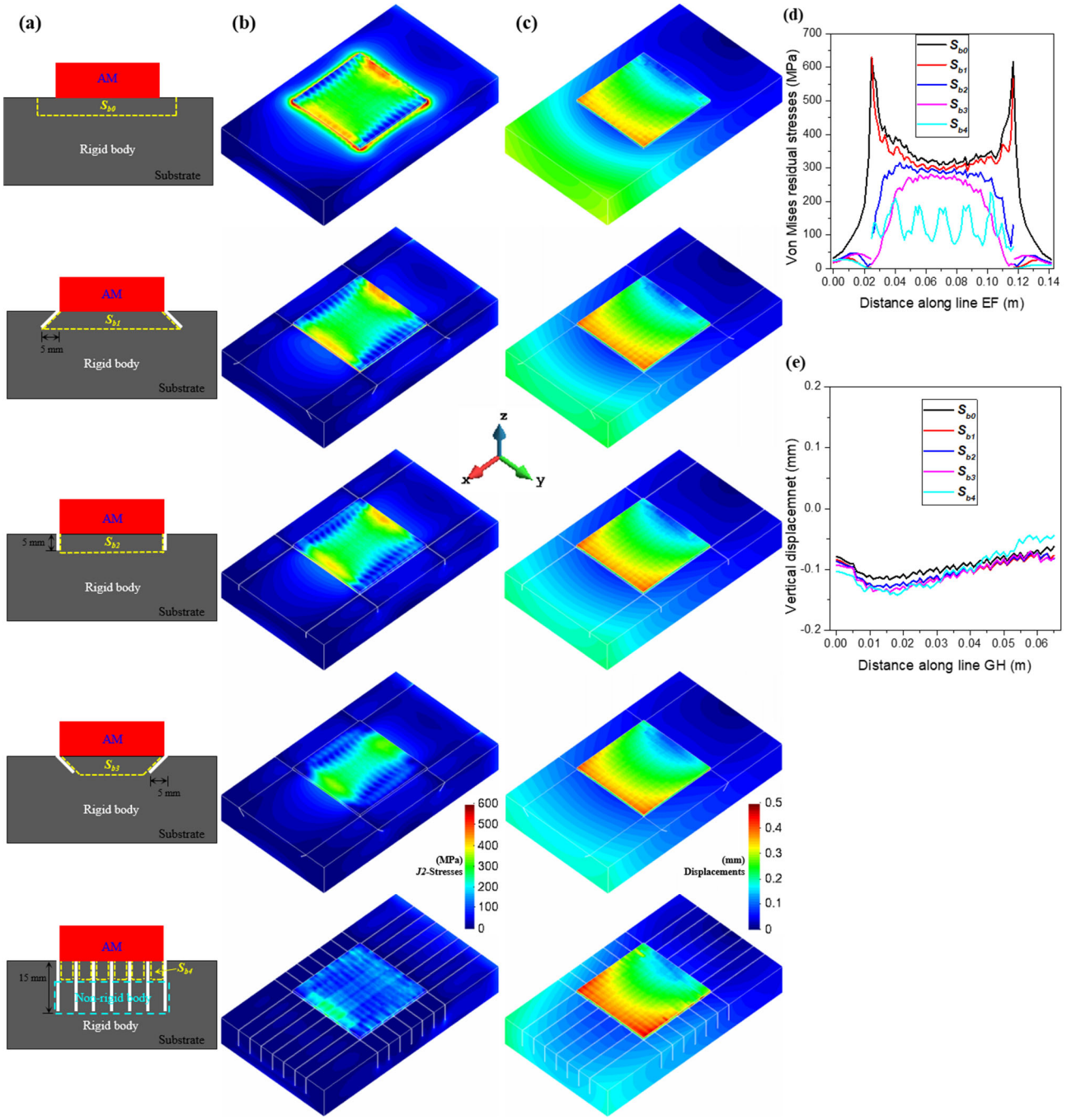


**Figure 7.** Square block: (**a**) different substrate designs; (**b**) von Mises stress field; (**c**) final distortions (displacements norm); (**d**) residual von Mises stresses along the EF line at the baseplate top; (**e**) vertical displacements along the GH line at the deposit top.

Referring to the bar model (see Figure 4c), the upper part of the substrate near the AM deposit acts as a base-bar, while the rest of the substrate is rigid (see Figure 7a). According to Equation (16), the area of the upper of the substrate (marked by yellow lines) decreases from $S_{b0}$ to $S_{b4}$, as shown in Figure 7a; thus, the corresponding yield temperature $T_Y$ rises in sequence, favoring the mitigation of the residual stress (plastic deformation) during AM.

Figure 7b,d display the contour-fills of the residual stresses and the stress distributions at the deposit–substrate interface for different substrate settings. Note that the residual stresses are remarkably minimized by lowering the mechanical restraint of the substrate. For the $S_{b4}$ sample, both the inner stresses and the stress concentration at the corner of

the deposit are much lowered, almost without compromising the distortions, as shown in Figure 7c,e.

Regarding the part geometry, the square block yields a larger residual stress (Figure 7b) than the rectangular block (see Figure 5d), due to the use of longer scan lines during the deposition of the last layer.

## 5. Conclusions

In this work, a 3D coupled thermomechanical FE model for AM is firstly calibrated by in situ temperature and displacement measurements using a 40-layer block. This done, a three-bar model is used as a conceptual aid to understand the generation of residual stresses in AM and to extract the two key causes: (i) the maximum temperature gradient, MTG, and (ii) the yield temperature, $T_Y$, related to the mechanical restraint during thermal deformation. Next, utilizing the calibrated thermomechanical model, several strategies on reducing the residual stresses, such as the optimization of path and process parameter and preheating of the substrate and design of the substrate, are systematically evaluated. It is found that the approaches previously developed based on the MTG control can minimize the inner residual stress of the builds but are useless for avoiding the residual stress concentrations at the deposited basement, this often being the source of cracking and failure of the parts. Contrarily, the proposed strategy of increasing $T_Y$, by lowering the mechanical restraint of the substrate to AM deposit, efficiently prevents the development of the residual stress and stress concentration during the printing process.

Concurrently controlling the MTG and $T_Y$ and utilizing the IHT annealing (if possible) can be used for mitigating the residual stresses during the DED processes. However, the LPBF process is typically characterized by higher MTG and weaker IHT; thus, increasing $T_Y$ to control the stress accumulation would be highly beneficial.

**Author Contributions:** Conceptualization, X.L. (Xufei Lu); Funding acquisition, X.L. (Xin Lin); Software, M.C. (Michele Chiumenti); Supervision, M.C. (Miguel Cervera), M.C. (Michele Chiumenti) and X.L. (Xin Lin); Writing—original draft, X.L. (Xufei Lu); Writing—review & editing, M.C. (Miguel Cervera). All authors have read and agreed to the published version of the manuscript.

**Funding:** This work was funded by the National Key R&D Program of China (No. 2016YFB1100100), the European KYKLOS 4.0 project (No. 872570) and the China Scholarship Council (No. 201906290011).

**Data Availability Statement:** Data are contained within the article.

**Conflicts of Interest:** The authors declare no conflict of interest.

## References

1. Baiges, J.; Chiumenti, M.; Moreira, C.A.; Cervera, M.; Codina, R. An adaptive Finite Element strategy for the numerical simulation of additive manufacturing processes. *Addit. Manuf.* **2021**, *37*, 101650. [CrossRef]
2. Chiumenti, M.; Lin, X.; Cervera, M.; Lei, W.; Zheng, Y.; Huang, W. Numerical Simulation and Experimental Calibration of Additive Manufacturing by Blown Powder Technology. Part I: Thermal Analysis. *Rapid Prototyp. J.* **2017**, *23*, 448–463. [CrossRef]
3. Lu, X.; Lin, X.; Chiumenti, M.; Cervera, M.; Li, J.; Ma, L.; Wei, L.; Hu, Y.; Huang, W. Finite Element Analysis and Experimental Validation of the Thermomechanical Behavior in Laser Solid Forming of Ti-6Al-4V. *Addit. Manuf.* **2018**, *21*, 30–40. [CrossRef]
4. Lu, X.; Chiumenti, M.; Cervera, M.; Tan, H.; Lin, X.; Wang, S. Warpage Analysis and Control of Thin-Walled Structures Manufactured by Laser Powder Bed Fusion. *Metals* **2021**, *11*, 686. [CrossRef]
5. Zhang, W.; Tong, M.; Harrison, N.M. Scanning strategies effect on temperature, residual stress and deformation by multi-laser beam powder bed fusion manufacturing. *Addit. Manuf.* **2020**, *36*, 101507. [CrossRef]
6. Lu, X.; Lin, X.; Chiumenti, M.; Cervera, M.; Hu, Y.; Ji, X.; Ma, L.; Huang, W. In situ measurements and thermo-mechanical simulation of Ti–6Al–4V laser solid forming processes. *Int. J. Mech. Sci.* **2019**, *153–154*, 119–130. [CrossRef]
7. Lu, X.; Lin, X.; Chiumenti, M.M.; Cervera, M.; Hu, Y.; Ji, X.; Ma, L.; Huang, W. Residual Stress and Distortion of Rectangular and S-Shaped Ti-6Al-4V Parts by Directed Energy Deposition: Modelling and Experimental Calibration. *Addit. Manuf.* **2019**, *26*, 166–179. [CrossRef]
8. Cao, Y.; Lin, X.; Kang, N.; Ma, L.; Wei, L.; Zheng, M.; Yu, J.; Peng, D.; Huang, W. A novel high-efficient finite element analysis method of powder bed fusion additive manufacturing. *Addit. Manuf.* **2021**, *46*, 102187. [CrossRef]
9. Cao, J.; Gharghouri, M.A.; Nash, P. Finite-element analysis and experimental validation of thermal residual stress and distortion in electron beam additive manufactured Ti-6Al-4V build plates. *J. Mater. Process. Technol.* **2016**, *237*, 409–419. [CrossRef]

10. Lu, X.; Cervera, M.; Chiumenti, M.; Li, J.; Ji, X.; Zhang, G.; Lin, X. Modeling of the Effect of the Building Strategy on the Thermomechanical Response of Ti-6Al-4V Rectangular Parts Manufactured by Laser Directed Energy Deposition. *Metals* **2020**, *10*, 1643. [CrossRef]
11. Levkulich, N.; Semiatin, S.; Gockel, J.; Middendorf, J.; DeWald, A.; Klingbeil, N. The effect of process parameters on residual stress evolution and distortion in the laser powder bed fusion of Ti-6Al-4V. *Addit. Manuf.* **2019**, *28*, 475–484. [CrossRef]
12. Mugwagwa, L.; Dimitrov, D.; Matope, S.; Yadroitsev, I. Influence of process parameters on residual stress related distortions in selective laser melting. *Procedia Manuf.* **2018**, *21*, 92–99. [CrossRef]
13. Hönnige, J.; Colegrove, P.; Ahmad, B.; Fitzpatrick, M.; Ganguly, S.; Lee, T.L.; Williams, S. Residual stress and texture control in Ti-6Al-4V wire + arc additively manufactured intersections by stress relief and rolling. *Mater. Des.* **2018**, *150*, 193–205. [CrossRef]
14. Kalentics, N.; Boillat, E.; Peyre, P.; Ciric-Kostic, S.; Bogojevic, N.; Logé, R.E. Tailoring residual stress profile of Selective Laser Melted parts by Laser Shock Peening. *Addit. Manuf.* **2017**, *16*, 90–97. [CrossRef]
15. Sames, W.; List, F.; Pannala, S.; Dehoff, R.; Babu, S. The metallurgy and processing science of metal additive manufacturing. *Int. Mater. Rev.* **2016**, *61*, 315–360. [CrossRef]
16. Guo, W.; Sun, R.; Song, B.; Zhu, Y.; Li, F.; Che, Z.; Li, B.; Guo, C.; Liu, L.; Peng, P. Laser shock peening of laser additive manufactured Ti6Al4V titanium alloy. *Surf. Coatings Technol.* **2018**, *349*, 503–510. [CrossRef]
17. Mugwagwa, L.; Yadroitsava, I.; Makoana, N.W.; Yadroitsev, I. Residual stress in laser powder bed fusion. In *Fundamentals of Laser Powder Bed Fusion of Metals*; Elsevier BV: Amsterdam, The Netherlands, 2021; pp. 245–276.
18. Fang, Z.-C.; Wu, Z.-L.; Huang, C.-G.; Wu, C.-W. Review on residual stress in selective laser melting additive manufacturing of alloy parts. *Opt. Laser Technol.* **2020**, *129*, 106283. [CrossRef]
19. Bartlett, J.L.; Li, X. An overview of residual stresses in metal powder bed fusion. *Addit. Manuf.* **2019**, *27*, 131–149. [CrossRef]
20. Lu, X.; Chiumenti, M.; Cervera, M.; Zhang, G.; Lin, X. Mitigation of residual stresses and microstructure homogenization in directed energy deposition processes. *Eng. Comput.* **2021**, in press.
21. Chiumenti, M.; Cervera, M.; Salmi, A.; de Saracibar, C.A.; Dialami, N.; Matsui, K. Finite element modeling of multi-pass welding and shaped metal deposition processes. *Comput. Methods Appl. Mech. Eng.* **2010**, *199*, 2343–2359. [CrossRef]
22. Chiumenti, M.; Neiva, E.; Salsi, E.; Cervera, M.; Badia, S.; Moya, J.; Chen, Z.; Lee, C.; Davies, C. Numerical Modelling and Experimental Validation in Selective Laser Melting. *Addit. Manuf.* **2017**, *18*, 171–185. [CrossRef]
23. Chiumenti, M.; Cervera, M.; Moreira, C.; Barbat, G. Stress, strain and dissipation accurate 3-field formulation for inelastic isochoric deformation. *Finite Elements Anal. Des.* **2021**, *192*, 103534. [CrossRef]
24. Chiumenti, M.; Cervera, M.; Dialami, N.; Wu, B.; Jinwei, L.; de Saracibar, C.A. Numerical modeling of the electron beam welding and its experimental validation. *Finite Elem. Anal. Des.* **2016**, *121*, 118–133. [CrossRef]
25. Lu, X.; Zhang, G.; Li, J.; Cervera, M.; Chiumenti, M.; Chen, J.; Lin, X.; Huang, W. Simulation-assisted investigation on the formation of layer bands and the microstructural evolution in directed energy deposition of Ti6Al4V blocks. *Virtual Phys. Prototyp.* **2021**, *16*, 387–403. [CrossRef]
26. Lu, X.; Chiumenti, M.; Cervera, M.; Li, J.; Lin, X.; Ma, L.; Zhang, G.; Liang, E. Substrate design to minimize residual stresses in Directed Energy Deposition AM processes. *Mater. Des.* **2021**, *202*, 109525. [CrossRef]
27. Ueda, Y.; Murakawa, H.; Ma, N. *Welding Deformation and Residual Stress Prevention*; Elsevier BV: Amsterdam, The Netherlands, 2012; pp. 5–25.
28. Sun, L.; Ren, X.; He, J.; Zhang, Z. Numerical investigation of a novel pattern for reducing residual stress in metal additive manufacturing. *J. Mater. Sci. Technol.* **2021**, *67*, 11–22. [CrossRef]
29. Xue, A.; Lin, X.; Wang, L.; Lu, X.; Ding, H.; Huang, W. Heat-affected coarsening of β grain in titanium alloy during laser directed energy deposition. *Scr. Mater.* **2021**, *205*, 114180. [CrossRef]
30. Denlinger, E.R.; Michaleris, P. Effect of stress relaxation on distortion in additive manufacturing process modeling. *Addit. Manuf.* **2016**, *12*, 51–59. [CrossRef]
31. Chen, W.; Xu, L.; Han, Y.; Zhao, L.; Jing, H. Control of residual stress in metal additive manufacturing by low-temperature solid-state phase transformation: An experimental and numerical study. *Addit. Manuf.* **2021**, *42*, 102016. [CrossRef]

# Crack-free laser powder bed fusion by substrate design optimization

X. Lu, M. Cervera & M. Chiumenti

*Additive Manufacturing*

Submitted

# Crack-free laser powder bed fusion by substrate design optimization

Xufei Lu*, Michele Chiumenti and Miguel Cervera

*International Centre for Numerical Methods in Engineering, Universidad Politécnica de Cataluña, Barcelona, Spain*

**Abstract:** Additively manufactured components by laser powder bed fusion (LPBF) often suffer from stress-induced cracks (e.g. delamination), especially at the build-substrate interfaces where stiff mechanical constraints and large thermal gradients coexist. To reduce the probability of cracking, this work proposes an innovative strategy to optimize the geometry of the substrate by reducing its mechanical stiffness and, consequently, the stress accumulation during LPBF. To assess the feasibility of the strategy, a coupled thermomechanical finite element model firstly is calibrated with the experimental evidence obtained from the LPBF metal deposition of a bridge-type structure, and then validated to predict the thermo-mechanical behavior of two T-shape AM parts built on (i) a typical solid substrate and (ii) a groove patterned substrate, respectively. The results show that several visible cracks appear at the interface between the build and the typical solid substrate due to stress concentration (up to 1600 MPa), while a crack-free component can be manufactured by adding grooves through the thickness of the substrate, without compromising the resulting microstructure and microhardness of the metallic materials with high crack sensitivity. The difference between the groove patterned substrate design with respect to the use of support structures used for printing cantilever structures is clarified to further justify the novelty of the proposed approach.

**Key words:** Laser powder bed fusion; Cracking; Structural optimization; Thermomechanical simulation.

* Corresponding author.

*E-mail address*: (X. Lu) xlu@cimne.upc.edu.

## 1 Introduction

Laser powder bed fusion (LPBF) additive manufacturing (AM) has been broadly utilized to fabricate complex and high-performance metallic components in different industrial sectors (e.g. aerospace or automotive) due to its intrinsic design and fabrication freedoms, if compared to traditional manufacturing technologies [1,2]. However, the metal deposition process in LPBF induces repeated heating and cooling cycles, and thus the material suffers from cyclic expansions and contractions. These deformations are usually restrained by a thick substrate in the practical AM processes and transform into large residual stresses in the manufactured part [3-5] and, cracking and delamination can occur eventually at some concentration points, contributing to the failure of the AM-build [6-8]. Thereby, this work aims at mitigating the residual stresses in LPBF and avoiding the occurrence of macro-cracking.

To better understand the thermo-mechanical behavior, a simple bar model shown in Fig. 1(a) is used to analyze the formation mechanisms of residual stresses in AM; the reader can refer to [9,10] for more details. Because of the heating and cooling cycles induced by the AM process, the AM-bar inevitably accumulates residual stresses and their magnitude is closely related to the peak temperature, $T_{peak}$, recorded at points $a$, $c$ or $e$. $T_Y$ denotes the yield temperature, which induces the yielding of the AM-bar during either heating or cooling process [10], and can be defined as:

$$T_Y = \left(\frac{A_{AM}}{A_{base}} + 1\right)\frac{\sigma_Y}{\alpha \cdot E} \tag{1}$$

where $A_{AM}$ and $A_{base}$ are the area of the central cross-section of the AM-bar and the Base-bar, respectively. $E$ is the (temperature-dependent) Young's modulus, $\alpha$ is the (temperature-dependent) thermal expansion coefficient and $\sigma_Y$ is the (temperature-dependent) yield stress. Hence, if $T_{peak} \leq T_Y$, no further residual stresses are formed; if $T_Y < T_{peak} \leq 2T_Y$, the magnitude of the residual stresses equals the absolute value of the segment $|od|$; if $2T_Y < T_{peak}$, the residual stresses reach the yield strength [9].

Normally, thick substrates (e.g. >10 mm) are employed in LPBF to minimize warpage of the fabricated components. However, a large stiffness prevents the thermal expansion of the cold substrate (i.e. compressive stresses are generated), as well as the contraction of the newly deposited layers (i.e. tensile stresses are generated) as shown in Fig. 1(b). Furthermore, as the molten pool solidifies, steep temperature gradients appear at the heat affected zone [11] and, consequently, large tensile stresses are rapidly developed, contributing to the solidification crack in the inter-dendritic region in some nickel-based and aluminum alloys [12-14]. Also, the longer the cooling process takes, the higher the residual tensile stresses are. This is particularly true in case of the LPBF process because the heating is very much localized close to the molten pool and the mechanical constraint induced by the (cold) substrate and the rest of the build (also cooled down during the recoating process) is higher compared to other AM technologies such as the directed energy deposition (DED) [15,16]. Thereby, macro cracks and delamination can easily be produced and particularly at the build-substrate interface (Fig. 1(b)).

To increase the cracking resistance in AM, most of the current strategies are focused on reducing the maximum thermal gradient (MTG), by optimizing scanning path [11], process parameters [16] and support structures [4], or by substrate preheating prior to the AM process [10]. However, their effect is limited because of the characteristic of LPBF: the applied high-energy beam heat source is directly responsible for the sharp MTG that appears [17-19]. A higher preheating temperature of the substrate favors a lower magnitude of residual stresses, but it increases the

oxygen content in the manufactured parts, and thus inferior mechanical properties are obtained [20]. Support structures are necessary when printing overhangs in LPBF, and some additional supports also are used in the non-cantilever building to facilitate substrate removal. However, this requires more raw material, increases both the manufacturing time and cost, and causes larger warpage or even cracks when using an inappropriate support design [21]. In addition, using these strategies in AM inevitably changes the thermal histories that the builds experience and affect their microstructural evolution and the resulting mechanical properties, narrowing the process window of metal AM and its industrial application [22,23].

From Eq. (1), it is clear that reducing the substrate area $A_{base}$ can increase $T_Y$. Hence, reducing the mechanical constraining from the substrate can mitigate the formation of stress-induced cracking during AM processes. For the same reason, thinner substrates with a lower stiffness are beneficial with regard to reducing cracking, although causing larger part warpage.

In this work, a novel approach to optimize the stiffness of the conventional thick substrates is proposed. As shown in Fig. 1(c), by adding several grooves, the substrate is divided into different small regions while preserving the overall structural stiffness of the substrate. Therefore, the heat affected zone is allowed to expand during heating, avoiding that the thermal deformations transform into plastic strains; also, lower compressive stresses are generated thanks to the weak substrate constraint. Similarly, during the cooling period, an elastic recovery is favored, resulting in lower tensile stresses, and thus allowing for a crack-free AM fabrication.

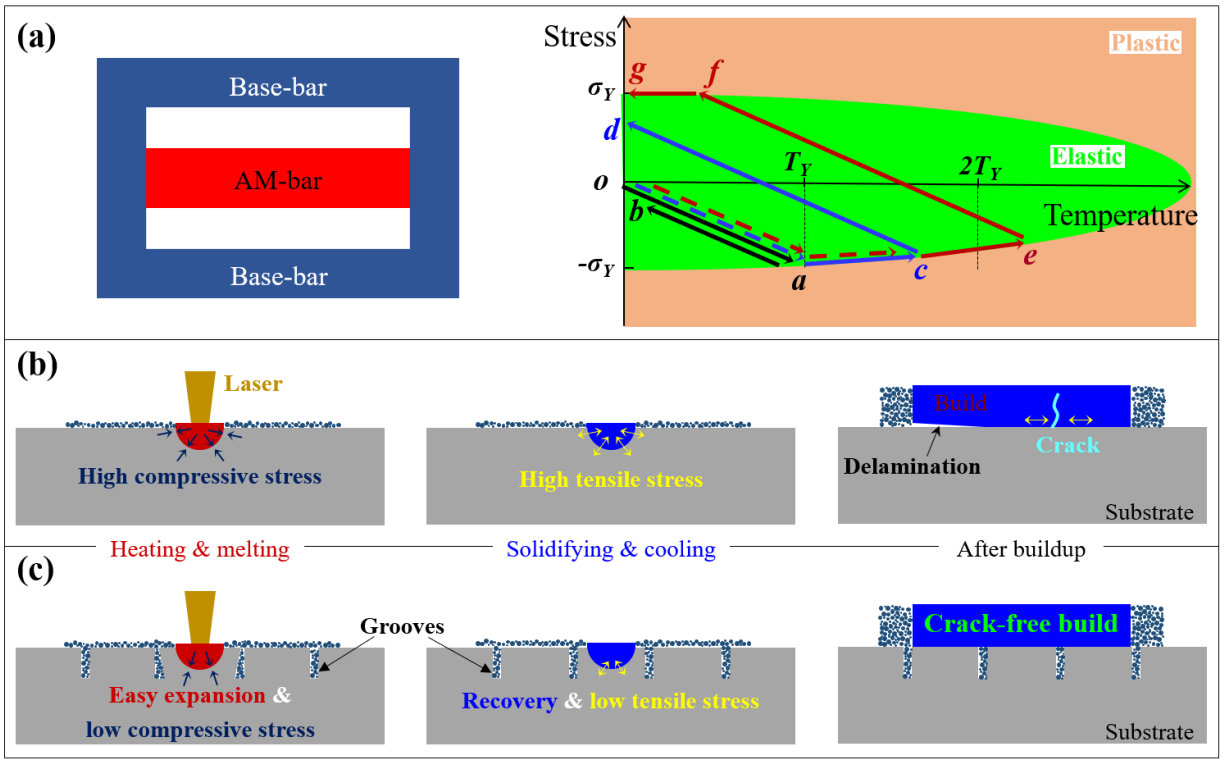


Fig. 1. (a) Three-bar model: the thermo-mechanical relationship of the AM-bar; (b) formation mechanism of residual stresses and cracks in AM; (c) crack prevention at the part-substrate interface by designing substrate structure.

## 2 Experimental conditions

Fig. 2 shows two Ti-6Al-4V T-shape parts with a nominal dimension of 40×24×10 mm$^3$ printed by a Realizer SLM50 LPBF system in the AMBER AR-Lab in TCD. This AM machine is equipped with a CW fibre laser with a

wavelength of 1064 nm. For comparison purpose, two annealed cylindrical Ti-6Al-4V substrates with a size of Ø70×10 $mm^3$ are used. The first one is kept in its original format while the second one is characterized by several grooves (Fig. 2). Before printing, the 5 mm deep and 0.25 mm wide grooves on the substrate are cut by a wire electric discharge machining (Excetez V440G EDM). The AM builds are carried out under an argon atmosphere with a gas flow speed of 65 L/min. An alternating scanning path is used as shown by the red lines in Fig. 2(b). Typically, the longitudinal stresses along the scanning path are mainly responsible for the residual stresses; thus, to reduce the risk of cracking, the grooves are cut following a pattern perpendicular to the printing path. Before depositing the first layer in LPBF, the grooves are filled with loose powder by the recoater to facilitate the powder spreading process of the subsequent layers (see Fig. 1(c)).

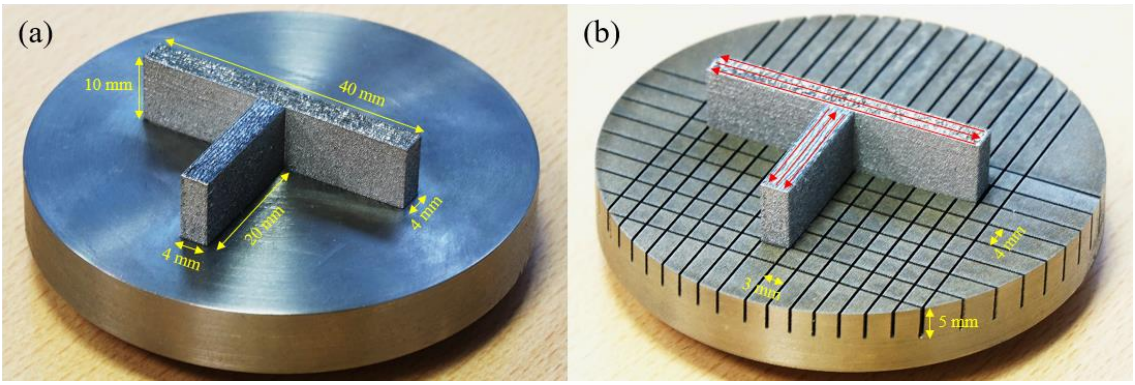


Fig. 2. Two T-shape components fabricated on (a) the typical (no grooves) and (b) the patterned (with grooves) substrates.

In addition, a Ti-6Al-4V bridge geometry is fabricated by a KUL-SLM powder bed machine equipped by a Yb:YAG laser with a wavelength of 1085 nm, as shown in Fig. 3. Like with the T-shapes, several longitudinal (along X-direction) scan vectors with a length of 20 mm were used to build the bridge without support. The details of the fabrication of this bridge structure are given in [24].

The process parameters used for fabricating the two LPBF parts are listed in Table 1.

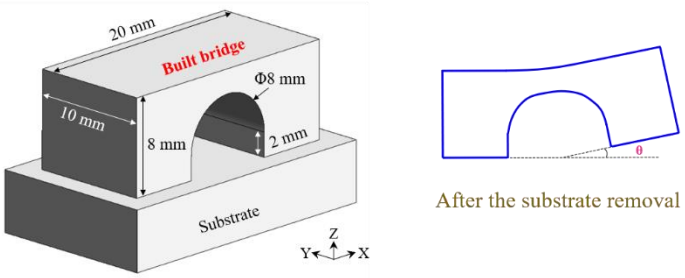


Fig. 3. The size of the bridge structure and the scheme of its bending warpage after the substrate removal, adapted from [24].

Table 1. LPBF processing parameters for printing the T-shape and bridge parts.

| | Laser power (W) | Scan speed (mm/s) | Hatch spacing (μm) | Layer thickness (μm) | Laser spot diameter (μm) |
|---|---|---|---|---|---|
| T-shape | 90 | 500 | 80 | 25 | 170 |
| Bridge [24] | 42 | 225 | 74 | 30 | 80 |

After the LPBF process was completed, the bridge is cut from the substrate to measure the curling angle $\theta$ due to stress relaxation (see Fig. 3) and this angle is used to validate the numerical model; the T-shape samples are cut by EDM to analyze the crack formation and the microstructure distribution. Vickers microhardness of the T-shape

deposits is measured using a Mitutoyo MVK-H1 hardness testing machine. In each sample, 10 points are considered to get an average value. Both an optical microscope and a scanning electron microscopy are employed to analyse the Ti-6Al-4V microstructure of all the T-shape samples.

## 3 Computational simulation

In this work, an in-house 3D thermo-mechanical finite element (FE) software, *COMET*, is employed to perform the LPBF modelling [25]. The sequentially coupled thermo-mechanical modelling, where the temperature field is independent of the stress field, is performed as follows: (i) for each time-step, the transient thermal analysis is conducted first; (ii) then the mechanical analysis is solved by importing the calculated temperature field. Details of this thermo-mechanical coupled software and framework for AM can be found in the authors' previous publications, validated by a number of in-situ thermo-mechanical experimental measurements [18,26,27].

### 3.1 Thermal analysis for AM

In the sequentially coupled thermo-mechanical modelling, the heat transfer process is independent of the mechanical behavior of material and the governing equation for the transient thermal analysis can be expressed as:

$$\dot{H} = -\nabla \cdot \mathbf{q} + \dot{Q} \tag{2}$$

where $\dot{H}$ for enthalpy rate, $\mathbf{q}$ for heat flux, $\dot{Q}$ for heat source (per unit of volume), which can be calculated by the total laser input $\dot{P}$, the laser absorption efficiency $\eta_p$, and the volume of the molten pool $V_{pool}^{\Delta t}$:

$$\dot{Q} = \frac{\eta_p \dot{P}}{V_{pool}^{\Delta t}} \tag{3}$$

The thermal transfer mechanisms that are considered in the thermal analysis include: heat conduction to the substrate and previously deposited material, conduction to the surrounding powder, convection, and radiation from the top surface to the environment before the next layer is added. The heat flux $\mathbf{q}$ due to heat conduction is formulated via Fourier's law:

$$\mathbf{q} = -k\nabla T \tag{4}$$

where $k$ and $\nabla T$ are the (temperature-dependent) thermal conductivity and the thermal gradient, respectively.

The heat dissipation due to convection from the top surface of the build to the surrounding environment is defined by Newton's law:

$$q_{conv} = h_{conv}(T - T_{room}) \tag{5}$$

where $h_{conv}$ is the convective Heat Transfer Coefficient (HTC), $T$ is the surface temperature of the workpiece and $T_{room}$ is the room temperature.

The heat loss caused by the radiation $q_{rad}$ is computed by Stefan-Boltzmann's law:

$$q_{rad} = \varepsilon_{rad}\sigma_{rad}(T^4 - T_{room}^4) \tag{6}$$

where $\varepsilon_{rad}$ and $\sigma_{rad}$ are the surface emissivity and the Stefan-Boltzmann constant, respectively.

### 3.2 Mechanical analysis

The stress analysis is performed after the thermal analysis, which is implemented by computationally solving the balance of momentum and the continuity equations:

$$\nabla \cdot \mathbf{s} + \nabla p + \mathbf{b} = 0 \tag{7}$$

$$(\nabla \cdot \mathbf{u} - e^T) - \frac{p}{K(T)} = 0 \tag{8}$$

where $\mathbf{b}$ is the body force (per unit of volume), $K(T)$ is the (temperature-dependent) bulk modulus, and the Cauchy stress tensor $\boldsymbol{\sigma}$ can be split into its spherical (pressure) $p$ and deviatoric $\mathbf{s}$ parts:

$$\boldsymbol{\sigma} = p\boldsymbol{I} + \mathbf{s}(\mathbf{u}) \tag{9}$$

The thermal deformation $e^T$ is determined by:

$$e^T(T, f_S) = e^{cool}(T) + e^{pc}(f_S) \tag{10}$$

where $e^{cool}(T)$ and $e^{pc}(f_S)$ are the thermal expansion and thermal shrinkage in the liquid-to-solid phase transformation, as a function of the initial temperature $T_0$ and the solid fraction $f_S$, and can be expressed as:

$$e^{cool}(T) = \alpha(T)(T - T_0) \tag{11}$$

$$e^{pc}(f_S) = \beta f_S \tag{12}$$

where $\alpha$ and $\beta$ are the (temperature-dependent) thermal expansion and the shrinkage coefficients, respectively.

The mechanical equations in Eqs. (7) and (8) are determined by both the displacement $\mathbf{u}$ and the pressure field $p$, and they are suitable for both compressible and the fully incompressible (isochoric) material behavior.

With the repeated heating-cooling cycles in LPBF, the temperature of material fluctuates up and down between room temperature $T_{room}$ and temperatures above the melting point ($T_{melt}$). Thus, the materials must be featured in its solid, mushy and liquid phases. A *J2*-thermo-elasto-visco-plastic model is adopted in the solid phase, from $T_{room}$ to the annealing temperature $T_{anneal}$. All the material properties are assumed as temperature-dependent. The von-Mises yield-surface can be formulated as:

$$\Phi(\mathbf{s}, q_h, T) = \|\mathbf{s}\| - \sqrt{\frac{2}{3}}\left[\sigma_y(T) - q_h\right] \tag{13}$$

where $\sigma_y$ is the temperature-dependent yield stress that is accounted for the thermal softening and $q_h$ is the stress-like variable controlling the isotropic strain-hardening, which can be defined as:

$$q_h(\xi, T) = -\left[\sigma_\infty(T) - \sigma_y(T)\right]\left[1 - e^{-\delta(T)\xi}\right] - h(T)\xi \tag{14}$$

where $\xi$ and $\sigma_\infty$ are the isotropic strain-hardening variable and the temperature-dependent saturation flow stress, respectively, while $\delta$ and $h$ are the temperature-dependent parameters to model the exponential and linear hardening laws, respectively.

The deviatoric counterpart of Cauchy's stress tensor $\mathbf{s}$ can be expressed as follows:

$$\mathbf{s} = 2G(\mathbf{e} - \mathbf{e}^{vp}) \tag{15}$$

where $G$ is the (temperature-dependent) shear modulus, $\mathbf{e}$ is the total (deviatoric) strain, which is obtained from the total strain tensor $\boldsymbol{\varepsilon}(\mathbf{u}) = \nabla^{sym}(\mathbf{u})$, and $\mathbf{e}^{vp}$ is the visco-plastic strain. The evolution laws of both the visco-plastic strain tensor and the isotropic strain-hardening variable are obtained from the principle of maximum plastic dissipation:

$$\dot{\mathbf{e}}^{vp} = \dot{\gamma}^{vp}\frac{\partial \Phi(\mathbf{s}, q_h)}{\partial \mathbf{s}} = \dot{\gamma}^{vp}\frac{\mathbf{s}}{\|\mathbf{s}\|} = \dot{\gamma}^{vp}\mathbf{n} \tag{16}$$

$$\dot{\xi} = \dot{\gamma}^{vp}\frac{\partial \Phi(\mathbf{s}, q_h)}{\partial q_h} = \sqrt{\frac{2}{3}}\dot{\gamma}^{vp} \tag{17}$$

where $\mathbf{n}$ stands for the normal to the yield surface, and $\dot{\gamma}^{vp}$ is the visco-plastic multiplier and can be expressed as:

$$\dot{\gamma}^{vp} = \left\langle \frac{\partial \Phi(\mathbf{s}, q_h)}{\eta} \right\rangle^{\frac{1}{m}} \tag{18}$$

where $\langle\cdot\rangle$ are the Macaulay brackets, and $m$ and $\eta$ are the temperature-dependent rate sensitivity and plastic viscosity, respectively.

Note that when the temperature of material gets close to $T_{anneal}$ the yield limit $\sigma_y$ tends to be 0. Thereby, the deviatoric Cauchy stress reduces to:

$$\mathbf{s} = \eta(\dot{\gamma}^{vp})^m \mathbf{n} = \eta_{eff}\dot{\mathbf{e}}^{vp} \tag{19}$$

where $\eta_{eff} = \eta(\dot{\gamma}^{vp})^{m-1}$ is the effective viscosity. Thus, the material is featured by a purely viscous law when the temperature is higher than $T_{anneal}$ [28]. A non-Newtonian behavior with $m > 1$ is adopted for the mushy phase (from $T_{anneal}$ to $T_{melt}$), while a Newtonian law, $m = 1$, is featured for the liquid phase (for $T > T_{melt}$).

### 3.3. Computational modelling of LPBF

To simulate the LPBF process, a time discretization framework is needed. The time-marching scheme is characterized by a time step, $\Delta t = t^{n+1} - t^n$. Thereby, the molten pool is allowed to move in a step-by-step manner based on the pre-defined scan path from the location at time $t^n$ to that at time $t^{n+1}$. During this time interval, the heat is input into the elements that belong to the molten-pool volume and then the scanned powder conforms as the AM deposit.

Thereby, the software parses the same input file (Common Layer Interface format) following the actual building sequence as adopted to inform the physical LPBF system. The *birth-death-element* technique is utilized to gradually activate the elements corresponding to each newly deposited layer. Therefore, the numerical strategy for the LPBF process requires an ad-hoc procedure to categorize the elements into: *active*, *inactive,* and *activated* elements. At each time step, an octree-based searching algorithm is employed to search the elements belonging to the molten pool (*active*) and to the new deposit (*activated*). The current computational domain consists of both *active* and *activated* elements, while the *inactive* elements are neither assembled nor computed into the global matrix of the analysis [25]. For the convenience of computational modelling, the powder bed surrounding the build is excluded in the computational domain while its effect is considered using an equivalent boundary condition: the HTC by conduction between the powder bed and the AM-build is set to 5 W/(m$^2$·ºC) [29].

Fig. 4 shows different 3D structures of LPBF components and the corresponding meshes generated by the pre-post-processor *GiD* [30]. Fig. 4(a) depicts the bridge structure used to validate the FE thermo-mechanical model. Fig. 4(b-d) show the T-shape structure built on the typical and patterned substrates and the additional supports, respectively, in order to distinguish their effect on the mechanical response of AM-parts. Fig. 4(e) displays the cantilever T-shape structure with supports, manufactured on the patterned substrate to demonstrate the effectiveness of substrate design. Table 2 lists the dimensions of all the LPBF-components presented in Fig. 4 and the corresponding numbers of hexahedral elements and nodes. To reduce the computational cost while preserving high accuracy, ten physical layers are lumped into a computational one [31,32], so the mesh sizes are set as 0.33×0.33×0.3 mm$^3$ for the bridge structure and 0.5×0.5×0.25 mm$^3$ for the T-shape parts. A coarser mesh is adopted for the substrate based on a previous mesh convergence study [29].

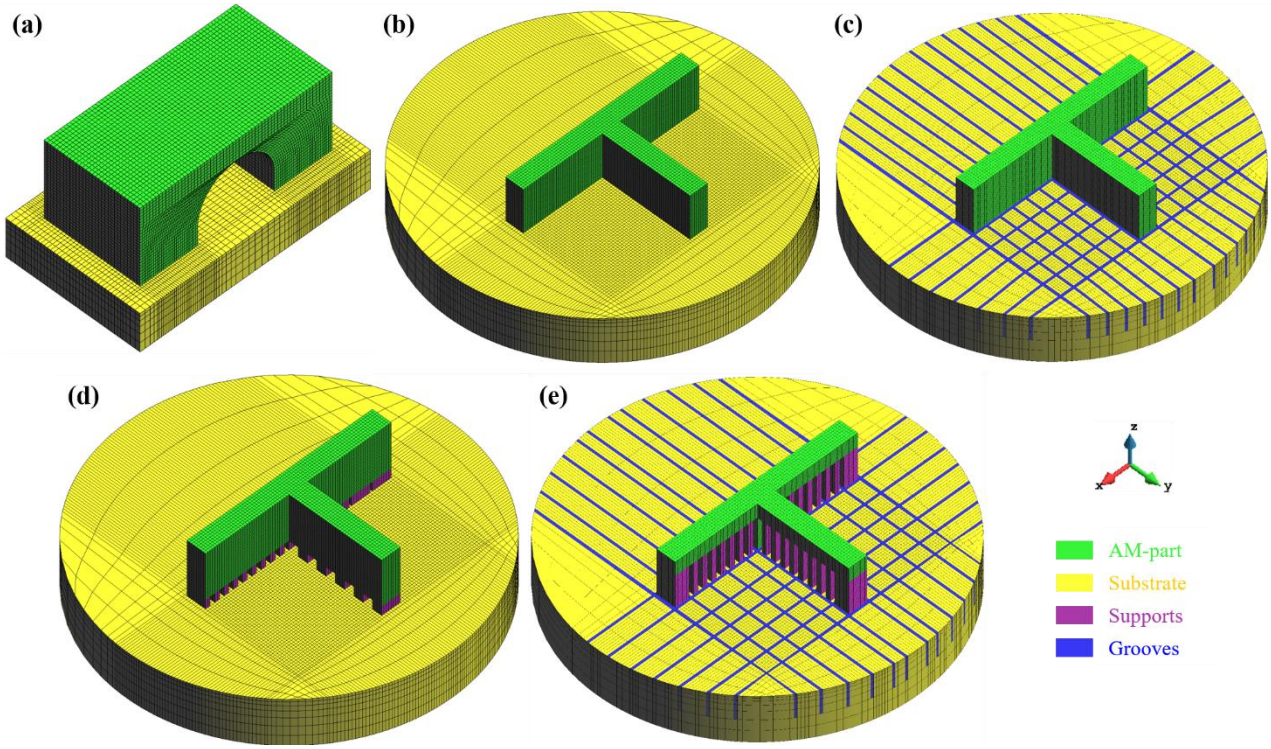


Fig. 4. FE models: (a) the bridge part; the T-shape parts built on the (b) typical and (c) patterned substrates and (d) on the additional supports with a height of 2 mm and three different thicknesses of 1, 2 and 4 mm; (e) the T-shape cantilever part with 7 mm high supports manufactured on the patterned substrate. (The grooves in the patterned substrate are filled by loose powder in LPBF).

Table 2. Part sizes and the numbers of FE elements and nodes.

| | Size of LPBF-parts ($mm^3$) | Number of elements | Number of nodes |
|---|---|---|---|
| Bridge part | 20×10×8 | 69,240 | 76,902 |
| T-shape on the typical substrate | 40×22×10 | 78,328 | 90,432 |
| T-shape on the patterned substrate | 40×22×10 | 78,328 | 90,432 |
| T-shape on the additional supports | 40×22×10 + 40×22×2 (supports) | 83,320 | 97,632 |
| T-shape cantilever part | 40×22×10 (support height: 7) | 67,128 | 84,438 |

### 3.4 Material properties and boundary conditions

Table 3 lists the (temperature-dependent) thermodynamic properties of Ti-6Al-4V used for both the AM-build and the substrate in the computational modelling [5]. A higher heat conductivity is defined when $T > T_{melt}$ to consider the effect of the convective flow inside the molten pool [16]. In the case of the patterned substrate, the thermal and mechanical properties of materials for the groove elements (filled by loose powder) are assumed as 5% and 0.01% of the solids, respectively.

Table 3. Thermodynamic properties of Ti-6Al-4V [5].

| Temperature (ºC) | Thermal conductivity (W/(m·°C)) | Density ($kg/m^3$) | Heat capacity (J/(kg·°C)) | Poisson's ratio | Elastic limit (MPa) | Thermal expansion coefficient (μm/(m·°C)) | Young's modulus (GPa) |
|---|---|---|---|---|---|---|---|
| 20 | 7 | 4420 | 546 | 0.345 | 850 | 8.78 | 110 |
| 205 | 8.75 | 4395 | 584 | 0.35 | 630 | 10 | 100 |
| 500 | 12.6 | 4350 | 651 | 0.37 | 470 | 11.2 | 76 |
| 995 | 22.7 | 4282 | 753 | 0.43 | 13 | 12.3 | 15 |
| 1100 | 19.3 | 4267 | 641 | 0.43 | 5 | 12.4 | 5 |
| 1200 | 21 | 4252 | 660 | 0.43 | 1 | 12.42 | 4 |
| 1600 | 25.8 | 4198 | 732 | 0.43 | 0.5 | 12.5 | 1 |
| 1650 | 83.5 | 3886 | 831 | 0.43 | 0.1 | 12.5 | 0.1 |
| 2000 | 83.5 | 3818 | 831 | 0.43 | 0.01 | 12.5 | 0.01 |

To simulate the LPBF process, the heat dissipation through convection and radiation is considered for all the

free surfaces of the LPBF-parts, being the corresponding HTCs set to 12.7 W/(m$^2$·ºC) and 0.35, respectively [33]. The laser efficiency is set as 0.4 [33] and the room temperature is fixed at 27ºC in all simulations.

The mechanical boundary conditions in simulation follows the actual LPBF experimental setups: the whole bottom surface of the substrate used to fabricate the bridge structure is clamped, while a small circular area (Ø10 mm) in the central region of the lower surface of the substrate is fixed for the T-shape samples.

## 4 Results and discussion

### 4.1 FE model validation

The thermo-mechanical model used for the AM analysis has been validated in previous works to optimize both process parameters and material properties, but for different geometries and parameters [18,26]. For ensuring the simulation accuracy in this study, the model is further calibrated by comparing the experimental measurements reported in [24]. Fig. 5(a) shows the predicted curling angle of 2.76º, by plotting the Z coordinates of nodes on the central line of the bottom surface of the bridge structure. The calculated angle agrees remarkably well with the experimental evidence (about 2.8º) [24], within less than 2% difference.

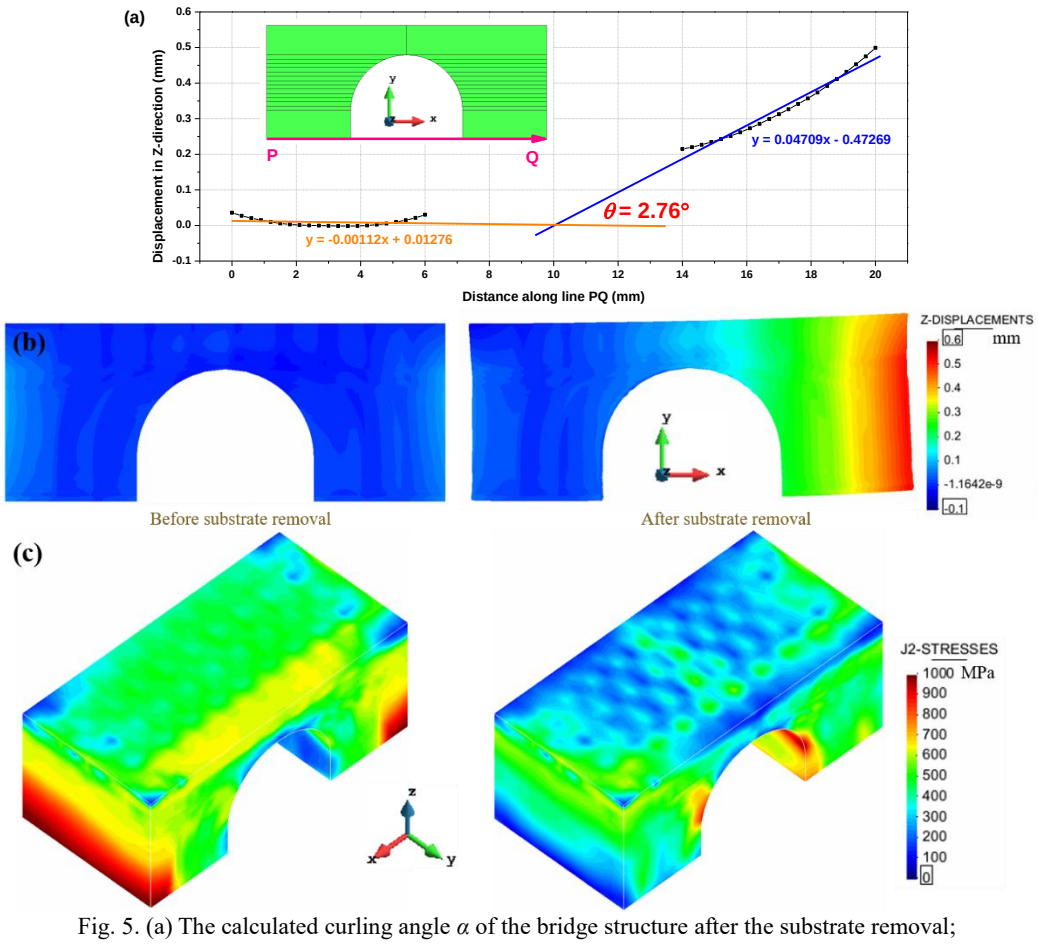


Fig. 5. (a) The calculated curling angle $\alpha$ of the bridge structure after the substrate removal;
(b) the vertical displacement profile and (c) the residual Von Mises fields before and after the substrate removal.

Fig. 5(b) and (c) present the profiles of the vertical displacement and the residual Von Mises stresses before and after the substrate removal, respectively. Observe that before cutting the substrate, the part distortion is quite small (less than 0.1 mm) while the residual stresses are high (up to 1000 MPa) at the basement of the bridge deposit.

Once the substrate is removed, the residual stresses are dramatically released by the development of plastic deformation, up to 0.53 mm at the end of the bridge. Similar results have been previously reported in [32,34-36].

### 4.2 Effect of substrate stiffness on cracking

By cutting both the part and the substrate through a plane perpendicular to their interface, it is more visible to check if any cracks occur after the cooling for the two base-plate geometries (i.e. with and without grooves). The corresponding cross-sections are shown in Fig. 6. Note that in the typical substrate (without grooves) visible cracks (delamination) with a length of more than 2 mm appear at the basement of the T-shape part (positions Ⅰ and Ⅱ), as shown in Fig. 6(a). Also, a small crack is developed at the end of the short-wall (position Ⅲ). However, it can be seen from Fig. 6(b) that no cracks are found when the groove pattern is included in the substrate. Moreover, a good metallurgical quality is preserved in both configurations.

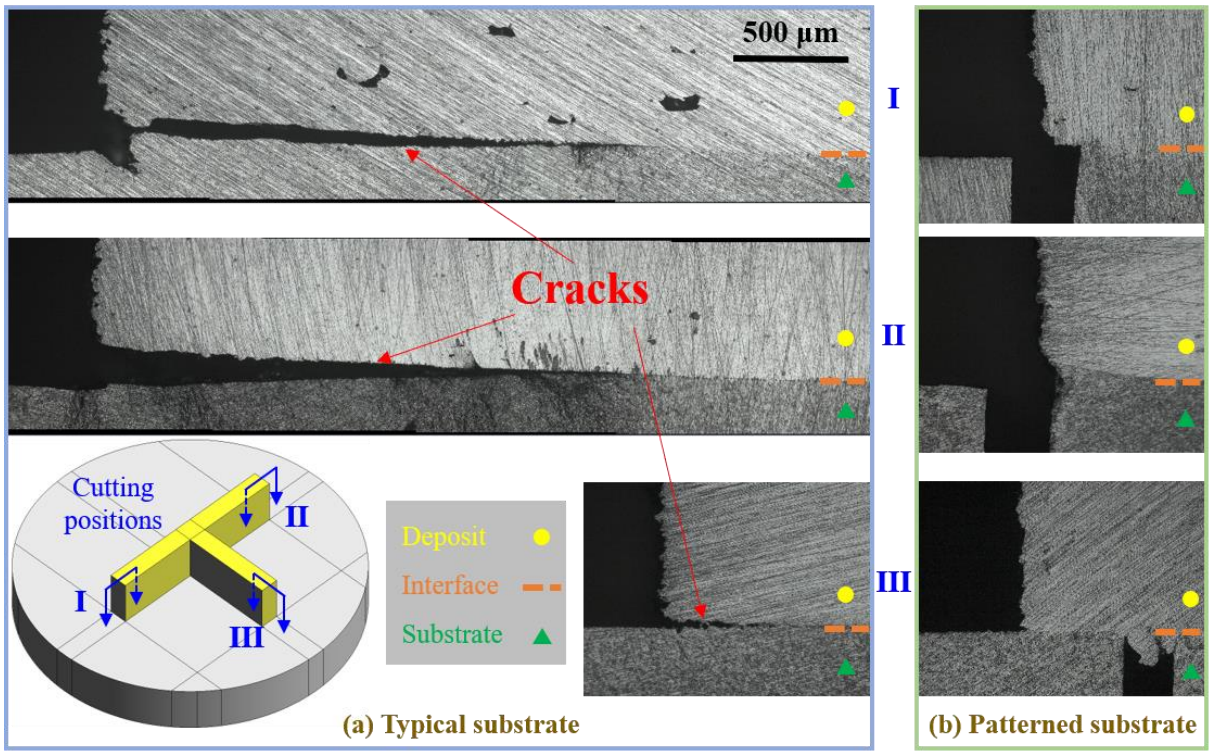


Fig. 6. T-shape components manufactured on two different substrates: cross-sections perpendicular to the build-substrate interface.

Fig. 7 shows the stress distributions in three orthogonal directions at the part-substrate interfaces. It is interesting to observe that by increasing the number of the deposited layers, the tensile stresses in the longitudinal ($\sigma_{xx}$ in Fig. 7(a)), transversal ($\sigma_{yy}$ in Fig. 7(c)) and vertical ($\sigma_{zz}$ in Fig. 7(e)) directions initially rise up during the deposition of the first 20 layers and then tend to stabilize. Undoubtedly, such high tensile stresses (up to 1600 MPa) contribute to the crack initiation and propagation at the basement of the T-shape part (Fig. 6(a)). However, this is not the case for the groove-patterned substrate because the stress concentration at both extremes of the part is avoided by reducing the local stiffness of the thick substrate (see Fig. 7(b) and 7(d)). Fig. 8 shows the evolution of the Von Mises stress field for both cases. Obviously, the proposed substrate design is able to drastically reduce (approximately 50%) the residual stresses (particularly in the bottom region), eliminating the cracking risk during LPBF. The predicted stress concentrations at the basement of the T-shape builds are similar with the experimentally measured results of the Ti-

6Al-4V LPBF-parts in previous reports [37,38].

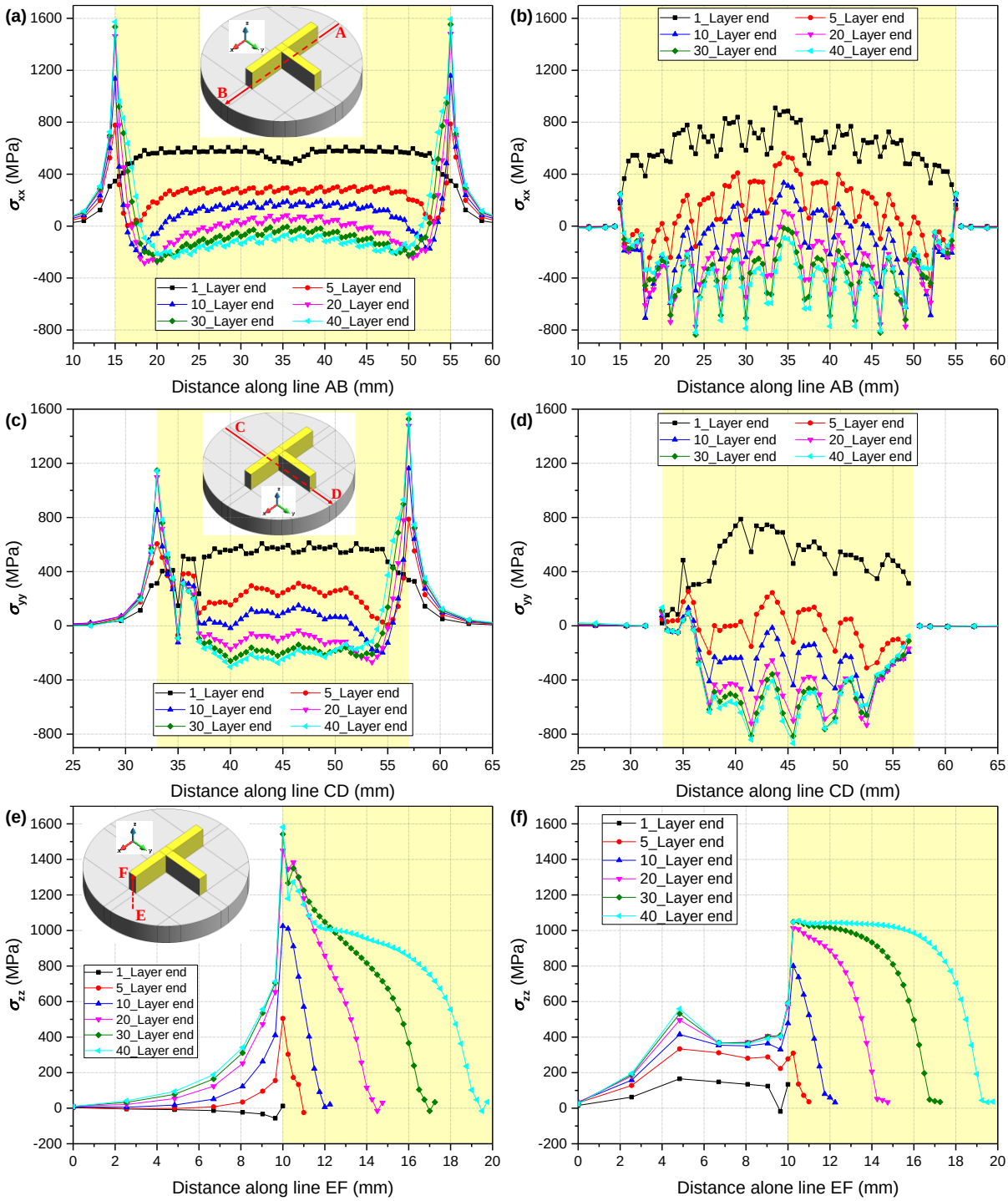


Fig. 7. Evolution of the predicted stresses of the T-shape parts in three orthogonal directions: (a,c,e) typical substrate; (b,d,f) patterned substrate.

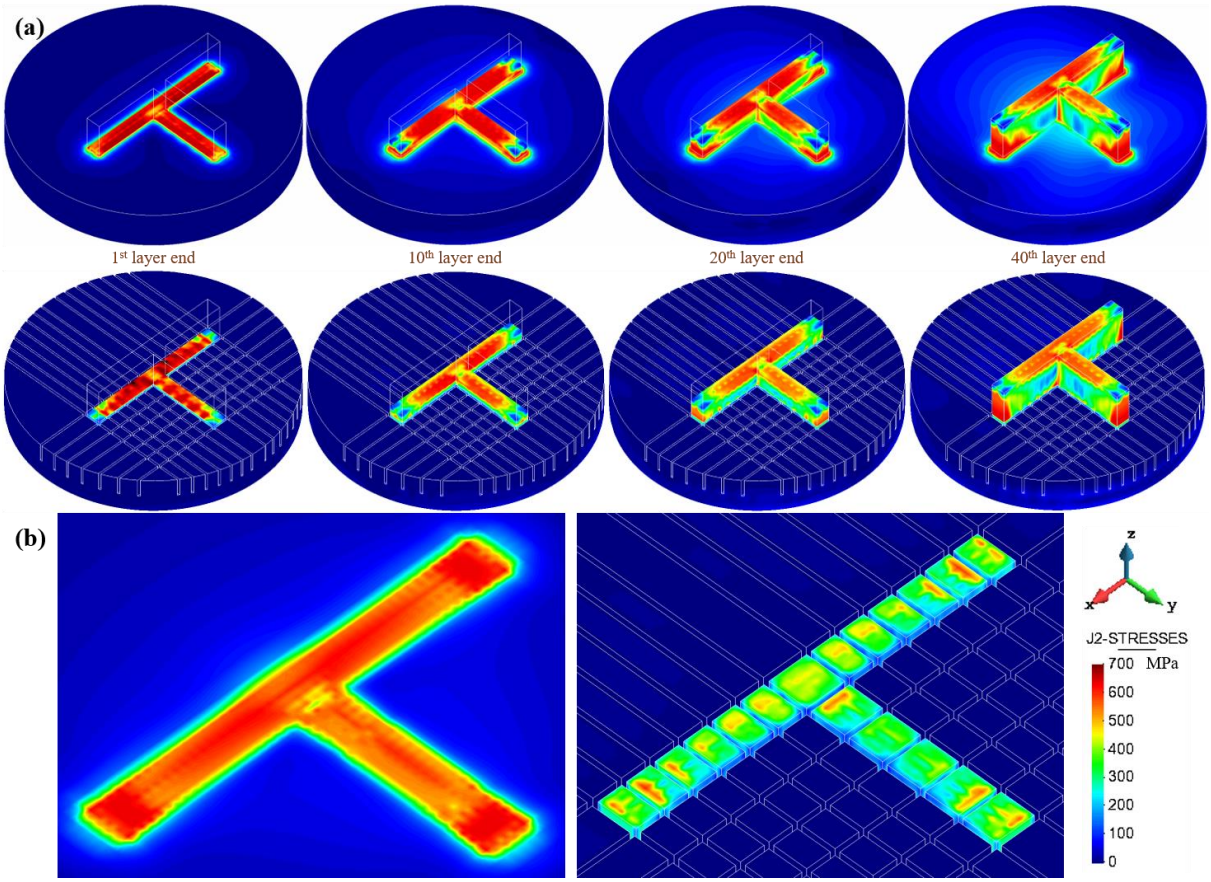

Fig. 8. (a) Evolution of the simulated Von Mises stress field of the T-shape parts fabricated on two different substrates; (b) enlarged part-substrate interface after the deposition of the 10th layer.

### 4.3 Comparison between substrate design and support assistance

To further clarify the novelty of substrate design and to distinguish it from the support assistance normally used in printing cantilever geometries in LPBF [21,39,40], a comprehensive comparison between them is performed in this section based on the mechanical analysis of two kinds of typical AM structures: without (Fig. 4(d)) and with (Fig. 4(e)) cantilever.

Firstly, the same T-shape structure without cantilever presented in Section 4.2 is virtually fabricated on the additional supports to check if stress reduction and crack prevention can be achieved by applying sacrificial support structures. Figs. 9 and 10 show the stress evolution in three orthogonal directions and the development of the Von Mises stress field of the T-shaped part with supports, respectively. Note that after the support structure is printed and before printing the T-shape build, the thermal stresses have accumulated at the basement of the supports, especially for the thicker supports (up to 1100 MPa in Fig. 9(a)). This is not the case for the substrate design in which the substrate is stress-free before LPBF (Fig. 2(b)). Furthermore, once new layers are stacked on the supports to form the T-shape build, the stress distributions pronouncedly change. Stress concentrations appear at the bottom ends of the supports and the build, and their magnitude is up to 1500 MPa (Fig. 9), easily triggering cracks at these corners, similarly to the case of the typical substrate (Figs. 6 and 7). Additionally, the residual stress accumulations at the built basement are hardly controlled by changing the thickness of the support legs (Fig. 10). Thereby, using additional supports to lower the crack risk is not effective and they increase both manufacturing time and cost.

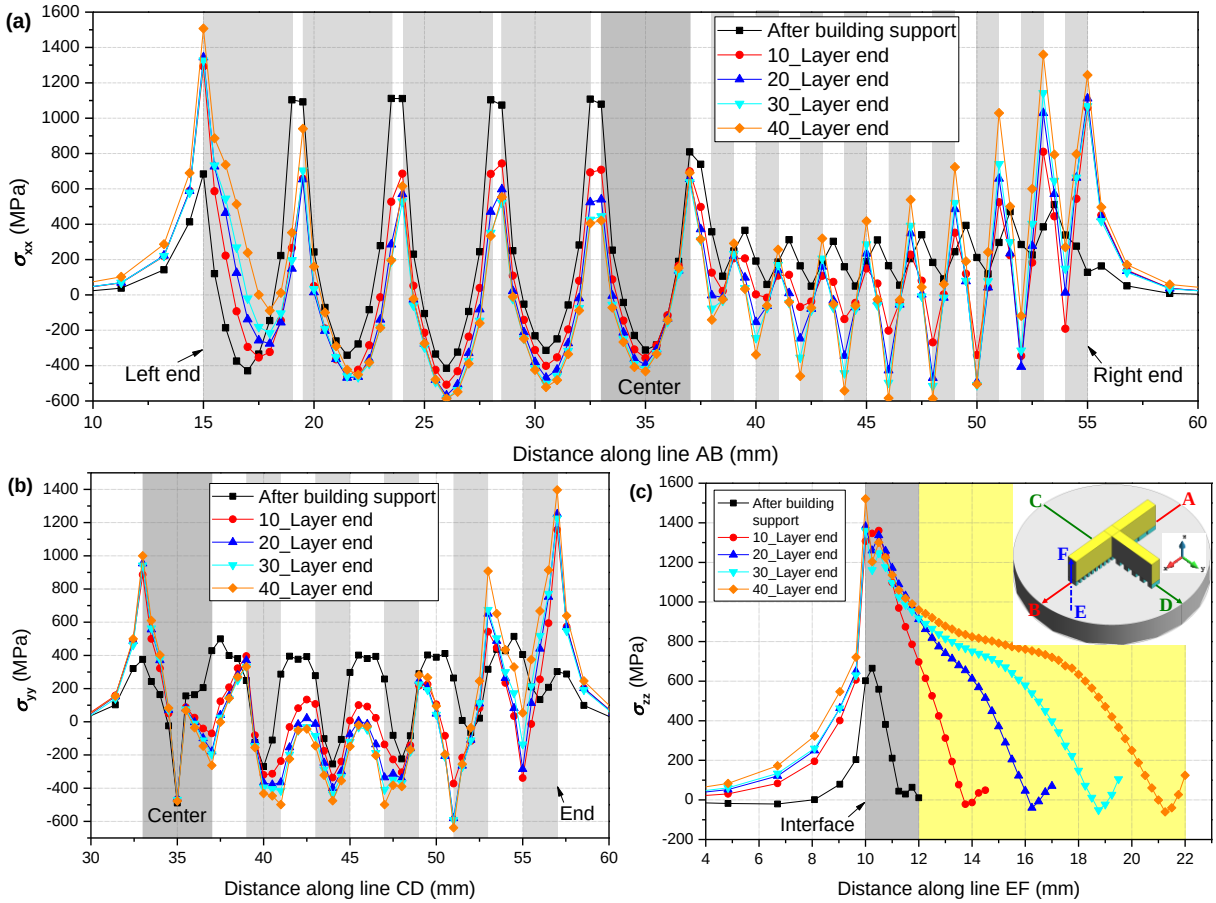


Fig. 9. Evolution of the predicted stresses of the T-shape part fabricated on the additional supports: (a) $\sigma_{xx}$ along the line AB; (b) $\sigma_{yy}$ along the line CD; (c) $\sigma_{zz}$ along the line EF.

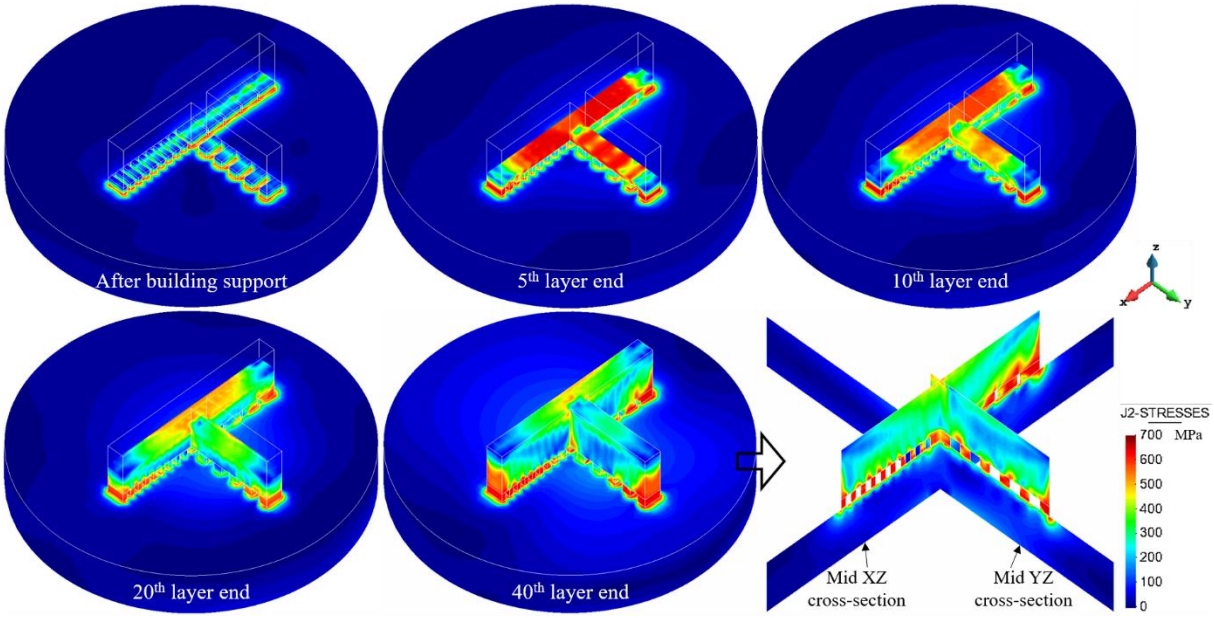


Fig. 10. Evolution of the predicted Von Mises stress contours of the T-shape part fabricated on the additional supports.

Secondly, a typical structure with cantilever is additively manufactured with the assistance of necessary supports. Here, the mechanical behavior of two T-shape cantilever parts deposited on the typical and patterned substrates, respectively, is compared, as shown in Figs. 11 and 12. In this case, it is still possible to apply the substrate design strategy to avoid the stress-induced cracks in LPBF. Observe that the typical substrate yields high stress

concentrations at the bottom ends of the built part. Nevertheless, the stress level is much lower for the patterned substrate. Also, the substrate design strategy provides more design freedom and support optimization in LPBF of cantilever structures.

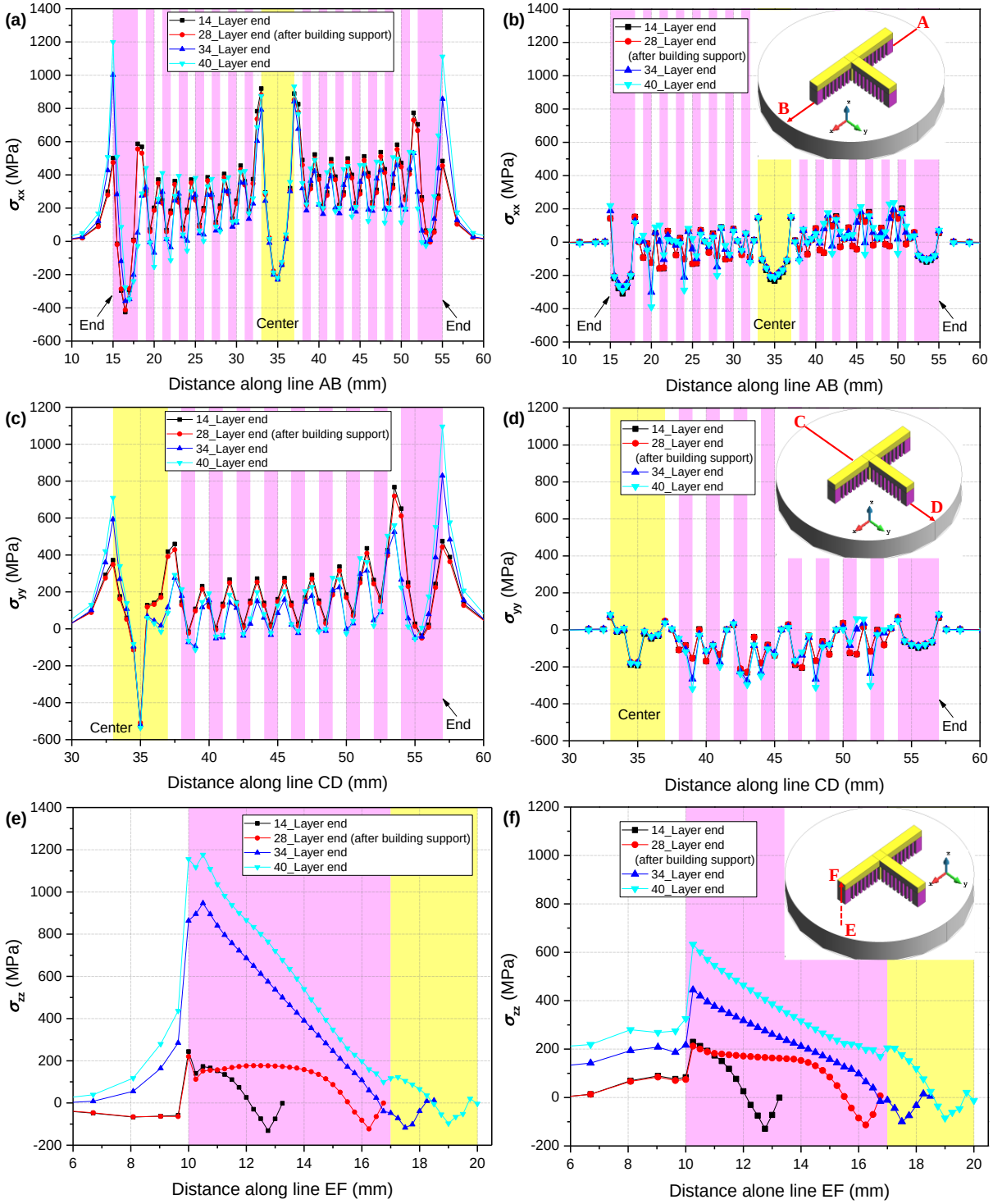


Fig. 11. Comparison of the predicted stress evolution of the T-shape cantilever structure deposited on the typical and patterned supports: (a) $\sigma_{xx}$ along the line AB; (b) $\sigma_{yy}$ along the line CD; (c) $\sigma_{zz}$ along the line EF.

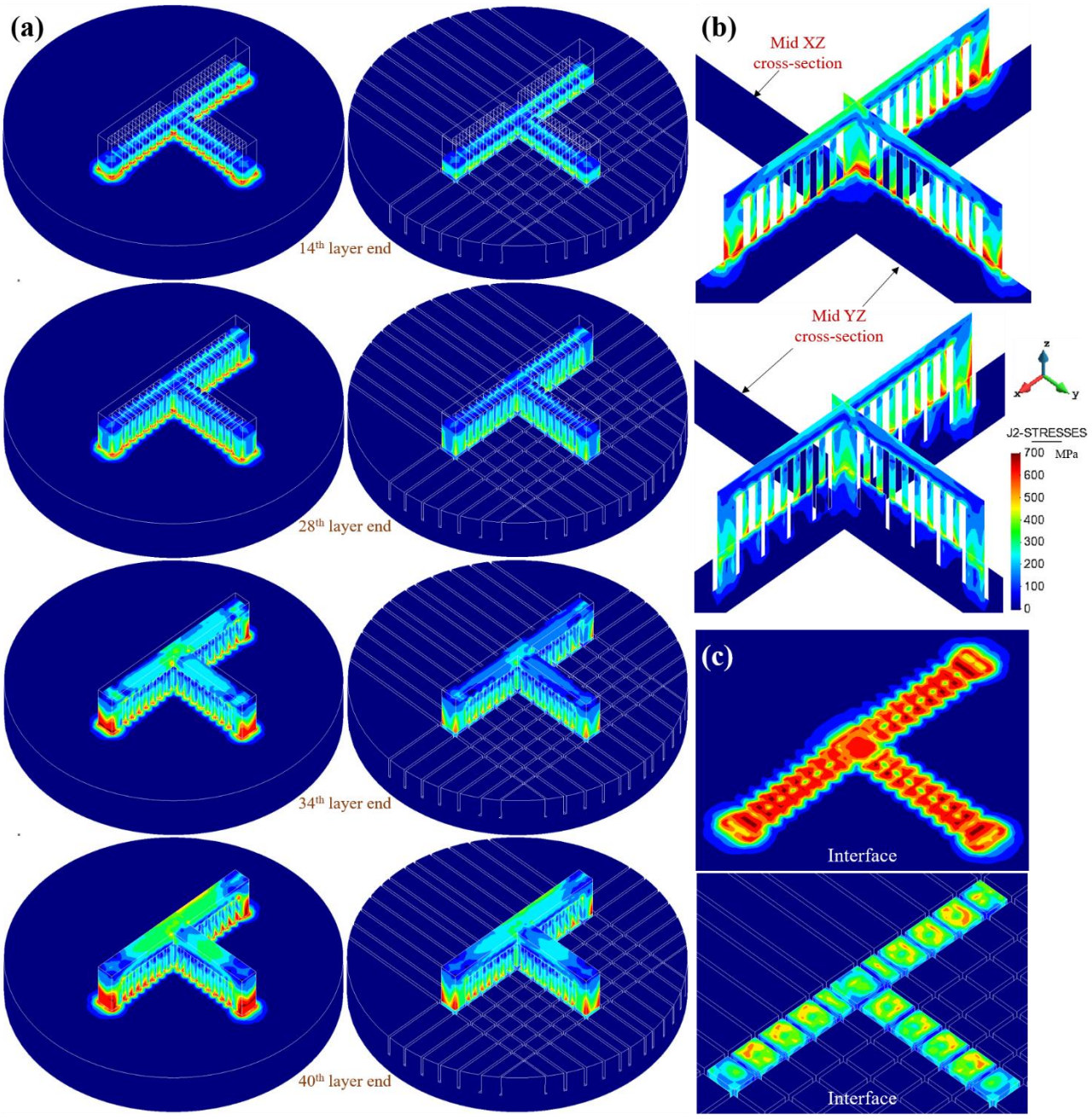


Fig. 12. (a) Comparison of the Von Mises stress evolution of the T-shape cantilever structure deposited on the typical and patterned supports; (b) Residual stresses at the mid XZ and YZ cross-sections; (c) Residual stresses at the build-substrate interface.

It should be mentioned that in this work the selected substrate ($\Phi 70 \times 10$ mm$^3$) is small and presents a reduced clamping condition. Thus, it is characterized by a small stiffness if compared to other industrial solutions. Moreover, the Ti-6Al-4V alloy used has a lower crack sensitivity than some other aluminum or Inconel super-alloys [41-43]. Thus, the proposed solution can be even more attractive in those AM configurations, offering a proven mitigation of residual stresses and a visible reduction of the cracking risk in metal AM processing.

### 4.4 Effect of substrate design on microstructure and microhardness

In this section, the microstructures and micro-hardness are analyzed to check against the possible drawbacks of adopting the proposed groove pattern in LPBF processes. Figs. 13 and 14 compare the temperature histories and the corresponding microstructures and microhardness at the center and different building heights of the short-wall of the

T-shape components fabricated with the two substrates, respectively. Note that both substrates produce similar microstructures and resulting microhardness because the two AM components experience very close temperature histories at these positions (see Fig. 13). This can be foreseen based on the following facts. The metallurgical evolution of Ti-6Al-4V strongly depends on the thermal histories in the high-temperature stage (e.g. >600ºC) rather than on the low-temperature stage [44]. On the one hand, the molten-pool shape, its temperature distribution and its rapid solidification during cooling are almost the same for the typical and patterned substrates due to the same process parameters used and, thus, the initially solidified microstructures are quite similar. On the other hand, unlike DED, the LPBF process without substrate preheating is characterized by a weak thermal accumulation and the Ti-6Al-4V microstructures do not change under such lower-temperature intrinsic heat treatment (see Fig. 13). Furthermore, the microhardness results as a function of microstructure [45] are similar for both cases.

Adding grooves in the substrate is purely a modification of the mechanical constraining and its influence on the heat dissipation and the temperature distribution in the build is very weak.

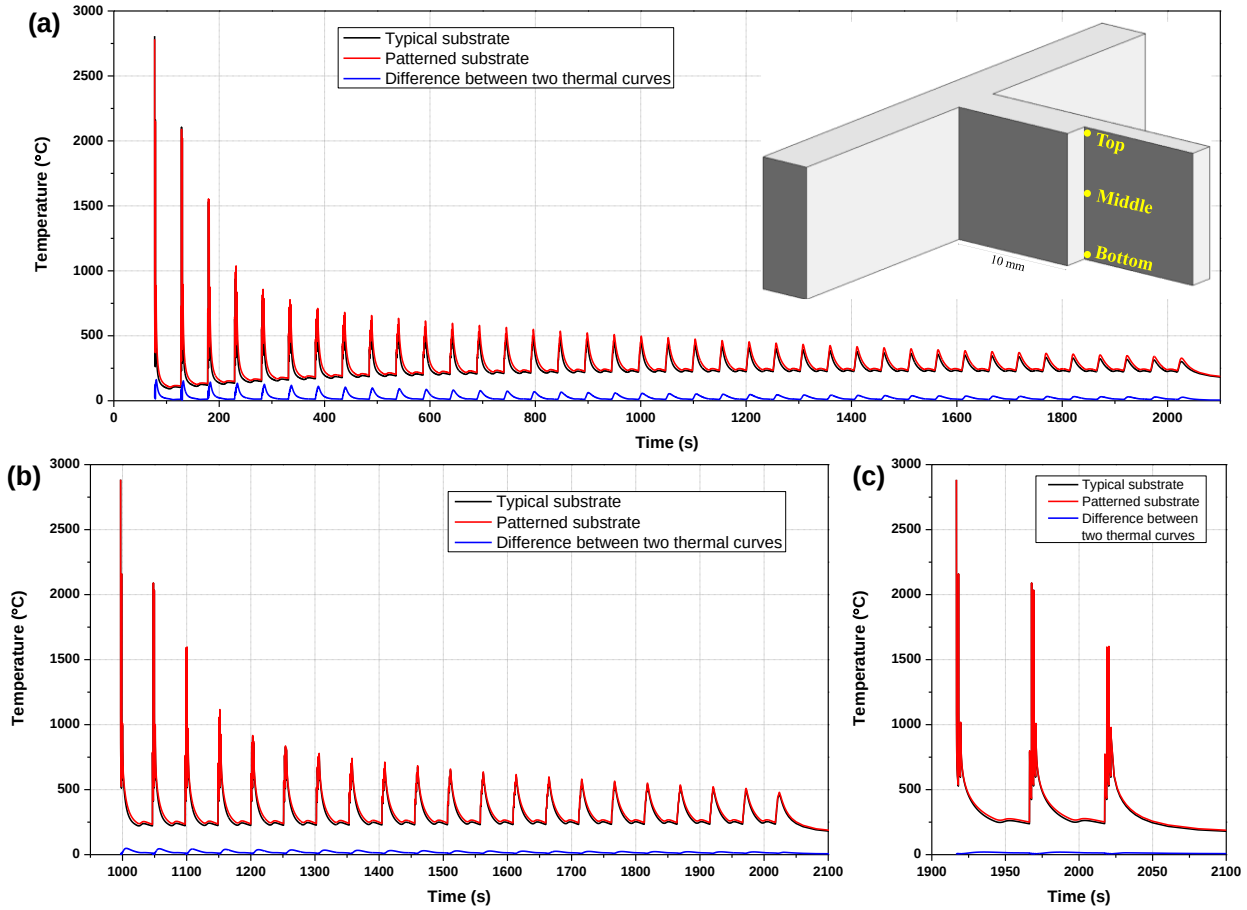


Fig. 13. Predicted thermal histories at different deposit heights of the short-wall of the T-shape build: (a) bottom; (b) middle; (c) top.

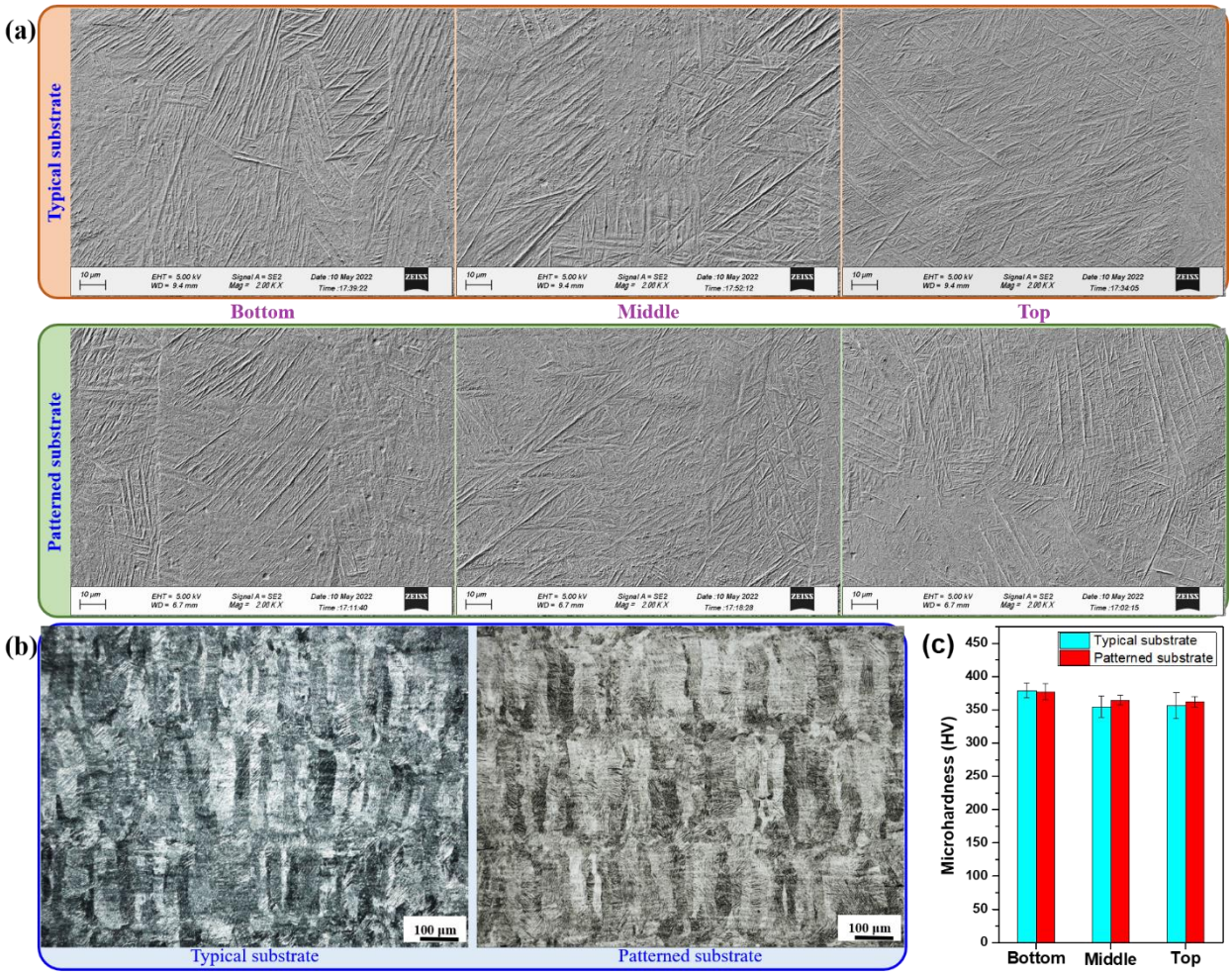


Fig. 14. Comparison of (a,b) microstructures and (c) microhardness in the T-shape deposits.

## 5 Conclusions

The main conclusions drawn from this work are as follows:

(1) The thermomechanical FE software is firstly validated with the experimental evidence from a bridge structure fabricated by LPBF. The calculated curling angle (2.76º) induced by the stress relief during the substrate removal process is very close to the measured value of about 2.8º [22]. Thus, the model can be employed to analyze the LPBF process.

(2) In AM, two key factors of MTG and yield temperature are responsible for the generation of residual stresses. Lower MTG or/and higher yield temperature (i.e. weaker mechanical constraint) favor the stress reduction. Based on this, a novel strategy of substrate design to optimize its structural stiffness is proposed to prevent stress accumulations and crack initiation in LPBF processes.

(3) Two T-shape components are printed on two different substrates: without and with grooves. In the former several cracks are observed while the latter is crack-free. The numerical simulation shows a higher stress concentration (up to 1600 MPa) at the bottom ends of the T-shape part when deposited on the typical substrate. However, optimizing the substrate design by adding the proposed groove-pattern successfully mitigates the residual stresses avoiding cracking.

(4) The comparison between the substrate design and the support assistance illustrates that for non-cantilever

structures, using additional supports instead of a modified substrate design fails to mitigate the stress accumulations at the built basement in LPBF process. For cantilever structures, using the patterned substrate efficiently curbs the stress development in LPBF, and can further reduce the cracking risk by combining support optimization.

(5) Remarkably, the substrate design approach has no significant influence on the metallurgy and microhardness of the build, while this is not the case when the MTG reduction approach is adopted.

(6) The proposed strategy is easy to apply and cost-effective. It can be applied to improve the printability of metallic materials with high crack sensitivity.

## 6 Acknowledgments

This work was funded by the European KYKLOS 4.0 project (No. 872570) and the China Scholarship Council (No. 201906290011).

## 7 References

[1] Plessis, A., S. Javad, M. Benedetti, S. Murchio, M. Leary, M. Watson, D. Bhate, and F. Berto. 2021. "Properties and applications of additively manufactured metallic cellular materials: a review." Progress in Materials Science: 100918. https://doi.org/10.1016/j.pmatsci.2021.100918

[2] Zhang, W., M. Tong, and N. Harrison. 2019. "Resolution, energy and time dependency on layer scaling in finite element modelling of laser beam powder bed fusion additive manufacturing." Additive Manufacturing 28: 610-620. https://doi.org/10.1016/j.addma.2019.05.002

[3] Huang, H., N. Ma, J. Chen, Z. Feng, and H. Murakawa. 2020. "Toward large-scale simulation of residual stress and distortion in wire and arc additive manufacturing." Additive Manufacturing 34: 101248. https://doi.org/10.1016/j.addma.2020.101248

[4] Mugwagwa, L., I. Yadroitsava, N. Makoana, and I. Yadroitsev. 2021. "Residual stress in laser powder bed fusion." In Fundamentals of Laser Powder Bed Fusion of Metals, 245-276. Elsevier. https://doi.org/10.1016/B978-0-12-824090-8.00014-7

[5] Lu, X., M. Chiumenti, M. Cervera, J. Li, X. Lin, L. Ma, G. Zhang, and E. Liang. 2021. "Substrate Design to Minimize Residual Stresses in Directed Energy Deposition AM Processes." Materials & Design 202: 109525. https://doi.org/10.1016/j.matdes.2021.109525

[6] Platl, J., S. Bodner, C. Hofer, A. Landefeld, H. Leitner, C. Turk, M. Nielsen, A. Demir, B. Previtali, J. Keckes, and R. Schnitzer. 2022. "Cracking mechanism in a laser powder bed fused cold-work tool steel: The role of residual stresses, microstructure and local elemental concentrations." Acta Materialia 225: 117570. https://doi.org/10.1016/j.actamat.2021.117570

[7] Liu, F., X. Lin, H. Yang, X. Wen, Q. Li, F. Liu, and W. Huang. 2017. "Effect of microstructure on the fatigue crack growth behavior of laser solid formed 300M steel." Materials Science and Engineering: A 695: 258-264. https://doi.org/10.1016/j.msea.2017.04.001

[8] Yu, X., X. Lin, H. Tan, Y. Hu, S. Zhang, F. Liu, H. Yang, and W. Huang. 2021. "Microstructure and fatigue crack growth behavior of Inconel 718 superalloy manufactured by laser directed energy deposition." International Journal of Fatigue 143: 106005. https://doi.org/10.1016/j.ijfatigue.2020.106005

[9] Ueda, Y., H. Murakawa, and N. Ma. 2012. Welding deformation and residual stress prevention. Elsevier.

[10] Lu, X., M. Cervera, M. Chiumenti, and X. Lin. 2021. "Residual Stresses Control in Additive Manufacturing." Journal of Manufacturing and Materials Processing 5(4): 138. https://doi.org/10.3390/jmmp5040138

[11] Zhang, W., M. Tong, and N. Harrison. 2020. "Scanning strategies effect on temperature, residual stress and deformation by multi-laser beam powder bed fusion manufacturing." Additive Manufacturing 36: 101507. https://doi.org/10.1016/j.addma.2020.101507

[12] Hu, Y., X. Lin, X. Yu, J. Xu, M. Lei, and W. Huang. 2017. "Effect of Ti addition on cracking and microhardness of Inconel 625 during the laser solid forming processing." Journal of Alloys and Compounds 711: 267-277. https://doi.org/10.1016/j.jallcom.2017.03.355

[13] Wang, W., W. Lin, R. Yang, Y. Wu, J. Li, Z. Zhang, and Z. Zhai. 2022. "Mesoscopic evolution of molten pool during selective laser melting of superalloy Inconel 738 at elevating preheating temperature." Materials & Design 213: 110355. https://doi.org/10.1016/j.matdes.2021.110355

[14] Wang, Y, X. Lin, N. Kang, Z. Wang, Q. Wang, Y. Liu, and W. Huang. 2022. "Laser powder bed fusion of Zr-modified Al–Cu–Mg alloy: Crack-inhibiting, grain refinement, and mechanical properties." Materials Science and Engineering: A 838: 142618. https://doi.org/10.1016/j.msea.2022.142618

[15] Svetlizky, D., M. Das, B. Zheng, A. Vyatskikh, S. Bose, A. Bandyopadhyay, J. Schoenung, E. Lavernia, and N. Eliaz. 2021. "Directed energy deposition (DED) additive manufacturing: Physical characteristics, defects, challenges and applications." Materials Today 49: 271-295. https://doi.org/10.1016/j.mattod.2021.03.020

[16] Lu, X., X. Lin, M. Chiumenti, M. Cervera, Y. Hu, X. Ji, L. Ma, and W. Huang. 2019. "In Situ Measurements and ThermoMechanical Simulation of Ti-6Al-4V Laser Solid Forming Processes." International Journal of Mechanical Sciences 153-154: 119–130. https://doi.org/10.1016/j.ijmecsci.2019.01.043

[17] Cao, J., M. Gharghouri, and P. Nash. 2016. "Finite-element analysis and experimental validation of thermal residual stress and distortion in electron beam additive manufactured Ti-6Al-4V build plates." Journal of Materials Processing Technology 237: 409-419. https://doi.org/10.1016/j.jmatprotec.2016.06.032
[18] Lu, X., X. Lin, M. Chiumenti, M. Cervera, Y. Hu, X. Ji, L. Ma, H. Yang, and W. Huang. 2019b. "Residual Stress and Distortion of Rectangular and S-Shaped Ti-6Al-4V Parts by Directed Energy Deposition: Modelling and Experimental Calibration." Additive Manufacturing 26: 166–179. https://doi.org/10.1016/j.addma.2019.02.001
[19] Song, X., S. Feih, W. Zhai, C. Sun, F. Li, R. Maiti, J. Wei, Y. Yang, V. Oancea, L. Brandt, A. Korsunsky. 2020. "Advances in additive manufacturing process simulation: Residual stresses and distortion predictions in complex metallic components." Materials & Design 193: 108779. https://doi.org/10.1016/j.matdes.2020.108779
[20] SHIPLEY, H. 2022. "Density Optimisation & In-Situ Microstructure Decomposition of As-Built Selective Laser Melted Ti-6Al-4V." PhD diss., University of Dublin. http://hdl.handle.net/2262/97868
[21] Cheng, L., X. Liang, J. Bai, Q. Chen, J. Lemon, and A. To. 2019. "On utilizing topology optimization to design support structure to prevent residual stress induced build failure in laser powder bed metal additive manufacturing." Additive Manufacturing 27: 290-304. https://doi.org/10.1016/j.addma.2019.03.001
[22] Wang, Z., X. Lin, N. Kang, J. Chen, Y. Tang, H. Tan, X. Yu, H. Yang, and W. Huang. 2021. "Directed energy deposition additive manufacturing of a Sc/Zr-modified Al–Mg alloy: effect of thermal history on microstructural evolution and mechanical properties." Materials Science and Engineering: A 802: 140606. https://doi.org/10.1016/j.msea.2020.140606
[23] Xue, A., X. Lin, L. Wang, X. Lu, H. Ding, and W. Huang. 2021. "Heat-affected coarsening of β grain in titanium alloy during laser directed energy deposition." Scripta Materialia 205: 114180. https://doi.org/10.1016/j.scriptamat.2021.114180
[24] Kruth, J., J. Deckers, E. Yasa, and R. Wauthlé. 2012. "Assessing and comparing influencing factors of residual stresses in selective laser melting using a novel analysis method." Proceedings of the institution of mechanical engineers, Part B: Journal of Engineering Manufacture 226(6): 980-991. https://doi.org/10.1177/0954405412437085
[25] Chiumenti, M., M. Cervera, A. Salmi, C. A. Saracibar, N. Dialami, and K. Matsui. 2010. "Finite element modeling of multi-pass welding and shaped metal deposition processes." Computer methods in applied mechanics and engineering 199(37-40): 2343-2359. https://doi.org/10.1016/j.cma.2010.02.018
[26] Lu, X., M. Chiumenti, M. Cervera, G. Zhang, and X. Lin. "Mitigation of residual stresses and microstructure homogenization in directed energy deposition processes." Engineering with Computers (2022): 1-20. https://doi.org/10.1007/s00366-021-01563-9
[27] Lu, X., X. Lin, M. Chiumenti, M. Cervera, J. Li, L. Ma, L. Wei, Y. Hu, and W. Huang. 2018. "Finite Element Analysis and Experimental Validation of the Thermomechanical Behavior in Laser Solid Forming of Ti-6Al-4V." Additive Manufacturing 21: 30–40. https://doi.org/10.1016/j.addma.2018.02.003
[28] Chiumenti, M., M. Cervera, N. Dialami, B. Wu, L. Jinwei, and C. Saracibar. 2016. "Numerical modeling of the electron beam welding and its experimental validation." Finite Elements in Analysis and Design 121: 118-133. https://doi.org/10.1016/j.finel.2016.07.003
[29] Chiumenti, M., E. Neiva, E. Salsi, M. Cervera, S. Badia, J. Moya, Z. Chen, C. Lee, and C. Davies. 2017. "Numerical modelling and experimental validation in Selective Laser Melting." Additive Manufacturing 18: 171-185. https://doi.org/10.1016/j.addma.2017.09.002
[30] GiD, The Personal Pre and Post-Processor, CIMNE, Technical University of Catalonia, 2002. https://www.gidsimulation.com/
[31] Ganeriwala, R., M. Strantza, W. King, B. Clausen, T. Phan, L. Levine, D. Brown, and N. Hodge. 2019. "Evaluation of a thermomechanical model for prediction of residual stress during laser powder bed fusion of Ti-6Al-4V." Additive Manufacturing (27): 489-502. https://doi.org/10.1016/j.addma.2019.03.034
[32] Li, C., Z. Y. Liu, X. Y. Fang, and Y. B. Guo. 2018. "On the simulation scalability of predicting residual stress and distortion in selective laser melting." Journal of Manufacturing Science and Engineering 140(4). https://doi.org/10.1115/1.4038893
[33] Zhang, W., M. Tong, and N. Harrison. 2021. "Multipart Build Effects on Temperature and Residual Stress by Laser Beam Powder Bed Fusion Additive Manufacturing." 3D Printing and Additive Manufacturing. https://doi.org/10.1089/3dp.2021.0143
[34] Salem, M., S. Roux, A. Hor, and G. Dour. 2020. "A new insight on the analysis of residual stresses related distortions in selective laser melting of Ti-6Al-4V using the improved bridge curvature method." Additive Manufacturing 36: 101586. https://doi.org/10.1016/j.addma.2020.101586
[35] Strantza, M., R. Ganeriwala, B. Clausen, T. Phan, L. Levine, D. Pagan, J. Ruff, W. King, N. Johnson, R. Martinez, V. Anghel, G. Rafailov, D. Brown. 2021. "Effect of the scanning strategy on the formation of residual stresses in additively manufactured Ti-6Al-4V." Additive Manufacturing 45: 102003. https://doi.org/10.1016/j.addma.2021.102003
[36] Promoppatum, P., and S. Yao. 2020. "Influence of scanning length and energy input on residual stress reduction in metal additive manufacturing: Numerical and experimental studies." Journal of Manufacturing Processes 49: 247-259. https://doi.org/10.1016/j.jmapro.2019.11.020
[37] Hodge, N., R. Ferencz, and R. Vignes. 2016. "Experimental comparison of residual stresses for a thermomechanical model for the simulation of selective laser melting." Additive Manufacturing 12: 159-168. https://doi.org/10.1016/j.addma.2016.05.011
[38] Ahmad, B., S. Veen, M. Fitzpatrick, and H Guo. 2018. "Residual stress evaluation in selective-laser-melting additively manufactured titanium (Ti-6Al-4V) and inconel 718 using the contour method and numerical simulation." Additive Manufacturing 22: 571-582. https://doi.org/10.1016/j.addma.2018.06.002
[39] Zhang, Z., O. Ibhadode, U. Ali, C. Dibia, P. Rahnama, A. Bonakdar, and E. Toyserkani. 2020. "Topology optimization parallel-computing framework based on the inherent strain method for support structure design in laser powder-bed fusion additive manufacturing." International Journal of Mechanics and Materials in Design 16(4): 897-923. https://doi.org/10.1007/s10999-020-09494-x
[40] Fang, Z., Z. Wu, C. Huang, and C. Wu. 2020. "Review on residual stress in selective laser melting additive manufacturing of alloy parts." Optics & Laser Technology 129: 106283. https://doi.org/10.1016/j.optlastec.2020.106283
[41] Mondal, B., T. Mukherjee, and T. DebRoy. 2022. "Crack free metal printing using physics informed machine learning." Acta Materialia 226: 117612. https://doi.org/10.1016/j.actamat.2021.117612
[42] Cao, Y., X. Lin, N. Kang, L. Ma, L. Wei, M. Zheng, J. Yu, D. Peng, and W. Huang. 2021. " A novel high-efficient finite element

analysis method of powder bed fusion additive manufacturing." Additive Manufacturing 102187. https://doi.org/10.1016/j.addma.2021.102187

[43] Zhang, W., F. Liu, F. Liu, C. Huang, H. Zheng, Q. Zhang, Y. Zheng, and J. Gao. 2022. "Microstructural evolution and cracking behavior of Hastelloy X superalloy fabricated by laser directed energy deposition." Journal of Alloys and Compounds 905: 164179. https://doi.org/10.1016/j.jallcom.2022.164179

[44] Song, T., T. Dong, S. Lu, K. Kondoh, R. Das, M. Brandt, and M. Qian. 2021. "Simulation-informed laser metal powder deposition of Ti-6Al-4V with ultrafine α-β lamellar structures for desired tensile properties." Additive Manufacturing 46: 102139. https://doi.org/10.1016/j.addma.2021.102139

[45] Lu, X., G. Zhang, J. Li, M. Cervera, M. Chiumenti, J. Chen, X. Lin, and W. Huang. 2021. "Simulation-assisted investigation on the formation of layer bands and the microstructural evolution in directed energy deposition of Ti6Al4V blocks." Virtual and Physical Prototyping: 1-17. https://doi.org/10.1080/17452759.2021.1942077

# Mitigation of residual stresses and microstructure homogenization in directed energy deposition processes

X. Lu, M. Cervera, M. Chiumenti, G. Zhang & X. Lin

*Engineering with Computers*

https://doi.org/10.1007/s00366-021-01563-9

Engineering with Computers
https://doi.org/10.1007/s00366-021-01563-9

ORIGINAL ARTICLE

# Mitigation of residual stresses and microstructure homogenization in directed energy deposition processes

Xufei Lu[1] · Michele Chiumenti[1] · Miguel Cervera[1] · Guohao Zhang[2] · Xin Lin[2]

Received: 18 October 2021 / Accepted: 28 November 2021


**Abstract**
In additive manufacturing (AM), residual stresses and microstructural inhomogeneity are detrimental to the mechanical properties of as-built AM components. In previous studies, the reduction of the residual stresses and the optimization of the microstructure have been treated separately. Nevertheless, the ability to control both them at the same time is mandatory for improving the final quality of AM parts. This is the main goal of this paper. Thus, a thermo-mechanical finite element model is firstly calibrated by simulating a multi-track 40-layer Ti–6Al–4V block fabricated by directed energy deposition (DED). Next, the numerical tool is used to study the effect of the baseplate dimensions and the energy density on both residual stresses and microstructure evolution. On the one hand, the results indicate that the large baseplate causes higher residual stresses but produces more uniform microstructures, and contrariwise for the smaller baseplate. On the other hand, increasing the energy density favors stress relief, but its effect fails to prevent the stress concentration at the built basement. Based on these results, two approaches are proposed to control both the stress accumulation and the metallurgical evolution during the DED processes: (i) the use of a forced cooling suitable for small baseplates and, (ii) the adoption of grooves when large baseplates are used. The numerical predictions demonstrated the effectiveness of the proposed manufacturing strategies.

**Keywords** Additive manufacturing · Thermo-mechanical simulation · Residual stress reduction · Microstructure control · Processing optimization

## 1 Introduction

Metal additive manufacturing (AM) is an advanced fabrication technology broadly applied in industry because of its ability to produce complex structural components [1, 2]. Directed energy deposition (DED) is one of the most promising AM techniques due to its high deposition efficiency suitable for manufacturing large-scale components [3]. However, AM is a complicated multi-physics and multi-scale process characterized by several thermal cycles with large temperature gradients as well as melting and solidification phase changes. As a consequence, AM-built products typically show non-uniform microstructure distribution, large residual stresses, thermal distortions, cracks and unsatisfactory mechanical properties [4–10]. Such drawbacks significantly prevent the extensive application of AM technologies in high-end manufacturing industry.

Taking into account the large number of variables (process parameters, material data, etc.) involved in AM, the use of numerical methods is generally employed to optimize the AM process. To date, several numerical models for AM have been developed to investigate the thermal, mechanical and microstructure evolutions [9–13]. Among them, Smith et al. [11] utilized the FE simulation coupled with the computational phase diagram thermodynamics to predict both the thermo-mechanical and the microstructural behavior. Denlinger et al. [12] developed a FE model to simulate the thermo-mechanical responses of Ti–6Al–4V and Inconel® 625 during DED; they found that only in Ti–6Al–4V it is possible to reduce both residual stress and distortion induced by solid-state phase-transformation (SSPT). Furthermore, Wang et al. [13] utilized compression tests at 600 °C and 700 °C with

✉ Xufei Lu
xlu@cimne.upc.edu

✉ Xin Lin
xlin@nwpu.edu.cn

[1] International Centre for Numerical Methods in Engineering, Universidad Politécnica de Cataluña, Barcelona, Spain

[2] State Key Laboratory of Solidification Processing, Northwestern Polytechnical University, Xi'an, China

Published online: 22 January 2022

in-situ neutron diffraction analysis to investigate the stress relief of Ti-6Al-4V using AM and conventional processing; their results showed that stresses are faster relaxed with the temperature rise.

The influence of different AM variables is investigated to try to reduce both residual stresses and part warpage [14–19]. In this sense, Mukherjee et al. [14] illustrated that the part warpage is dependent on the scanning strategy, the preheating and cooling conditions, the material properties and the printing parameters. Usually, residual stresses and warpage can be mitigated by preheating the substrate before AM, optimizing the deposition sequence and/or the process parameters [15–17]. It must be noted that the effect of different AM variables on the material behavior is not fully understood yet, especially for large-scale AM parts adopting complex scanning sequences.

On the other hand, the homogenization of the final microstructure is also a challenge in AM because of the temperature histories experienced at any location of the AM builds [20–22]. For instance, the lower part of the builds often undergoes a larger number of subsequent thermal cycles during the DED process than the top of the metal deposition. Consequently, the microstructure initially formed is generally coarsened and the martensitic phase ($\alpha'$ in AM titanium alloy) is decomposed because of an intrinsic heat treatment (IHT) [21, 22]. In addition, AM titanium alloys also present regularly distributed layer-bands along the building direction [23]. By modifying the scanning patterns (i.e. the induced thermal history), it is possible to tailor the microstructure and, thus, the final material properties. Kürnsteiner et al. [24] demonstrated that adopting a periodic interlayer dwell-time produce martensite and, thus, the yield strength and ductility of a maraging steel by DED can be increased.

Generally, most of the reported studies are focused on either the microstructural control or the reduction of residual stresses and part warpage. Controlling both of them is a complex task even if it is mandatory to satisfy the fabrication requirements for high-quality AM parts. Thus, the main objective of this work is to propose a fabrication strategy able to deal with both issues: the mitigation of the residual stresses and the homogenization of the resulting microstructure. In AM, this can be achieved by optimizing the temperature field and its evolution during the printing process allowing for the IHT effect on the microstructural transformation and stress relaxation.

It has been also observed that the mechanical response of the AM builds is closely related to the mechanical constraining with the baseplate. This is especially true when large/thick baseplate are utilized to avoid the part warpage. Nevertheless, such rigid baseplates easily yield high residual stresses that transform into part-distortion after the baseplate removal [9]. Therefore, the optimization of the baseplate stiffness is key to mitigate residual stresses and warpage. Figure 1 presents the diagram for the simultaneous control of residual stresses and microstructure evolution by optimizing both the temperature histories (i.e. thermal cycles) and the mechanical constraints (baseplate geometry) during DED processes.

To this end, an in-house 3D thermo-mechanical FE model is first calibrated adopting in-situ temperature and displacement measurements from two part-scale Ti–6Al–4V blocks by DED. Next, the validated model is employed to investigate the influence of the baseplate size and the laser energy density on the thermal, metallurgical and mechanical responses. Finally, two strategies are proposed to effectively reduce both the stress accumulation and the microstructural coarsening in DED components: (i) the use of a forced cooling suitable for small baseplates and, (ii) the adoption of grooves when large baseplates are used.

## 2 Experimental campaign

Until now, the influence of the processes parameters on AM process has been often reported, while the effect of the baseplate size has seldom been studied. Thereby, two baseplates annealed Ti–6Al–4V of different sizes and, thus, characterized by different heat-retaining capability and structural stiffness were investigated to assess their respective thermomechanical behavior. As shown in Fig. 2, the larger baseplate ($200\times100\times25$ mm$^3$) is fixed as a cantilever while the smaller one ($140\times50\times6$ mm$^3$) is clamped at both ends because of its reduced bending stiffness. These two baseplates are used to manufacture the same multi-layer multi-pass blocks by DED technology. The DED system used consists of a semiconductor laser

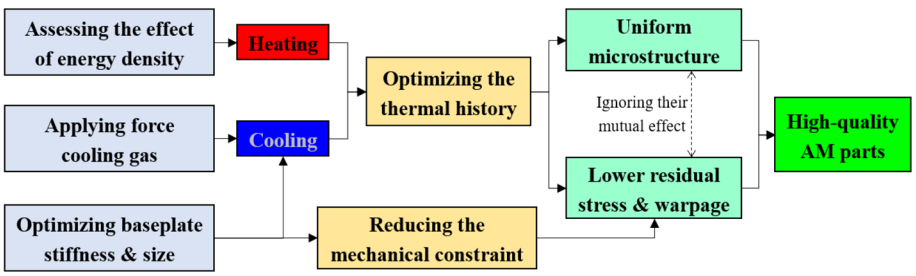


**Fig. 1** Concurring control of residual stress and microstructure in AM

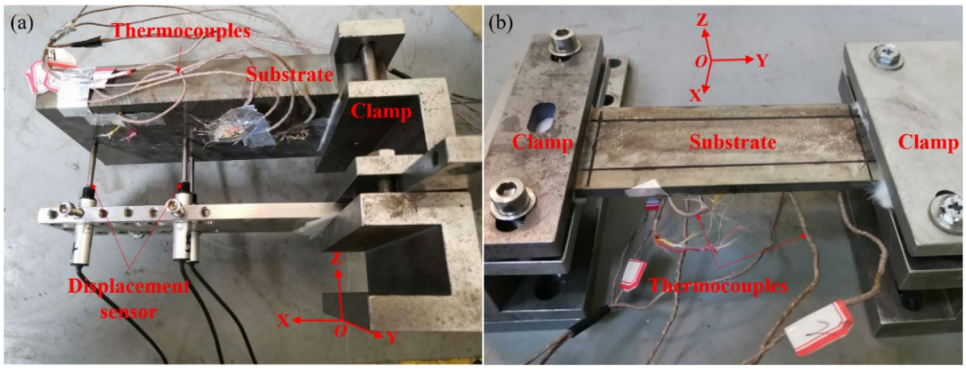


**Fig. 2** Experimental equipment of in-situ temperature and displacement measurement during the DED process: **a** the large baseplate is clamped as a cantilever, **b** the small baseplate is fixed at both ends

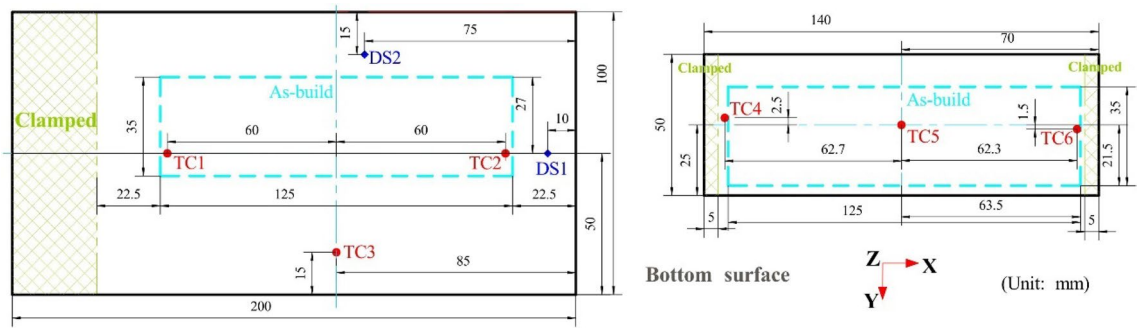


**Fig. 3** Part sizes and the locations of the six thermocouples (TC1–TC6) and two displacement sensors (DS1–DS2) on the bottom surface of the baseplates

diode with a maximum output power of 6 kW, a five-axis numerical control workbench, a DPSF-2 high-accuracy adjustable automatic power feeder and an argon purged processing chamber with very low oxygen content. The material used to deposit the blocks is spherical Ti–6Al–4V powder with 53–325 µm diameter and low oxygen, produced by a plasma electrode process. The powder is dried in a vacuum oven at 125 °C for 3 h before the DED.

Figure 3 shows the baseplates and the corresponding location of both the thermocouples (TC1–TC6) and the displacement sensors (DS1–DS2) used to record the temperature and displacement evolutions of the bottom surface of the baseplates, respectively. Six *Omaga GG-K-30* type thermocouples with a measurement uncertainty of 2.2 °C (±7.5%) and two *WXXY PM11-R1-20L* displacement sensors with a maximum range of 20 mm and an accuracy of 0.02% were employed. All the temperature and displacement signals during the DED process are recorded via a *Graphtec GL-900* 8 high-speed data-logger.

Figure 4 shows the printing path defined by four different sequences repeated every 4-layers. Table 1 displays the DED process parameters. Case-1 setting is used to fabricate two 40-layers blocks with the same dimension of $125 \times 35 \times 20$ mm$^3$. The other settings in Table 1 are used for the sensitivity analysis of the volumetric energy density, $E = P/(\mathrm{VHD})$, on the thermo-metallurgical-mechanical responses.

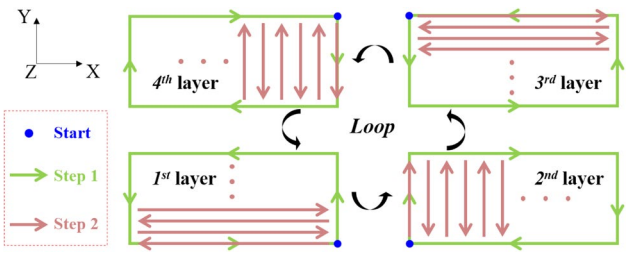


**Fig. 4** Schematic of scanning strategy used to build the two blocks

**Table 1** DED processing parameters utilized for printing the blocks

| | Laser power, $P$ (W) | Scan speed, $V$ (mm/s) | Energy density, $E$ (J/mm$^3$) | Up-lift height, $H$ (mm) | Beam radius, $D$ (mm) |
|---|---|---|---|---|---|
| Case 1 | 2000 | 15.0 | 53 | 0.5 | 5.0 |
| Case 2 | 1000 | 15.0 | 27 | 0.5 | 5.0 |
| Case 3 | 1333 | 10.0 | 53 | 0.5 | 5.0 |
| Case 4 | 2000 | 10.0 | 80 | 0.5 | 5.0 |
| Case 5 | 3000 | 15.0 | 80 | 0.5 | 5.0 |

To examine the microstructure, the samples extracted from the mid-YZ plane are firstly etched using Kroll's solution (1 ml HF, 3 ml $HNO_3$ and 46 ml $H_2O$) and then featured by optical microscopy (Keyence VH-Z50L). Next, the α-lath width is measured from 5 photographs with a magnification of 2000. In each case the number of measures is higher than 100. Finally, the average value of the α-lath size is calculated. Additionally, the Vickers hardness corresponding to the above microstructure is tested using a Duranmin-A300 micro-hardness tester with a load of 2000 g and an acting time of 15 s. Twenty different points are chosen to measure the mean hardness at each position.

## 3 Numerical simulation

In this work, an in-house 3D thermo-mechanical FE software, *COMET*, is used to perform high-fidelity modelling of the AM process. The sequential thermo-mechanical coupling is undertaken as follows: (i) for each time-step, the transient thermal analysis is firstly carried out; next (ii) the stress analysis is solved adopting to the obtained thermal field. The details of this thermo-mechanical model in terms of both the governing equations and the constitutive laws can be found in previous works [25–27].

### 3.1 Thermal analysis for AM

The governing equation for the transient thermal analysis is the balance of energy equation:

$$\dot{H} = -\nabla \cdot \mathbf{q} + \dot{Q}, \tag{1}$$

where $\dot{H}$ and $\dot{Q}$ are the enthalpy rate and the heat source (per unit of volume), respectively. The latter is defined in terms of the total laser input, $\dot{P}$, the laser absorption efficiency, $\eta_{\mathrm{p}}$, and the volume of the melt pool, $V_{\mathrm{pool}}^{\Delta t}$, as:

$$\dot{Q} = \frac{\eta_{\mathrm{p}} \dot{P}}{V_{\mathrm{pool}}^{\Delta t}}. \tag{2}$$

The heat flux $\mathbf{q}$ is defined according to Fourier's law

$$\mathbf{q} = -k \nabla T, \tag{3}$$

where $k$ and $\nabla T$ are the (temperature-dependent) thermal conductivity and the thermal gradient, respectively.

The heat dissipation due to convection is defined through Newton's law:

$$q_{\mathrm{conv}} = h_{\mathrm{conv}} \left( T - T_{\mathrm{room}} \right), \tag{4}$$

where $h_{\mathrm{conv}}$ is the convective Heat Transfer Coefficient (HTC), $T$ is the surface temperature of the workpiece and $T_{\mathrm{room}}$ is the room temperature.

The heat loss by the radiation, $q_{\mathrm{rad}}$, is computed by Stefan-Boltzmann's law:

$$q_{\mathrm{rad}} = \varepsilon_{\mathrm{rad}} \sigma_{\mathrm{rad}} \left( T^4 - T_{\mathrm{room}}^4 \right), \tag{5}$$

where $\varepsilon_{\mathrm{rad}}$ and $\sigma_{\mathrm{rad}}$ are the surface emissivity and the Stefan–Boltzmann constant, respectively.

### 3.2 Mechanical analysis

The stress analysis is governed by the balance of momentum and the continuity equations:

$$\nabla \cdot \mathbf{s} + \nabla p + \mathbf{b} = 0, \tag{6}$$

$$\left( \nabla \cdot \mathbf{u} - e^{T} \right) - \frac{p}{K} = 0, \tag{7}$$

where the Cauchy stress tensor $\boldsymbol{\sigma}$ is split into its spherical (pressure) $p$ and deviatoric $\mathbf{s}$ parts, respectively, as:

$$\boldsymbol{\sigma} = p\boldsymbol{I} + \mathbf{s}(\mathbf{u}), \tag{8}$$

$\mathbf{b}$ and $K(T)$ are the body force (per unit of volume) and the (temperature-dependent) bulk modulus, respectively. The thermal deformation $e^{\mathrm{T}}$ is determined as

$$e^{\mathrm{T}}\left(T, f_S\right) = e^{\mathrm{cool}}(T) + e^{\mathrm{pc}}\left(f_{\mathrm{S}}\right), \tag{9}$$

where $e^{\mathrm{cool}}(T)$ and $e^{\mathrm{pc}}(f_{\mathrm{S}})$ are the thermal expansion/contraction and thermal shrinkage in the liquid-to-solid phase transformation, as a function of the initial temperature $T_0$ and the solid fraction $f_{\mathrm{S}}$, respectively and expressed as

$$e^{\mathrm{cool}}(T) = \alpha(T)\left(T - T_0\right), \tag{10}$$

$$e^{\mathrm{pc}}\left(f_{\mathrm{S}}\right) = \beta f_{\mathrm{S}}, \tag{11}$$

where $\alpha$ and $\beta$ are the (temperature-dependent) thermal expansion and the shrinkage coefficients, respectively.

Note that the mechanical problem defined by Eqs. (6), (7) is dependent on both the displacement $\mathbf{u}$ and the pressure field $p$, and it is suitable for both compressible and the fully incompressible (isochoric) material behavior.

In AM, the temperature fluctuates between $T_{\mathrm{room}}$ and temperatures above the melting point ($T_{\mathrm{melt}}$). Thus, the materials must be featured in its solid, mushy and liquid phases.

A *J2*-thermo-elasto-visco-plastic model is adopted in the solid phase, thus from $T_{\mathrm{room}}$ to the annealing temperature $T_{\mathrm{anneal}}$. All the material properties are assumed as temperature-dependent. The von-Mises yield surface is determined as

$$\Phi\left(\mathbf{s}, q_{\mathrm{h}}, T\right) = \|\mathbf{s}\| - \sqrt{\frac{2}{3}}\left[\sigma_{\mathrm{y}}(T) - q_{\mathrm{h}}\right], \tag{12}$$

where $\sigma_y$ is the (temperature-dependent) yield stress accounting for the thermal softening while $q_h$ is the stress-like variable controlling the isotropic strain-hardening, defined as

$$q_h(\xi, T) = -\left[\sigma_\infty(T) - \sigma_y(T)\right]\left[1 - e^{-\delta(T)\xi}\right] - h(T)\xi, \tag{13}$$

where $\xi$ and $\sigma_\infty$ are the isotropic strain-hardening variable and the (temperature-dependent) saturation flow stress, respectively, while $\delta$ and $h$ are the (temperature-dependent) parameters to model the exponential and linear hardening laws, respectively.

The deviatoric counterpart of Cauchy's stress tensor is expressed as

$$\mathbf{s} = 2G(\mathbf{e} - \mathbf{e}^{vp}), \tag{14}$$

where $G$ is the (temperature-dependent) shear modulus, while $\mathbf{e}$ and $\mathbf{e}^{vp}$ are the total (deviatoric) strain and the visco-plastic strain, respectively. The former is obtained from the total strain tensor $\boldsymbol{\varepsilon}(\mathbf{u}) = \nabla^{sym}(\mathbf{u})$, while the evolution laws of both the visco-plastic strain tensor and the isotropic strain-hardening variable are obtained from the principle of maximum plastic dissipation as

$$\dot{\mathbf{e}}^{vp} = \dot{\gamma}^{vp}\frac{\partial\Phi\left(\mathbf{s}, q_h\right)}{\partial\mathbf{s}} = \dot{\gamma}^{vp}\frac{\mathbf{s}}{\|\mathbf{s}\|} = \dot{\gamma}^{vp}\mathbf{n}, \tag{15}$$

$$\dot{\xi} = \dot{\gamma}^{vp}\frac{\partial\Phi\left(\mathbf{s}, q_h\right)}{\partial q_h} = \sqrt{\frac{2}{3}}\dot{\gamma}^{vp}, \tag{16}$$

where $\mathbf{n}$ stands for the normal to the yield surface, and $\dot{\gamma}^{vp}$ is the visco-plastic multiplier, expressed as.

$$\dot{\gamma}^{vp} = \left\langle \frac{\partial\Phi\left(\mathbf{s}, q_h\right)}{\eta} \right\rangle^{\frac{1}{m}}, \tag{17}$$

where $\langle\dot{\rangle}$ is the Macaulay bracket, while $m$ and $\eta$ are the temperature-dependent rate sensitivity and plastic viscosity, respectively.

Note that, when the temperature gets close to $T_{anneal}$, the yield limit $\sigma_y$ tends to 0. Thereby, the deviatoric Cauchy stress reduces to

$$\mathbf{s} = \eta(\dot{\gamma}^{vp})^m\mathbf{n} = \eta_{eff}\dot{\mathbf{e}}^{vp}, \tag{18}$$

where $\eta_{eff} = \eta(\dot{\gamma}^{vp})^{m-1}$ is the effective viscosity. Thus, above $T_{anneal}$ the material is featured by a purely viscous law [28]. A non-Newtonian behavior with $m > 1$ is adopted for the mushy phase (from $T_{anneal}$ to $T_{melt}$), while a Newtonian law, $m = 1$, features the liquid phase (for $T > T_{melt}$).

### 3.3 FE modelling of AM

To model the advance of the AM process, a time discretization procedure is needed. The time-marching scheme is characterized by a time step, $\Delta t = t^{n+1} - t^n$. Thereby, the melt pool is allowed to move step-by-step according to the printing pattern from the current location defined at time $t^n$ to that at time $t^{n+1}$. Within this interval, the heat is input to the elements belonging to the melt-pool volume and, at the same time, the feeding powder conforms the AM deposit.

Hereby, the software parses the same input file (CLI format) following the actual building sequence as adopted to inform the AM printer. The *birth–death-element* technique is utilized to activate the elements corresponding to each new layer. Therefore, the numerical strategy for the AM process requires an ad-hoc procedure to categorize the elements into: *active*, *inactive* and *activated* elements. At each time step, an octree-based searching algorithm is employed to search the elements belonging to the melt pool (*active*) and to the new deposit (*activated*). The current computational domain consists of both *active* and *activated* elements, while the *inactive* elements are neither assembled nor computed into the global matrix of the analysis [29].

### 3.4 Geometrical model and mesh generation

In this work, the generation of the CAD geometries and the FE meshing, as well as the results post-processing are carried out through the pre–post-processor *GiD* [30]. Figure 5 presents different 3D geometries of DED parts and the corresponding generated meshes. Figure 5a, b show the same multi-layer multi-pass block deposited on the large and small baseplates, respectively. Figure 5c depicts an optimized baseplate with some grooves to control the stress development. Table 2 summarizes the geometrical dimensions of all the samples shown in Fig. 5 and the corresponding numbers of elements and nodes. According to the mesh convergence investigations [16], the mesh size is set to $1.25 \times 1.25 \times 0.5$ mm$^3$ for the build, while a coarser mesh is used for the baseplate, balancing the computing cost and an acceptable simulation accuracy.

### 3.5 Material properties and boundary conditions

Table 3 shows the values of the temperature-dependent thermal and mechanical properties of Ti–6Al–4V titanium alloy used for the material characterization of both the metal depositions and the baseplates in all the numerical predictions [9]. A higher heat conductivity of 83.5 W/(m °C) is assumed when the temperatures is above $T_{melt}$, to account for the convective flow inside the melt pool [31].

The heat transfer by convection and radiation between the DED parts and the surrounding is considered for all the

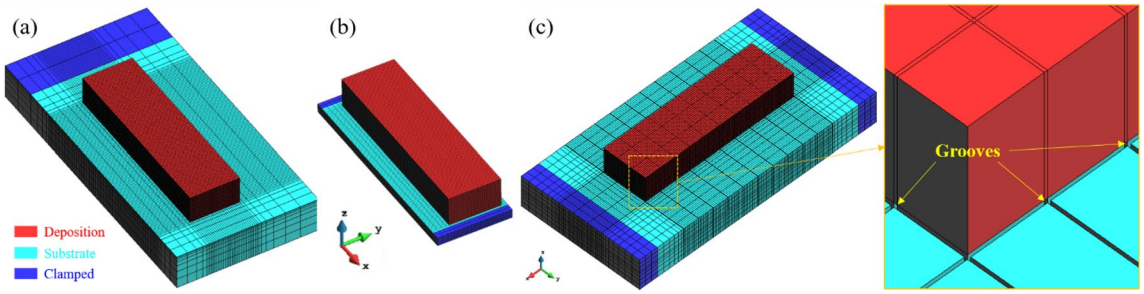


**Fig. 5** 3D FE meshes of the blocks deposited on the: **a** large baseplate, **b** small baseplate, **c** large baseplate with grooves

**Table 2** Baseplate dimensions and the numbers of FE elements and nodes

| | Baseplate size (mm) | Number of hexahedral elements | Number of nodes |
|---|---|---|---|
| Large baseplate | 200×100×25 | 142,576 | 153,320 |
| Small baseplate | 140×50×6 | 141,104 | 151,180 |
| Large baseplate with grooves | 200×100×25 | 191,336 | 210,780 |

free surfaces of the workpiece. The calibrated value of the HTC by convection and emissivity are $h_{conv} = 5$ W/m$^2$ °C and $\varepsilon_{rad} = 0.45$, respectively. Also, an HTC of 40 W/(m$^2$ °C) is adopted to account for the heat conduction at the interface between the fixture and the baseplate. The room temperature, $T_{room} = 25$ °C, is assumed for all thermal analyses. The laser efficiency is set as $\eta = 0.37$.

## 4 Calibration of the thermo-mechanical FE model

In previous works, the coupled thermomechanical model adopted was validated to optimize both material properties and processing parameters for the AM analysis with Ti–6Al–4V [7]. Here, to guarantee the accuracy of the simulation, the FE model is calibrated by in-situ temperature and displacement measurements. Figure 6 compares the predicted and experimental temperature histories at different points (see Fig. 3). Note that a remarkable agreement between numerical (dash lines) and experimental (solid lines) results is achieved, as reported in reference [21]. Also, the average numerical error during the entire processing is calculated, resulting in less than 3% for each thermocouple.

Based on this calibrated thermal model, the mechanical response induced by the DED process is predicted by the fully coupled thermo-mechanical analysis. To assess the model precision, Fig. 7 compares the computed and measured vertical displacements of points DS1 and DS2 at the baseplate bottom along the deposition direction. Also in this case, the numerical results agree with the experimental evidence. A slight discrepancy is due to the simplification of

**Table 3** Temperature-dependent material properties of Ti–6Al–4V [8]

| Temperature (°C) | Density (kg/m$^3$) | Thermal conductivity (W/(m °C)) | Heat capacity (J/(kg °C)) | Poisson's ratio | Thermal expansion coefficient (μm/(m °C)) | Young's modulus (GPa) | Elastic limit (MPa) |
|---|---|---|---|---|---|---|---|
| 20 | 4420 | 7 | 546 | 0.345 | 8.78 | 110 | 850 |
| 205 | 4395 | 8.75 | 584 | 0.35 | 10 | 100 | 630 |
| 500 | 4350 | 12.6 | 651 | 0.37 | 11.2 | 76 | 470 |
| 995 | 4282 | 22.7 | 753 | 0.43 | 12.3 | 15 | 13 |
| 1100 | 4267 | 19.3 | 641 | 0.43 | 12.4 | 5 | 5 |
| 1200 | 4252 | 21 | 660 | 0.43 | 12.42 | 4 | 1 |
| 1600 | 4198 | 25.8 | 732 | 0.43 | 12.5 | 1 | 0.5 |
| 1650 | 3886 | 83.5 | 831 | 0.43 | 12.5 | 0.1 | 0.1 |
| 2000 | 3818 | 83.5 | 831 | 0.43 | 12.5 | 0.01 | 0.01 |

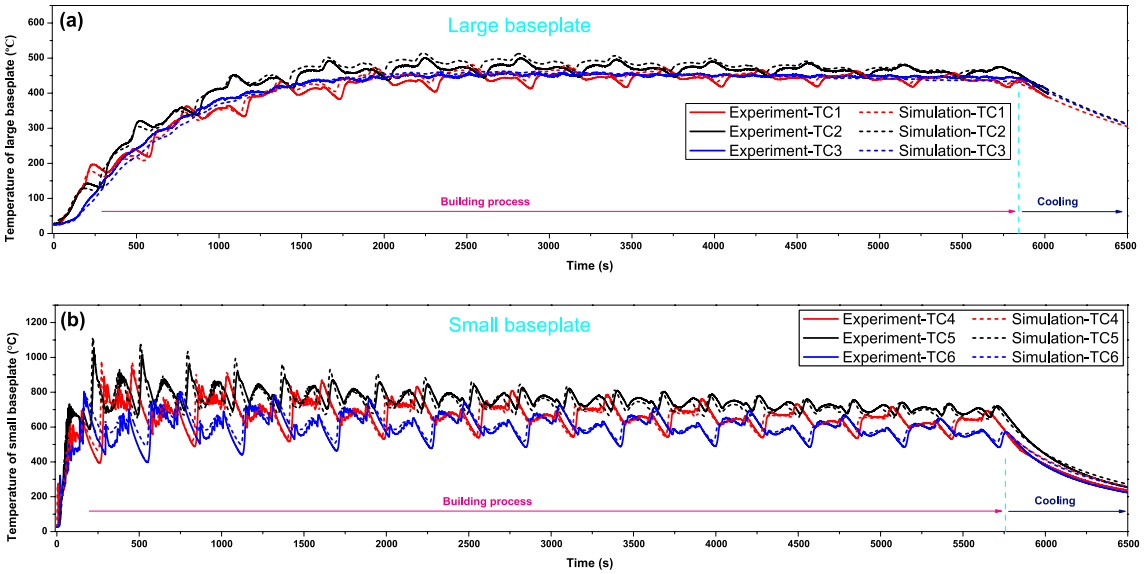


**Fig. 6** Comparison between the predicted and measured temperature histories at the bottom of **a** the large baseplate, **b** the small baseplate

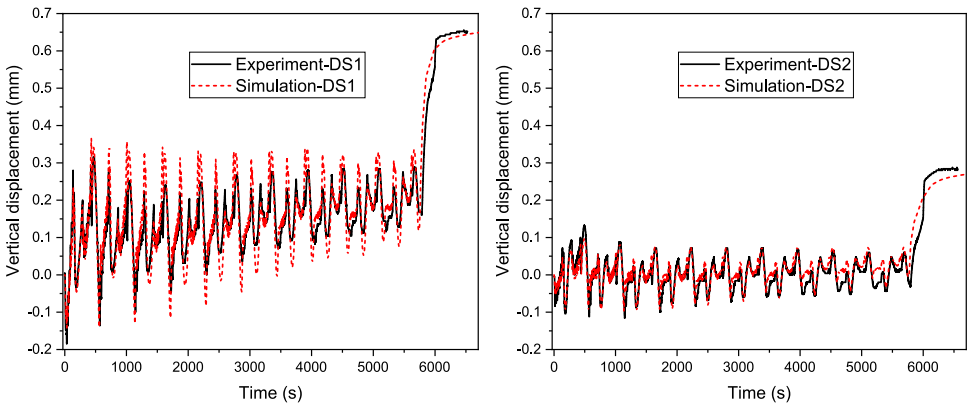


**Fig. 7** Large baseplate comparison between the simulated and the experimental results of the vertical displacement of points DS1 and DS2 at the bottom of the baseplate

the boundary conditions used and the possible experimental uncertainties.

## 5 Thermo-metallurgical–mechanical responses

In this section, the baseplate size and the sensitivity to the energy density input are analyzed in terms of thermal, metallurgical and mechanical responses during the AM process. Thereby, their influence is evaluated to deepen the understanding of AM processes and to improve the metal printing process.

### 5.1 Effect of the baseplate size

First, the evolution of the temperature field for two different baseplates is simulated and shown in Fig. 8. Note that when the laser beam crosses the center of the building region during the fabrication of the 1st layer, the large baseplate yields sharp thermal gradients (up to 8E + 6 °C/m) around the melt pool, while the maximum thermal gradient is lower than 5E + 5 °C/m for the small baseplate. After finishing the deposition of the 2nd layer, the average temperature of the small baseplate reaches about 800 °C, but it is less than 400 °C for the larger one. During the subsequent printing process (3rd–40th layers), the small baseplate holds the high-temperature field (Fig. 6b). However, the heat is slowly accumulated in the larger baseplate during the initial building stage and the quasi-steady state occurs after completing the deposition of more than 10 layers when the temperature field is of approximately 500 °C (Fig. 8a). Thus, the level of the heat accumulation is closely related with the baseplate size.

The microstructure and the microhardness at different building heights of the two manufactured blocks are shown in Fig. 9. Figure 9a schematically presents the locations

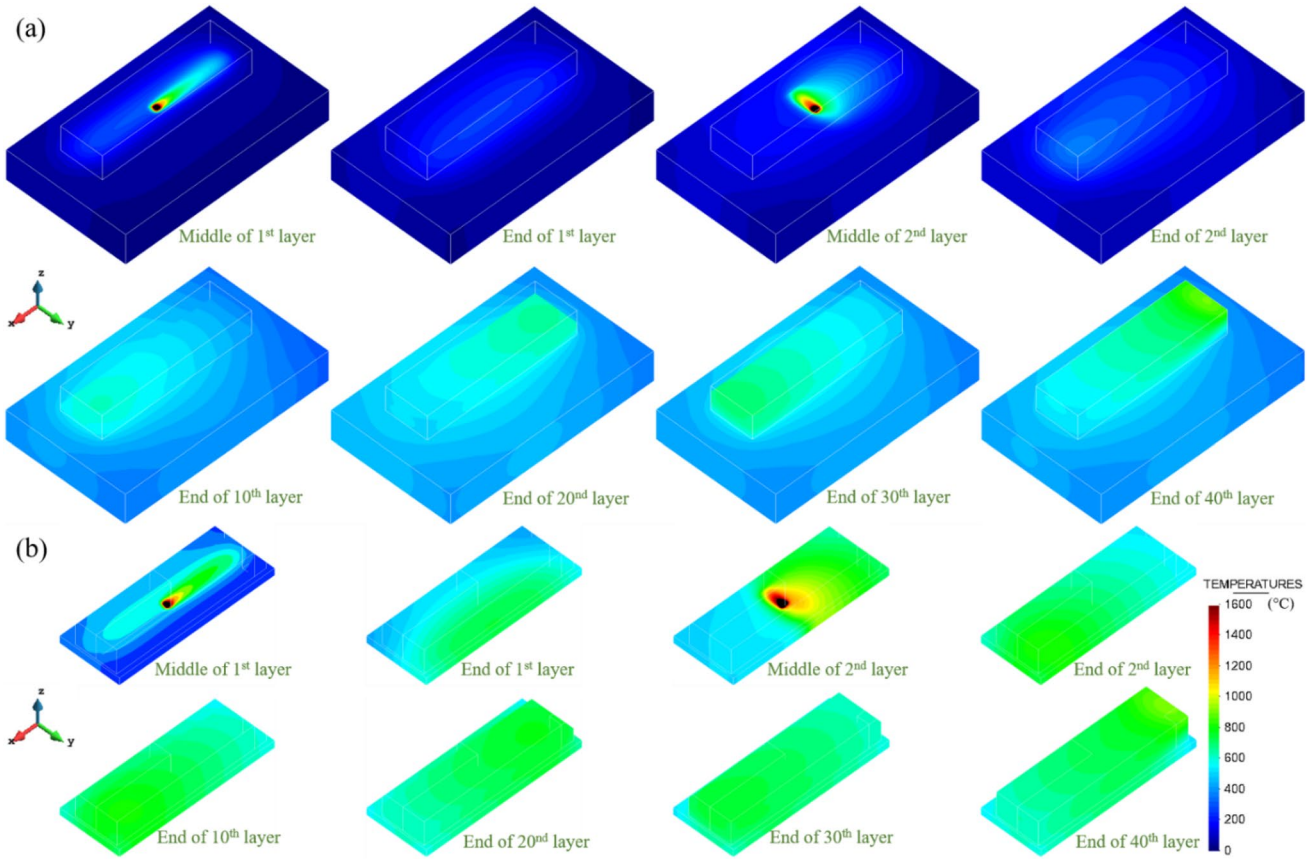


**Fig. 8** Temperature filed evolution in DED process in the cases of **a** the large baseplate, **b** the small baseplate

of interest. Figure 9b, c show the microstructures and the statistically averaged values in terms of α-lath width and the corresponding microhardness. Observe that the large baseplate achieves a relatively homogenous microstructural distribution ($\overline{W_\alpha} \approx 1.15\,\mu m$) and a consistent microhardness ($\overline{H} \approx 330\,HV$) along the building direction. This is not the case for the small baseplate, in which the α-lath at the lower part of the build experiences a remarkable coarsening by IHT ($W_\alpha = 2.21 \pm 0.27\,\mu m$) due to the high-temperature field which is above α dissolution temperature $T_{diss} = 747\,°C$ [23] (see Fig. 8b). As a result, the related microhardness decreases to about $H = 266 \pm 8\,HV$ (Fig. 9c). This is because by increasing the particle (α-lath) size the amount of sub-structure boundaries is reduced and, thus, hinders the dislocation slipping as the material deforms under loading. Therefore, the large baseplate is preferable from the metallurgical point of view.

Finally, the evolution of the stress field is analyzed for the two baseplates. Figure 10 shows the development of the von Mises stresses in the case of the large baseplate. Observe that during the printing of the 1st layer, the large thermal gradients lead to high thermal stress of approximately 700 MPa as the metal deposition cools down and shrinks. The deposition of the 2nd layer uses the shorter scan pattern which favors the heat concentration (Fig. 8a), relaxing the large stresses previously triggered, down to about 300 MPa (Fig. 10c, d). Nevertheless, the stresses resurge up to 500 MPa when the longer scan pattern is used to print the 3rd layer. This proves how reducing the scan length can mitigate residual stresses of AM parts, as reported in the literature [17, 32]. As the number of deposited layer increases, the stresses of the build gradually decrease because the overall temperature is higher and the temperature gradients are lower (Fig. 8a). When the buildup is finished, the maximum residual stresses appear at the build–baseplate interface, especially at the corners where the material suffers the highest thermal gradients and the strongest mechanical constraining from the baseplate. Figure 10j shows some details of the residual stress field for the large baseplate. Note that the tensile stresses in all the three directions are higher than to 700 MPa at the basement of the build, while the compressive stresses (above 250 MPa) exist at the upper part of the baseplate beneath the deposit. Such stress distribution is quite typical as reported in the literature [12, 33].

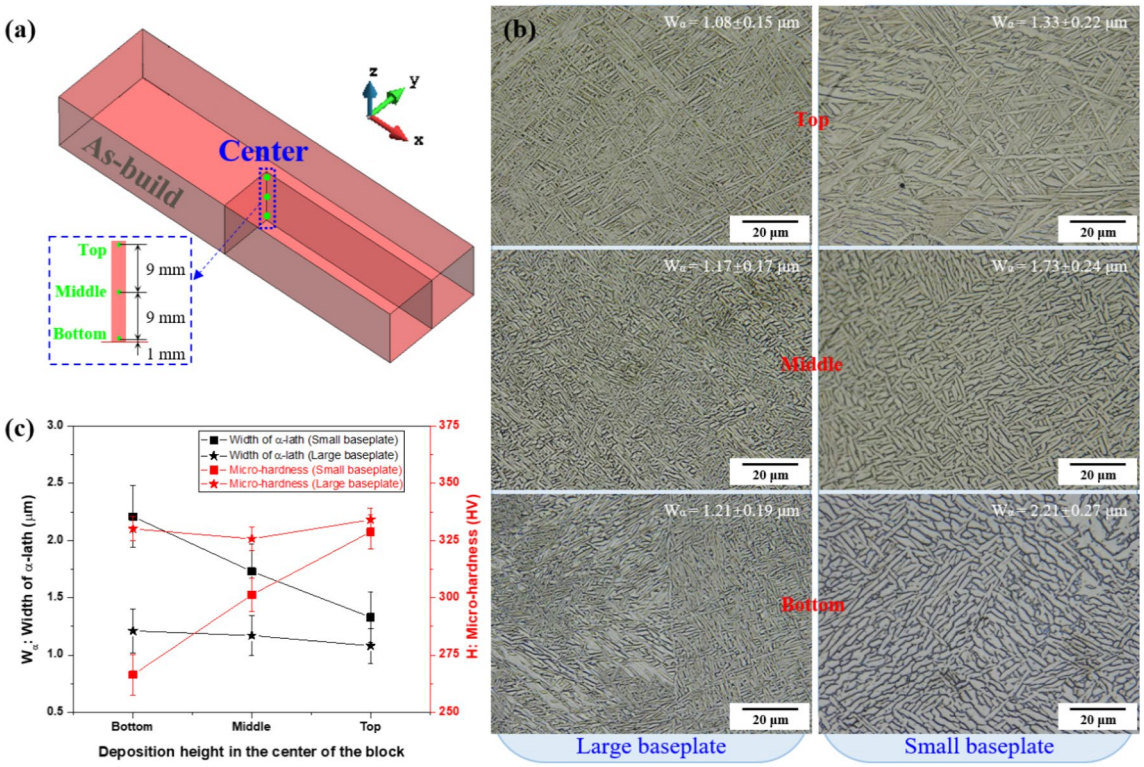


**Fig. 9** Comparison of the metallurgical response at different deposit heights for different baseplates: **a** locations of interest, **b** microstructure images, **c** α-lath width and the microhardness as a function of the deposition height

Figure 11 shows the evolution of the von Mises stresses when the small baseplate is used. Unlike the large baseplate, the small one achieves a pronounced stress reduction as the first two layers are built. During the subsequent printing process, the stresses in the part are lower than 150 MPa. Two reasons can justify this stress-relief: the weaker stiffness and the higher heat accumulation (annealing) in this baseplate (Fig. 8b). Hence, the small baseplate favors the stress mitigation in spite of yielding microstructural inhomogeneity.

Finally, Fig. 12 displays the part warpage at the end of the AM process for the two different baseplates. Observe that the maximum displacements of the blocks manufactured on the large and small baseplates are approximately 0.9 mm at the free end and about 0.6 mm at the deposition top, respectively.

## 5.2 Effect of the energy density

To mitigate the residual stress, especially for a thicker baseplate characterized by a higher stiffness, it is possible to play with the process parameters [34–37]. Thus, the influence of different input energy densities $E$ (see Table 1) on the mechanical behavior of large-scale AM blocks is studied in this section.

Figures 13 and 14 show the thermo-mechanical evolution in terms of temperature, thermal gradient and von Mises stresses at the center (point P) and corner (point Q) of the deposits, respectively. Note that as $E$ increases, the thermal gradients rise during the deposition of the first few layers, while all of them reduce to a lower level ($<5\text{E}+4$ °C/m) in the second half of the building process due to increased heat accumulation. On the one hand, higher energy density $E$ tends to produce larger thermal stresses; but, on the other hand, favors the stress mitigation by annealing because of the elevated-temperature over a long duration of time. Especially at the center of the block, the residual stress level reduces from 340 MPa for $E = 27\,\text{J/mm}^3$ to 70 MPa for $E = 80\,\text{J/mm}^3$ (see Fig. 13). Unlike the center, during the DED process the stresses notoriously fluctuate at the corner, where higher cooling rates exist. Notably, higher $E$ promotes the stress relief during the printing process, but triggers remarkable stress increments in the final cooling stage, and consequently, the residual stresses at point Q are very similar (495–545 MPa) for different $E$ (see Fig. 14). Note that the thermo-mechanical behaviors for the two points are not the same even for the same $E$ (see Figs. 13c, d and 14c, d). The reason for this is that the cooling time varies when using different scanning speeds, influencing the level of the heat accumulation and the stress annealing.

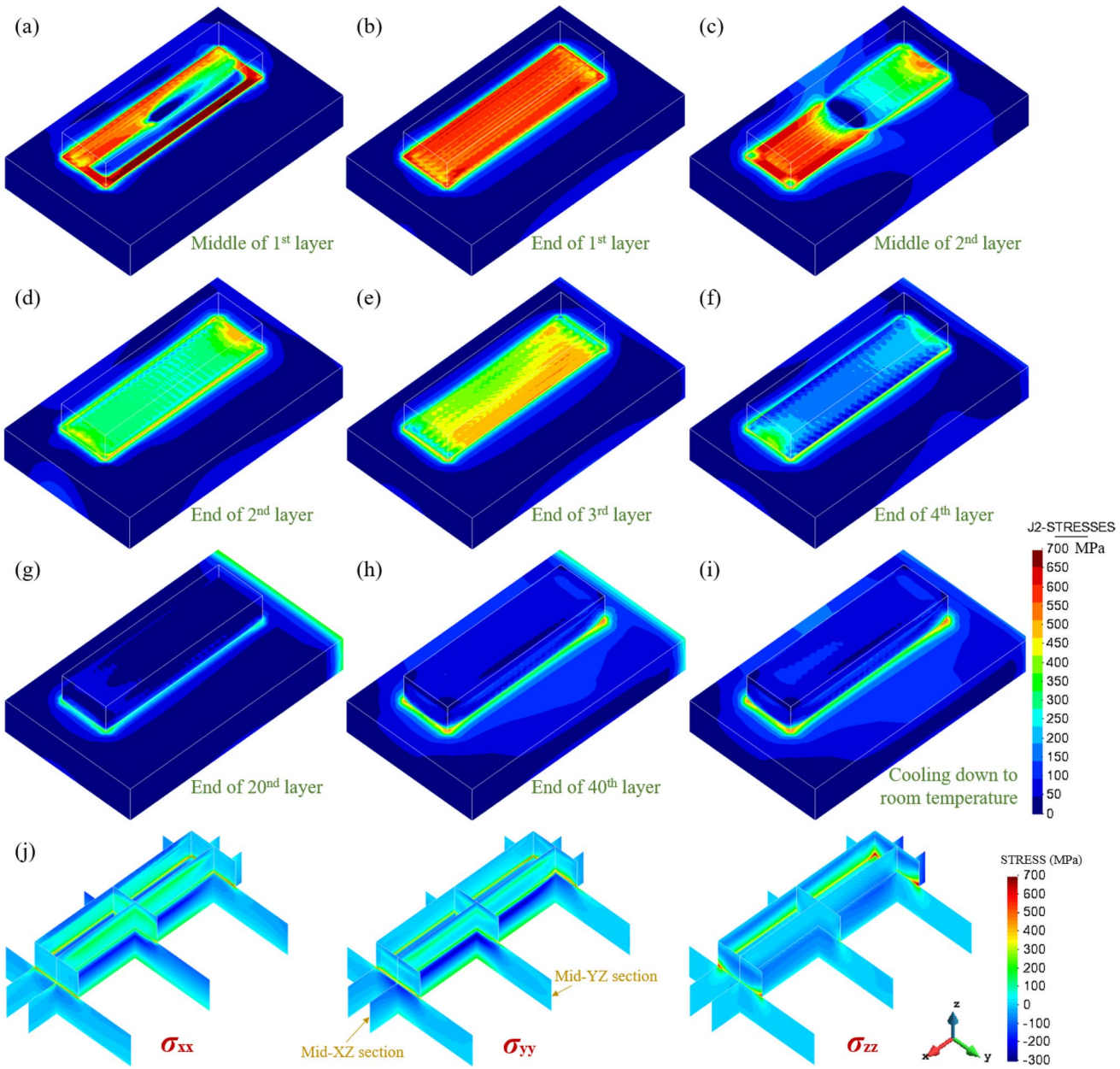


**Fig. 10** Large baseplate: **a–i** the evolution of Von Mises stress field, **j** the inside residual stresses in the three components

Figure 15a shows the residual von Mises stress fields for different energy densities $E$. Increasing $E$ reduces the stress accumulation at the basement of the large blocks due to the stress annealing. This is not the case for small AM parts that do not experience annealing temperatures [38, 39]. Figure 15b, c show the displacement field and the evolution of the vertical displacement at point M at the free end of the baseplate, respectively. It can be seen from Fig. 15b that the smallest $E$ leads to the largest displacement whereas the smallest value appears in the case of the moderate $E = 53\,\mathrm{J/mm^3}$. Such result can be explained as follows: increasing $E$, the displacements significantly grow in the initial deposition phase (Fig. 15c) due to the high thermal gradients (see Fig. 13). During the subsequent building process, the displacements gradually increase for $E = 27\,\mathrm{J/mm^3}$, but reduces for $E = 80\,\mathrm{J/mm^3}$. In the final cooling process, higher $E$ results in a larger displacement, up to 0.674 mm for $E = 80\,\mathrm{J/mm^3}$ ($V = 15\,\mathrm{mm/s}$), increasing the final warpage. Even though the residual stresses are mitigated by rising $E$, they are still high at the build–baseplate interface. Thus, the optimization of process parameters alone has a limited effect for controlling the residual stress in DED.

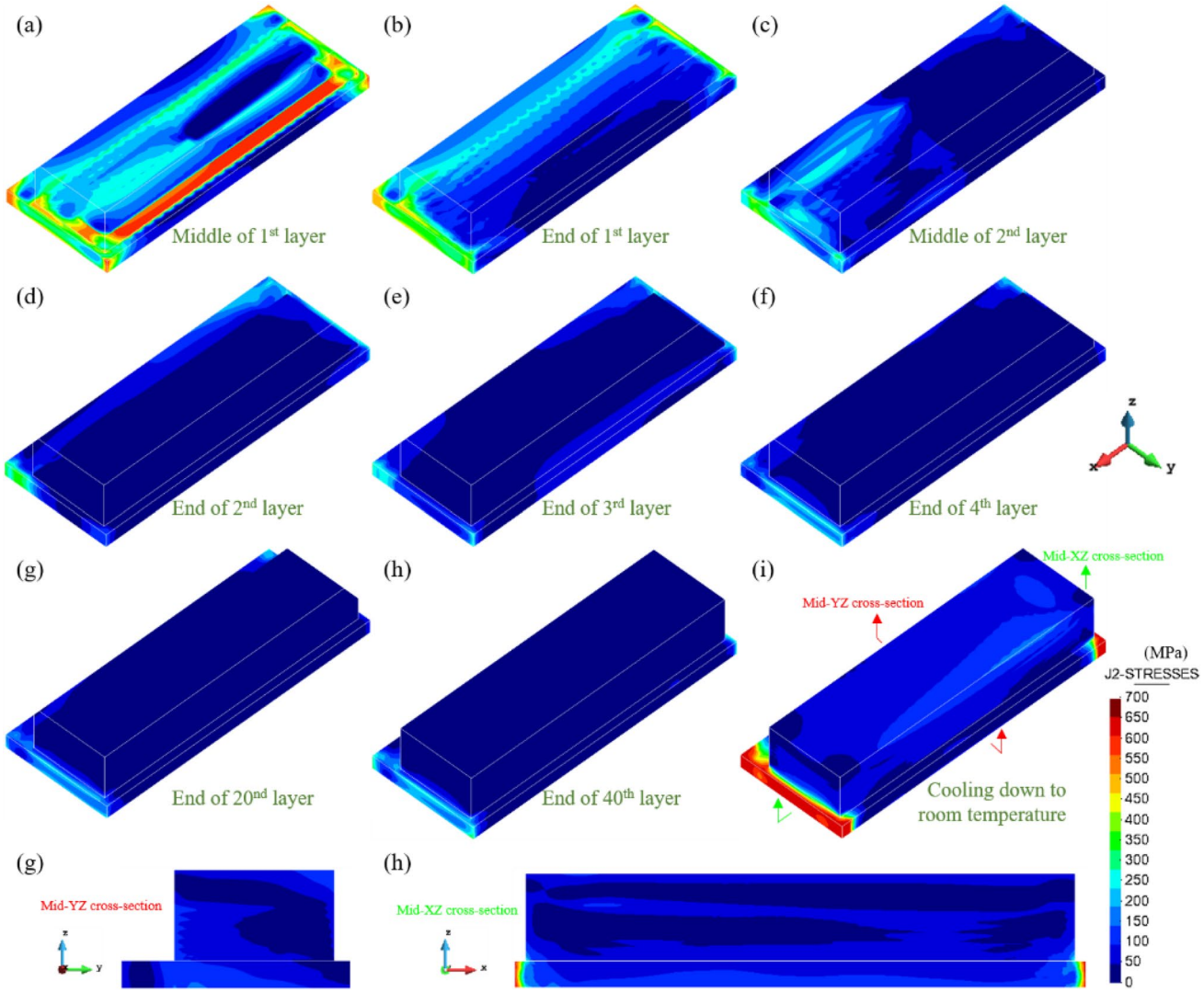


**Fig. 11** Small baseplate: the evolution of the von Mises stress field in DED process

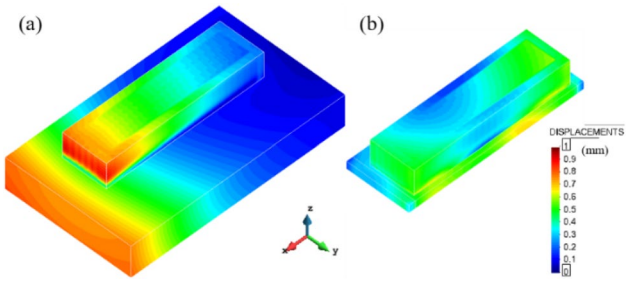


**Fig. 12** Final distortion (displacement norm) for **a** the large baseplate, **b** the small baseplate

## 6 Strategies for the concurrent control of microstructure and residual stresses

As concluded above, the small baseplate favors the reduction of the residual stresses but causes a non-uniform microstructure, and contrariwise for the large one. To achieve the control of both the residual stresses and the metallurgical quality, two strategies are proposed in the following, based on the thermo-mechanical response of the two baseplates used.

### 6.1 Structural optimization of the thick baseplates

Using a thick baseplate, a better homogeneity of the final metallurgy can be guaranteed in DED because of the high heat absorption which allows for a fast cooling of the melt pool. Thereby, only the mechanical response is analyzed in this section. Particularly, to mitigate the residual stresses

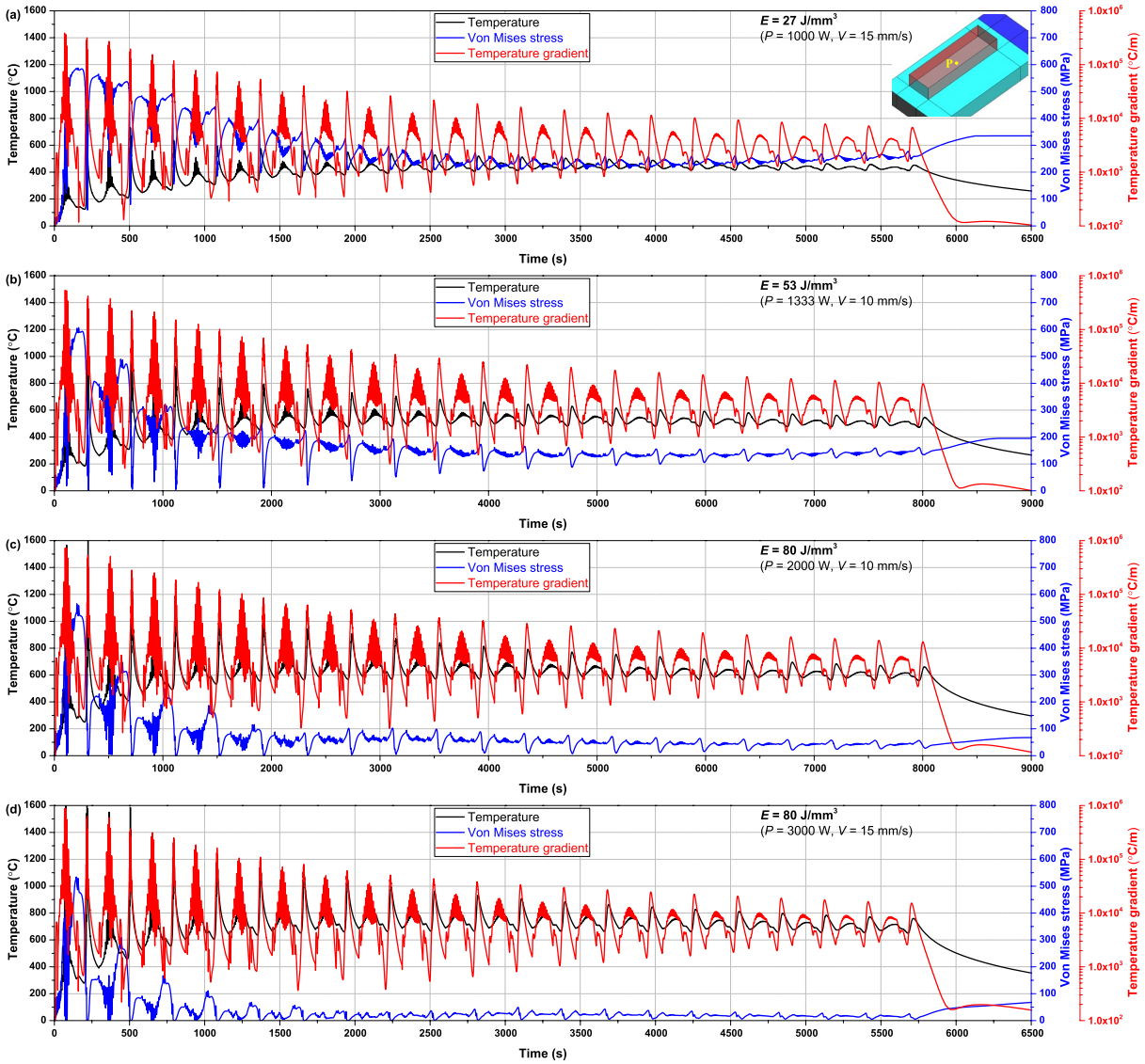


**Fig. 13** Evolution of temperature, von Mises stress and temperature gradient at point P at the center/bottom of the blocks for different energy densities

due to the strong constraining (stiff baseplate) of the AM-build, several grooves are added in the baseplates, as shown in Fig. 16.

Two types of groove settings are analyzed: the first proposal assumes the division of the baseplate into different smaller $1\times4$, $2\times7$ and $3\times10$ regions, respectively, with a uniform cutting depth of 10 mm. A second proposal considers an increasing cut depth of 5 mm, 10 mm and 15 mm, respectively, for a fix baseplate division into $3\times10$ regions.

In both cases, the two ends of all baseplates are clamped.

Figures 17a and 18a show the contour fills of residual von Mises stresses and the stress distributions at the deposit-baseplate interface for different baseplate structures, respectively. Observe that the original residual stresses, up to about 640 MPa of the reference configuration, are systematically mitigated by adding the grooves and especially at the block-baseplate interface. By increasing the layout density or the cut depth of the grooves, the residual stresses gradually reduce because of the higher flexibility of the baseplate. Note that increasing the cut depth results in a more pronounced influence on the residual stresses mitigation than increasing the density of the groves pattern. Notably, the residual stresses for a cut depth of 15 mm are the lowest. The stress value is further reduced after the baseplate removal.

Figures 17b and 18b display the final displacements contour fills and the displacement evolution on the top surface of the baseplate for different baseplate geometries. It can be observed the clear mitigation of the residual stresses compared to the reference configuration as well as the sensitivity to both the grooves density and the cutting depth.

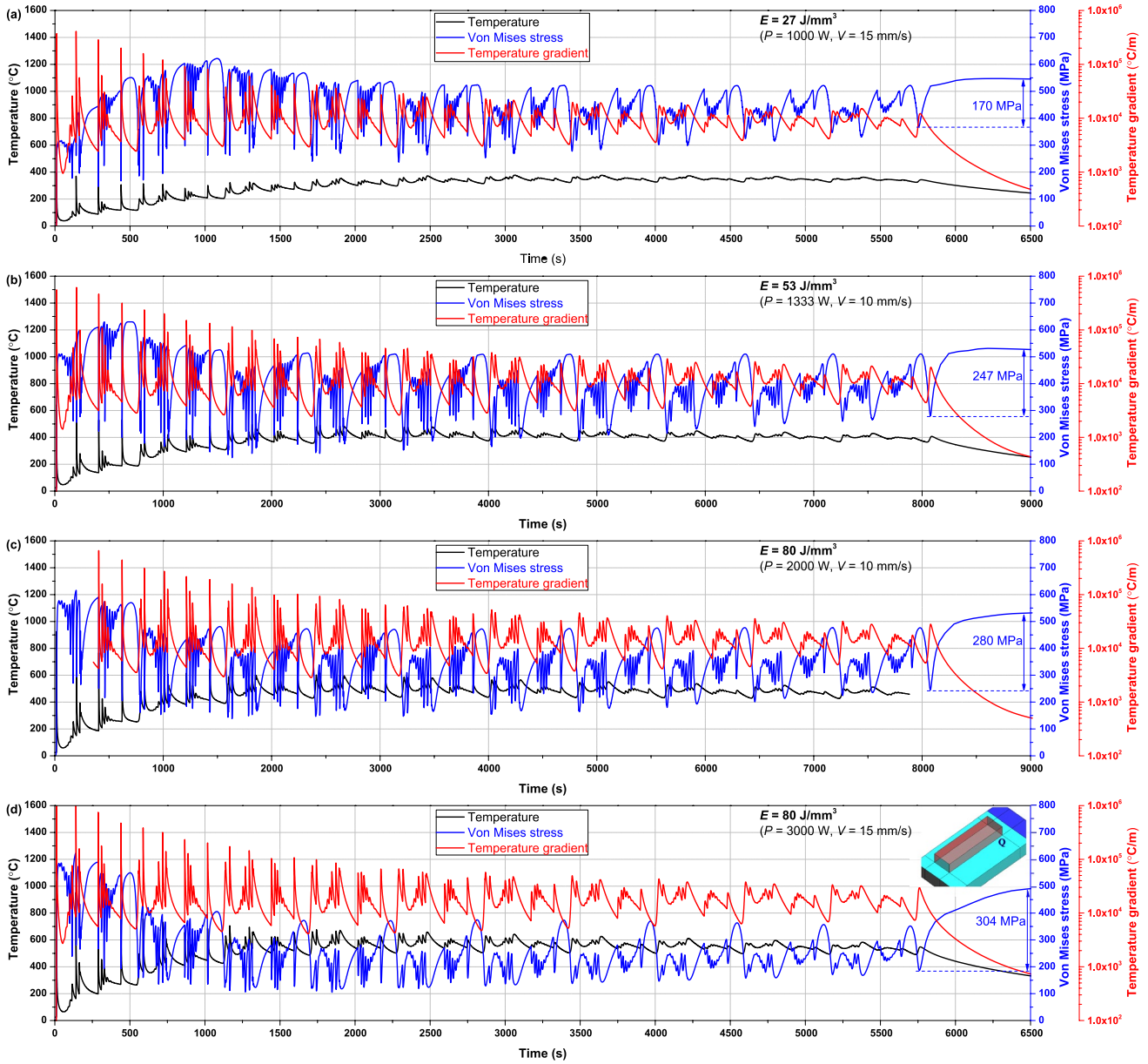


**Fig. 14** Evolution of temperature, von Mises stress and temperature gradient at point Q at the corner/bottom of the blocks for different energy densities

## 6.2 Forced cooling for the thin baseplate

When adopting a thin baseplate, the heat accumulation during the DED process allows for the microstructural coarsening. Moreover, the reduced stiffness of the support induces lower residual stresses. Hence, the proposed strategy consists of using a forced cooling to increase the heat loss (see Fig. 19a).

Highly purified argon with a flow rate of 50 L/min is used as cooling gas. Figure 19b shows the corresponding CAD models used in the simulation. The forced cooling is modelled assuming an increased HTC by convection of 95 W/(m$^2$ °C) at the bottom surface of the baseplate.

Figure 20a compares the in-situ measurements and temperature evolution as predicted by the thermal analysis at point N, located at the bottom/center of the baseplate 1 (see Fig. 19b). A remarkable agreement between them is obtained.

Based on this calibration, the thermal model is used to predict the temperature evolution at the bottom/center of the blocks (see Fig. 9a) for the thick and the thin baseplates, respectively, as shown Fig. 20b. Note that: (i) for

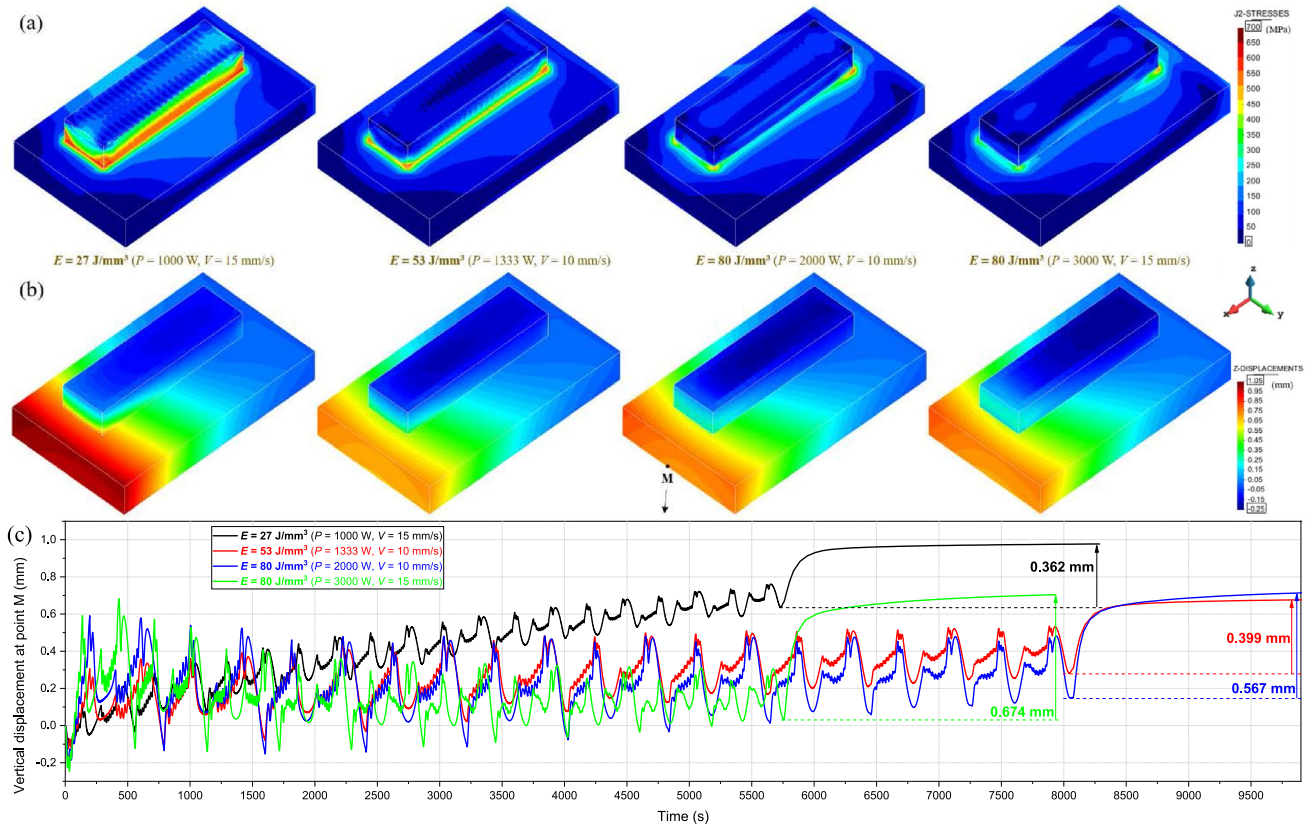


**Fig. 15** Mechanical response of the blocks for different energy densities: **a** residual von Mises stresses, **b** final vertical displacement distribution, **c** evolution of vertical displacement of point M at the free end of the baseplate

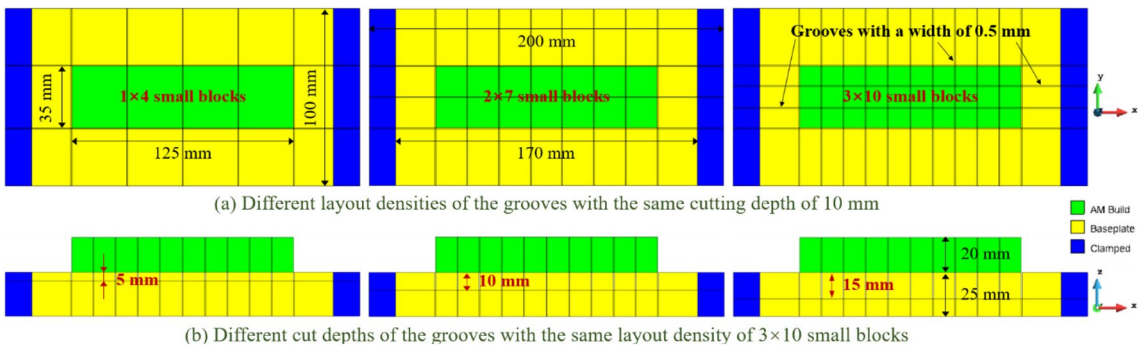


**Fig. 16** Baseplates with different groove settings

AM Ti–6Al–4V, the microstructures formed in the initial stage can be wiped out if the subsequent temperature field is above the β-transus temperature ($T_\beta \approx 1000\,°C$); and (ii) the $\alpha$ structures do not change (freezed) once the temperature is kept below $T_{diss}$ [23]. Thereby, only the thermal cycles in the yellow region are responsible for the final microstructural characterization. Thus, by applying the forced cooling to the thin baseplate it is possible to obtain a microstructure very similar to the one of the large baseplate.

In our previous work [21], an Integral Area (IA) index (the area colored in green in Fig. 20b) has been proposed to assess the α coarsening during DED process. The calculated IA are 1.11E + 5 °C s for the large baseplate (Fig. 5a) and 1.18E + 5 °C s for the thin baseplate with forced cooling, respectively. Such values are much lower than 1.19E + 6 °C s when the forced cooling is not adopted (see Fig. 9b). Hence, the forced cooling limits the microstructural coarsening induced by IHT during the whole printing process. Figure 21 shows the microstructures at different printing heights at the

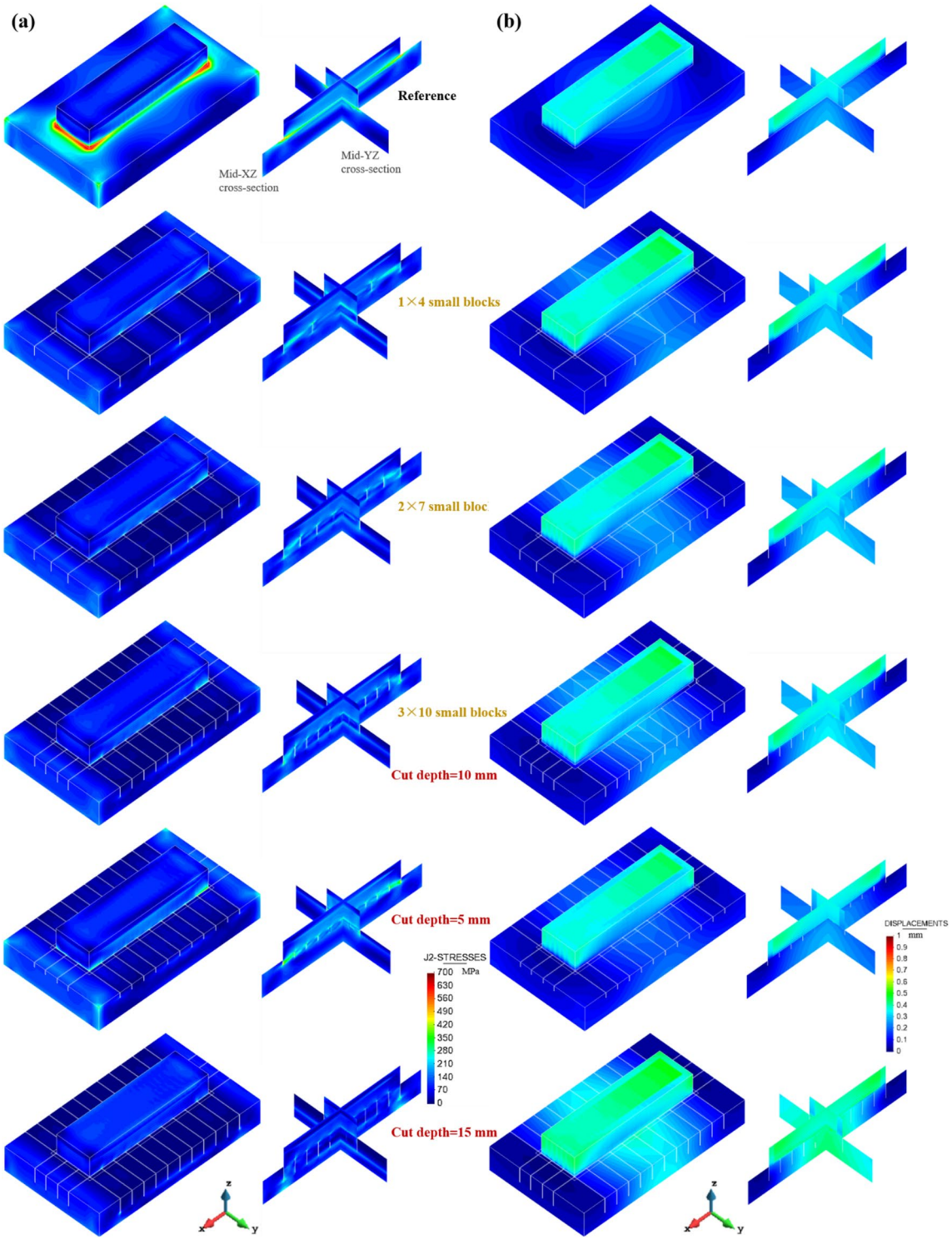


**Fig. 17** Stress analysis of the AM-blocks deposited on different baseplate structures: **a** residual von Mises stresses, **b** displacement norm

center of the block over the thin baseplate 1. Remarkably, a homogenous microstructural distribution is achieved, and the average width of α-lamellar is $\overline{W_\alpha} \approx 1.12\,\mu m$, similar to the one ($\overline{W_\alpha} \approx 1.15\,\mu m$) observed in the case of the large baseplate (see Fig. 9b).

Figure 22a shows the residual stress field of the block printed on the thin baseplate 1 (see Fig. 19b) with forced cooling. Observe that the basement near the clamp presents high residual stresses (up to 500 MPa) while the stress values in the inner zone are smaller. This is because after

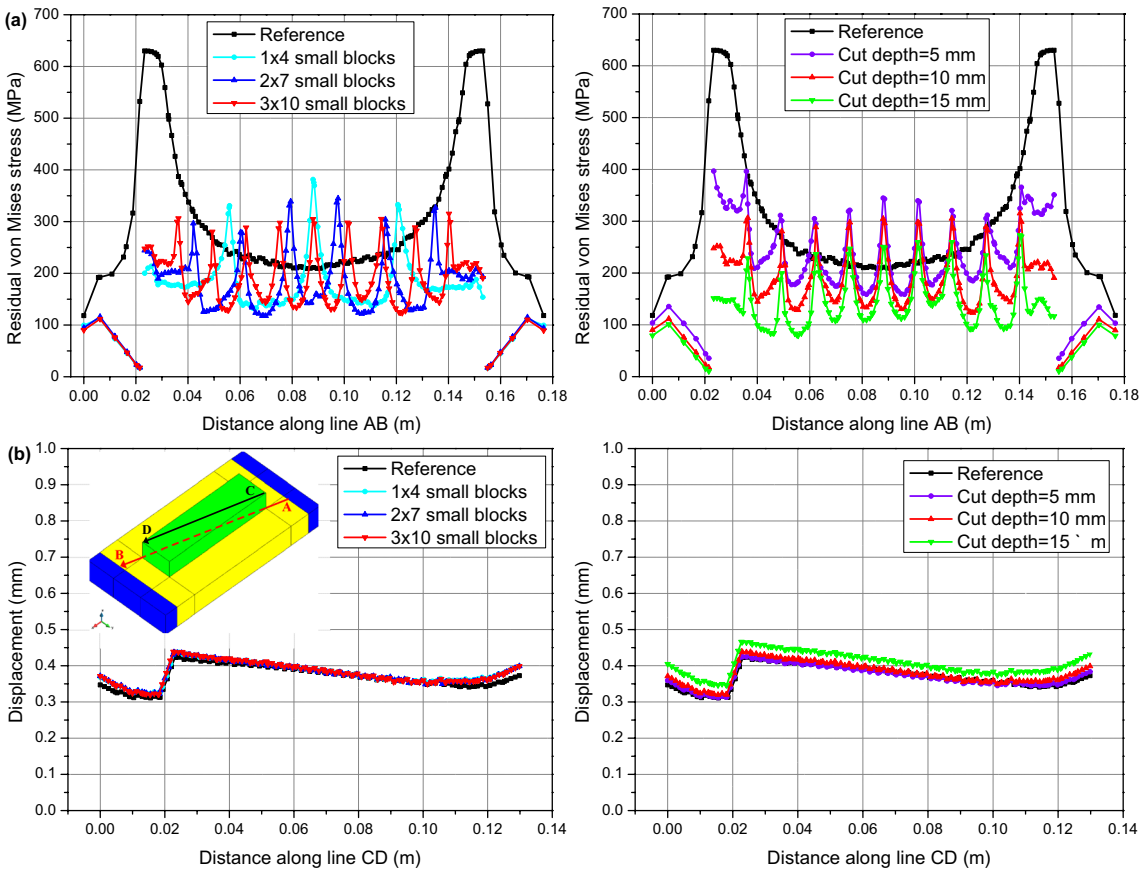


**Fig. 18** Distributions of **a** the residual von Mises stresses along the AB line at the baseplate top, **b** the final distortions (displacement norm) along the CD line at the deposit top

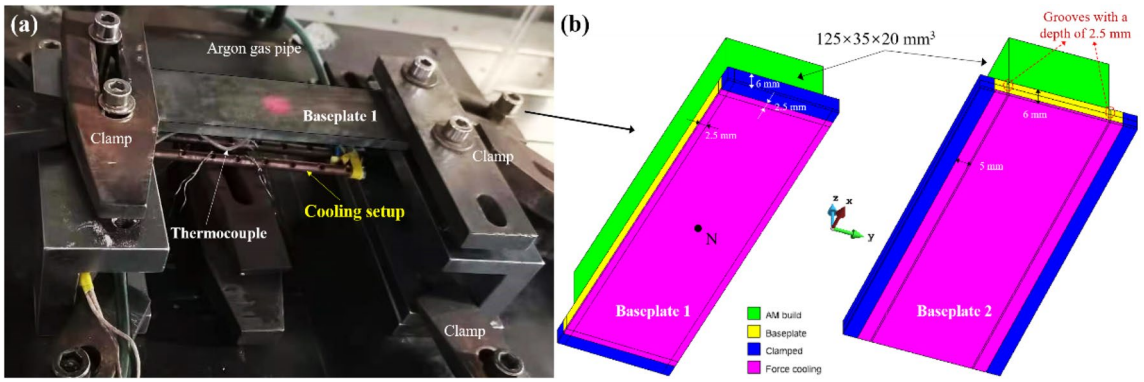


**Fig. 19** Forced cooling used to control the heat accumulation in the block: **a** experimental setup, **b** CAD geometrical models

printing the last layer, the metal deposition quickly cools and shrinks but such contraction is constrained by the baseplate clamping. Figure 22b, c show the predicted vertical displacement and the corresponding experimental result. It can be seen that a longitudinal bending is produced, leading to an unacceptable deformation (up to 1.4 mm) at the bottom/middle of the fabricated block.

To reduce this distortion, the geometry of the baseplate is further optimized to achieve the final design of baseplate 2 (see Fig. 19b). Figure 23 shows the results of the block fabricated on the baseplate 2 with forced cooling. In this case both the residual stresses and the part warpage are smaller.

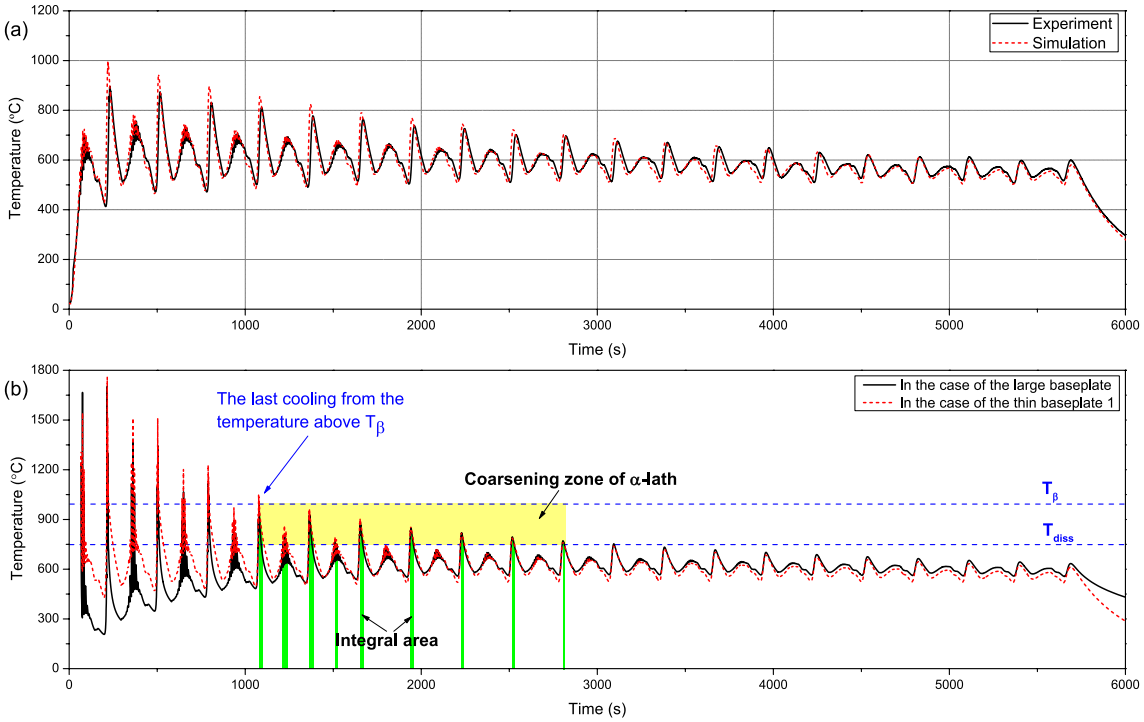


**Fig. 20** **a** Comparison between the measured and numerical thermal histories of point N at the bottom/center of the baseplate, **b** comparison of the temperature evolutions at the bottom/center of the blocks printed on the large and thin baseplates

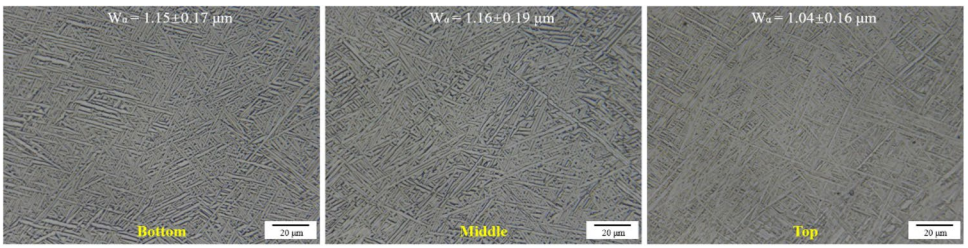


**Fig. 21** Microstructures at different building heights in the center of the block deposited on the thin baseplate 1 with forced cooling

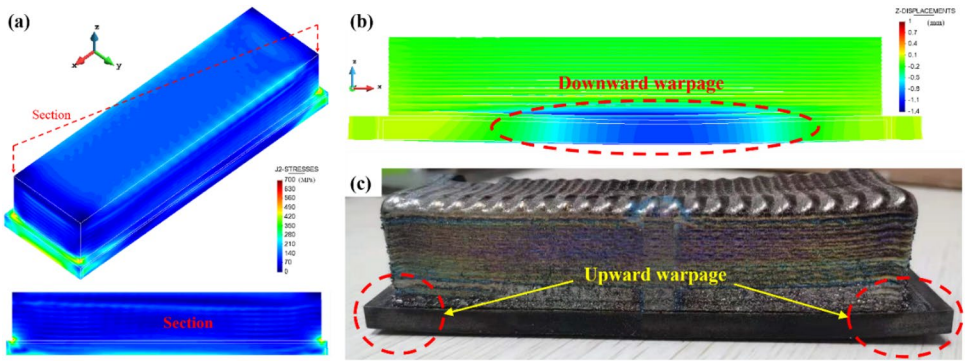


**Fig. 22** Thin baseplate-1 with forced cooling: simulated results of **a** the residual stress field and **b** the vertical displacements of the block part before releasing the clamping, **c** experimental result of distortion after releasing the clamping

Thus, the proposed cooling strategy and the new baseplate design can accomplish with the microstructure control without a significant increase of the residual stresses and warpages of the AM part.

## 7 Conclusions

In this study, different strategies for the simultaneous control of the residual stress accumulation and the microstructural

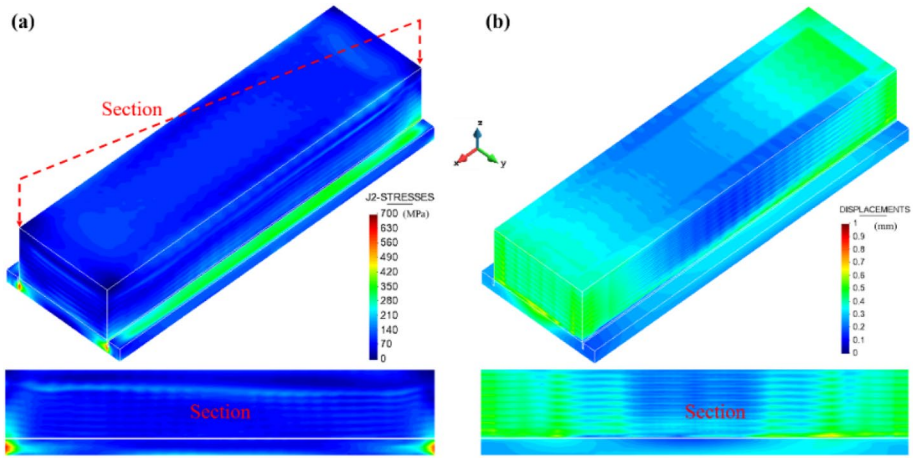


**Fig. 23** Thin baseplate 2 with forced cooling **a** residual stresses, **b** the final distortion (displacement norm) of the block

evolution during the DED process are proposed.

A 3D thermo-mechanical FE model suitable for DED processes is first calibrated by in-situ temperature and displacement measurements. The validated model is used to analyze the influence of the baseplate size and the energy density input on both the microstructure evolution and the induced residual stresses.

The main conclusions drawn are as follows:

(1) The simulation software is a powerful tool to simulate the DED process as confirmed by the remarkable agreement with the in-situ experimental evidence. Thus, the software can be used to optimize the DED processes by modifying the baseplate design, the process parameters (e.g. the energy density) or the boundary conditions (e.g. forced cooling).

(2) The size of the baseplate influences the whole thermo-mechanical behavior of the AM components: the temperature field, the heat capacity and the actual stiffness (constraining) depend on the baseplate thickness. Thicker baseplates are able to faster dissipate the power input allowing for a finer and more uniform microstructure. However, the higher stiffness produces higher residual stresses; contrariwise for thinner baseplate.

(3) To simultaneously mitigate the residual stresses while controlling the microstructural evolution in DED, two strategies are proposed. On the one hand, when a thick baseplate is adopted, it is possible to introduce a groove pattern to split the surface of the baseplate into smaller regions offering a reduced constraining to the metal deposition and avoiding stress concentrations. Hence, the final residual stresses can be effectively mitigated. On the other hand, a forced cooling under the bottom surface of thin baseplates can increase the heat dissipation favoring the formation of more uniform and finer microstructures. Moreover, the higher flexibility of the thin baseplate avoids stress accumulation but the warpage must be monitored.

**Acknowledgements** This work was funded by the National Key R&D Program of China (No. 2016YFB1100100), the European KYKLOS 4.0 project: An Advanced Circular and Agile Manufacturing Ecosystem based on rapid reconfigurable manufacturing process and individualized consumer preferences (no. 872570), and the China Scholarship Council (no. 201906290011).

## Declarations

**Conflict of interest** The author declares that they have no conflict of interest.

## References

1. Gu D, Shi X, Poprawe R, Bourell D, Setchi R, Zhu J (2021) Material-structure-performance integrated laser-metal additive manufacturing. Science. https://doi.org/10.1126/science.abg1487
2. Baiges J, Chiumenti M, Moreira CA, Cervera M, Codina R (2021) An adaptive finite element strategy for the numerical simulation of additive manufacturing processes. Addit Manuf 37:101650. https://doi.org/10.1016/j.addma.2020.101650
3. Xue A, Lin X, Wang L, Lu X, Ding H, Huang W (2021) Heat-affected coarsening of β grain in titanium alloy during laser directed energy deposition. Scripta Mater 205:114180. https://doi.org/10.1016/j.scriptamat.2021.114180
4. Lu X, Chiumenti M, Cervera M, Tan H, Lin X, Wang S (2021) Warpage analysis and control of thin-walled structures manufactured by laser powder bed fusion. Metals 11(5):686. https://doi.org/10.3390/met11050686
5. Zhao Z, Chen J, Lu X, Tan H, Lin X, Huang W (2017) Formation mechanism of the α variant and its influence on the tensile properties of laser solid formed Ti-6Al-4V titanium alloy. Mater Sci Eng A 691:16–24. https://doi.org/10.1016/j.msea.2017.03.035
6. Chiumenti M, Neiva E, Salsi E, Cervera M, Badia S, Moya J, Chen Z, Lee C, Davies C (2017) Numerical modelling and experimental

validation in selective laser melting. Addit Manuf 18:171–185. https://doi.org/10.1016/j.addma.2017.09.002
7. Lu X, Lin X, Chiumenti M, Cervera M, Li J, Ma L, Wei L, Hu Y, Huang W (2018) Finite element analysis and experimental validation of the thermomechanical behavior in laser solid forming of Ti-6Al-4V. Addit Manuf 21:30–40. https://doi.org/10.1016/j.addma.2018.02.003
8. Cao Y, Lin X, Kang N, Ma L, Wei L, Zheng M, Yu J, Peng D, Huang W (2021) A novel high-efficient finite element analysis method of powder bed fusion additive manufacturing. Addit Manuf. https://doi.org/10.1016/j.addma.2021.102187
9. Lu X, Chiumenti M, Cervera M, Li J, Lin X, Ma L, Zhang G, Liang E (2021) Substrate design to minimize residual stresses in directed energy deposition AM processes. Mater Des 202:109525. https://doi.org/10.1016/j.matdes.2021.109525
10. Chiumenti M, Lin X, Cervera M, Lei W, Zheng Y, Huang W (2017) Numerical simulation and experimental calibration of additive manufacturing by blown powder technology. Part I: thermal analysis. Rapid Prototyp J 23(2):448–463. https://doi.org/10.1108/RPJ-10-2015-0136
11. Smith J, Xiong W, Cao J, Liu W (2016) Thermodynamically consistent microstructure prediction of additively manufactured materials. Comput Mech 57(3):359–370. https://doi.org/10.1007/s00466-015-1243-1
12. Denlinger E, Michaleris P (2016) Effect of stress relaxation on distortion in additive manufacturing process modeling. Addit Manuf 12:51–59. https://doi.org/10.1016/j.addma.2016.06.011
13. Wang Z, Stoica A, Ma D, Beese A (2017) Stress relaxation behavior and mechanisms in Ti-6Al-4V determined via in situ neutron diffraction: application to additive manufacturing. Mater Sci Eng A 707:585–592. https://doi.org/10.1016/j.msea.2017.09.071
14. Mukherjee T, Manvatkar V, De A, DebRoy T (2017) Mitigation of thermal distortion during additive manufacturing. Scripta Mater 127:79–83. https://doi.org/10.1016/j.scriptamat.2016.09.001
15. Lu X, Lin X, Chiumenti M, Cervera M, Hu Y, Ji X, Ma L, Yang H, Huang W (2019) Residual stress and distortion of rectangular and s-shaped Ti-6Al-4V parts by directed energy deposition: modelling and experimental calibration. Addit Manuf 26:166–179. https://doi.org/10.1016/j.addma.2019.02.001
16. Cao J, Gharghouri M, Nash P (2016) Finite-element analysis and experimental validation of thermal residual stress and distortion in electron beam additive manufactured Ti-6Al-4V build plates. J Mater Process Technol 237:409–419. https://doi.org/10.1016/j.jmatprotec.2016.06.032
17. Lu X, Cervera M, Chiumenti M, Li J, Ji X, Zhang G, Lin X (2020) Modeling of the effect of the building strategy on the thermomechanical response of Ti-6Al-4V rectangular parts manufactured by laser directed energy deposition. Metals 10(12):1643. https://doi.org/10.3390/met10121643
18. Chen W, Xu L, Han Y, Zhao L, Jing H (2021) Control of residual stress in metal additive manufacturing by low-temperature solid-state phase transformation: an experimental and numerical study. Addit Manuf 42:102016. https://doi.org/10.1016/j.addma.2021.102016
19. Hong M, Kim Y (2020) Residual stress reduction technology in heterogeneous metal additive manufacturing. Materials 13(23):5516. https://doi.org/10.3390/ma13235516
20. Zhao Z, Chen J, Tan H, Tang J, Lin X (2020) In situ tailoring microstructure in laser solid formed titanium alloy for superior fatigue crack growth resistance. Scripta Mater 174:53–57. https://doi.org/10.1016/j.scriptamat.2019.08.028
21. Lu X, Zhang G, Li J, Cervera M, Chiumenti M, Chen J, Lin X, Huang W (2021) Simulation-assisted investigation on the formation of layer bands and the microstructural evolution in directed energy deposition of Ti6Al4V blocks. Virtual Phys Prototyp. https://doi.org/10.1080/17452759.2021.1942077
22. Song T, Dong T, Lu SL, Kondoh K, Das R, Brandt M, Qian M (2021) Simulation-informed laser metal powder deposition of Ti-6Al-4V with ultrafine α-β lamellar structures for desired tensile properties. Addit Manuf 46:102139. https://doi.org/10.1016/j.addma.2021.102139
23. Wang J, Lin X, Li J, Hu Y, Zhou Y, Wang C, Li Q, Huang W (2019) Effects of deposition strategies on macro/microstructure and mechanical properties of wire and arc additive manufactured Ti6Al4 V. Mater Sci Eng A 754:735–749. https://doi.org/10.1016/j.msea.2019.03.001
24. Kürnsteiner P, Wilms MB, Weisheit A, Gault B, Jägle EA, Raabe D (2020) High-strength damascus steel by additive manufacturing. Nature 582(7831):515–519. https://doi.org/10.1038/s41586-020-2409-3
25. Chiumenti M, Cervera M, Moreira C, Barbat G (2021) Stress, strain and dissipation accurate 3-field formulation for inelastic isochoric deformation. Finite Elem Anal Des 192:103534. https://doi.org/10.1016/j.finel.2021.103534
26. Chiumenti M, Cervera M, Salmi A, Saracibar CA, Dialami N, Matsui K (2010) Finite element modeling of multi-pass welding and shaped metal deposition processes. Comput Methods Appl Mech Eng 199(37–40):2343–2359. https://doi.org/10.1016/j.cma.2010.02.018
27. Lu X, Lin X, Chiumenti M, Cervera M, Hu Y, Ji X, Ma L, Huang W (2019) In situ measurements and thermomechanical simulation of Ti-6Al-4V laser solid forming processes. Int J Mech Sci 153–154:119–130. https://doi.org/10.1016/j.ijmecsci.2019.01.043
28. Chiumenti M, Cervera M, Dialami N, Wu B, Jinwei L, Saracibar CA (2016) Numerical modeling of the electron beam welding and its experimental validation. Finite Elem Anal Des 121:118–133. https://doi.org/10.1016/j.finel.2016.07.003
29. Neiva E, Chiumenti M, Cervera M, Salsi E, Piscopo G, Badia S, Martín A, Chen Z, Lee C, Davies C (2020) Numerical modelling of heat transfer and experimental validation in powder-bed fusion with the virtual domain approximation. Finite Elem Anal Des 168:103343. https://doi.org/10.1016/j.finel.2019.103343
30. GiD, The Personal Pre and Post-Processor, CIMNE, Technical University of Catalonia, 2002. https://www.cimne.com/comet
31. Fallah V, Alimardani M, Corbin S, Khajepour A (2011) Temporal development of melt-pool morphology and clad geometry in laser powder deposition. Comput Mater Sci 50(7):2124–2134. https://doi.org/10.1016/j.commatsci.2011.02.018
32. Promoppatum P, Uthaisangsuk V (2021) Part scale estimation of residual stress development in laser powder bed fusion additive manufacturing of Inconel 718. Finite Elem Anal Des 189:103528. https://doi.org/10.1016/j.finel.2021.103528
33. Wu Q, Mukherjee T, Liu C, Lu J, DebRoy T (2019) Residual stresses and distortion in the patterned printing of titanium and nickel alloys. Addit Manuf 29:100808. https://doi.org/10.1016/j.addma.2019.100808
34. Wei H, Mukherjee T, Zhang W, Zuback J, Knapp G, De A, DebRoy T (2021) Mechanistic models for additive manufacturing of metallic components. Prog Mater Sci 116:100703. https://doi.org/10.1016/j.pmatsci.2020.100703
35. Yeung H, Lane B, Fox J (2019) Part geometry and conduction-based laser power control for powder bed fusion additive manufacturing. Addit Manuf 30:100844. https://doi.org/10.1016/j.addma.2019.100844
36. Carraturo M, Lane B, Yeung H, Kollmannsberger S, Reali A, Auricchio F (2020) Numerical evaluation of advanced laser control strategies influence on residual stresses for laser powder bed fusion systems. Integr Mater Manuf Innov 9(4):435–445. https://doi.org/10.1007/s40192-020-00191-3
37. Williams R, Piglione A, Rønneberg T, Jones C, Pham M, Davies C, Hooper P (2019) In situ thermography for laser powder bed

fusion: effects of layer temperature on porosity, microstructure and mechanical properties. Addit Manuf 30:100880. https://doi.org/10.1016/j.addma.2019.100880

38. Mishurova T, Artzt K, Haubrich J, Requena G, Bruno G (2019) Exploring the correlation between subsurface residual stresses and manufacturing parameters in laser powder bed fused Ti-6Al-4V. Metals 9(2):261. https://doi.org/10.3390/met9020261
39. Li H, Ramezani M, Chen Z, Singamneni S (2019) Effects of process parameters on temperature and stress distributions during selective laser melting of Ti–6Al–4V. Trans Indian Inst Met 72(12):3201–3214. https://doi.org/10.1007/s12666-019-01785-y